EDITED BY
C.A. Brebbia & M. Maugeri

EARTHQUAKE RESISTANT ENGINEERING STRUCTURES VIII

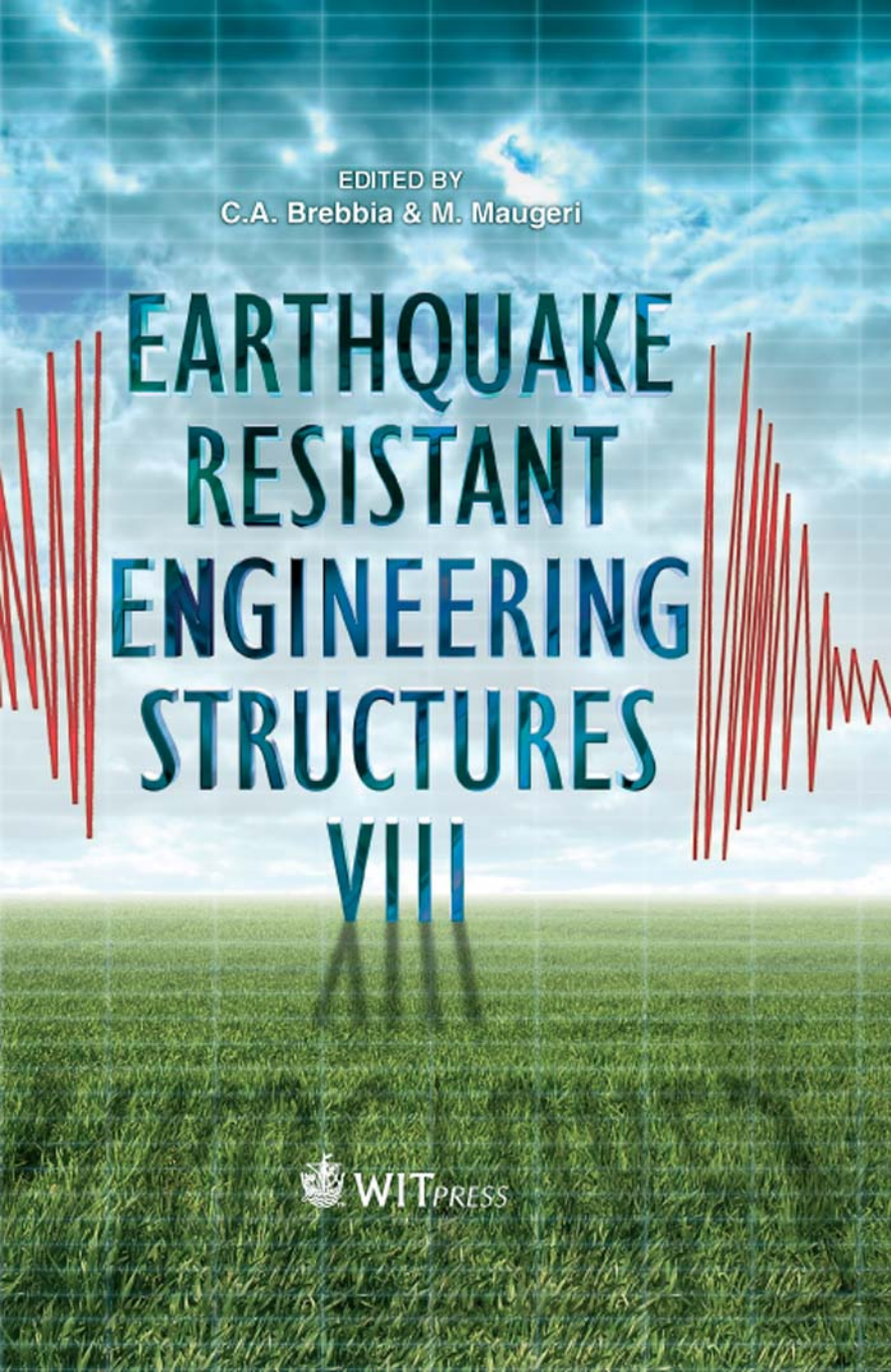

WIT PRESS

EIGHTH WORLD CONFERENCE ON
EARTHQUAKE RESISTANT ENGINEERING STRUCTURES

ERES VIII

CONFERENCE CHAIRMEN

C.A. Brebbia
Wessex Institute of Technology, UK
M. Maugeri
University of Catania, Italy

INTERNATIONAL SCIENTIFIC ADVISORY COMMITTEE

Y. Ariga
G. Dundulis
K. Fuchida
P. Komodromos
A. Martelli
M. Maugeri
M. Phocas
E. Sapountzakis
O. Sircovich Saar

Organised by
Wessex Institute of Technology, UK

Sponsored by
WIT Transactions on The Built Environment

WIT Transactions

Transactions Editor

Carlos Brebbia
Wessex Institute of Technology
Ashurst Lodge, Ashurst
Southampton SO40 7AA, UK
Email: carlos@wessex.ac.uk

Editorial Board

Earthquake Resistant Engineering Structures VIII

WIT PRESS

WIT Press publishes leading books in Science and Technology.
Visit our website for the current list of titles.
www.witpress.com

WIT eLibrary

Home of the Transactions of the Wessex Institute.
Papers presented at ERES VIII are archived in the WIT elibrary in volume 120 of
WIT Transactions on The Built Environment (ISSN 1743-3509).
The WIT electronic-library provides the international scientific community with
immediate and permanent access to individual papers presented at WIT conferences.
Visit the WIT eLibrary at www.witpress.com.

B Ribas Spanish National Centre for Environmental Health, Spain

K Richter Graz University of Technology, Austria

S Rinaldi Politecnico di Milano, Italy

F Robuste Universitat Politecnica de Catalunya, Spain

J Roddick Flinders University, Australia

A C Rodrigues Universidade Nova de Lisboa, Portugal

F Rodrigues Poly Institute of Porto, Portugal

C W Roeder University of Washington, USA

J M Roesset Texas A & M University, USA

W Roetzel Universitaet der Bundeswehr Hamburg, Germany

V Roje University of Split, Croatia

R Rosset Laboratoire d'Aerologie, France

J L Rubio Centro de Investigaciones sobre Desertificacion, Spain

T J Rudolphi Iowa State University, USA

S Russenchuck Magnet Group, Switzerland

H Ryssel Fraunhofer Institut Integrierte Schaltungen, Germany

S G Saad American University in Cairo, Egypt

M Saiidi University of Nevada-Reno, USA

R San Jose Technical University of Madrid, Spain

F J Sanchez-Sesma Instituto Mexicano del Petroleo, Mexico

B Sarler Nova Gorica Polytechnic, Slovenia

S A Savidis Technische Universitat Berlin, Germany

A Savini Universita de Pavia, Italy

G Schmid Ruhr-Universitat Bochum, Germany

R Schmidt RWTH Aachen, Germany

B Scholtes Universitaet of Kassel, Germany

W Schreiber University of Alabama, USA

A P S Selvadurai McGill University, Canada

J J Sendra University of Seville, Spain

J J Sharp Memorial University of Newfoundland, Canada

Q Shen Massachusetts Institute of Technology, USA

X Shixiong Fudan University, China

G C Sih Lehigh University, USA

L C Simoes University of Coimbra, Portugal

A C Singhal Arizona State University, USA

P Skerget University of Maribor, Slovenia

J Sladek Slovak Academy of Sciences, Slovakia

V Sladek Slovak Academy of Sciences, Slovakia

A C M Sousa University of New Brunswick, Canada

H Sozer Illinois Institute of Technology, USA

D B Spalding CHAM, UK

P D Spanos Rice University, USA

T Speck Albert-Ludwigs-Universitaet Freiburg, Germany

C C Spyrakos National Technical University of Athens, Greece

I V Stangeeva St Petersburg University, Russia

J Stasiek Technical University of Gdansk, Poland

G E Swaters University of Alberta, Canada

S Syngellakis University of Southampton, UK

J Szmyd University of Mining and Metallurgy, Poland

S T Tadano Hokkaido University, Japan

H Takemiya Okayama University, Japan

I Takewaki Kyoto University, Japan

C-L Tan Carleton University, Canada

E Taniguchi Kyoto University, Japan

S Tanimura Aichi University of Technology, Japan

J L Tassoulas University of Texas at Austin, USA

M A P Taylor University of South Australia, Australia

A Terranova Politecnico di Milano, Italy

A G Tijhuis Technische Universiteit Eindhoven, Netherlands

T Tirabassi Institute FISBAT-CNR, Italy

S Tkachenko Otto-von-Guericke-University, Germany

N Tosaka Nihon University, Japan

T Tran-Cong University of Southern Queensland, Australia

R Tremblay Ecole Polytechnique, Canada

I Tsukrov University of New Hampshire, USA

R Turra CINECA Interuniversity Computing Centre, Italy

S G Tushinski Moscow State University, Russia

J-L Uso Universitat Jaume I, Spain

E Van den Bulck Katholieke Universiteit Leuven, Belgium

Earthquake Resistant Engineering Structures VIII

Editors

C.A. Brebbia
Wessex Institute of Technology, UK
M. Maugeri
University of Catania, Italy

WIT*PRESS* **Southampton, Boston**

Editors:

C.A. Brebbia
Wessex Institute of Technology, UK

M. Maugeri
University of Catania, Italy

Published by
WIT Press
Ashurst Lodge, Ashurst, Southampton, SO40 7AA, UK
Tel: 44 (0) 238 029 3223; Fax: 44 (0) 238 029 2853
E-Mail: witpress@witpress.com
http://www.witpress.com

For USA, Canada and Mexico

Computational Mechanics Inc
25 Bridge Street, Billerica, MA 01821, USA
Tel: 978 667 5841; Fax: 978 667 7582
E-Mail: infousa@witpress.com
http://www.witpress.com

British Library Cataloguing-in-Publication Data

A Catalogue record for this book is available
from the British Library

ISBN: 978-1-84564-548-9
ISSN: 1746-4498 (print)
ISSN: 1743-3509 (on-line)

The texts of the papers in this volume were set individually by the authors or under their supervision. Only minor corrections to the text may have been carried out by the publisher.

Printed in Great Britain by CMP (UK) Ltd, Poole, Dorset.

Preface

The 1st Earthquake Resistant Engineering Structures Conference was held in Thessaloniki organised by the School of Engineering of Aristotle University and the Wessex Institute of Technology. Since then it has been reconvened in a series of outstanding locations and in collaboration with local institutions. The 2011 meeting was held in Tuscany in a region rich in the type of cultural and architectural heritage that needs to be protected against earthquakes.

The problem of protecting the built environment in earthquake-prone regions involves not only the optimal design and construction of new facilities, but also the upgrading and rehabilitation of existing structures including heritage buildings. The type of highly specialised retrofitting employed to protect Tuscany's heritage, as well as other regions of the world, is an important area of research and appropriate to the conference objective of designing better earthquake resistant buildings.

Major earthquakes and associated effects such as tsunamis continue to stress the need to carry out more research on the topics of this conference. The problems will intensify as population pressure results in buildings in regions of high seismic vulnerability. A better understanding of these phenomena is required to design earthquake resistant structures.

This Conference addressed these problems and continued to expand on the development of previous meetings in the series. Papers presented at ERES are an invaluable record of the state of the art on the topic. Those published from 1993 to 2009 are now freely available on the Website administered by WIT Press (http://library.witpress.com) where they are a permanent record demonstrating the quality of the research presented at the ERES conference series.

The present volume offers most of the papers presented at ERES/11, grouped in the following sections:

- The 2009 Abruzzo Earthquake: site effects and seismic isolation
- Seismic isolation and energy dissipation
- Ground motion
- Soil structure interaction
- Structural performance

The Editors are indebted to the members of the International Scientific Advisory Committee and other colleagues for helping to select the papers included in this Volume. They are also grateful to all authors for the quality of their papers.

The Editors
Tuscany, 2011

Contents

Section 3: Ground motion

Section 4: Soil structure interaction

Section 5: Structural performance

This page intentionally left blank

Section 1
The 2009 Abruzzo Earthquake: site effects and seismic isolation (Special session organised by Michele Maugeri)

This page intentionally left blank

Seismic action to withstand the structures: the case history of 2009 Abruzzo earthquake

M. Maugeri[1], G. Totani[2], P. Monaco[2] & S. Grasso[1]
[1]*Department of Civil and Environmental Engineering, University of Catania, Italy*
[2]*Department of Structural, Water and Soil Engineering, University of L'Aquila, Italy*

Abstract

The evaluation of the seismic action which the structures must withstand is the most critical item of the full process of analysis, monitoring and mitigation of seismic risk. Seismic action has been recorded worldwide for moderate to severe earthquakes. In the last 30 years the recorded accelerations have significantly increased. One reason could be due to the increasing number of recorded stations and to the location of a considerable amount of recorded stations on soft soil, where significant site amplification can occur. By the way the recorded accelerations have exceeded the designed acceleration given by seismic codes. That particularly occurs in the case of strong earthquakes, where the evaluation of seismic action given by source mechanism gives, in some cases, a seismic design earthquake greater than that given by the probabilistic evaluation reported by the codes.

Also in the case of the moderate M_L = 5.8 Abruzzo earthquake, the recorded acceleration exceeded the provisions given by Italian Code. Mainly two factors could explain that. One factor is related to the different results obtained by the probabilistic evaluation of seismic action given by the codes and the deterministic seismic action evaluated by source modelling of the scenario earthquake. The second factor is related to the role of site amplification, which is higher for small to moderate earthquakes and lower for severe scenario earthquakes. These two factors are discussed for the case of the Abruzzo 2009 earthquake, where, because of the normal fault mechanism, severe vertical components of the acceleration were recorded; also significant site effects occurred, particularly in the Aterno valley.

WIT Transactions on The Built Environment, Vol 120, © 2011 WIT Press
www.witpress.com, ISSN 1743-3509 (on-line)
doi:10.2495/ERES110011

1 Introduction

The seismic prevention of damage is a challenge for the third millennium. In spite of the tremendous work on analytical and experimental studies to reduce seismic risk it was increasing exponentially in the past century.

The evaluation of the seismic action to which the structures must withstand is the most critical item of the full process of analysis, monitoring and mitigation of seismic risk. Seismic action has been recorded worldwide for moderate to severe earthquakes. In the last 30 years the recorded accelerations have been significantly increased. One reason could be due to the increasing number of recorded stations and to the location of considerable amount of recorded stations on soft soil, where significant site amplification can occur. Due to the increased values of recorded acceleration, the design acceleration given by the codes has been significantly increased; also some other parameters such velocity and displacement have been included in the Code for the design of buildings and infrastructures.

By the way the recorded accelerations trend is still higher than the design acceleration given by National and International Codes, so the structures must withstand with acceleration greater than that used for the design.

That particularly occurs in the case of strong earthquakes, where the evaluation of seismic action given by source mechanism gives, in some cases, a seismic design earthquake greater than that given by the probabilistic evaluation reported by the codes, as it will be explained in the following section 2.

Also in the case of the moderate $M_L = 5.8$ Abruzzo earthquake, the recorded acceleration exceeded the provisions given by Italian Code, as it will be shown in the section 3. Mainly two factors could explain that. One factor is related to the different results obtained by the probabilistic evaluation of seismic action given by the codes and the deterministic seismic action evaluated by source modelling of the scenario earthquake. By the way, the Abruzzo earthquake was characterised by a normal fault, which gave in the central area a significant vertical component, which is in general underestimated by the Codes.

The second factor is related to the role of site amplification, which is higher for small to moderate earthquakes and lower for severe scenario earthquakes. The amplification factor is discussed in the section 4. Amplification factors are comparable with the stratigraphic amplification factors given by the Italian Code [1], while in the Aterno valley the amplification factors exceed those given by the Code.

2 Seismic action recorded during recent earthquakes

In the last 20 years the seismic acceleration recorded during strong earthquakes has been increased considerably. Maugeri et al. [2] show that for severe earthquakes the acceleration recorded exceeds almost 0.8g (Table 1). Thus, do dot means that the seismicity has been increased in the last period. The increasing in the acceleration recorded could depends on the increasing number on recorded stations and also to the fact that these recorded stations have been

Table 1: Acceleration recorded during destructive earthquakes in the last 20 years ([2], modified).

Località	Nazione	A_{max} recorded (g)
Landheers (1992)	USA	0.86
Kushiro-BRI (1993)	Japan	0.73
Northridge (1994)	USA	0.91
Sylimar (1994)	Japan	0.84
Tarzana (1994)	Japan	1.78
Kobe (1995)	Japan	0.83
Fukiai (1995)	Japan	0.82
Kocaeli (1999)	Turkey	>0.8
Chi-Chi (1999)	Taiwan	1.01
Tattoni-Ken Seibu (2001)	Japan	0.95

located recently in soft soil deposits, while in the past they were located on rock. Higher values of acceleration than those reported in Table 1 have been recorded during recent acceleration such as the 2004 Niigata Chuetsu [3], the 2007 Peru and the 2011 Sendai earthquakes, where the acceleration exceeded 2g.

Because of the increasing of the recorded acceleration, the National seismic codes increased the design acceleration, year by year, as reported in Table 2.

Table 2: Peak ground accelerations and design criteria [4].

Year	70	75	80	85	90	95	00	05	10	15
Seismicity	**200-300 gal**		**400-500 gal**			**600-800 gal**				
Nuclear power facilities	**Equivalent Liner analysis**							**Strengthening**		
Structures (Buildings, Bridges)	**Pseudo static analysis**		**Linear analysis**		**Non-linear analysis**		**Vibration control Isolation**			
Geotechnics (Liquefaction, Landslide, Soil structure interaction)	**Pseudo-static analysis (F_s >1.2)**		• **Equivalent linear analysis** • **Effective stress-based analysis**			• **Permanent displacement analysis** • **Performance-based design** • **Hazard map. Risk map**				

To allow the structures to withstand with these increased accelerations, the methods of analysis to be used have been refined. The pseudo-static analysis is commonly used up to 0.3g for structures (buildings and bridges) and about up to 0.4g for geotechnical analysis. For an acceleration level of 0.4-0.5g, from pseudo-static analysis it is more convenient to move to non linear analysis for structures and linear equivalent analysis for geotechnical works. For acceleration levels of about 0.6-0.8g, vibration control by isolation, are required for structures [5] and permanent displacement analysis and performance based design are required for geotechnical works. Perhaps in the near future (2010-2015), the design acceleration will be still increased, particularly for nuclear power facilities and for strategic buildings (hospitals, fire stations, etc.). It must be also considered that the expected acceleration given by National Codes is given by a probabilistic approach. For instance in Italy, according to the Italian Regulation [1], the design acceleration is that which has a probability of exceedance less than 10% in 50 years, which correspond to a return period of 475 years. In different countries also a big earthquake with a longer return period up to 2375 years is considered. An alternative way to evaluate the seismic action to which the buildings must withstand is given by the deterministic analysis based on the maximum credible earthquake. In this case a source mechanism will be modelled, the shear wave propagation attenuation is taken into consideration, as well as the amplification given at the surface by site effects. These two ways of evaluation of seismic action could lead to different results. For instance in the case of the seismic risk evaluation of the city of Catania (Italy), the probabilistic evaluation according to Italian Code gives an expected acceleration (Figure 1), considerably lower than the acceleration given by the deterministic approach (Figure 2).

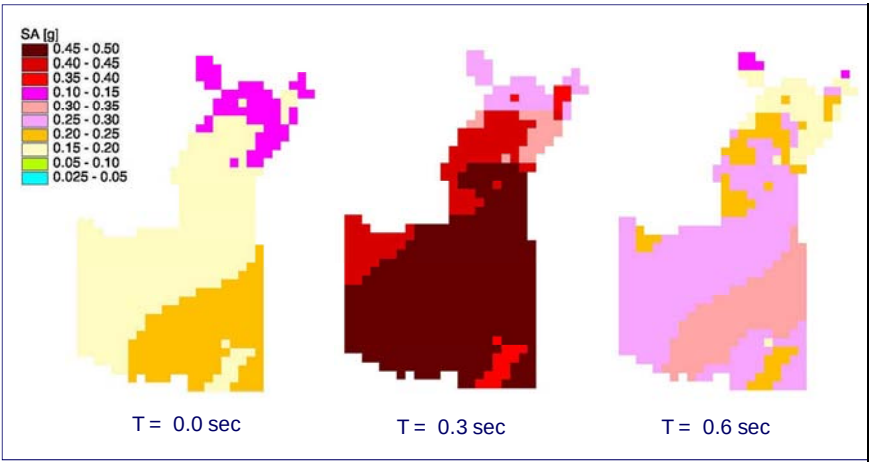

Figure 1: Probabilistic evaluation of spectral acceleration at the city of Catania (Italy) for different periods T [6].

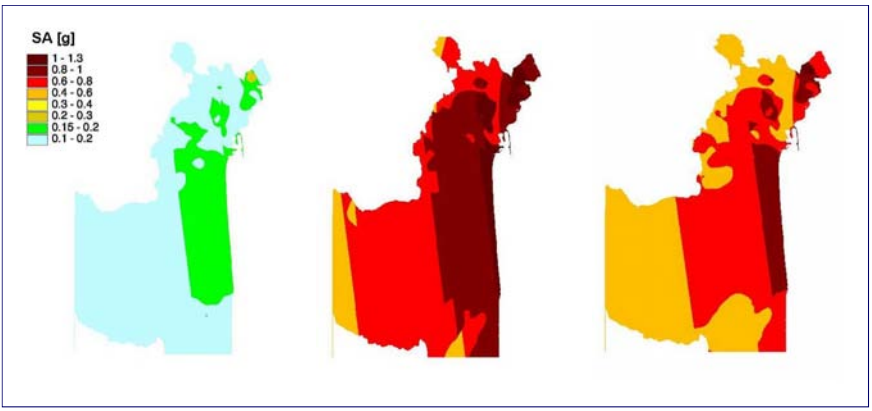

Figure 2: Deterministic evaluation of spectral acceleration at the city of Catania (Italy) for different periods T [6].

In general in Italy when you are dealing with a maximum credible earthquake with a magnitude M = 7.0 or greater, as in the case of the city of Catania, the deterministic approach gives a spectral acceleration value bigger than the probabilistic approach. On the opposite, when you are dealing with a maximum credible earthquake with a magnitude M = 5.5 or lower, is the probabilistic approach which gives a spectral acceleration value greater than the deterministic approach.

In Table 3 is reported the comparison between expected probabilistic evaluation of peak acceleration, with a probability of exceedance less than 10% in 50 years, and the observed acceleration during destructive earthquakes [7]. It is possible to see that observed acceleration exceeds always the expected probabilistic values, particularly for the case of the 2003 Bam (M_W=6.6), the 2010 Haiti (M_W=7.0) and the 2011Sendai (M_W=9.0) earthquakes.

Table 3: Comparison between expected probabilistic evaluation of peak acceleration (% g), with a probability of exceedance less than 10% in 50 years, and the observed acceleration during destructive earthquakes [7].

	EXPECTED	OBSERVED
KOBE	**0.4-0.48**	**0.7-0.8**
GUJARAT	**0.16-0.24**	**0.5-0.6**
BOUMERDES	**0.08-0.16**	**0.3-0.4**
BAM	**0.16-0.24**	**0.7-0.8**
E-SICHUAN	**0.16-0.24**	**0.6->0.8**
HAITI	**0.08-0.16**	**0.3-0.6**
SENDAI	**0.24-0.32**	**1.1-2.9**

3 Seismic acceleration recorded during the April 6, 2009 Abruzzo earthquake

According to Italian Institute of Geophysics and Volcanology (INGV), the main shock of the L'Aquila earthquake has been on April 6, 2009, at 3.32 a.m. (M_L = 5.8 and M_w = 6.3). The epicentre was located at few kilometres W-SW from the town of L'Aquila. Maximum MCS intensity was: I= X at Onna I=IX at L'Aquila (73,000 inhabitants). Focal depth was about 8,8 km. 308 deaths, 1600 injured, 40,000 homeless, damages about 30 billions €, plus the intangible value of monuments. The main shock, foreshocks and aftershocks locations around the city of L'Aquila are reported in Figure 3.

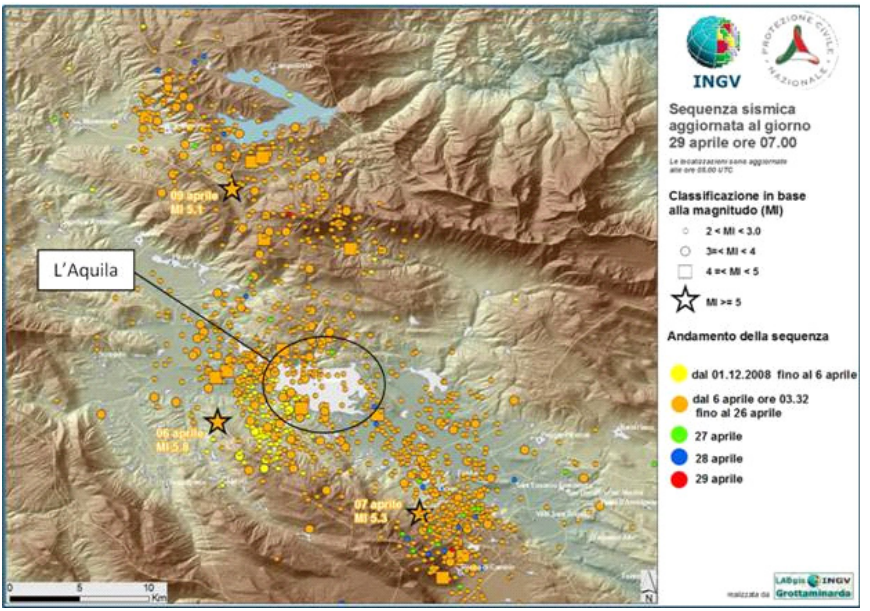

Figure 3: Foreshocks, main shock and aftershocks locations around the city of L'Aquila, after INGV.

Most of the deaths took place in vulnerable masonry houses which were subjected to unusually strong motions. Several reports on the main features of the recorded ground motions were compiled by different teams, among which the group of Italian investigators ([8, 9]) under the umbrella of Italian Geotechnical Association (AGI) and the National Network of Earthquake Engineering Laboratories (ReLUIS) project; detailed reports was also produced by the Geo-Engineering for Extreme Events Reconnaissance (GEER) project [10] on seismological and geotechnical aspects of the earthquake and by Aydan et al. [11] on the damage occurred. The effects on the physical environment are reported, with reference to fractures, to large deformations, to rock falls, to sink

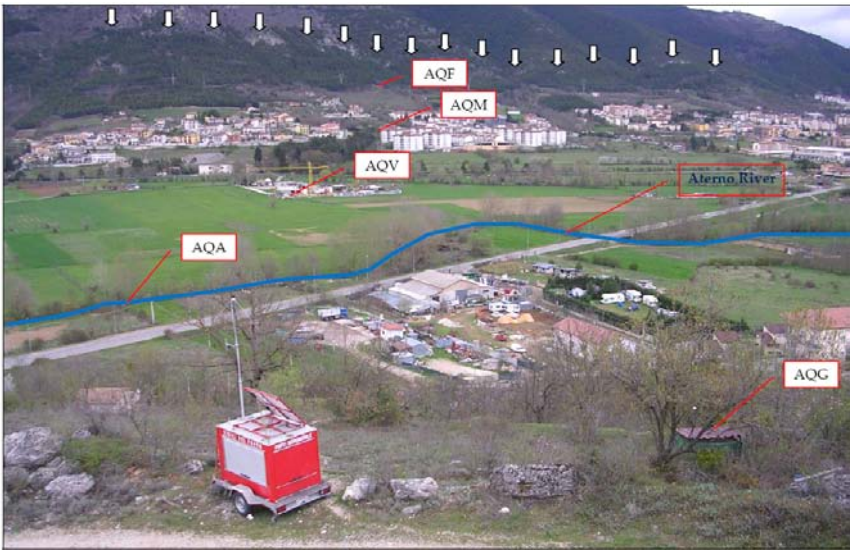

Figure 4: Location of the acceleration stations at the Aterno valley, recording the Abruzzo April 6, 2009 earthquake [13].

holes and to liquefaction. The soil liquefaction occurred at Vittorito is reported in detail by Monaco et al. [12].

Four accelerometric stations (AQG, AQA, AQV, AQM) were located across the Aterno valley (Figure 4) and recorded peak values ranging from about 0.4 to 0.6g; the station AQK was located in the city and recorded a peak value of about 0.35g. In table 4 are reported the recorded ground motion parameters in terms of maximum Peak Ground Acceleration (PGA) and Peak Ground Velocity (PGV) for the three components of each four stations considered. As regards the PGA, the recorded maximum value is 0.65g for the EW component of the AQV recording station, located on the alluvial soil, in the middle of the Aterno Valley.

Table 4: Recorded ground motion parameters in terms of maximum Peak Ground Acceleration (PGA) (g) and Peak Ground Velocity (PGV) (cm/s).

	AQG NS	AQG EW	AQG UP	AQA NS	AQA EW	AQA UP	AQV NS	AQV EW	AQV UP	AQK NS	AQK EW	AQK UP
PGA	0.51	0.47	0.24	0.45	0.40	0.47	0.54	0.65	0.52	0.35	0.33	0.37
PGV	35.9	31.2	10.4	24.5	32.0	9.39	40.4	36.7	12.5	36.3	30.3	19.8

Also, the strong portions of vertical and horizontal motions occurred almost simultaneously due to the short travel paths of P and S waves from the fault to the ground surface. This is evident because the severe horizontal motion start only about 1s after the vertical one, with a predominant period of 0.4-0.7s for S waves, while for P waves the predominant period is in the range 0.1-0.2s. These features are similar to fundamental frequencies of vibration of one-to-

eight-story buildings in L'Aquila and can be particularly dangerous for the weak non-ductile systems, such as the many old masonry structures in the area. The predominant frequency is between 1 and 2.5 Hz for the horizontal components; in particular for the AQV horizontal components it is 2 Hz. A comparison between the response spectra of AQV and AQG horizontal E-W and N-S components shows that for AQV station resting on soil formation there are some peaks ranging from a period T=0.15-0.5 s and for AQG station resting on soft rock the predominant period is T=0.25s for E-W component and it is ranging from T= 0.2-0.5s for N-S component.

As regards the AQK station, located in stiff soil on the city of L'Aquila, the maximum recorded peak ground acceleration in the NS component, is 0.35g; it must be stressed that L'Aquila is located in the vicinity of the normal fault, and because of that the recorded vertical acceleration (UP) of 0.37g is slight bigger than the horizontal one in NS component. It could be interesting to compare the recorded accelerations with those predicted by the new Italian Code [1], at L'Aquila city. According to this Code, the peak ground acceleration, is a_g = 0.250 – 0.275g as can be read in the specific site by the regulation.

4 Evaluation of site effects

Seismic response analyses were carried out at the AQV station, located on alluvial soil in the middle of Aterno valley [14]. The subsoil model was built according to the geotechnical data available for AQV station subsoil conditions reported in Figure 5; Figure 5b shows the Vs profile measured by D-H; Figure 5c shows the modified Vs profile according to the discontinuity given by the

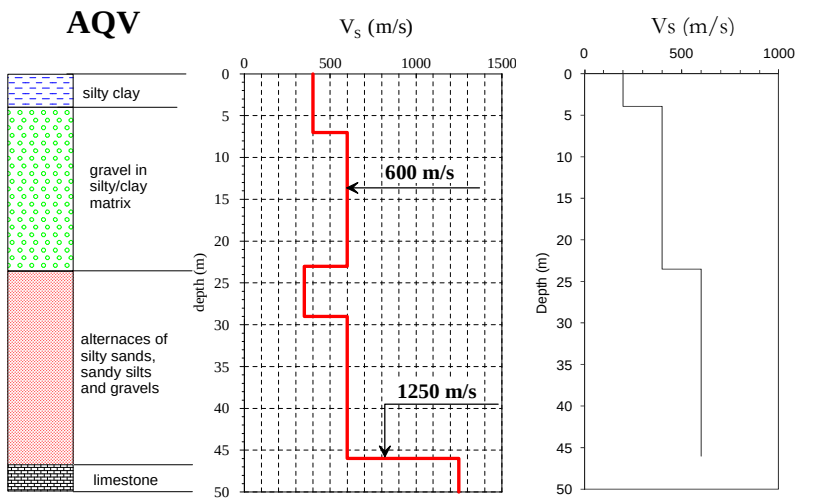

Figure 5: Shear wave profiles at AQV recording station: (a) Soil stratigraphy; (b) shear wave velocity profile obtained by Down Hole (D-H) test; (c) modified shear wave profile.

stratigraphy and of general increasing of the Vs with depth. The unit weight was increased with depth and with soil type from 19.00 up to 22.00 kN/m^3. The bedrock was located at a depth of 46 m, where the shear waves velocity becomes higher than 800 m/s. The shear modulus decay and damping ratio increasing with shear strain, evaluated by Resonant Column Test, are reported in Figure 6, referring to different localities. The input accelerograms are reported by [14].

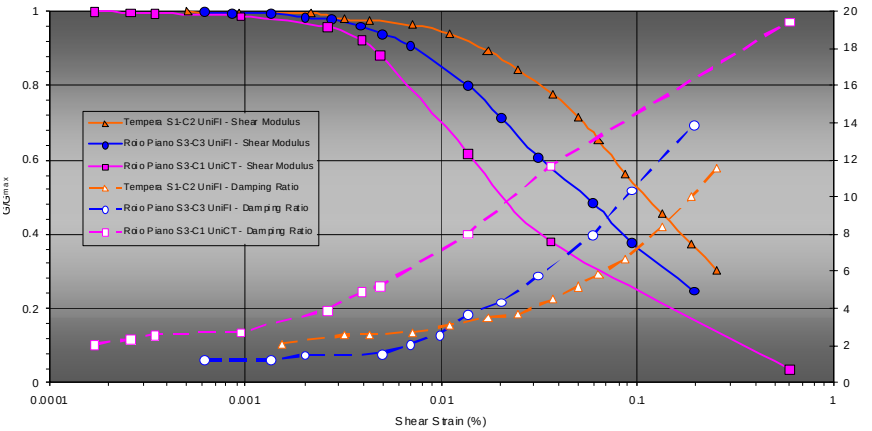

Figure 6: Normalised shear modulus and damping ratio versus shear strain from RC – TS Roio Piano and Tempera tests.

The recorded (Table 4) and the computed values of maximum acceleration show an average amplification factor of about $S_s = 2.5$, which is considerable higher for soil type B than the $S_s = 1.14$ given by the Italian regulation code and the $Ss = 1.20$, given by the Eurocode. It must be stressed that, while the horizontal acceleration at the bedrock was in some agreement with the predicted one by the Italian Regulation, the vertical component of acceleration was much higher than that recommended by the Italian Code for the design of geotechnical structures (slope, earth retaining wall, etc.). In general it is recommended by Italian Code and Eurocode 8, to consider a vertical acceleration equal to 50% of the horizontal one. Because of the occurrence of a normal fault in the proximity of L'Aquila City, the recorded vertical acceleration was much higher than that recommended by the Regulations and its value was very similar to horizontal acceleration in the AQK station, located in the city of L'Aquila. This last aspect, which is outside the scope of this paper, must be considered by the Code in the future for a better design of geotechnical structures and of buildings resting on the proximity of normal faults.

Site amplification, performed by EERA code [15], was carried out by all the normalized shear modulus and damping ratio reported in Figure 6 and for different curves given by literature, such as that reported by Kokusho and Esashi [16].

The results reported in figure 7 show that the site responses, evaluated by normalized shear modulus and damping ratio results obtained at Roio Piano and Tempera localities, are in good agreement with the recorded values of

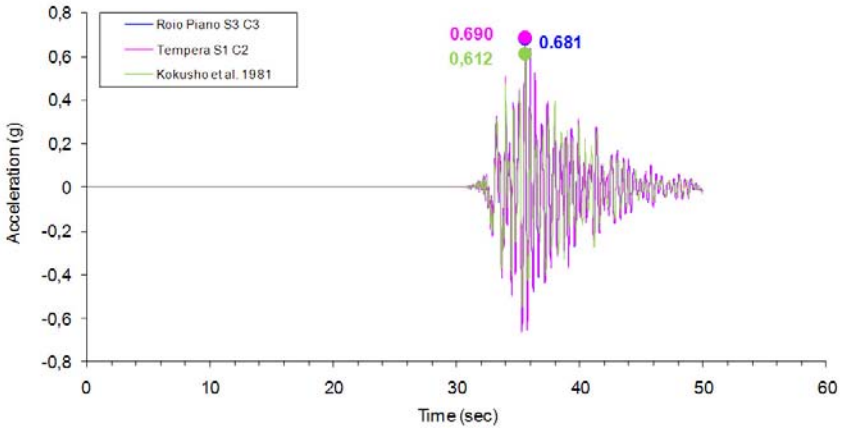

Figure 7: Results of site response analyses evaluated by normalized shear modulus and damping ratio obtained at Roio Piano and Tempera localities.

acceleration. Also using normalized shear modulus and damping ratio the given by Kokusho and Esashi [16], the results are slight lower, but sufficiently closed to the recorded one.

Seismic response analyses in the historical centre of L'Aquila have been carried out by Monaco et al. [17]. The site response analysis, performed at the historical building named Palazzo Camponeschi, was made at two layered soil with an inverse shear wave velocity profile, characterized by Vs = 800-1000 m/s for the upper layer, with a thickness of about 100m, and by Vs = 600-700 m/s for the second layer, resting over the bedrock, placed at a depth of 300 m.

The soil shear wave profile was measured by the Seismic Dilatometer (SDMT) in a non-penetrable soil [18]; for the upper layer made by Breccias, the normalized shear modulus and damping ratio were selected by literature results measured in similar soils, for the second layer made by lacustrine silt were obtained by Resonant Column Test performed at Roio Piano [19].

The results, performed by the EERA code [15] show that the spectral acceleration S_a is greater than that given by the Italian regulation NTC [1] particularly for a period ranging between 0.2s and 0.4s, which is the fundamental period more representative for masonry buildings present in the area.

The evidence of low frequency amplification in the city of L'Aquila was underlined by De Luca et al. [20], before the occurrence of the destructive 2009 Abruzzo earthquake.

5 Conclusions

The key-point for the evaluation of the seismic risk is the evaluation of the seismic hazard, related to the evaluation of the seismic action by probabilistic or deterministic approaches. By the way in general for low seismicity area the

probabilistic approach is overestimated the seismic action, while for very high seismicity area it underestimate the seismic action, as in the case of the city of Catania. In the case of the Abruzzo earthquake, acceleration bigger than that given by Italian Regulation was recorded. Thus, mainly because the soil amplification was in the soft soil of Aterno Valley greater than that given by Italian Regulation. Also in the centre of L'Aquila city, the spectral acceleration given by Italian Regulation is too simple for the evaluation of the soil response in a soil with inverse profile of velocity.

References

[1] NTC (2008). Norme Tecniche per le costruzioni. D. M. 14/01/2008 by the Ministry of Public Works of Italy. G.U. 04/02/2008.

[2] Maugeri M., Castelli F., Massimino M.R. (2006). Analysis, modeling and seismic improvement of foundations of existing buildings. Italian Geotechnical Journal. No. 4-2006, pp. 52-122 (in Italian with extended abstract in English).

[3] Ishihara K. (2009). Perspectives in geotechnics for vastly strong earthquake shaking". Special discussion session-future directions of performance-based design. Proc.1st International Conference on Performance-Based Design in Earthquake Geotechnical Engineering, IS- Tokyo, June 15-17, 2009.

[4] Ishihara K. (2008). Challenges in perspective in geotechnics for intense earthquake shaking". Invited Lecture. Seismic Engineering International Conference commemorating the 1908 Messina and Reggio Calabria Earthquake, Reggio Calabria.

[5] Martelli, A., Forni M., Panza G. (2011). Features, recent application and conditions for the correct use of seismic isolation systems. Earthquake Resistant Engineering Structures (ERES 2011). Chianciano Terme (Italy). September 07-09, 2011.

[6] Faccioli E., Pessina V., Vecchiotti M. (2002). Risk-UE WP2 meeting 23-25 Jan 2002, Barcelona.

[7] Peresan A., Vaccari F. (2011). Integrated seismic hazard assessment: a neo-deterministic time-dependent approach. Workshop Seismic Information System for Monitoring and Alert. ASI, Rome. May 4, 2011.

[8] Simonelli A. L., Sica S., Moccia F., Penna A., Lucadamo C., Mitrione A., Mosca P., Moscato T., Rotella M., Spatola M. G., Zarra S. (2009). Rapporto preliminare sugli effetti indotti sull'ambiente fisico dalla sequenza sismica dell'aquilano - Ver. 1.5, Working group AGI-ReLUIS, www.reluis.it.

[9] Monaco P., Totani G., Barla G., Cavallaro A., Costanzo A., D'onofrio A., Evangelista L., Foti S., Grasso S., Lanzo G., Madiai C., Maraschini M., Marchetti S., Maugeri M., Pagliaroli A., Pallara O., Penna A., Saccenti A., Santucci De Magistris F., Scasserra G., Silvestri F., Simonelli A.L., Simoni G., Tommasi P., Vannucchi G., Verrucci L. (2009). Geotechnical Aspects of 2009 L'Aquila Earthquake. Proc. Earthquake Geotechnical Engineering

Satellite Conference, 2-3 October 2009 in Alexandria, Egypt. (Invited Lecture).
[10] Stewart J. P. (Ed.), Di Capua G., Kayen R. E., Scott Kieffer D., Button E., Biscontin G., Scasserra G., Lanzo G., Tommasi P., Pagliaroli A., Silvestri F., d'Onofrio A., Simonelli A.L., Puglia R., Mylonakis G., Athanasopoulos G., Vlahakis V. - GEER Association Report No. GEER-016, (Version 1. May 6, 2009), Preliminary Report on the Seismological and Geotechnical Aspects of the April 6 2009 L'Aquila Earthquake in Central Italy, www.geerassociation.org.
[11] Aydan O., Kumsar H., Toprak S., Barla G. (2009). Characteristics of 2009 L'Aquila earthquake with an emphasis on earthquake prediction and geotechnical damage. Personal communication of the draft.
[12] Monaco P., Santucci De Magistris F., Grasso S., Marchetti S., Maugeri M., Totani G. (2011). Analysis of the liquefaction phenomena in the village of Vittorito (L'Aquila). Bull Earthquake Eng (2011) 9, pp. 231–261. DOI 10.1007/s10518-010-9228-0. ISSN: 1570-761X (print version), ISSN: 1573-1456 (electronic version).
[13] Di Capua G, Lanzo G, Luzi L, Pacor F, Paolucci R, Peppoloni S, Scasserra G, Puglia R (2009): "Caratteristiche geologiche e classificazione di sito delle stazioni accelerometriche della RAN ubicate a L'Aquila". Report S4 Project (http://esse4.mi.ingv.it/), June 2009.
[14] Maugeri M., Simonelli A.L., Ferraro A., Grasso S., Penna A. (2011). Recorded ground motion and site effects evaluation for the April 6, 2009 L'Aquila earthquake. Bull Earthquake Eng (2011) 9, pp.157–179. DOI 10.1007/s10518-010-9239-x. ISSN: 1570-761X (print version), ISSN: 1573-1456 (electronic version).
[15] EERA (2000). http://gees.usc.edu/GEES/Software/EERA2000/Default.htm
[16] Kokusho T., Esashi Y. (1981). Cyclic triaxial tests on sands and coarse materials, X ICSMFE, Vol. 1, 673-676, (1981).
[17] Monaco P., Totani G., Totani F., Amoroso A., Maugeri, M., Grasso, S. (2011). Modello di sottosuolo e analisi di risposta sismica locale nel centro storico dell'Aquila. XIV Convegno ANIDIS – L'Ingegneria Sismica in Italia – Bari, 18-22 settembre 2011.
[18] Totani, G., Monaco, P., Marchetti, S. and Marchetti, D. (2009). VS measurements by seismic dilatometer (SDMT) in non-penetrable soils. Proc. 17th ICSMGE, Alexandria, Egypt, Vol. 2, 977-980. M. Hamza et al. (eds). IOS Press.
[19] Gruppo di Lavoro (2010). La Microzonazione Sismica dell'area aquilana. 3 Vol. + DVD. Regione Abruzzo. In print.
[20] De Luca, G., Marcucci, S., Milana, G. and Sanò, T. (2005). Evidence of low-frequency amplification in the city of L'Aquila, Central Italy, through a multidisciplinary approach including strong- and weak-motion data, ambient noise, and numerical modeling. Bull. Seism. Soc. Am., 95(4), 1469-1481.

Features, recent application and conditions for the correct use of seismic isolation systems

A. Martelli[1], M. Forni[2] & G. Panza[3]
[1]*Faculty of Architecture, University of Ferrara, Italy*
[2]*Technical Unit on Seismic Engineering, ENEA, Italy*
[3]*Department of Geosciences, University of Trieste, Italy*

Abstract

Over 16,000 structures have been protected in the world by seismic isolation (SI) and other anti-seismic systems. Such structures are located mostly in Japan, but they are more or less numerous in more than 30 other countries, including Italy (which is now fourth at worldwide level for the number of isolated buildings, after Japan, China and the Russian Federation). Application of SI is increasing everywhere, although its extent is strongly influenced by earthquake lessons and the features of the design rules used. It concerns both new and existing structures of all kinds. This paper provides a short overview on its recent progress worldwide and on the behaviour of seismically isolated buildings during recent earthquakes, based on the most recent information available to the authors (including some preliminary data on the effects of the 2011 *Christchurch* and *Tohoku* events). Particular attention is paid to the isolated buildings in Italy, in the context of the effects of recent quakes (2002 *Molise and Puglia* and 2009 *Abruzzo* events). Based on the Italian experience, some important conditions for the correct use of the anti-seismic systems are also stressed in the Conclusions.
Keywords: anti-seismic systems; seismic isolation; energy dissipation; seismic input; new constructions; retrofits; seismic codes.

1 Introduction

Over 16,000 structures in the world have been protected by anti-seismic (AS) techniques, mainly by seismic isolation (SI) or energy dissipation (ED) [1–7]. They are located in more than 30 countries (fig. 1) and concern both new constructions and retrofits of existing structures of all kinds: bridges and

WIT Transactions on The Built Environment, Vol 120, © 2011 WIT Press
www.witpress.com, ISSN 1743-3509 (on-line)
doi:10.2495/ERES110021

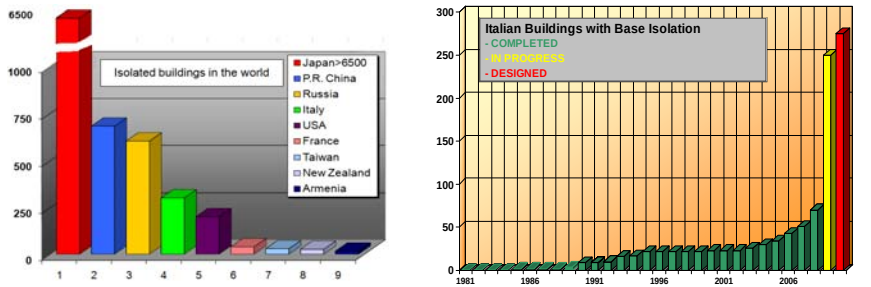

Figure 1: Overall numbers of buildings with SI in the most active countries (left) and in Italy during years (right).

viaducts, civil and industrial buildings, cultural heritage and industrial components and installations, including some high risk nuclear and chemical plants.

The use of the AS systems in a civil context already includes not only the strategic structures (civil defence centres, hospitals) and the public ones (schools, churches, commercial centres, hotels, airports), but also residential buildings and even many small and light private houses. Everywhere, the number of such applications is increasing, although it is strongly influenced by earthquake lessons and the availability and features of the design rules used.

Most SI systems rely on the use of rubber bearings (RBs), namely High Damping Rubber Bearings (HDRBs), or Lead Rubber Bearings (LRBs) or (mainly in Japan) Low Damping Rubber Bearings (LDRBs) in parallel with dampers; in buildings, some plane surfaces steel-Teflon (PTFE) Sliding Devices (SDs) are frequently added to the RBs to support their light parts and (if they are significantly asymmetric in the horizontal plane) to minimize the torsion effects.

2 Application in Japan

Japan, thanks to the availability of an adequate specific code since 2000 and the free adoption of SI since 2001, is consolidating its worldwide leadership on the use of the AS systems and devices. In fact, at the end of 2009, over 5,000 Japanese buildings or houses had already been protected by SI (fig. 1) and about 3,000 more had been provided with ED systems [3] (according to recent information, the Japanese isolated buildings are now about 6,000 [8]).

Japan, where the first application of base SI dates back to 1985, is continuing the extensive adoption of the AS systems initiated after the excellent behaviour of two isolated buildings near Kobe during the 1995 *Hyogo-ken Nanbu* quake, of magnitude M = 7.3 [3, 7]. At least until the extremely violent *Tohoku* quake and tsunami of March 11, 2011 (M = 9.0), this behaviour was confirmed for all Japanese buildings protected by SI during all severe events which followed that of 1995, namely those of *Tokachi Offshore* (M = 8.0, 2003), *Niigata Chuetsu* (M = 6.8, 2004), *Fukuoka West Offshore* (M = 7.0, 2005), *Niigata Chuetsu Offshore* (M = 6.8, 2007) and *Iwate-Miyagi Inland* (M = 7.2, 2008) [8]. Japanese, on the one hand, have confirmed the trend of their country, initiated

some years ago, to isolate even high-rise buildings and sets of buildings supported by a common isolated reinforced concrete (r.c.) structure (the so called "artificial ground", a solution which enables large savings of construction costs) and, on the other hand, are more and more using SI to protect even very small and light private houses [3, 4, 7].

Based on recent data [8], the Japanese isolated high-rise buildings are rather numerous and include 250 condominiums, while the isolated houses are already about 3,500 (they were about 3,000 at the end of 2009 [3]). More generally, 46% (1,100) of the Japanese isolated large buildings (e.g. excluding houses) are condominiums, 20% offices, 12% hospitals and 2% schools; most of these large buildings are new constructions (the retrofits of the existing ones are 90).

About 1,000 Japanese buildings (including several high-rise ones) and 2,000 private houses had also been protected by various kinds of dampers at the end of 2009 [3, 4, 7]. The use of the AS systems also recently increased in Japan for the protection of cultural heritage and for that of bridges and viaducts [3, 4, 7]. For the latter it began rather later than for buildings; it is largely based on the use of HDRBs and LRBs and considerably extended especially after the 1995 *Hygo-ken Nanbu* earthquake (by becoming obligatory for overpasses in Kobe).

As to the industrial plants, besides performing detailed studies for the SI (even with three-dimensional – 3D – systems) of various kinds of future nuclear reactors, Japanese erected the *Nuclear Fuel Related Facility* on 32 LDRBs and LRBs at the beginning of the 2000s [3, 4, 7]. In 2006, they also began the application of SI to large industrial factories: the first, concerning the fabrication of semi-conductors, was built on LRBs and Viscous Dampers (VDs). At least two further similar factories were already in use at the end of 2009 [3, 4, 7].

With regard to the *Tohoku* (or *Sendai*) earthquake, it is noted that the related seismic hazard was considerably underestimated, as for several previous violent events all over the world (table 1) [9]. Moreover, the main event of March 11, 2011 (which took place at 2:46 p.m. local time) was followed by a very large number of secondary shocks: on March 28 they had already been 3 of $M > 7.0$ (during the same afternoon), 44 of $M > 6.0$ and 180 of $M > 5.0$ [10]. Furthermore, on April 7 a new earthquake of $M > 7.0$ took place, with epicentre at 66 km from Sendai, which, besides causing 3 casualties and 140 wounded persons and the temporary interruption of electric energy distribution, damaged the Onagawa nuclear installation (where its 3 Boiling Water Reactors, BWRs, had not shown any damage during the event of March 11).

The dynamic behaviour of the Japanese isolated buildings during the *Tohuku* earthquake and its aftershocks was not yet exactly known to the authors of this paper at the time at which they wrote it (April 2011), due to the understandable confusion still reigning in Japan and other priorities of the local experts.

Thus, the authors of this paper had only some general information on this topic, received from Dr. Nagahide Kani, Director of the *Japan Society of Seismic Isolation* (JSSI) [10], only a few days prior to the event of April 7 (similar to the Italian association GLIS – Isolation and Other Anti-Seismic Design Strategies,

Table 1: List of the top eleven deadliest earthquakes occurred during the period 2000-2011, and the corresponding intensity differences (ΔI) among the observed values and those predicted by the Global Seismic Hazard Assessment Program, or GSHAP (ΔI is computed from the observed magnitude M and the maximum Peak Ground Acceleration (PGA) values given by GSHAP around the observed epicentre, respectively, using existing relationships [9]; Roman numerals give the difference in natural values of macroseismic intensity; for 9 out of 11 events the GSHAP values severely underestimate the observed ones).

Earthquake name and location	Date	Magnitude (M)	Intensity difference (ΔI)	Casualties
Tohuku or Sendai (Japan)	March 11, 2011	9.0	III	> 20,000 ??
Port-au-Prince (Haiti)	January 12, 2010	7.3	II	222,570
Padang (Southern Sumatra, Indonesia)	September 30, 2009	7.5	II	1,117
Wenchuan (Sichuan, P.R. China)	May 12, 2008	8.1	III	87,587
Yogyakarta (Java, Indonesia)	May 26, 2006	6.3	=	5.749
Kashmir (Northern India - Pakistan border region)	October 08, 2005	7.7	II	86,000
Nias (Sumatra, Indonesia)	March 28, 2005	8.6	III	1,313
Sumatra-Andaman (Indian Ocean)	December 26, 2004	9.0	IV	227,898
Bam (Iran)	December 26, 2003	6.6	=	31,000
Boumerdes (Algeria)	May 21, 2003	6.8	II	2,266
Bhuj (Gujarat, India)	January 26, 2001	8.0	III	20,085

JSSI is a corporate member of the *A*nti-*S*eismic *S*ystems *I*nternational *Soc*iety – *ASSISi*). In particular, on April 4, Dr. Kani wrote them that:

- in the *Tohoku* area there are about 130 seismically isolated buildings, most of which behaved well, at least without considering the tsunami effects;
- several isolated buildings are located in the area hit by the tsunami and JSSI was checking their integrity, but no information was available yet;
- in the Tokyo area (450 km from the epicentre), where long period and long duration seismic vibrations were felt, the isolated buildings behaved well;
- in the Kobe and Osaka areas (850 km from epicentre) few of the isolated buildings were slowly shifted for a long time (approximately 15 to 20 minutes) by long period and long duration vibrations, due to low damping of the dampers installed in these buildings (this behaviour was different for the different buildings, depending on the kind of dampers installed inside them);
- at Fukushima an isolated building located at the site of the nuclear power plants was already extremely useful and was considered as tentative headquarters for the emergency activities of TEPCO (the company owning the plants), compatibly with the level of the radiations present in the site.

Some information concerning the isolated bridges and viaducts was also provided, by Prof. Kazuhiko Kawashima of *Tokyo Institute of Technology*, some days later [11]. He showed that, contrary to the steel bearings, the RBs which have been installed on this structure kind since 1990s (LRBs and HDRBs) mitigated damage. However, several RBs failed at two locations of the *East Sendai Expressway* (for reasons to be clarified). He also showed that a number of bridges was damaged by the tsunami. Damage was possibly developed by deck rotation toward the upstream side, resulted from the uplifting force. Japanese believe that, if failure of bearings (particularly downstream side bearings) due to the uplifting force can be prevented, damage of the tsunami may be mitigated. Thus, it has been recommended to install "unseating prevention devices for tsunami", by considering that restrainers which are widely used for unseating prevention devices for quakes may be effective if set in the vertical direction.

3 Application in the P.R. China

In the Peoples' Republic (P.R.) of China very ancient monasteries, temples and bridges, protected by means of rough sliding SI systems, are still standing, which withstood numerous earthquakes, including very violent events, up to M = 8.2 [1, 7]; however, the application of modern SI systems began only in 1991. In any case, initially the SI systems, then the ED devices too have rapidly got a footing since that year [1, 3, 4, 7].

In October 2008, the number of isolated Chinese buildings was about 650 [7]. In November 2009 a further significant extension of the applications of SI and the other AS device kinds in China was reported; in particular, the number of the newly erected isolated buildings per year doubled there after the M = 8,1 *Wenchuan* earthquake of May 12, 2008, by increasing from 50 to 100 per year [3, 4]. This more rapid increase of the number of building applications of SI was due to both the excellent behaviour of two r.c. isolated buildings and even a

6-storey masonry one during the aforesaid earthquake (although, as shown by table 1, its violence had been largely underestimated, by a factor close to 10 for the peak ground acceleration, PGA) and the fact that the Chinese code (which still requires the submission of the projects the isolated buildings to the approval of a special commission) permits to reduce the seismic loads acting on the superstructure and, consequently, the foundations of such buildings [3, 7].

In November 2009 SI systems had been installed in the P.R. China in 32 bridges and 690 buildings, while 83 buildings had been protected by ED devices, 16 by Tuned Mass Dampers (TMDs) and 5 by semi-active or hybrid systems [3, 4]. The latter had also been installed in 8 bridges. Several building applications of SI are to dwelling buildings, even new masonry constructions. SI is also applied to rather tall buildings (to 19 storeys) and not only at the building base or at the top of the lowest floor, but also on more elevated floors (for risings or for erecting highly vertically asymmetric constructions), or at the building top (to sustain, in the case of retrofit, one or more new floors acting as a TMD), or also on structures that join adjacent buildings having different vibrational behaviours. Chinese applications of SI also include sets of buildings on "artificial grounds", base and roof SI of stadiums, isolation from both seismic and traffic vibrations (by means of 3D devices), as well as the protection of valuable objects (e.g. electronic equipment and art objects) by means of SI tables and that large chemical components, like new Liquefied Natural Gas (LNG) tanks [3, 4, 7].

4 Application in the Russian Federation

The Russian Federation is now third for the number of isolated buildings, with over 600 applications at the end of 2009 [3, 4]. The use of modern SI systems, formed by RBs, frequently in conjunction with SDs and/or dampers (similar to those adopted in the other countries), is going on replacing that of the previous so called "low cost" isolators (reversed mushroom-shaped r.c. elements), which had been installed since the years 1970s. After the retrofits of some important historical buildings [1, 6], recent Russian application includes even high-rise buildings, in particular in Sochi [3, 4, 7]. For some of these Italian isolators have been used (e.g. for the new r.c. 27 storeys *Sea Plaza Hotel*, which is protected by 102 Italian HDRBs [3, 4]).

5 Application in the USA

The USA are still at the second place, after Japan, for the overall number of applications of the AS systems and devices [3, 4]. In this country, however, such applications are satisfactorily progressing only for bridges and viaducts and for buildings protected by ED systems [3, 7]. They concern both new constructions and retrofits. More precisely, HDRBs, LRBs and, more recently ED devices and Shock Transmitter Units (STUs) have already been installed in about 1,000 U.S. bridges and viaducts, located in all U.S. states [3], while dampers of various types already protect over 1,000 buildings [1, 3].

On the contrary, as far as SI of buildings is concerned, the number of new applications remains still limited (recently 3 or 4 per year), in spite of the excellent behaviour of some important U.S. isolated buildings during the 1994 *Northridge* earthquake [1, 6], and the long experience of application of this technique to such structures (since 1985). This is a consequence of the very penalizing design code in force in the USA for the isolated buildings: according to recent information, the US seismically isolated buildings remain now "only" 100÷200, although they are mostly very important and half of them are retrofits, even of monumental buildings [3, 4, 7].

SI of US buildings has been performed using HDRBs, LRBs (in some cases in conjunction with LDRBs, SDs, VDs and other ED devices), as well as, more recently, the Friction Pendulum System (FPS), which was the first kind of Curved Surface Sliders (CSSs) to be developed. As to the design earthquake levels adopted in California, we note that they correspond to very large magnitudes M (e.g. M = 8.3 for the new *911 Emergency Communications Centre* erected in San Francisco in the years 1990s and M = 8.0 for the *San Francisco City Hall* retrofitted with 530 LRBs in 2000 [3, 4, 7]): this imposes the adoption of SI (as the only possibility) for these applications, in spite of its large cost in the USA.

6 Application in Italy

Fifth and first in the Western Europe for the overall number of applications of the AS devices remains Italy (fig. 1) [1, 3, 4, 7]. There the use of the AS systems began in 1975 for bridges and viaducts and in 1981 (namely 4 years before Japan and the USA), for buildings [7], but, later, it was rather limited several years long (due to the lack of design rules to the end of 1998, then to their inadequacy and very complicated and time-consuming approval process to May 2003) [1].

Significant application has restarted in Italy for some years, initially as a consequence of the collapse of the *Francesco Jovine* primary school in San Giuliano di Puglia (Campobasso) during the 2002 *Molise and Puglia* quake and the subsequent enforcement of the new Italian seismic code (May 2003), which freed and simplified the adoption of the AS systems [3, 7]. However, the use of SI became particularly rapid especially after the *Abruzzo* earthquake of April 6, 2009 (M = 6.3), as a consequence of the damage caused by this event to the conventionally founded structures and cultural heritage [3, 4]. Thus, in 2009, Italy overtook the USA for the number of isolated buildings and industrial structures and components: those in use were about 70 before the *Abruzzo* earthquake, with further 20÷30 under construction or design (see, for instance, figs. 2–5), while they are now approximately 300 and several further applications to new-built and retrofitted structures of these kinds are in progress.

Figure 2: The main building, erected on 10 HDRBs of 1 m diameter (shown at the centre and on the right, covered by provisional protections) and the adjacent service building, isolated by means of HDRBs and SDs, of the *Emergency and Management Operative Centre* of the new Civil Defence Centre of Central Italy in Foligno, near Perugia (their construction was completed in 2010 and its safety was certified by A. Martelli in February 2011 [3, 4, 7]).

Figure 3: The new school of Marzabotto (Bologna, seismic zone 3), which was isolated (with the collaboration of ENEA) by means of 28 HDRBs and 14 SDs, with 500 mm diameters (it is the first isolated school in Northern Italy; its safety was certified by A. Martelli in September 2010).

Figure 4: A new 8-storey dwelling building being erected in Messina, in seismic zone 1 (June 2010), the tallest isolated Italian building (its safety will be certified by A. Martelli), and one of the LRBs forming its SI system together with SDs.



Figure 5: One of the three tanks of the company *Polimeri Europa* of the Italian ENI Group located in Priolo Gargallo (Augusta, Syracuse, seismic zone 2*), which were seismically retrofitted using U.S. FPS devices in the years 2005-2008 and one of the isolators during and after its installation [4] (this is the only application of SI to chemical plants and components so far existing in Italy; prior to the 2009 *Abruzzo* quake, it was also the only Italian application of CSSs).

The recent applications of SI include 184 pre-fabricated houses erected in L'Aquila, each on a large isolated large r.c. slab (fig. 6), to provisionally host 17,000 homeless residents (at least in the first years). These have been isolated using Italian CSS devices (fig. 6), but the use of the traditional HDRBs or LRBs, in conjunction with some SDs, is also going on, for both new constructions and retrofits (figs. 7-9). In particular, the new *Francesco Jovine*, protected by a SI system designed with the collaboration of ENEA and formed by 600 and 700 mm diameter HDRBs (61) and SDs (13), which has been the first Italian isolated school (certified as safe by the first author of this paper in September 2009) [3, 4], has been followed by several further projects of this kind (see, for instance, figs. 3 and 7): seismic protection of schools by means of SI, besides that of hospitals and other strategic structures, is now a "priority 1" objective in Italy.



Figure 6: One of the 184 pre-fabricated houses (wood, or r.c., or steel structure) erected in l'Aquila for homeless residents after the 2009 *Abruzzo* earthquake and some of the 40 CSS devices, manufactured in Italy, installed at the top of columns to isolate its supporting slab (the lower floor is used as garage).

Figure 7: The *Romita High School* for scientific studies (1,300 students) in Campobasso (seismic zone 2) prior to the demolition of its blocks "A" and "B" (left); reconstruction of block "B" in progress in October 2010 (at the centre); two HDRBs and one SD in its underground technical floor (right).

Figure 8: The dwelling building of Via Borgo dei Tigli 6-8-10 in L'Aquila (Pianola area), just completed before the 2009 *Abruzzo* earthquake (left) and damage caused to the building by this event. Its retrofit by means of HDRBs and SDs has been planned, with safety certification of A. Martelli.

Figure 9: The monumental building *Palazzo Margherita* in L'Aquila put in safe conditions after of the damages suffered during the 2009 *Abruzzo* earthquake (left and at the centre); this and further monumental buildings in L'Aquila (including the renowned *De Amicis* school) may be retrofitted by sub-founding them and inserting a SI system in the sub-foundations, in order to respect the severe conservation requirements applicable in Italy to cultural heritage (among the sub-foundation techniques, that shown on the right, patented by ENEA and the Polytechnic of Torino in 2010, should be used [4]).

The previous blocks “A” and “B” of the school had been found to be very unsafe by investigations on the quality of construction materials carried out (with the cooperation of ENEA) after the 2002 *Molise and Puglia* earthquake [1, 3, 4].

At last, they were demolished in 2010, due to violent polemics on the safety of the school which took place in Campobasso after the 2009 *Abruzzo* earthquake.

Block “A” should also be reconstructed, as soon as funds become available.

Retrofit with SI at the top of the first floor has been recommended for block “C”, which was not demolished because it was found to be characterized by somewhat better construction materials.

Safety of at least block “B” will be certified by A. Martelli.

Moreover, the use of the AS systems is going on for bridges and viaducts (those with such systems were already at least 250 in 2009 [5, 7]) and cultural heritage (fig. 9) [3, 4]: new retrofit techniques using SI, applicable to monumental buildings, will also be applied for reconstructing L’Aquila (fig. 9).

7 Application in other countries

For the overall number of applications of the AS systems, Italy is followed by South Korea, Taiwan, Armenia, New Zealand, France, Mexico, Canada, Chile and other countries [3, 4, 7]: many of them make use of Italian AS devices (e.g. Turkey, Greece, Portugal, Spain) and some have also been designed by Italians (Cyprus, Romania). In New Zealand, one of the motherlands of AS devices (in particular of those based on the use of lead) and third in the world for the number of applications of such devices per inhabitants, the isolated structures had an excellent behaviour in both the 2010 *Canterbury* earthquake, of M = 7.1, and the 2011 *Christchurch* event, of M = 6.3 (fig. 10) [4, 12]. Similarly, the isolated structures in Santiago had an excellent behaviour in Chile too, during the 2010 *Maule* earthquake, of M = 8.8 (fig. 10) [4].

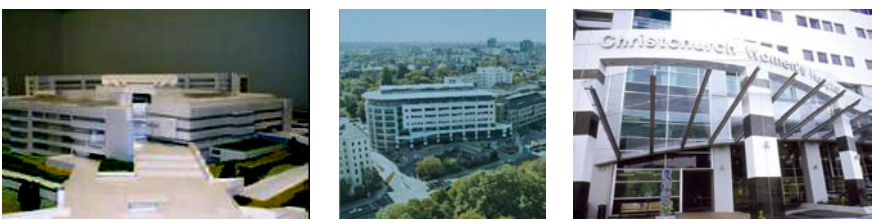

Figure 10: The isolated *Nuevo Hospital Militar La Reina* in Santiago (Chile), which survived undamaged the *Maule* earthquake of February 27, 2010 (left), and the isolated *Christchurch Woman’s Hospital* (New Zealand), which had the same behaviour during the event of *Canterbury* on September 3, 2010 and that of *Christchurch* on February 21, 2011 (at the centre and right).

8 Conclusions and remarks on the correct use of anti-seismic systems

The large effects of earthquake lessons and seismic design code features on the extent of the use of the AS systems in the various countries shall be stressed [2, 3, 4]. With regards to the code features, in countries like Japan, the USA and Chile SI is considered as a safety measure additional to the conventional design; consequently, the use of SI obviously always introduces additional construction costs. In spite of this, this technique is being widely adopted by the Japanese, due to their high level of perception of the seismic risk and because violent quakes are very frequent in their country. The aforesaid level of perception is much lower elsewhere: this is the reason why, to limit or even balance the additional construction costs entailed by the use of SI (and, thus, promote a significant application of such a technique), the seismic codes of other countries (Italy, China, Armenia, etc.) allow for some lowering of the seismic forces acting on the superstructure and (consequently) foundations when SI is used. Thus, in these countries, a real safety will be ensured to the isolated structures if and only if great care is paid to: (1) the selection of the SI devices (taking into account the amplitude of vertical and low frequency vibrations), their qualification, production quality, installation, protection, maintenance and verification that their design features remain unchanged during the entire structure life; (2) some further construction details (structural gaps, their protections, interface elements – e.g. gas and other safety-related pipes, cables, stairs and lifts, etc.). Otherwise, the isolators, instead of largely enhancing the seismic protection, will make the structure less earthquake resistant than a conventionally founded one and, thus, will expose both human life and the entire SI technology to great risks.

Finally, [2, 13], a common key requirement for the optimal performance of all the AS systems and devices (but especially of the isolators) is the realistic and reliable definition of seismic input, which cannot rely upon the oversimplified routine probabilistic methods, mainly when dealing with displacements definition (on which the design of isolated structures is based): thus, the ongoing rapid extension of the use of the AS systems and devices requires a considerable improvement of the *Probabilistic Seismic Hazard Assessment* (PSHA) approach, which is now in use in several countries (including Italy). Such a change is very urgent now and can be achieved by complementing PSHA through the development and application of deterministic models (e.g. the *Neodeterministic Seismic Hazard Assessment*, NDSHA) [4, 13]. This particularly applies to China, Italy, New Zealand and Japan, to ensure safe reconstruction after the quakes of *Wenchuan* (2008), *Abruzzo* (2009), *Canterbury* and *Christchurch* (2010 and 2011) and *Tohuku* (2011), because SI is widely used in the concerned areas.

All the aforesaid items are being discussed (April 2011) by the Commission on Environment, Territory and Public Works of the Italian Chamber of Deputies, to recommend modifications of the seismic design code to the government [4]).

References

[1] Dolce, M., Martelli, A. & Panza, G., *Moderni Metodi di Protezione dagli Effetti dei Terremoti*, ed. A. Martelli, 21mo Secolo: Milan, 2006 (in Italian).

[2] Martelli, A., On the need for a reliable seismic input assessment for optimized design and retrofit of seismically isolated civil and industrial structures, equipment and cultural heritage. *Pure and Applied Geophysics*, DOI 10.1007/s00024-010-0120-2, 2010.

[3] Martelli, A. & Forni, M., Seismic isolation and other anti-seismic systems: recent applications in Italy and worldwide. *Seismic Isolation And Protection Systems (SIAPS)*, Mathematical Sciences Publishers (MSP): Berkeley, DOI 10.2140/siaps.2010.1.75, **1(1)**, p. 75-123, 2010.

[4] Martelli, A. & Forni, M., Recent worldwide application of seismic isolation and energy dissipation and conditions for their correct use. *Proc. on CD-ROM of the Structural Engineering World Congress*, Cernobbio, 2011.

[5] Martelli, A., Sannino, U., Parducci A. &. Braga, F., *Moderni Sistemi e Tecnologie Antisismici. Una Guida per il Progettista*, 21mo Secolo: Milan, 2008 (in Italian).

[6] Sannino, U., Sandi, H., Martelli A. & Vlad, I., *Modern Systems for Mitigation of Seismic Action*, AGIR Publishing House: Bucharest, 2009.

[7] Martelli, A., Progress of the application of passive anti-seismic systems. *Earthquake Resistant Engineering Structures VII*, eds. M. Phocas, C.A. Brebbia & P. Komodromos, Wit Press: Southampton, pp. 281-293, 2009.

[8] Kani, N., *Recent Trends of Seismically Isolated Structures in Japan*, Japan Society for Seismic Isolation (JSSI), Tokyo, Japan, 2011.

[9] V.G. Kossobokov & A. Nekrasova, Global Seismic Hazard Assessment Program maps are misleading. *Proc. of the AGU Fall Meeting 2010*, 2010.

[10] Kani, N. Personal communications, April 2011, Director, JSSI, Japan.

[11] Kawashima, K. Personal communication, April 2011, Professor, Department of Civil Engineering, Tokyo Institute of Technology, Japan.

[12] Whittaker, D. Personal communications, September 2010 and April 2011, Technical Director, Beca, Singapore.

[13] Panza, G., Irikura, K., Kouteva, M., Peresan, A., Wang, Z. & Saragoni, R., (eds.). *Advanced seismic hazard assessment, Pageoph Topical Volume*, ISBN 978-3-0348-0039-6 and ISBN: 978-3-0348-0091-4, 2011.

This page intentionally left blank

Site effects and site amplification due to the 2009 Abruzzo earthquake

P. Monaco[1], G. Totani[1], F. Totani[1], S. Grasso[2] & M. Maugeri[2]
[1]*Department of Structural, Water and Soil Engineering, University of L'Aquila, Italy*
[2]*Department of Civil and Environmental Engineering, University of Catania, Italy*

Abstract

This paper presents the results of numerical analyses carried out to assess the different seismic response of two sites in the urban area of L'Aquila, selected as representative of typical subsoil conditions in the old city centre and in the recently developed suburban Pettino district. Both areas were severely damaged by the April 6, 2009 earthquake. The geotechnical model of the subsoil at each of the two sites and the related parameters, defined based on accurate site investigations, are described. The comparison of results of seismic response analyses at the two sites, in agreement with strong motion recordings of the April 6, 2009 main shock, confirms that site effects due to different subsoil conditions played an important role in the observed non-uniform damage distribution. Particularly in the city centre, characterized by an inversion of the shear wave velocity V_S with depth, the simplified approach based on elastic response spectra defined according to ground type ($V_{S,30}$) of the Italian building code tends to underestimate the seismic action and should be used with caution.
Keywords: site seismic response analysis, site effects, L'Aquila 2009 earthquake.

1 Introduction

The April 6, 2009 Abruzzo earthquake (M_L = 5.8, M_W = 6.3) caused considerable damage to structures over an area of approximately 600 square kilometres, including the city of L'Aquila (MCS Intensity I = VIII-IX) and several villages of the middle Aterno River valley. A maximum MCS Intensity I = IX-X was experienced at Onna and Castelnuovo. Even for similar types of buildings the

WIT Transactions on The Built Environment, Vol 120, © 2011 WIT Press
www.witpress.com, ISSN 1743-3509 (on-line)
doi:10.2495/ERES110031

distribution of damage within the affected area was irregular, creating speculation for both rupture directivity and site amplification effects.

Soon after the earthquake evaluations of site effects (GEER Working Group [1]) were obtained from the available strong motion recordings in the epicentral area, including the city of L'Aquila. In the middle Aterno River valley, where such recordings were not available, a preliminary assessment of site effects was carried out based on the survey of the variable damage distribution (in nearby villages, or within the same village), which was related to geological and morphological conditions, accounting for the different types of buildings.

In the following months quantitative evaluations of site effects based on numerical site response analyses were made available, as a result of a comprehensive seismic microzonation project of the area of L'Aquila, entrusted by the Italian Department of Civil Protection (MS–AQ Working Group [2]).

In this paper the attention is focused on site effects in the urban area of L'Aquila. In particular, two zones of significant interest are considered: (a) the old city centre of L'Aquila, which includes most of the historical heritage and several old masonry buildings, heavily damaged by the main shock, and (b) the area of Pettino, a recently developed suburban residential district located NW of the city centre, also affected by considerable damage, where most buildings are 3-6 storey reinforced concrete frame structures. The paper presents the results of numerical analyses carried out to assess the different seismic response of two test sites (Figure 1), one located in the city centre (Palazzo Camponeschi) and one in the Pettino district (Via Sila Persichelli), selected as representative of the typical subsoil conditions in each of the two examined areas.

Figure 1: Location of the two test sites in the area of L'Aquila.

2 Subsoil conditions in the urban area of L'Aquila

The subsoil conditions in the urban area of L'Aquila were reconstructed based on geological information and on a large amount of results of geotechnical and geophysical investigations executed in the area of L'Aquila in the period 2009-2011, in particular for the seismic microzonation project (MS–AQ Working Group [2]) and for ongoing research at the University of L'Aquila, Centre for Research and Education in Earthquake Engineering (CERFIS).

The site investigation data base includes borehole logs, in situ measurements of shear wave velocity V_S by various techniques (Down-Hole, Cross-Hole, surface wave tests, seismic dilatometer) and seismic noise measurements. In particular this study is largely based on V_S profiles obtained in situ by seismic dilatometer (SDMT). The SDMT test procedure and interpretation are described by Marchetti *et al.* [3]. A comprehensive review of SDMT results obtained in the area of L'Aquila following the April 6, 2009 earthquake can be found in Amoroso *et al.* [4]. Due to the characteristics of the soils commonly encountered in this area (mostly coarse-grained, non-penetrable), SDMT measurements (V_S-only) were generally executed in backfilled boreholes, according to the procedure devised by Totani *et al.* [5].

The subsoil conditions in the urban area of L'Aquila are quite complex. In the city centre (Figure 2a) the upper portion of the subsoil is constituted by the deposit known as "Brecce dell'Aquila" (fine to coarse calcareous fragments of variable size, mostly of some centimetres, embedded in sandy or silty matrix, characterized by highly variable cementation and mechanical properties), ≈ 80-100 m thick, where generally V_S ≈ 600-1000 m/s. The breccias are superimposed to fine- to medium-grained, mostly silty lacustrine deposits of average thickness ≈ 250-270 m, where V_S ≈ 400 to 600-700 m/s, placed on the bedrock (limestone). Gravimetric investigations (MS–AQ Working Group [2]), confirmed directly by a 300 m deep borehole in Piazza Duomo (Amoroso *et al.* [6]), indicate that the top surface of the bedrock in the city centre is located below 300 m depth.

The area of Pettino, NW of the city centre (Figure 2b), is mostly characterized by the presence of coarse-grained debris materials (calcareous gravel in sandy silty matrix), having V_S ≈ 600-1000 m/s, placed on the lacustrine deposits (here of very small thickness) or directly on the calcareous bedrock. The gravel layer is frequently covered with soft silty-clayey sediments of variable thickness (maximum ≈ 10-15 m), generally having V_S ≈ 200-300 m/s.

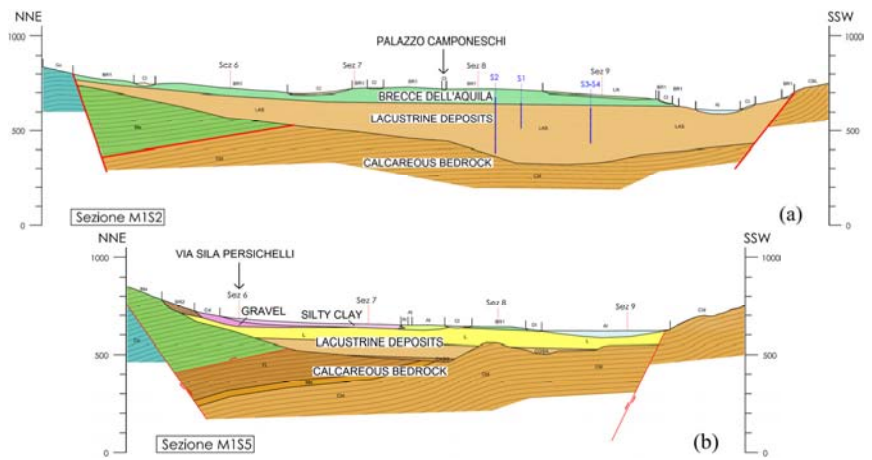

Figure 2: Schematic geological sections across (a) the city centre of L'Aquila, and (b) the Pettino area (modified after MS–AQ working group [2]).

The above schematic description highlights substantially different subsoil conditions in the two areas. Basically, in the city centre the subsoil is characterized by an inversion of the shear wave velocity with depth, at the transition from the breccias to the lacustrine silts, and the bedrock (*geological* and *seismic*) is over 300 m deep. In contrast in the area of Pettino the shear wave velocity increases with depth and the *seismic* bedrock (V_S > 800 m/s) is frequently encountered at ≈ 20 m depth or less. Also, significant contrasts of V_S may be detected at the shallow contact silty clay/gravel. Such dissimilar pattern was confirmed by a large number of seismic noise measurements carried out for the seismic microzonation (MS–AQ Working Group [2]). In the city centre these measurements clearly identified, in the H/V spectral ratio, the presence of a peak of f_0 (frequency of the first significant amplification peak) at 0.5-0.6 Hz, corresponding to the top surface of the deep calcareous bedrock. (Low-frequency amplification effects in L'Aquila city centre had already been signaled by De Luca *et al.* [7]). In the area of Pettino amplification peaks were frequently observed between 3 and 7-8 Hz, suggesting contrasts of V_S at shallow depth.

3 Numerical site response analysis method and seismic input

3.1 Method of analysis

Numerical analyses of seismic response at the two selected sites were carried out using a 1D linear equivalent model, as implemented in the computer code EERA (Bardet *et al.* [8]). It is recognized that 2D or 3D effects may have played an important role in the non-uniform amplification effects observed at different sites (as well as many other factors, e.g. vertical component of ground motion, directivity effects, etc.). However, as a first approximation, the simple 1D model was assumed adequate to compare different responses of the two examined sites.

3.2 Seismic input data

The ground motion input data used in the numerical analyses include six different accelerograms applied at the bedrock (Figure 3). Five of these accelerograms were defined for the seismic microzonation of the area of L'Aquila (MS–AQ Working Group [2]): (NTC-08) compatible with the uniform hazard response spectrum (UHS) of the Italian building code, (PROB) compatible with the UHS spectrum obtained by probabilistic seismic hazard assessment, (DET_1, DET_2 and DET_3) obtained using a deterministic approach. The sixth (natural) accelerogram was selected from the Italian strong motion data base (http://itaca.mi.ingv.it) by use of strict criteria, e.g. source characteristics, ground type at the recording station, magnitude, distance from the source, maximum horizontal acceleration expected at the site. The selected accelerogram (UM) is the strong motion (EW component) recorded at the Assisi station during the September 26, 1997 Umbria-Marche earthquake (M_w = 6, on outcrop, normal fault, site-source distance ≈ 20 km), scaled to a peak ground acceleration similar to the other five accelerograms (scaling factor ≈ 2).

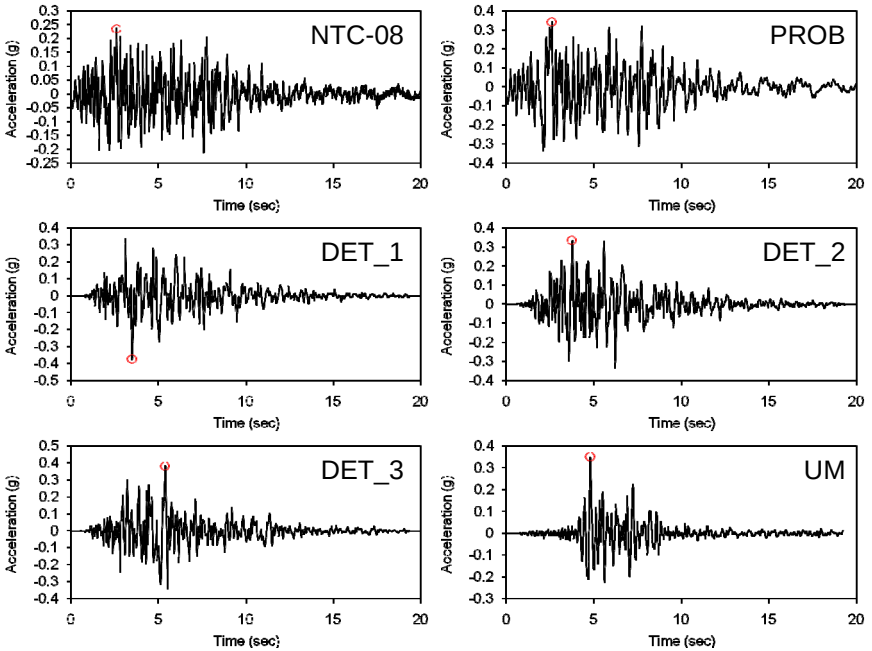

Figure 3: Input accelerograms used in site seismic response analyes.

4 Site response analysis in L'Aquila city centre

4.1 Input soil data

The geotechnical model of the subsoil at the site of Palazzo Camponeschi (L'Aquila city centre), including the soil parameters used in the numerical analyses, is schematized in Figure 4. The subsoil was modelled as a two-layer system: an upper 80 m thick coarse-grained layer (breccias), having V_S generally > 800-1000 m/s, and a lower 270 m thick fine-grained layer (lacustrine silts) having $V_S \approx$ 600-700 m/s, placed on the calcareous bedrock (350 m depth).

The profile of V_S in the breccias was defined as an average of five V_S profiles obtained by SDMT in backfilled boreholes to 74 m depth (Figure 5). In the lower lacustrine silts, in absence of direct measurements to this depth, the profile of V_S was defined as an average of V_S estimated as a function of depth or stress level by the experimental relationships by Chiara [9] and Crespellani *et al.* [10]. Such V_S profile is in reasonable agreement with V_S measured by Cross-Hole (Cardarelli and Cercato [11]) and by SDMT (Amoroso *et al.* [4]) at sites located at a lower elevation at the border of L'Aquila city centre (Ponte Rasarolo – Aterno River, Fontana 99 Cannelle), where the top of the same lacustrine formation was encountered near the ground surface. The calcareous bedrock was characterized by V_S = 1250 m/s, derived from a Cross-Hole test executed at the site of the strong motion station AQV (a few km West of the city centre), where the bedrock was found at ≈ 50 m depth (Di Capua *et al.* [12]).

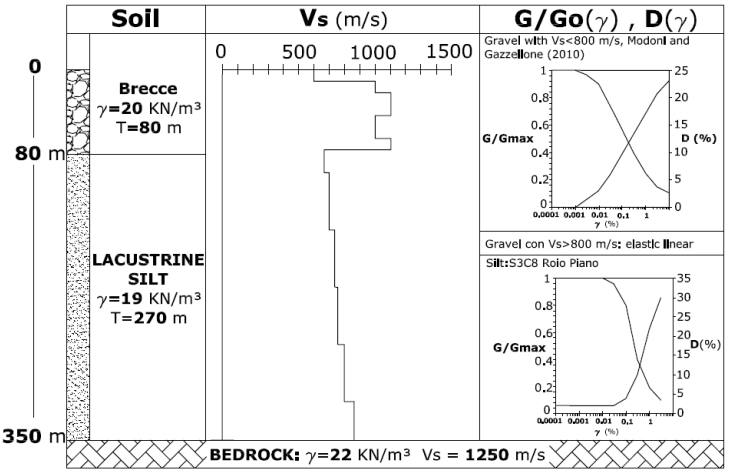

Figure 4: Geotechnical model of the subsoil and soil parameters for 1D seismic response analysis at the site of Palazzo Camponeschi.

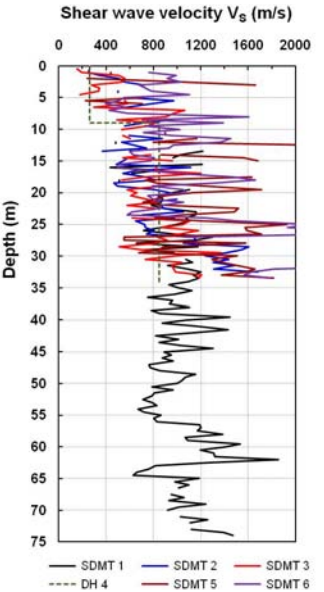

Figure 5: Profiles of shear wave velocity V_S obtained by SDMT (in backfilled boreholes) and Down-Hole (DH) at the site of Palazzo Camponeschi.

A specific difficulty in characterizing the non-linear and dissipative soil behaviour for seismic response analyses in the city centre of L'Aquila is the lack of laboratory curves of the normalized shear modulus G/G_0 and damping ratio D versus shear strain γ (undisturbed sampling is impossible in the breccias and

prohibitive in the lower very deep lacustrine silts). In absence of specific G/G_0 - γ and D - γ laboratory curves at the site of Palazzo Camponeschi, in the breccias literature G/G_0 - γ and D - γ curves, proposed by Modoni and Gazzellone [13] for dense gravel, were assumed in the upper 10 m (weakly cemented, $V_S \approx 600$ m/s). Between 10 and 80 m (higher cementation, $V_S > 1000$ m/s) the soil behaviour was assumed as linear elastic, as a first approximation. The lacustrine silt was characterized by G/G_0 - γ and D - γ laboratory curves obtained by resonant column/torsional shear tests carried out at the University of Naples Federico II on an undisturbed sample (S3C8) taken in the same lacustrine formation, at 50 m depth, in the C.A.S.E. Project site of Roio Piano (MS–AQ Working Group [2]).

4.2 Results and comparisons

Figure 6 shows the comparison of the elastic acceleration response spectra resulting from the numerical analysis using six different input accelerograms, the corresponding average spectrum and the elastic response spectrum defined according to the simplified approach of the Italian building code (NTC 2008 [14]), for a reference return period T_R = 475 years and type B ground. It can be noted in Figure 6 that the spectral acceleration S_a calculated by the numerical analysis (average of the six input accelerograms) is generally higher than S_a calculated according to NTC 2008 [14] in the range of periods $T \approx 0.2$-0.4 s, similar to the fundamental period of many old masonry buildings located in L'Aquila city centre. For all the input accelerograms the diagram exhibits

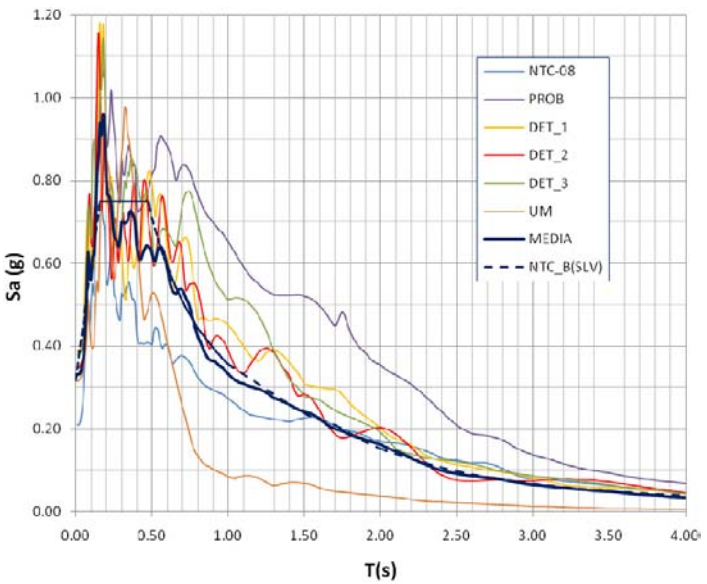

Figure 6: Comparison of elastic acceleration response spectra obtained by site response analysis and according to NTC 2008 [14], for a return period T_R = 475 years and type B ground, at the site of Palazzo Camponeschi.

marked peaks of S_a concentrated within a very narrow range of periods ($T \approx$ 0.15-0.2 s). At higher periods the average trend of S_a resulting from the site response analysis tends to become similar to the building code spectrum. In general, the NTC 2008 [14] simplified approach underestimates the seismic action calculated by site response analysis over the whole range of periods.

Table 1 summarizes the values obtained by the numerical analysis, for each of the six input accelerograms, of the peak ground horizontal acceleration (*PGA*), the peak ground horizontal displacement (*PGD*) and the Housner [15] spectral intensity (I_H), calculated from velocity response spectra in the range of periods 0.2 to 2 s. The values of *PGA* obtained from the site response analysis, mostly in the range 0.31-0.39 g, are in agreement with the values (0.33-0.35 g in horizontal direction) recorded during the April 6, 2009 main shock at the strong motion station AQK, located in the city centre at ≈ 1 km distance, except the much lower *PGA* = 0.21 g calculated using the input accelerogram (NTC-08). Also, the *PGA* calculated by the site response analysis is generally higher than the *PGA* = 0.30 g predicted by the Italian building code, for T_R = 475 years and type B ground. A similar agreement is observed between the values of horizontal *PGD* calculated (5.9-14.2 cm) and recorded at AQK during the main shock (7.65-12.50 cm), except the lower *PGD* = 1.2 cm calculated using the input accelerogram (UM). The values of the Housner intensity I_H obtained from the site response analysis for the six input accelerograms vary from 0.50 m (UM) to 1.75 m (PROB) and, on average, are slightly higher than the values calculated from the main shock recording at AQK (1.07-1.09 cm, Masi *et al.* [16]). The value calculated according to NTC 2008 [14] is much lower (I_H = 0.90 m).

Table 1: Peak ground horizontal acceleration (*PGA*), peak ground horizontal displacement (*PGD*) and Housner intensity (I_H) in the range of periods T = 0.2-2 s evaluated by site seismic response analysis at the site of Palazzo Camponeschi for six input accelerograms.

	NTC-08	PROB	DET_1	DET_2	DET_3	UM
PGA (g)	0.21	0.39	0.39	0.35	0.38	0.31
PGD (cm)	6.6	14.2	7.8	5.9	9.6	1.2
I_H (m)	0.80	1.75	1.24	1.12	1.32	0.50

5 Site response analysis in the Pettino area

5.1 Input soil data

The geotechnical model of the subsoil at the site of Via Sila Persichelli (Pettino), including the soil parameters used in the numerical analyses, is schematized in Figure 7. The model is composed of an upper soil layer of variable composition (clayey silt including cobbles), with V_S increasing from ≈ 300 to 550 m/s, placed on the *seismic* bedrock (V_S = 900 m/s), located at 21 m depth. The profile of V_S was defined as an average of three V_S profiles obtained by SDMT in backfilled boreholes to ≈ 27-30 m depth (Figure 8). The upper soil layer was characterized by laboratory G/G_0 - γ and D - γ curves obtained by resonant column/torsional

shear tests carried out at the Politecnico di Torino on an undisturbed sample (S1C1), taken in a soil layer of similar characteristics, at 5 m depth, in the C.A.S.E. Project site of Camarda (MS–AQ Working Group [2]).

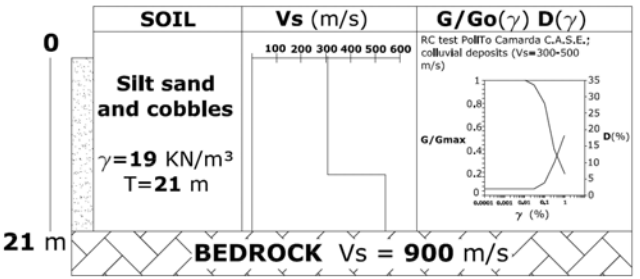

Figure 7: Geotechnical model of the subsoil and soil parameters for 1D seismic response analysis at the site of Via Sila Persichelli.

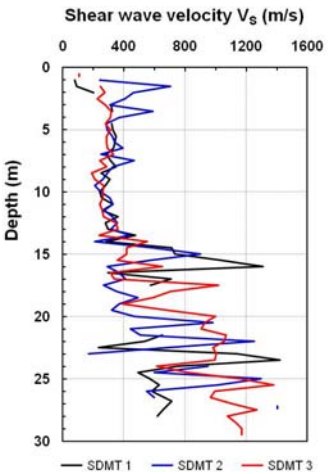

Figure 8: Profiles of shear wave velocity V_S obtained by SDMT (in backfilled boreholes) at the site of Via Sila Persichelli.

5.2 Results and comparisons

Figure 9 shows the comparison of the elastic acceleration response spectra resulting from the numerical analysis using six different input accelerograms, the corresponding average spectrum and the elastic response spectrum defined according to the simplified approach suggested by the Italian building code (NTC 2008 [14]), for a reference return period T_R = 475 years (SLV) and type E ground. Figure 9 shows that the spectral acceleration S_a calculated by the numerical analysis (average of the six input accelerograms) is generally higher than S_a calculated according to NTC 2008 [14] in the range of periods $T \approx$ 0.2-0.6 s. Also in this case marked peaks of *S*a are observed, concentrated within the range of

periods $T \approx 0.15$-0.4 s (less narrow than in the city centre). The maximum amplitude of *S*a is much higher than in the city centre. For $T > 0.5$ s the average trend of S_a resulting from the numerical analysis tends to become lower than the building code spectrum. Compared to the site response analysis results, the NTC 2008 [14] simplified approach seems to largely underestimate the seismic action at low periods and to overestimate it at high periods. A similar trend is observed, in Figure 9, even in comparison to the elastic response spectrum defined according to NTC (2008) [14] for a return period $T_R = 975$ years (SLC).

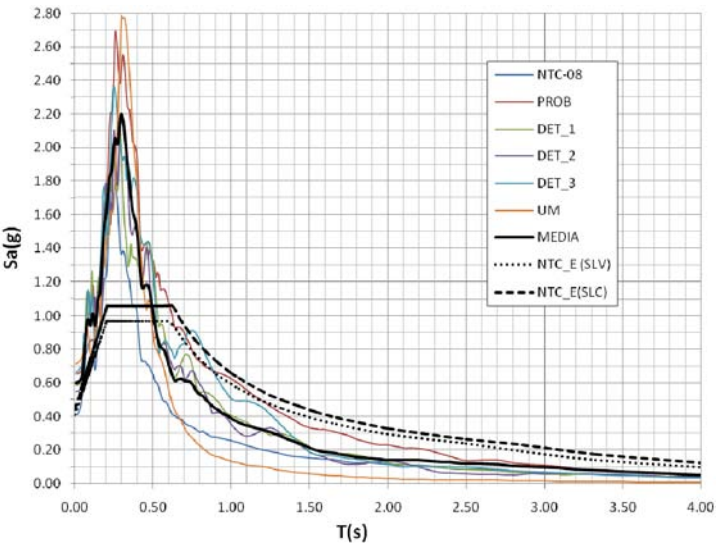

Figure 9: Comparison of elastic acceleration response spectra obtained by site response analysis and according to NTC 2008 [14], for return periods $T_R = 475$ years (SLV) and $T_R = 975$ years (SLC) and type E ground, at the site of Via Sila Persichelli.

Table 2 summarizes the values obtained by the numerical analysis, for each of the six input accelerograms, of the peak ground horizontal acceleration (*PGA*), the peak ground horizontal displacement (*PGD*) and the Housner intensity (I_H) calculated in the range of periods 0.2 to 2 s. The values of *PGA* = 0.42-0.71 g calculated by the site response analysis are almost twice than the *PGA* = 0.21-0.39 g calculated in the city centre, and higher than *PGA* = 0.40 g (SLV) predicted

Table 2: Peak ground horizontal acceleration (*PGA*), peak ground horizontal displacement (*PGD*) and Housner intensity (I_H) in the range of periods $T = 0.2$-2 s evaluated by site seismic response analysis at the site of Via Sila Persichelli for six input accelerograms.

	NTC-08	PROB	DET_1	DET_2	DET_3	UM
PGA (g)	0.42	0.42	0.59	0.55	0.67	0.71
PGD (cm)	0.7	1.4	1.1	1.0	1.1	1.4
I_H (m)	0.88	1.90	1.34	1.31	1.56	0.98

by NTC 2008 [14]. In contrast, the values of PGD = 0.7-1.4 cm obtained from the site response analysis are considerably lower than PGD = 1.2-14.2 cm calculated in the city centre. The values of the Housner intensity I_H obtained from the site response analysis for the six input accelerograms vary in the range 0.88 to 1.90 m and are similar to I_H = 0.5 to 1.75 m calculated in the city centre.

6 Conclusions

The comparison of results of seismic response analyses at the two sites confirms that site effects, related to different subsoil conditions, played an important role in the observed non-uniform damage distribution due to the April 6, 2009 earthquake. The above results are in agreement with previous observations based on comparisons of strong motion recordings of main shock at different stations (e.g. Masi *et al.* [16]), as well as with results of the seismic microzonation of the area of L'Aquila (MS–AQ Working Group [2]).

In L'Aquila city centre, despite the peak ground horizontal acceleration is not particularly high (the values of PGA = 0.33-0.35 g recorded at the AQK station during the main shock were the lowest recorded in the epicentral area), the values of the Housner intensity and of the peak ground horizontal displacement ($I_H \approx$ 1-1.10 m, $PGD \approx$ 7-12 cm measured at AQK, Masi *et al* [16]) are similar to or higher than the values recorded at the stations where much higher PGA were measured (0.66 g at AQV). In this case, as noted in previous studies, the PGA alone appears a poor indicator of the damage potential of ground motion, while the Housner intensity I_H appears a more effective parameter to correlate the severity of ground motion to structural damage. Particularly in the city centre, characterized by an inversion of V_S with depth, the simplified approach based on elastic response spectra defined according to ground type ($V_{S,30}$) of the Italian building code tends to underestimate the seismic action.

In the area of Pettino the site response analysis provided values of PGA = 0.42-0.71 g, almost twice than PGA calculated in the city centre. This result is in agreement with the grade-3 microzonation map obtained by MS–AQ Working Group [2], where the Pettino district is classified as the zone of maximum amplification within the urban area of L'Aquila.

References

[1] GEER Working Group, Preliminary Report on the Seismological and Geotechnical Aspects of the April 6 2009 L'Aquila Earthquake in Central Italy. Report No. GEER-016, Ver. 2.0, Sept. 2009, www.geerassociation.org

[2] MS–AQ Working Group, Microzonazione sismica per la ricostruzione dell'area aquilana. Regione Abruzzo – Dipartimento della Protezione Civile, L'Aquila, 3 vol. & Cd-rom, 2010.

[3] Marchetti, S., Monaco, P., Totani, G. & Marchetti, D., In Situ Tests by Seismic Dilatometer (SDMT). *From Research to Practice in Geotechnical Engineering*, ASCE Geotech. Spec. Publ. No. 180, pp. 292-311, 2008.

[4] Amoroso, S., Marchetti, D., Marchetti, S., Monaco, P., Totani, F. & Totani, G., Site characterization by seismic dilatometer (SDMT) in the area of L'Aquila. *Proc. Workshop "The Dynamic Interaction of Soil and Structure"*, L'Aquila, 19 March 2010, Aracne editrice: Roma, 2011.
[5] Totani, G., Monaco, P., Marchetti, S. & Marchetti, D., V_S measurements by seismic dilatometer (SDMT) in non-penetrable soils. *Proc. 17th ICSMGE*, Alexandria, Egypt, IOS Press, **2**, pp. 977-980, 2009.
[6] Amoroso, S., Del Monaco, F., Di Eusebio, F., Monaco, P., Taddei, B., Tallini, M., Totani, F. & Totani, G., Campagna di indagini geologiche, geotecniche e geofisiche per lo studio della risposta sismica locale della città dell'Aquila: la stratigrafia dei sondaggi giugno-agosto 2010. University of L'Aquila, Report CERFIS 1/10, 2010, www.cerfis.it
[7] De Luca, G., Marcucci, S., Milana, G. & Sanò, T., Evidence of low-frequency amplification in the city of L'Aquila, Central Italy, through a multi-disciplinary approach including strong- and weak-motion data, ambient noise, and numerical modeling. *Bull. Seism. Soc. Am.*, **95**(4), pp. 1469-1481, 2005.
[8] Bardet, J.P., Ichii, K. & Linn, C.H., EERA – A Computer Program for Equivalent-linear Earthquake site Response Analyses of Layered Soil Deposits. University of Southern California, 2000.
[9] Chiara, N., Investigation of Small-Strain Shear Stiffness Measured in Field and Laboratory Geotechnical Studies. MS Thesis, Department of Civil Engineering, University of Texas at Austin, 2001.
[10] Crespellani, T., Ghinelli A., Vannucchi, G., An Evaluation of the Dynamic Shear Modulus of a Cohesive Deposit near Florence, Italy. *Proc. XII ICSMFE*, Rio de Janeiro, 1989.
[11] Cardarelli, E. & Cercato, M., Relazione sulla campagna d'indagine geofisica per lo studio della Risposta Sismica Locale della città dell'Aquila. Prova crosshole sondaggi S3-S4. Report DICEA – University of Roma La Sapienza, 2010, www.cerfis.it
[12] Di Capua, G., Lanzo, G., Luzi, L., Pacor, F., Paolucci, R., Peppoloni, S., Scasserra, G. & Puglia, R., Caratteristiche geologiche e classificazione di sito delle stazioni accelerometriche della RAN ubicate a L'Aquila. Report Progetto S4: Banca dati accelerometrica, 2009, http://esse4.mi.ingv.it
[13] Modoni, G. & Gazzellone, A., Simplified theoretical analysis of the seismic response of artificially compacted gravels. *V Int. Conf. on Recent Advances in Geotech. Earthquake Eng. and Soil Dyn.*, San Diego, Paper No. 1.28a, 2010.
[14] NTC 2008 – Norme Tecniche per le Costruzioni. (Italian Building Code).
[15] Housner, G.W., Spectrum Intensity of Strong-Motion Earthquakes. *Proc. Symp. Earthquakes and Blast Effects on Structures*, UCLA, pp. 20-36, 1952.
[16] Masi, A., Chiauzzi, L., Braga, F., Mucciarelli, M., Vona, M. & Ditommaso, R., Peak and integral seismic parameters of L'Aquila 2009 ground motions: observed versus code provision values. *Bull. Earthquake Eng.*, **9**, pp. 139-156, 2011.

Application of seismic isolation in the retrofit of historical buildings

P. Clemente[1] & A. De Stefano[2]
[1]*ENEA, Rome, Italy*
[2]*Politecnico di Torino, Turin, Italy*

Abstract

In this paper the studies carried out for the retrofit of Margherita Palace, seriously damaged by L'Aquila earthquake, are shown. The buildings and the tower have been first analyzed by means of ambient vibration tests, in order to find out the dynamic characteristics of the structure even in a damaged situation. On the basis of the results obtained and of the microzoning analysis carried out after the seismic event, the base isolation has been proposed as the most suitable solution for the seismic retrofit of the structure, because allows to obtain a good structural result without compromising the architectural characteristic of the superstructure. A new isolation system is then proposed for the seismic retrofit of historical buildings, based on the realization of an isolated platform under the building foundation without any intervention on the building. The system can be used for single buildings but also for complex structure, typical of Italian historical centres.
Keywords: seismic isolation, historical buildings, cultural heritage.

1 Introduction

The traditional techniques, based on the increasing of strength and ductility, are not suitable for the seismic rehabilitation of cultural heritage buildings for the following reasons:

- they are often not reversible,
- they make use of materials different and incompatible with the original ones,
- they change the original structural conception.

WIT Transactions on The Built Environment, Vol 120, © 2011 WIT Press
www.witpress.com, ISSN 1743-3509 (on-line)
doi:10.2495/ERES110041

The last aspect is sometimes compulsory, because the building was design without accounting for the seismic actions, being vulnerable even to moderate events. Besides, historical buildings often present weak points, such as an irregular form both in plan and in elevation, the lack of vertical joints and transversal braces, in-plane flexibility of floor slabs and shallow foundations.

Furthermore, under earthquakes of high intensity, traditional structures can just guarantee against the collapse, but cannot avoid heavy damages both to structural and non-structural elements. As a result, for cultural heritage buildings, a suitable equilibrium between the two opposite requirements is usually accepted, i.e. a partial seismic improvement is obtained preserving their original monumental characteristics, identity and historical value.

It is worth noting that, due to the historical importance and to the daily presence of tourists, the seismic rehabilitation of historical buildings is quite delicate, aiming at the protection of both human life and cultural heritage.

Base isolation could be a suitable solution for the rehabilitation of historical structures. It aims to reduce seismic actions, thus avoiding significant damages to the structure and its contents even under strong earthquakes, and presents very low interference with the structure itself.

In this paper the seismic isolation of an earthquake damaged building in L'Aquila is proposed. First of all an experimental campaign has been carried out in order to find out the dynamic characteristics of the structure. Then a conventional improvement intervention has been defined, which allows the structure to be able to support minimum horizontal actions. On the basis of the effective earthquake resistance of the restored structure, several solutions for the base isolation system have been designed.

2 Margherita Palace and the Civic Tower

The erection of the City Hall in L'Aquila started in 1294 and a first important restoration was completed in 1541 (Fig. 1). Important works were done since 1573, when the building became the house of Margherita d'Austria, and most of the original characteristics were lost. At the beginning of the 20th century another

Figure 1: Margherita Palace: main facade and courtyard.

restoration intervention was done to realize a concrete ring beam under the roofing. The palace has two levels and rectangular plan of about 40*60 *m*, with an internal court. The vertical structure is made of stone and brick masonry with good mortar. The horizontal structures are made of masonry vaults, some of them with chains, and steel decks. Underground levels could be present under some parts of the building.

The Civic Tower, built from 1254 and 1374 at the N-E corner, was seriously damaged by the 1703 earthquake and rebuilt with lower height. In 1937 the tower was consolidated by inserting iron T-beams at the floors. It has an almost square cross-section of about 6.30 *m*. The thickness of the walls is equal to 2.0 *m* at the basement.

The palace suffered heavy damages during L'Aquila earthquake of April 6th, 2009. Several cracks are apparent and local collapse mechanisms have been activated. In more details the seismic events caused the disconnection between the orthogonal walls, the out of plane collapse of some masonry walls, the formation of large cracks, collapse of some floors and important damages to the stairs.

3 Dynamic characterization

Fifteen seismometers (velocimeter sensors) have been used, deployed in two configurations, the first one relative to the building and the second to the tower.

In the first one, the sensors have been deployed in the building in order to point put the global resonance frequencies and any mode of each part (Fig. 2). In the second configuration sensors have been deployed on different levels of in the tower.

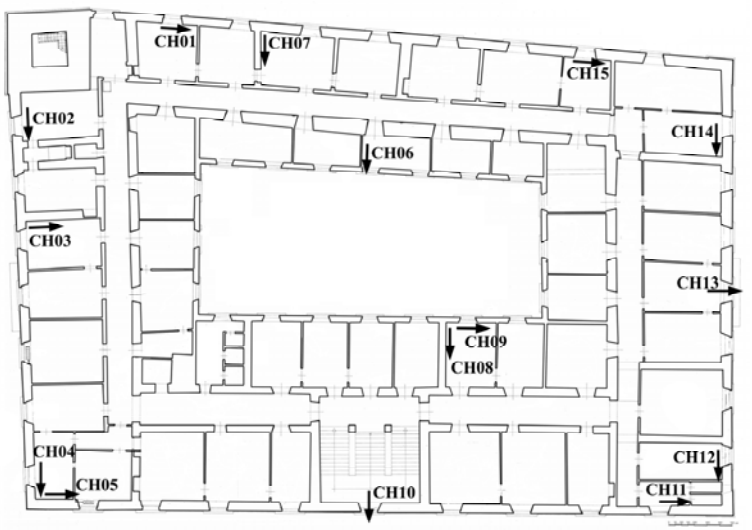

Figure 2: Second floor: sensor deployment.

For each configuration three tests of about 300 *s* have been carried out, with a sample rate of 200 *point/s* using ambient noise only as source of vibrations. With this low level of excitation the building showed a quasi-linear behaviour and a spectral analysis could be performed. The data has been analyzed in the frequency domain by plotting the power spectral density (PSD) of each record and the cross spectral densities (CSD), in terms of amplitude and phase factor, of selected couples of records with the corresponding coherence functions. As well known, peaks in PSD could be associated to structural frequencies while the same peaks in CSD, with value of phase factor equal to 0° or 180°, and value of coherence function close to unity, confirm this statement and give some indications on the modal shape associated to each structural frequency.

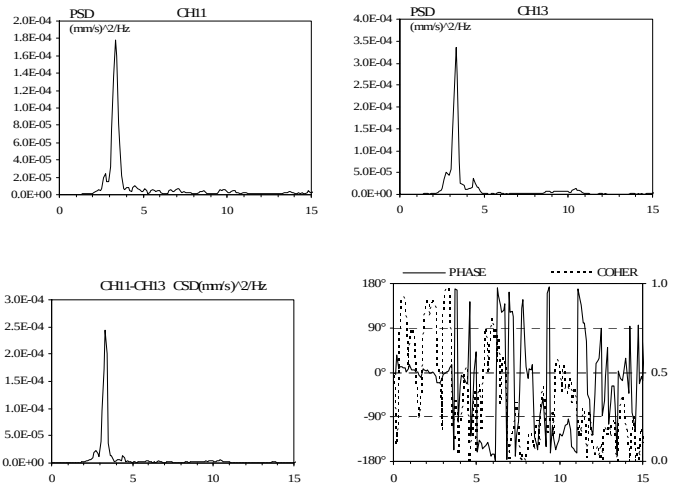

Figure 3: PSD and CSD of longitudinal sensors.

In Fig. 3 the PSDs and the CDS relative to sensors CH11 and CH13 in the first configuration are plotted. The experimental analysis pointed out the resonance frequencies of the building listed in Tab. 1.

Table 1: Resonance frequencies of the building.

Freq. (Hz)	*Description*
2.24	Transversal
2.74	Transversal + Tors.
3.32	Longitudinal
3.71	Torsional

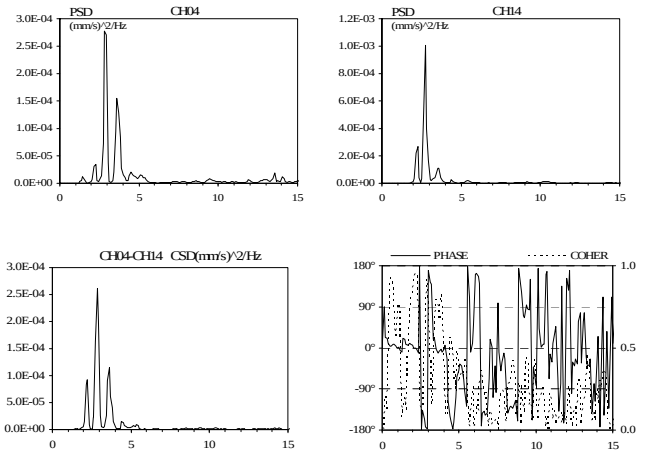

Figure 4: PSD and CSD of transversal sensors.

In Fig. 4 the PSDs and the CDS relative to the second configuration are shown. The experimental analysis pointed out the resonance frequencies of the tower listed in Tab. 2.

Table 2: Resonance frequencies of the tower.

Freq. (Hz)	*Description*
1.46	Transversal
1.46	Longitudinal
2.83	Transversal
3.22	Longitudinal
4.20	Longitudinal
4.98	Transversal
5.66	Longitudinal

4 The base isolation system

The obtained values must be taken into account in the design of the isolation system, in order to obtain a suitable decoupling between the motion of the building and the motion of the soil. As well known, in fact, the frequency of the isolated building should be lower enough with reference to the frequency of the superstructure, usually not higher than one third of it.

Besides, it is important reminding that the seismic microzoning, carried out by the Italian National Civil Protection Department, pointed out the presence of seismic amplifications in the range 0.4÷0.6 *Hz*. So the main resonance frequencies of the isolated system should be lower than the minimum value of this range.

Finally, the isolation system should be designed in order to reduce the seismic action in the structure to the value that the restored building will be able to support in the elastic range.

In more details, the frequency of the isolated building, or its first period of vibration, is chosen as the one corresponding, in the elastic spectrum relative to the life limit state (SLV), to the value of acceleration which can affects the superstructure.

From a preliminary analysis a value of 0.10*g* has been fixed as the maximum spectral acceleration in the superstructure and the corresponding period in the SLV spectrum has been assumed as the period of the isolated building. Then the corresponding acceleration and displacements values in the collapse limit state (SLC) spectrum has been evaluated (Fig. 5). Taking into account also what said about the local amplification, the isolation period has been fixed equal to 3.0 s. For this value of the period, tt is $S_e = 0.07g$ and $S_{De} = 0.30\ m$.

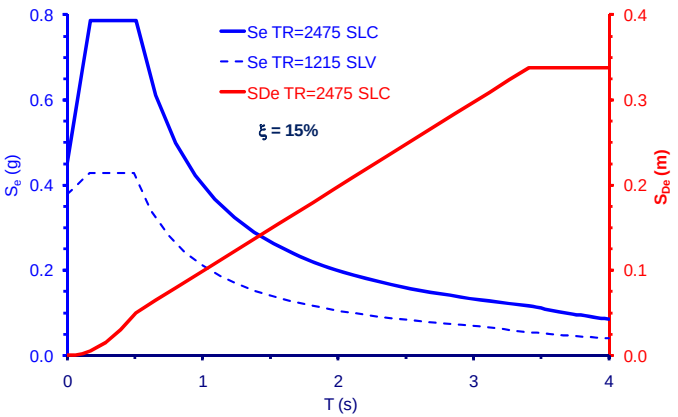

Figure 5: SLV and SLC spectra.

Different solutions have been considered for the seismic retrofit of the structure. In the following only two of them will be shown, the most traditional and the most innovative one, respectively.

4.1 Insertion of a base isolation system in the existing structure

In the first solution the isolation system has been inserted just below the ground level of the building. A gap between the masonry walls and the foundations can be created by cutting the masonry walls at their basement, as shown in figs. 6 and 7 and realizing two concrete beams under and above the isolators.

The construction phases are the following:

– realization of windows in the masonry walls at the isolation device positions. The window should be high enough to contain a lower and a upper beams and the isolator (Fig. 6);

- construction of the portion of the lower concrete beam, with the overlap steel bar between the beam portion of the considered window and the next ones;
- installation of the isolation device;
- realization of the portion of the upper concrete beam, with the overlap steel bar between the adjacent windows;
- cutting of masonry between the windows;
- connection of the lower concrete beam portions and of the upper ones (Fig. 7).

This solution requires traditional works and is not very expensive, but presents the disadvantages of requiring the modification of the foundations and of being not reversible. So it is not always applicable in practice for historical constructions.

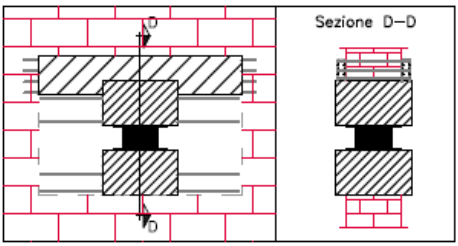

Figure 6: Window in the wall.

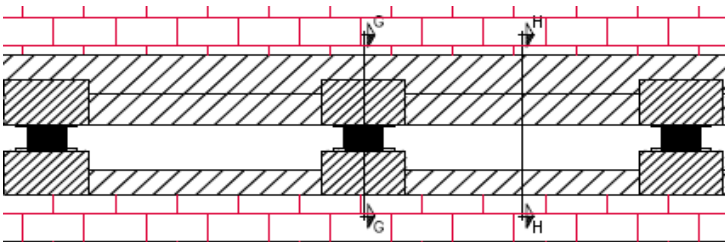

Figure 7: Isolation devices, lower and upper beams.

4.2 A new solution

The new solution proposed consists in the realization of an isolated platform under the foundations of the building, without touching the building itself (Fig. 8). A discontinuity between the foundations and the soil is created by means of the insertion of horizontal pipes and the positioning of isolation devices at the horizontal diametric plane. Then the building is separated from the surrounding soil in order to allow the horizontal displacements required by the isolation system. So the structure is seismically isolated but not interested by interventions

that could modify its architectural characteristics, which is very important for historical buildings.

Even underground level are not modified but can be part of the seismically protected building. In more details the construction phases are the following (Fig. 9):

- a trench is first excavated of at one side of the building and pipes are inserted by means of auger boring or micro-tunnelling technique; the diameter of pipes should be ≥ 2 *m*, in order to allow the inspection of the isolation system;

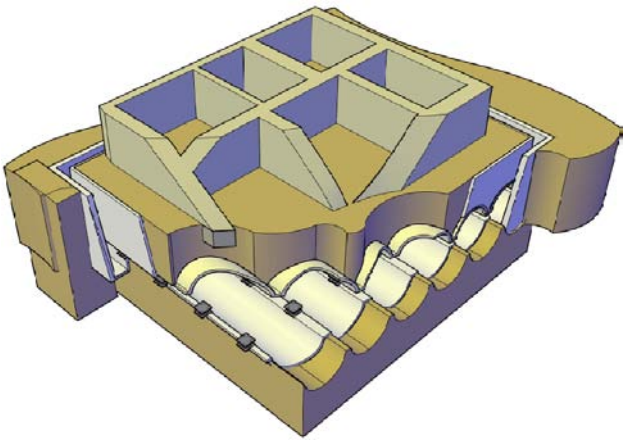

Figure 8: The new isolation system.

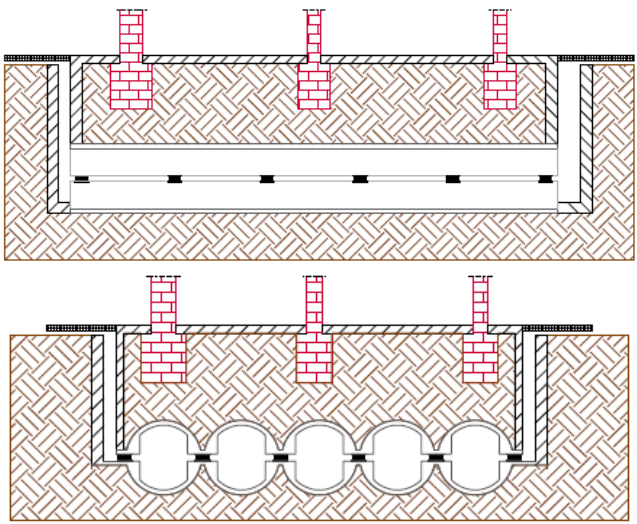

Figure 9: Longitudinal and transversal cross-sections of the new isolation system.

The pieces of pipe should have a particular shape and are composed by two portions, the lower and the upper sectors, respectively, which are connected by means of removable elements.

- the connection elements placed in correspondence of the isolation devices are removed and each pipe is joined with the two adjacent ones, for example by means of a reinforced concrete elements;
- the isolation devices are positioned and the upper adjacent sectors are connected in correspondence of the isolators;
- successively also the other connection elements are removed, so the lower and upper sectors are definitely separated;
- finally vertical walls are built along the four sides of the building and a rigid connection, a concrete slab or other, is realized between the building and the isolation system.

The system allows also the realization of a tunnel for pedestrian or vehicles. The size of the pipes must guarantee the accessibility and the possibility to substitute the devices.

It is worth reminding that the solution presents the advantages that the building and its architectural aspect are not changed and so are the underground levels; this is a very important requirement for historical and monumental structures.

5 Problems to consider: vibrations and settlements

During the micro-tunnelling operation two problems can arise: the soil settlement and the vibration induced at the surface level.

The literature related to the vibrations induced by micro-tunnelling is not very ample and often not strictly pertinent. Some suggestions can come from analogue experiences supplied by large tunnelling works or from vertical boreholes. These experiences suggest that minor threats should be expected from induced vibrations, but theoretical and experimental deeper studies are needed.

More serious problems can arise by settlements [1–3]. To reason concretely in a quantitative manner we will refer to a specific case study, which is Margherita Palace, the City Hall in L'Aquila, where, thanks to a previous experimental dynamic soil characterization at a near site, it is possible to model the mechanical properties of the ground with accuracy. A FE 2-D model has been set up and then exploited in a *Diana 2* environment. The model is necessarily at list a 2-D model, because it shall be useful to analyze a perturbation of limited width. The perturbation is due to the foundation of a building and to the micro-tunnels under it. The vertical edges of the model are kept far enough from the perturbed zone, to reduce their influence as much as possible. The nodes belonging to those edges are restrained by means of spring and dampers able to cut-off the wave reflection.

The dynamic characterization shows that stiffness and strength increase with depth. In the model the soil is described as a layered continuum indefinitely extended, supported by the bedrock at 17 *m* depth. Each layer is 1.0 *m* thick and

its elastic dynamic tangential modulus G_0 is coherent with the measured wave propagation velocities:

$$G_0 = \rho \cdot \upsilon_s^2 \tag{1}$$

The Young dynamic and static modulus is given, respectively, by:

$$E_{dyn} = G_0 \cdot 2 \cdot (1+\nu); \qquad E_{static} = E_{dyn}/3; \qquad (\nu = 0.3) \tag{2}$$

To realize the mesh of the FE model, eight node quadrangular elements have been used, paying attention to keep the aspect ratio near to one and regular as much as possible (Fig. 10). The plane deformation condition is imposed and the boundary nodes respect the following restraining conditions: the vertical displacement is inhibited for the nodes belonging to the lower horizontal edge; the horizontal displacement is inhibited for the nodes belonging to both the lateral vertical edges. A mass density of 2090 kg/m^3 has been assumed.

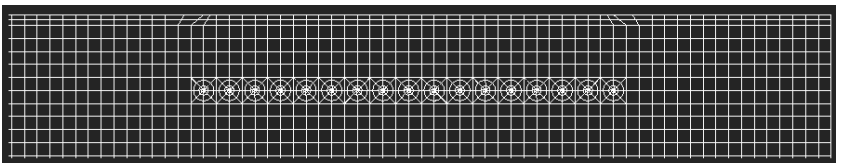

Figure 10: The sub-soil 2-D FE model.

If local perturbations due to building foundation and micro-tunnels are absent, the response of the model to horizontal base shaking or vertical uniform static pressure from the top level are comparable to the response, in similar conditions, of a multi-layered mono-dimensional model, except in proximity of the lateral vertical edges. The successful validation of the model has been based on this criterion.

On the validated model, the building imposes a load of 3000 *kN/m* uniformly distributed along its base width. That load induces a local settlement.

Then micro-tunnels, later named simply "pipes", are included in the model, following two different alternative strategies:

1. First strategy: one central pipe, then the two most external ones and all the other filling the layer from the external pipes to de centre.
2. Second strategy: one central pipe, then the two most external ones; other pipes are then inserted in intermediate positions, regularly spaced, filling gradually the layer.

The advances following the two strategies are shown in Figure 11a and b, respectively, where the settlement is also represented.

The boreholes induce an additional settlement that is the one that we are interested to estimate. The problem being non-linear, the settlement due to insertion of pipes, originated by a stress release process, is computed as difference between the settlement due to the weight of the building and the insertion of the pipes and the settlement due to the weight of the building alone.

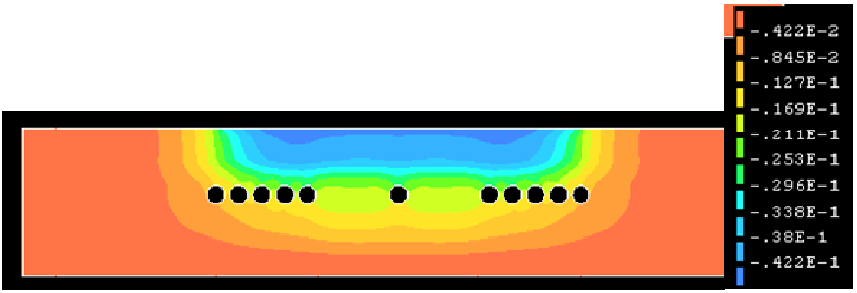

a) strategy 1

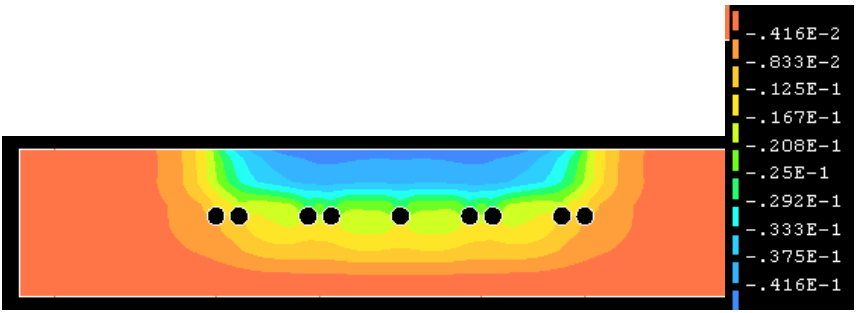

b) strategy 2

Figure 11: Filling the layer of pipes.

The stress release during micro-tunnelling is a three-dimensional mechanism that shall be described by a plane-strain two-dimensional model, as previously stated. It is possible to reach that goal through a conventional hole-boundary force reduction approach known as "β-value method" or Convergence-confinement method proposed by Panet and Guenot (1982) using the stress-release factor λ, varying inside the 0-1 range [1].

Analyses are then based on the decrement of a fictitious internal pressure at the boundary of the holes in agreement with the β-value method. To apply that method inside the FE model simply supporting elastic restrains are distributed along the hole boundaries, with operating direction orthogonal to them. By modifying the stiffness of the elastic supports it is possible to simulate the stress release. A null stiffness of the elastic support gives λ=1.

For the actual case study we assume λ=0.4 and H/D =3.5, where H is the depth of the pipe axis and D is the diameter of the pipe.

The strategy 1 is easier to apply, but the effect on soil adaptation is not so smooth and regular. The final computed value of the settlement is about 6.8 *mm*. The strategy 2 leads to more regular advancement and allows a slight settlement reduction to about 5.6 *mm*. Increasing the stress release factor λ to 0.6 the settlement values increase nearly with a multiplier 1.2. A larger H/D ratio reduces the problem but increases the cost of the trenches. Technologies to contrast the settlements exist and are consolidated but, of course, they push the cost up.

6 Conclusions

A new isolation system has been proposed for the seismic retrofit of historical buildings, based on the realization of an isolated platform under the building foundation without any intervention on the building. The system can be used for single buildings but also for complex structure, typical of Italian historical centers. In fact, the ability of the proposed system to work "under all" can make it useful also for every situation in which separate buildings or components are connected by complex lifelines, pipes and other links. Such condition is usual, for instance, in chemical and power production plants, including the nuclear-ones.

Acknowledgements

The authors thank G. Barla for his important support and contribution and the student Stefano Renna (Politecnico di Torino) who allowed them to use the results of his studies on the soil adaptation and settlements, extracted from his Master Thesis final work.

References

[1] Barla, G. B., Viggiani, G., Le opere in sotterraneo. Proc. of the XXI Italian National Conference of Geotechnics (in Italian), Vol. II, 2002.
[2] Miliziano, S., Soccodato, F.M., Burghignoli, A., Evaluation of damage in masonry buildings due to tunnelling in clayey soils. Proc. 3rd Int. Symp. on Geotechnical Aspects of Underground Construction in Soft Ground, Toulouse, France, pp. 335-340. 2002.
[3] Barla, M., Camusso, M., A method to design microtunnelling installations in the Torino randomly cemented alluvial soil. Tunnelling and Underground Space Technology, ISSN 0886-7798, in print, 2011.

Section 2
Seismic isolation and energy dissipation

This page intentionally left blank

Adaptable dual control systems for earthquake resistance

M. C. Phocas & T. L. Sophocleous
Department of Architecture, University of Cyprus, Nicosia, Cyprus

Abstract

The use of passive energy dissipation systems for seismic control has been proven internationally over the past years as most promising. The proposed concept of Adaptable Dual Control Systems (ADCS), presented in the present paper, relies on the seismic performance of braced frames with cables or tension only rods, following a closed circuit, and hysteretic dampers. ADCS are based on a dual function of the component members, resulting in two practically uncoupled systems: a primary and a secondary system. The primary frame is responsible for the normal vertical and horizontal forces, while the closed damper-bracing mechanism, for the earthquake forces and the necessary energy dissipation. The bracing members are fixed at the bottom of the columns and are free to move horizontally at the primary frame's joints. Relative displacements are induced between the energy dissipation system's component members and the main frame's members. The potentials for maximum energy dissipation of the proposed systems are investigated in three configurations of the control system. In all cases the damper utilizes the relative displacement between its end joints to yield in the inelastic region, enabling the primary frame to resist elastically. ADCS may result to significant energy dissipation, when all design parameters involved are accordingly predefined. The predominant parameters that characterize ADCS seismic behavior are verified in respect to the mechanical properties of the control elements under the action of ten selected earthquake records of the Greek-Mediterranean region. A comparative parametric analysis of the three systems' seismic behavior leads to significant recommendations for their application as alternative energy dissipation systems.

Keywords: earthquake resistance, frame structures, passive control, adaptable systems.

WIT Transactions on The Built Environment, Vol 120, © 2011 WIT Press
www.witpress.com, ISSN 1743-3509 (on-line)
doi:10.2495/ERES110051

1 Introduction

In most recent developments, buildings are usually stiffened for preventing seismic damage. Bracings add stiffness and damping to the structures, they reduce inter-storey drifts, but they increase floor accelerations. Flexible buildings instead produce under earthquake actions large displacements and small accelerations. The method of adding mechanical devices in frame structures that would passively absorb and dissipate the seismic energy has already proven to be a reliable and effective strategy. A number of energy dissipation devices has been developed and tested since the late 1990s [1, 10]. Such mechanical devices are usually attached to bracings of frames to deform and dissipate energy by different means such as: motion of a piston or a plate within a viscous fluid (viscous dampers), or viscoelastic action in polymeric materials (viscoelastic dampers), sliding friction (friction dampers), or yielding of mild steel (metallic dampers). Whereas the most significant advantage of the method is that the composition leads to a concentration of energy in the specified objective areas and therefore the plastic displacements in regions away from the frame members, some weaknesses of the approach restrain their broad application. High cost, disruptions during construction, heavy members, increase of the primary system's stiffness, residual deformations and minor hysteretic loops are sometimes in this context disadvantageous.

The recent international literature contains three examples of utilizing tendons in frames with the objective to overcome some of the mentioned disadvantages. In the first system the energy dissipation potential of frame structures is effected by the integrated Pall-Marsh modified friction mechanism [6]. The control system consists of an articulated quadrilateral with steel dissipaters, connected through tendons to the frame joints. The second control system consists of eccentrically connected elastic cables and a central energy dissipater working with cyclic bending of steel plates [2] and the third control system, of a friction damping mechanism [3]. All control systems developed concentrate on the optimal design of the section of the damper used through analytical and experimental studies.

In the present study a frame with an integrated hysteretic damper and a cable-bracing mechanism in three different configurations is parametrically investigated under actual earthquake motions. The dual structural systems developed are based on the concept originally proposed in [4]. Optimal systems parameters for each configuration of the damper-bracing mechanism have been derived under three international strong earthquake motions, as regards the energy dissipation behaviour of the systems and the dampers non-linear response. The systems have been verified in their earthquake response under ten earthquake motions of the Greek Mediterranean region.

2 Conceptual design principles of ADCS

An Adaptable Dual Control Mechanism may be developed when tension-only bracings and a hysteretic damper are integrated within a frame to provide

specific safety for strong earthquake hits. The control members form a kinetically closed circuit and participate in the energy dissipation process in a stable manner for a large number of strong excitation cycles, without any coupling effect with the elastic primary structure; gravity and wind loads are managed by the primary frame, whereas the earthquake loads, by the integrated damper-bracing mechanism.

Figure 1: ADCS S1, S2, S3.

The conceptual design principles are mastered by the dual property that generates the form of the systems, whereas the bracing members form a closed polygon shape, fig. 1. Ideally, the reactions from the added control device on the primary frame are almost neutralized due to the closed circuit of the bracing, i.e. the elongation of a bracing cable in one sense is equal in magnitude to the contraction of the other cable that follows the opposite sense, fig. 2.

The design objective of all ADCS configurations is based on achieving predefined performance levels of damage control, through the property of deformation. When the dual mechanism is subjected to earthquake loads, eccentrically placed discs at the main joint regions rotate and drag along the pretensioned bracing cables that induce relative deformations to the integrated hysteretic damper connected to a respective frames member, fig. 3. As soon as the motion between the dampers connection points takes place, dissipation of the seismic input energy initiates. Energy is concentrated on the fusers instead of on the primary system.

3 Connections design of ADCS

The ability of mild steel to dissipate energy through inelastic deformations is utilized in the proposed control systems in three examples of ADCS configurations [11]. The optimal position of the hysteretic damper is carefully selected so that it controls the seismic response most effectively, fig. 4. In all cases the parallel steel plates are connected with a cable bracing and a frames

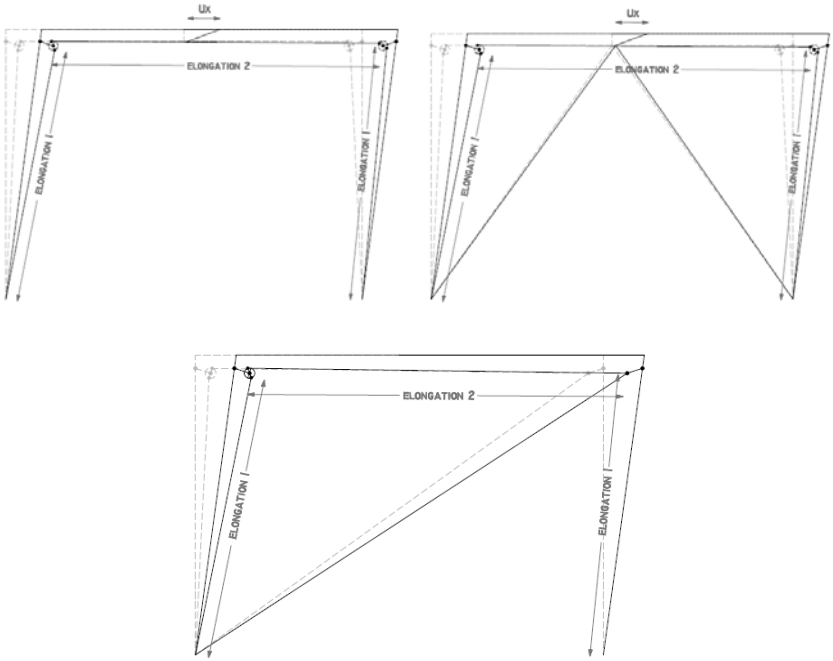

Figure 2: Kinematics of ADCS S1, S2, S3.

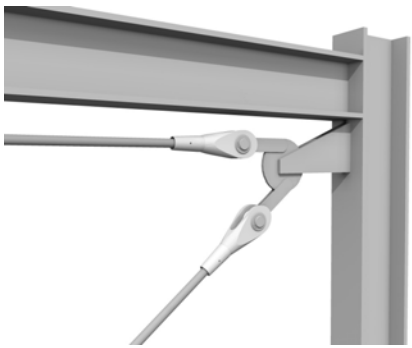

Figure 3: Typical rotating disc at the main joint region of ADCS.

member. The bending curvature that develops by the transverse force applied at the end joints of each triangular plate is uniform over the section's full height. All lines reach their maximum yielding potential at the same time.

Figure 4: Hysteretic dampers connections of ADCS S1, S2 and S3.

4 Preliminary design of ADCS

A typical geometry was assigned for the primary frame for a preliminary study of ADCS's response behavior. The primary frame was dimensioned to resist a vertical load of G= 1200 kN, a horizontal wind load of W= 15 kN and a minimum of 25% of the static equivalent seismic loads. According to Eurocode 3 an IPBL500 section was assigned for the 4.50 m high columns and an IPBL550 section for the 6.00 m long beam (S235, E= 2.1×10^4 kN/cm^2, ρ= 78.5 kN/m^3). Furthermore 0% damping was assumed for the dynamic loading.

4.1 Hysteretic behaviour of bracing-damper mechanism

The optimization method implies the selection of the maximum deformation and yield strength for the selected damper plates under the indicated hysteretic behavior modeled by the Bouc-Wen plasticity model of hysteresis. Three characteristic parameters were found to control the response: the device initial elastic stiffness, $k_{d,}$, the device yield force, P_y, and the tendon bracings' elastic stiffness. The former are given through the following equations:

$$k_d = \frac{nEbt^3}{4h^3}, \tag{1}$$

$$P_y = \frac{nf_y bt^2}{6h} \tag{2}$$

The geometry of the dissipaters, as triangular shaped plates, is characterized by the height, h, the width, b, the thickness, t, and the number of plates, n. f_y is the yield stress (for the material chosen, S235, f_y= 24 kN/cm^2, ρ = 78.5 kN/m^3) and E is the modulus of Elasticity (E= 2.1×10^4 kN/cm^2). The tendons' elastic stiffness was selected based on the study results as described in previous investigations by the authors [4, 5, 7–9].

4.2 Design variables for ADCS

A parametric analysis has been conducted by varying the members' stiffness and yield strength. In the present study all tendons have diameter of dc= 20 mm and

modulus of elasticity of E= $1.6x10^4$ kN/cm^2. The bracing configurations of the systems enable that the damper plates yield before any other member of the system. The sensitivity study verified that the ADCS's behavior is mainly governed by the hysteresis of the incorporated damper, i.e. the eligible stiffness and ductility levels, that is responsible for the respective energy dissipation and the relative motion between the damper's end joints defined as interdamper drift. The derived diagrams may be used to define the targeted energy dissipation, through the selection of a single Energy Toughness Indicator value, i.e. dissipated- to input energy, which is presented as a variation of a DR parameter, defined as the damper's elastic stiffness, kd, to its yield force, Py. The proposed ADCS were subjected to real records of international strong earthquakes that are characterised by peak ground acceleration values of 0.810g, 0.604g and 0.348g. The preliminary investigation has been conducted for the three selected configurations of the ADCS systems and for an arbitrary sample of possible combinations of design parameter values. The optimal design parameters DR of the systems have been derived based on the sensitivity study results for 342 combinations for S1 and S3 and 397 for S2. Subsequently ADCS have been evaluated in their dynamic behaviour under ten selected earthquake excitations of the Greek-Mediterranean region.

4.3 Energy toughness indicator

Based on the parametric investigation results as shown in fig. 5 for the three systems, the critical parameter is the non-linear link parameter DR, defined as the damper's stiffness to its yield strength. This parameter influences to a high degree the area of the dissipated energy through the yielding deformations of the hysteretic damper, as a portion of the input energy, for the earthquake cases with maximum ground acceleration PGA of 0.348g, 0.604g and 0.810g. As indicated in the individual diagrams, the favourable design parameter for all combinations lies between the areas of $100 < DR < 200$.

5 Earthquake response of ADCS

A selection of favourable ADCS responses with the selected DR parameter under the earthquake excitations of the Greek-Mediterranean region is shown in fig. 6. In the analysis the steel dampers dissipated a major part of the earthquake input energy, in dependence to the characteristics of the ground motions. The form of the hysteretic loops developed depends primarily on the grade of the plastic hysteretic damping. The hysteretic damper in the system S1 develops exclusively hysteresis curves, similar to the Ramberg-Osgood model. The systems S2 and S3 develop in most cases hysteresis curves of the rigid-plastic type model.

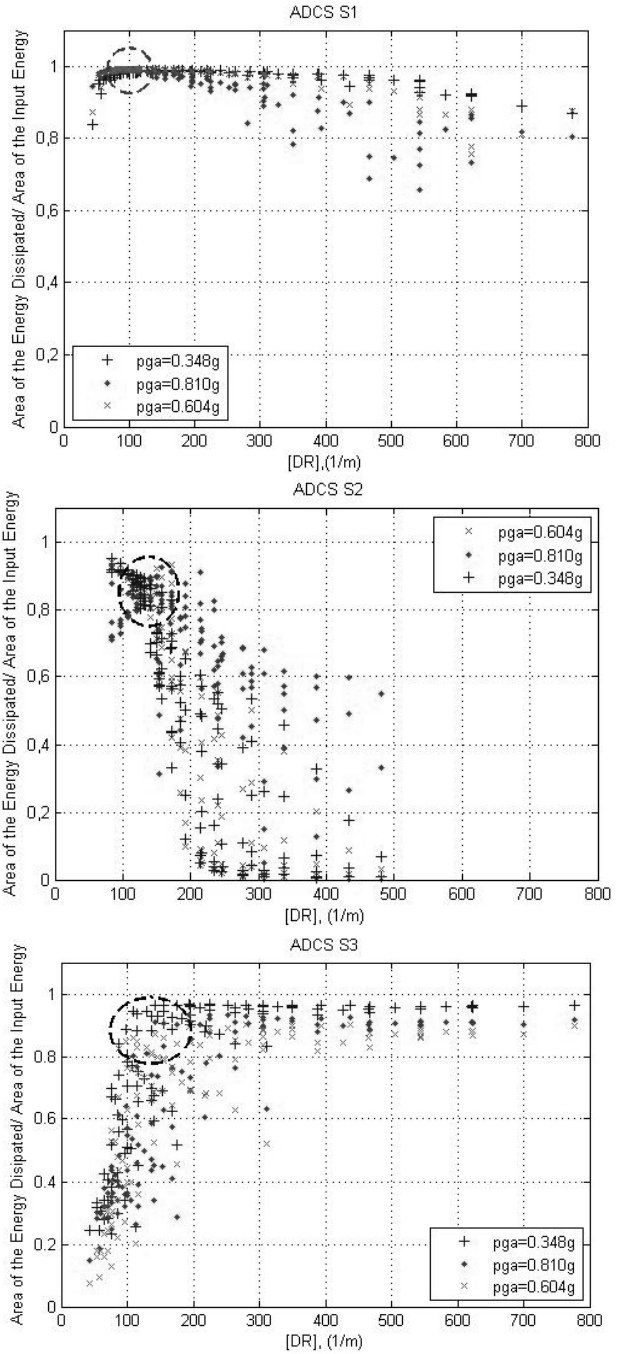

Figure 5: DR Parameters of ADCS S1, S2 and S3.

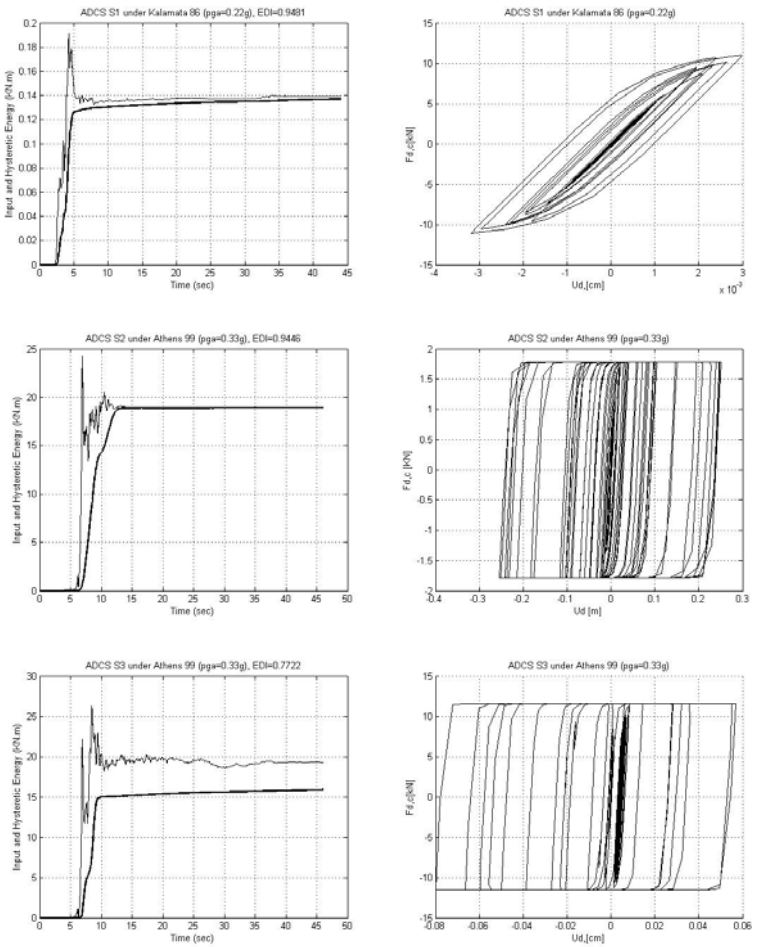

Figure 6: Favourable energy dissipation- and hysteretic behaviour of ADCS S1, S2 and S3.

5.1 Base shear

The comparison of the base shear's maximum values of S1, S2 and S3 with the bare frame's values proves that the secondary damper-bracing mechanism does not practically induce any coupling effects to the systems. The favourable case presented in Table 1, is characterized by the following geometry of the plate fusers: h= 15 cm, b= 5 cm, t= 12 mm and n= 6. In 83.33% of the cases the base shear decreased, when the tendons and the hysteretic steel plates were added to the frame system.

Table 1: Base shear of bare frame and ADCS S1, S2, S3.

Earthquake Records	Base Shear (kN)			
Max. Ground Acceleration	Bare Frame (T= 0.36 s)	ADCS S1 (T= 0.32 s)	ADCS S2 (T= 0.26 s)	ADCS S3 (T= 0.67 s)
Aigio 95 (Aigio, 0^0), 0.50g	-1563.00 1577.00	-63.76 40.49	-3048.43 3057.49	-1184.98 1225.26
Athens 99 (Sepolia, 0^0), 0.33g	-2048.00 1978.00	-34.22 29.04	-1176.91 1101.54	-1761.55 1611.12
Ionian 83 (Argostoli, 90^0), 0.24g	-500.30 480.40	-25.54 17.98	-324.24 379.65	-546.00 545.53
Kalamata 86 (Kalamata, 0^0), 0.22g	-1278.00 1270.00	-28.04 30.24	-1874.30 1883.07	-256.62 300.45
Heraklio 84 (Heraklio, 90^0), 0.21g	-1738.00 1735.00	-15.70 23.42	-1517.44 1516.73	-882.94 861.29
Aigio 90 (Aigio, 90^0), 0.20g	-1361.00 1361.00	-21.55 20.32	-665.95 593.36	-1191.58 1220.42
Etolia 88 (Valsamata, 90^0), 0.18g	-882.90 848.40	-15.83 20.79	-1358.78 1308.86	-1153.24 1182.53
Killini 88 (Zakinthos, 90^0), 0.15g	-2515.00 2516.00	-16.99 20.79	-525.65 561.32	-1193.32 1212.84
Preveza 81 (Preveza, 0^0), 0.14g	-2445.00 2381.00	-16.36 15.26	-1119.47 1168.68	-1551.07 1570.20
Gulf of Corinth 93 (Nafpaltos, 90^0), 0.10g	-372.80 519.10	-12.93 20.32	-316.91 248.97	-356.06 517.56

5.2 Relative horizontal displacement

For the same geometry assigned to the damper, the relative displacement of S1, S2 and S3 is compared to the bare frame's values. In 93.33% of the cases examined the response values are kept within the frame's limits. This is also valid for the case presented in Table 2.

5.3 Interdamper drift

Responsible for the energy dissipation of the systems is the inelastic action induced between the damper's end point joints, defined as interdamper drift. The one end of the damper follows the axial displacement of the connected tendon and the other end the frame's member translation. The damper utilizes the relative motion to yield and dissipate energy. Fig. 7 shows the relative

Table 2: Relative displacement.

Earthquake Records	Relative Displacement (cm)			
Max. Ground Acceleration	Bare Frame (T= 0.36 s)	ADCS S1 (T= 0.32 s)	ADCS S2 (T= 0.26 s)	ADCS S3 (T= 0.67 s)
Aigio 95 (Aigio, 0^0), 0.50g	1.918 -1.899	0.010 -0.011	1.918 -1.912	1.560 -1.620
Athens 99 (Sepolia, 0^0), 0.33g	2.494 -2.417	0.011 -0.009	2.498 -2.409	2.330 -2.150
Ionian 83 (Argostoli, 90^0), 0.24g	0.633 -0.587	0.003 -0.003	0.614 -0.594	0.750 -0.710
Kalamata 86 (Kalamata, 0^0), 0.22g	1.542 -1.533	0.013 -0.012	1.533 -1.505	0.340 -0.400
Heraklio 84 (Heraklio, 90^0), 0.21g	2.119 -2.113	0.006 -0.006	1.702 -1.716	1.160 -1.130
Aigio 90 (Aigio, 90^0), 0.20g	1.661 -1.660	0.006 -0.005	1.530 -1.599	1.570 -1.600
Etolia 88 (Valsamata, 90^0), 0.18g	1.067 -1.038	0.009 -0.008	1.044 -0.991	1.520 -1.560
Killini 88 (Zakinthos, 90^0), 0.15g	3.066 -3.065	0.005 -0.005	2.418 -2.459	1.570 -1.60
Preveza 81 (Preveza, 0^0), 0.14g	2.977 -2.897	0.008 -0.007	2.730 -2.647	2.080 -2.100
Gulf of Corinth 93 (Nafpaltos, 90^0), 0.10g	0.463 -0.629	0.004 -0.004	0.460 -0.624	0.470 -0.680

displacements response of S1, S2 and S3 respectively. It can be observed that the relative deformations of the damper are proportional to the energy dissipation of the control mechanism. Therefore the maximization of the interdamper drift is a design objective for ADCS.

6 Conclusions

In the present paper the concept of Adaptable Dual Control Systems is analytically investigated in three different configurations. The proposed systems consist of a hysteretic damper and a cable bracing mechanism of closed circuit that are integrated within the frame structure to dissipate satisfactory portions of the seismic input energy, leaving the primary frame to respond elastically. The unique configuration of the tendons avoids the undesirable effect from a possible increase in the base shear and it keeps the relative displacements of the systems under controllable limits. The systems have been investigated in their response, based on a parametric study using three international strong earthquake motions. The analyses conducted revealed the design parameters of the control mechanisms and the range of ADCS's possible applications. The ADCS's reliability was verified as regards their earthquake performance under ten real earthquake records of the Greek Mediterranean region.

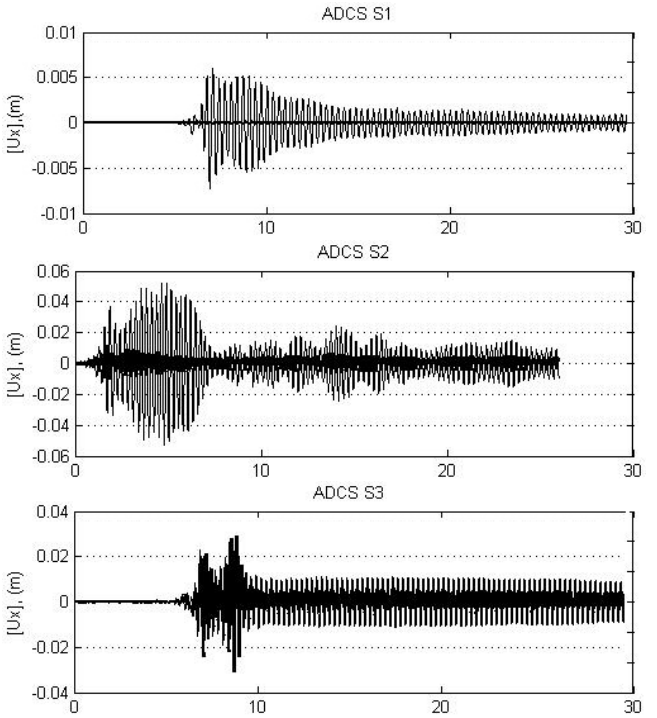

Figure 7: Interdamper drift in ADCS S1, S2 and S3.

References

[1] Housner, G.W., Bergman, L.A., Caughey, T.K., Chassiakos, A.G., Claus, R.O., Masri, S.F., Skelton, R.E., Soong, T.T., Spencer, Jr. B.F. & Yao, T.P., Structural Controls: Past, Present and Future. *Engineering Mechanics*, **123(9)**, pp. 897-971, 1997.

[2] Kurata, M., DesRoches, R. & Leon, R.T., Cable Damper Bracing for Partial Seismic Rehabilitation. *14th World Conference on Earthquake Engineering*, 14WCEE, 12.10-17.10.08: Beijing, China, October 2008.

[3] Mualla, I.H., Nielsen, L.O., Belev, B., Liao, W.I., Loh, C.H. & Agrawal, A., Performance of Friction-Damped Frame Structure: Shaking Table Testing and Numerical Simulations. *7th US National Conference on Earthquake Engineering*: Boston, USA, 2002.

[4] Phocas, M.C. & Pocanschi, A., Steel Frames with Bracing Mechanism and Hysteretic Dampers. *Earthquake Engineering and Structural Dynamics*, **32**, pp. 811–825, 2003.

[5] Phocas, M.C. & Sophocleous, T., Kinetic Structures in Architecture.*14th World Conference on Earthquake Engineering*, 14WCEE, 12.10-17.10.08: Beijing, China, October 2008.

[6] Renzi, E., Perno, S., Pantanella, S. & Ciampi, V., Design, Test and Analysis of a Light-Weight Dissipative Bracing System for Seismic Protection of Structures. *Earthquake Engineering and Structural Dynamics*, **36,** pp. 519–539, 2007.
[7] Sophocleous, T. & Phocas, M.C., Dual Earthquake Resistant Frames. (eds.), *Earthquake Resistant Engineering Structures VII*, eds. Phocas, M., Brebbia, C.A., Komodromos, P., WIT Press: Southampton, pp. 165-174, 2009.
[8] Sophocleous, T. & Phocas, M.C., Dual Structures Towards Kinetic Adaptability for Earthquake Resistance. *First International Conference on Structures & Architecture*, ICSA2010, 21.07 – 23.07.10: Guimaraes, Portugal, July 2010.
[9] Sophocleous, T. & Phocas, M.C., Model of Analysis for Earthquake Resistant Dual Systems. *2nd International Conference on Computational Methods in Structural Dynamics and Earthquake Engineering*, COMPDYN 2009, 22.06-24.06.09: Rhodes, Greece, June 2009.
[10] Symans. M.D., Charney, F., Constantinou, M.C., Kircher, C., Johnson, M.W. & McNamara, R.J. Energy Dissipation Systems for Seismic Applications: Current Practice and Recent Developments. *Structural Engineering*, **134(1)**, pp. 3-21, 2008.
[11] Tsai, K.C., Chen, H.W., Hong, C.P. & Su, Y.F., Design of Steel Triangular Plate Energy Absorbers for Seismic-Resistance Construction. *Earthquake spectra*, **9**, pp. 505-528, 1993.

Energy-based evaluation of seismic response of structures with passive and active systems

A. Yanik, U. Aldemir & M. Bakioglu
Department of Civil Engineering, Istanbul Technical University, Turkey

Abstract

In recent years, increased performance requirements and the strong desire for better utilization of new materials and lower costs have motivated the development of new concepts for protecting structures. Recent practical applications and research findings show that the passive and active control techniques have the potential of protecting civil engineering structures from severe earthquakes and strong winds. In this paper, application potentials of passive and active control systems to earthquake excited structures are investigated in terms of energy distribution in the structure. Dynamic behavior of a three storey shear frame structure, incorporating passive and active control systems, subjected to El Centro, Erzincan and the simulated ground motions is investigated. The well-known Kanai-Tajimi power spectral density function is used to generate the simulated ground motion. Instantaneous optimal control algorithm which minimizes a performance index defined as a time dependent quadratic scalar functional instead of a quadratic integral functional and takes into account only the current state is used as an active control algorithm. A computer program which takes into account the nonlinear material property is developed for the dynamic analysis of the controlled and the uncontrolled structure. Nonlinear differential equation of the motion is solved by Wilson-θ numerical method. The numerical simulation results are presented in a comparative way for uncontrolled, passively controlled, actively controlled structures by graphical representations with hysteretic curves and the distributions of the damping energy, total kinetic energy, strain energy and seismic energy. An energy based evaluation of the example structure incorporating different combinations of passive and active systems is made.
Keywords: energy, structural control, earthquake, active control, passive control.


WIT Transactions on The Built Environment, Vol 120, © 2011 WIT Press
www.witpress.com, ISSN 1743-3509 (on-line)
doi:10.2495/ERES110061

1 Introduction

The theoretical background of incorporating smart devices into structures was first given by Yao [1] in 1972. He stated in his paper that the control theories could be used in structural control problems. Structural control can be categorized as passive, active and hybrid control. In actively controlled system, structural responses are regulated by control forces based on a feedback system. Control forces are generated by external energy supply available in the system. External energy supply is not required in passive systems. Passive control devices transform the input seismic energy into different forms. Hybrid control systems incorporate both the active and passive devices. The history and the development of these systems are largely summarized in the work by Housner *et al.* [2]. Design of these systems with taking into account the energy and also energy based earthquake resistant design is still a growing research area. In this type of design the most important parameter is the amount of seismic energy input. As the amount of seismic energy input to structure is decreased or diminished by control devices, earthquake resistance of the structure increases. Some studies taking into account the energy of the structure in structural control problems are given in [3–8]. Actively controlled seismic excited structures was investigated with using optimal control theory in [9]. A study about a new control algorithm which is based on prediction of the near future earthquake excitations is given in [10]. A predictive semi active control method to suppress the earthquake response using a nonlinear semiactive damper was researched in [11]. A simple active control algorithm was proposed in [12].

The influence of the different control cases on the distribution of energy in a structure is studied in this paper. The material model is taken as bilinear elastoplastic. Three different cases of structural control are analysed and compared with each other and with uncontrolled structure. These cases are structure with base isolation, structure with base isolation and passive mass damper at the base of the building and structure with base isolation and active mass damper at the top of the building.

2 Formulation of the problem

The investigated shear building model is given for structure with base isolation, base isolation and passive mass damper at the base of the building and a base isolation and active mass damper at the top of the building respectively in fig. 1(a), (b), (c). The first two structures are the passively controlled structures while the last system can be classified as a hybrid control system.

For an inelastic shear-building with n degrees of freedom under the one dimensional ground motion and control forces, the equation of the motion of the structure can be written in matrix form as

$$\mathbf{M}\ddot{\mathbf{Y}}(t)+\mathbf{F}^{d}(t)+\mathbf{F}^{k}(t)=-\mathbf{M}\mathbf{V}\,f(t)+\mathbf{L}\mathbf{U}(t) \tag{1}$$

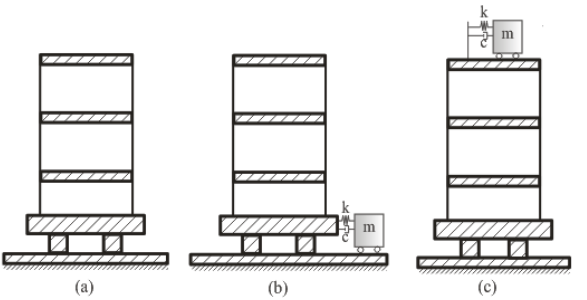

Figure 1: Structure with different control schemes.

where $\mathbf{Y}(t)=(y_1,y_2,.....,y_n)^{\mathrm{T}}$ is the n-dimensional response vector denoting the relative displacement of the each storey unit with respect to the ground; **M** is the $(n\times n)$-dimensional constant mass matrix with diagonal elements (m_i= mass of ith storey, i=1,2,…,n); $\mathbf{F}^d(t)$ and $\mathbf{F}^k(t)$ are n-dimensional damping and stiffness force vectors respectively, $\mathbf{V}=(1,.....,1)^{\mathrm{T}}$ is the n-dimensional vector; **L** is the $(n\times r)$-dimensional location matrix of r controllers; $\mathbf{U}(t)$ is the r-dimensional active control force vector and scalar function f (t) is the one-dimensional earthquake acceleration. For the uncontrolled and passively controlled case the second term in the right hand side of the equation becomes zero.

With introducing a 2n-dimensional state vector, $\mathbf{Z}(t)$, as follows:

$$\mathbf{Z}(t)=\begin{bmatrix}\mathbf{Y}(t)\\ \dot{\mathbf{Y}}(t)\end{bmatrix} \tag{2}$$

the second-order matrix equation of motion can also be rewritten as a first order matrix equation with dimension 2n in the following form:

$$\dot{\mathbf{Z}}(t)=\mathbf{A}\mathbf{Z}(t)+\mathbf{B}\mathbf{U}(t)+\mathbf{H}f(t) \qquad \mathbf{Z}(0)=\mathbf{Z}_0 \tag{3}$$

where

$$\mathbf{A}=\begin{bmatrix}\mathbf{0} & \mathbf{I}\\ -\mathbf{M}^{-1}\mathbf{K} & -\mathbf{M}^{-1}\mathbf{C}\end{bmatrix} \qquad \mathbf{B}=\begin{bmatrix}\mathbf{0}\\ \mathbf{M}^{-1}\mathbf{L}\end{bmatrix} \qquad \mathbf{H}=\begin{bmatrix}\mathbf{0}\\ -\mathbf{V}\end{bmatrix} \tag{4}$$

To obtain the control force $\mathbf{U}(t)$ in eqn. (3), a control algorithm must be chosen. After determining the control force, eqn. (3) can be solved. In this study, instantaneous optimal control algorithm which minimizes a performance index defined as a time dependent quadratic scalar functional instead of a quadratic integral functional and takes into account only the current state is used.

2.1 Instantaneous optimal control algorithm

This algorithm is developed for getting over the difficulties because of not knowing the earthquake time history in the beginning (Yang *et al.* [13], Akhiev

et al. [14]). Time dependent performance measure which will be minimized can be expressed as

$$J = \mathbf{Z}^{\mathrm{T}}(t)\mathbf{Q}\,\mathbf{Z}(t) + \mathbf{U}^{\mathrm{T}}(t)\mathbf{R}\mathbf{U}(t) \quad \rightarrow \ \min \tag{5}$$

In eqn.(5) **Q** is a (*2n*×*2n*)-dimensional positive semidefinite symmetric weighting matrix and **R** is a (*r*×*r*)-dimensional positive-definite symmetric weighting matrix. The values of **Q** and **R** matrices are assigned according to relative importance of the state variables and the control forces in the minimization procedure. If the elements of the matrix **Q** are chosen larger than the elements of **R**, minimizing the response of the structure is more important than the control forces otherwise the minimization of the control forces are more important.

The basic equation of the problem is given in eqn. (3). Let the eigenvalues of **A** in eqn.(3) are distinct and **T** is the (*2n*×*2n*)-dimensional modal matrix which is constituted by the eigenvectors of **A**. In this situation **Z** vector can be expressed as

$$\mathbf{Z} = \mathbf{T}\mathbf{X}(t) \tag{6}$$

In eqn. (6), **X**(*t*) is the modal state vector. If we insert eqn. (6) into eqn. (3)

$$\dot{\mathbf{Z}}(t) = \mathbf{T}\dot{\mathbf{X}}(t) = \mathbf{A}\mathbf{T}\mathbf{X}(t) + \mathbf{B}\mathbf{U} + \mathbf{H}f(t) \tag{7}$$

$$\dot{\mathbf{X}}(t) = \mathbf{T}^{-1}\mathbf{A}\mathbf{T}\mathbf{X}(t) + \mathbf{T}^{-1}\mathbf{B}\mathbf{U} + \mathbf{T}^{-1}\mathbf{H}f(t) \tag{8}$$

$\mathbf{T}^{-1}\mathbf{A}\mathbf{T}$ term in eqn. (8) is the $\mathbf{\Lambda}$ spectral matrix of **A** matrix. The matrix $\mathbf{\Lambda}$ is a diagonal matrix of which diagonal element are eigenvalues of **A**. By using $\mathbf{\Lambda}$ spectral matrix eqn. (8) can be expressed as

$$\dot{\mathbf{X}}(t) = \mathbf{\Lambda}\mathbf{X}(t) + \mathbf{q}(t) \qquad \mathbf{X}(0) = 0 \tag{9}$$

$$\mathbf{\Lambda} = \mathbf{T}^{-1}\mathbf{A}\mathbf{T} \qquad \mathbf{q}(t) = \mathbf{T}^{-1}\mathbf{B}\mathbf{U} + \mathbf{T}^{-1}\mathbf{H}f(t) \tag{10}$$

The solution of the differential equation in eqn. (9) can be written as

$$\mathbf{X}(t) = \mathbf{e}^{\Lambda t}\mathbf{X}(0) + \int_0^t \mathbf{e}^{\Lambda(t-\tau)}\mathbf{q}(\tau)d\tau = 0 + \int_0^t \mathbf{e}^{\Lambda(t-\tau)}\mathbf{q}(\tau)d\tau \tag{11}$$

$$\mathbf{X}(t) = \int_0^t \mathbf{e}^{\Lambda(t-\tau)}\mathbf{q}(\tau)d\tau + \int_{t-\Delta t}^t \mathbf{e}^{\Lambda(t-\tau)}\mathbf{q}(\tau)d\tau \tag{12}$$

By using numerical integration(trapezoidal rule) for eqn. (12) the equation given below can be obtained

$$\mathbf{X}(t) \approx \mathbf{e}^{\Lambda t}\mathbf{X}(t-\Delta t) + \frac{\Delta t}{2}[\mathbf{e}^{\Lambda\Delta t}\mathbf{q}(t-\Delta t) + \mathbf{q}(t)] \tag{13}$$

In eqn. (10) $\mathbf{e}^{\Lambda t}$ is a diagonal matrix and its diagonal elements are $\lambda_i\Delta t$ (λ'are the eigenvalues of **A** matrix and subscript *i* is from 1 to 2n). By using eqn. (6) and **q**(t) from eqn. (10) **Z** can be expressed as

$$\mathbf{Z}(t) = \mathbf{TD}(t-\Delta t) + \frac{\Delta t}{2}[\mathbf{BU}(t) + \mathbf{H}f(t)] \tag{14}$$

$$\mathbf{D}(t-\Delta t) = \exp(\mathbf{\Lambda}\Delta t)\mathbf{T}^{-1}\left\{\mathbf{Z}(t-\Delta t) + \frac{\Delta t}{2}[\mathbf{BU}(t-\Delta t) + \mathbf{H}f(t-\Delta t)]\right\} \tag{15}$$

Hamiltonian of the problem and the corresponding optimality conditions can be written as

$$\begin{aligned} H &= \mathbf{Z}^{\mathrm{T}}(t)\mathbf{Q}\,\mathbf{Z}(t) + \mathbf{U}^{\mathrm{T}}(t)\mathbf{R}\mathbf{U}(t) \\ &+ \boldsymbol{\lambda}^{\mathrm{T}}(t)\left\{\mathbf{Z}(t) - \mathbf{TD}(t-\Delta t) - \frac{\Delta t}{2}[\mathbf{BU}(t) + \mathbf{H}f(t)]\right\} \end{aligned} \tag{16}$$

$$\frac{\partial H}{\partial \mathbf{Z}^*} = 0 \;\; \frac{\partial H}{\partial \mathbf{U}^*} = 0 \;\; \frac{\partial H}{\partial \boldsymbol{\lambda}^*} = 0 \tag{17}$$

By using these optimality conditions, the following equations are obtained,

$$2\mathbf{Q}\mathbf{Z}^* + \boldsymbol{\lambda}^*(t) = 0 \tag{18}$$

$$2\mathbf{R}\mathbf{U}^* - \frac{\Delta t}{2}\mathbf{B}^{\mathrm{T}}\boldsymbol{\lambda}^*(t) = 0 \tag{19}$$

$$\mathbf{Z}^* = \mathbf{TD}^*(t-\Delta t) + \frac{\Delta t}{2}[\mathbf{BU}^*(t-\Delta t) + \mathbf{H}f(t-\Delta t)] \tag{20}$$

For closed loop control, assuming that

$$\boldsymbol{\lambda}^*(t) = \mathbf{P}\mathbf{Z}(t) \tag{21}$$

and substituting the eqn (21) into eqn (18), **P= -2Q** is obtained. Then from eqs (19) and (20), the following equations are derived;

$$\mathbf{U}^* = -\frac{\Delta t}{2}\mathbf{R}^{-1}\mathbf{B}^{\mathrm{T}}\mathbf{Q}\mathbf{Z}^*(t) \tag{22}$$

$$\mathbf{Z}^* = [\mathbf{I} + \frac{(\Delta t)^2}{4}\mathbf{B}\mathbf{R}^{-1}\mathbf{B}^{\mathrm{T}}\mathbf{Q}]^{-1}[\mathbf{TD}(t\text{-}\Delta t) + \frac{\Delta t}{2}\mathbf{H}f(t)] \tag{23}$$

3 Energy equations

If eqn. (1) is multiplied with the transpose of velocity vector $\dot{\mathbf{Y}}^{\mathrm{T}}(t)$ and integrated in the interval of (0-*t*), the energy equations will be obtained and expressed as

$$\int_0^t \dot{\mathbf{Y}}^{\mathrm{T}}(\tau)\mathbf{M}\,\ddot{\mathbf{Y}}(\tau)d\tau + \int_0^t \dot{\mathbf{Y}}^{\mathrm{T}}(\tau)\mathbf{F}^d(\tau)d\tau + \int_0^t \dot{\mathbf{Y}}^{\mathrm{T}}(\tau)\mathbf{F}^k(\tau)d\tau = -\int_0^t \dot{\mathbf{Y}}^{\mathrm{T}}(\tau)\mathbf{M}\mathbf{V}\,\ddot{x}_0 d\tau + \int_0^t \dot{\mathbf{Y}}^{\mathrm{T}}(\tau)\mathbf{L}\mathbf{U}d\tau \quad (24)$$

The first term in eqn. (24) is called kinetic energy (E_{kin}) and can be written as

$$E_{kin} = \int_0^t \dot{\mathbf{Y}}^{\mathrm{T}}(\tau)\mathbf{M}\,\ddot{\mathbf{Y}}(\tau)d\tau = \int_0^t [\dot{\mathbf{Y}}^{\mathrm{T}}(\tau)\mathbf{M}\,\dot{\mathbf{Y}}(\tau)\dot{]}d\tau = \frac{1}{2}\dot{\mathbf{Y}}^{\mathrm{T}}(t)\mathbf{M}\dot{\mathbf{Y}}(t) \quad (25)$$

E_{kin} is sum of the kinetic energy of all masses with respect to the ground. In eqn. (24) the second term is equal to the damping energy of the system, damping energy E_{damp} can be expressed as

$$E_{damp} = \int_0^t \dot{\mathbf{Y}}^{\mathrm{T}}(\tau)\mathbf{F}^k(\tau)d\tau \quad (26)$$

The third term in eqn. (25) is the strain energy E_{str} and can be written as

$$E_{str} = \int_0^t \dot{\mathbf{Y}}^{\mathrm{T}}(\tau)\mathbf{F}^k(\tau)d\tau \quad (27)$$

If the system is linear elastic $\mathbf{F}^k = \mathbf{K}\mathbf{Y}$ in which $\mathbf{K}$ is the stiffness matrix, the second term in eqn. (25) for linear elastic case, can be expressed as

$$E_{str}^{elas} = \int_0^t \dot{\mathbf{Y}}^{\mathrm{T}}(\tau)\mathbf{K}\mathbf{Y}(\tau)d\tau = \frac{1}{2}\mathbf{Y}^{\mathrm{T}}(t)\mathbf{K}\mathbf{Y}(t) \quad (28)$$

Eqn. (28) is valid if the system is totally elastic. If the strains of the system exceed the elastic limit, strain energy can be divided to two types, one of which is returned elastic energy and the other is unreturned hysteretic energy. For this case total strain energy can be expressed as total of two types of energy

$$E_{str} = E_{str}^{elas} + E_{str}^{his} \quad (29)$$

The first term in the right hand side of eqn. (24) is the earthquake energy of the structure E_{earth} and the last term is the control energy E_{con}, these energies can be expressed as

$$E_{earth} = -\int_0^t \dot{\mathbf{Y}}^{\mathrm{T}}(\tau)\mathbf{M}\mathbf{V}\,\ddot{x}_0 d\tau \qquad E_{con} = \int_0^t \dot{\mathbf{Y}}^{\mathrm{T}}(\tau)\mathbf{L}\mathbf{U}d\tau \quad (30)$$

If we add eqn (31) to the left side of the eqn.(24) it will have a negative sign in front of it. Although it has a negative sign it is positive because control forces generally depends negatively on displacement and velocity response so this makes control energy positive. After defining this, energy equilibrium can be expressed as

$$E_{kin} + E_{damp} + E_{str}^{elas} + E_{str}^{his} + E_{con} = E_{earth} \quad (31)$$

4 Numerical example

As an example problem a three-storey shear building with damping is considered under three different earthquake motions which are El-Centro, Erzincan and simulated ground motion. For simulated ground motion Kanai-Tajimi power spectral density function is used. More information about this function can be found Shinozuka and Deodatis [15]. All these three earthquakes can be classified as strong motions, simulated ground motion has maximum acceleration of 0.33 g. Acceleration time histories of El Centro, Erzincan and synthetic earthquakes are given in fig. (2). The columns of the building are assumed as massless and the mass of the structure is concentrated in floor level as lumped mass model. Each storey has the same mass, stiffness and damping parameters. As control elements base isolation and mass damper are chosen. Mass, stiffness and damping parameters of the base isolation are m_b=100 tons, k_b=2527×10^3 kN/m and c_b=63 kNs/m respectively. For passive and active mass damper the parameters are m_d=36.3 tons, k_d=1173 kN/m, c_d=31 kNs/m. Mass, stiffness and damping matrix of the structure for uncontrolled case are as follows:

$$\mathbf{M}=\begin{bmatrix}100 & 0 & 0\\ 0 & 100 & 0\\ 0 & 0 & 100\end{bmatrix}\text{ ton},\ \mathbf{C}=\begin{bmatrix}251.32 & -125.66 & 0\\ -125.66 & 251.32 & -125.66\\ 0 & -125.66 & 125.66\end{bmatrix}\text{kNs/m}$$
$$\mathbf{K}=\begin{bmatrix}31582.734 & -15791.34 & 0\\ -15791.34 & 31582.734 & -15791.34\\ 0 & -15791.34 & 15791.34\end{bmatrix}\text{kN/m} \tag{32}$$

Energy distributions and force-displacement responses of the structure are investigated for four cases which are uncontrolled case (1), structure with base isolation (2), structure with base isolation and passive mass damper(3), and structure with base isolation and active mass damper (4) . For active control case weighting matrix **R** (1×1) is chosen as 10^{-3}, a scalar number because only a single active mass damper is in the system. The other weighting matrix **Q** is chosen as (10 × 10) dimensional diagonal matrix of which diagonal elements are equal to 1000.

Peak values of the relative displacements for the storeys and supplemental elements are given in Table 1. It can be seen from the table that for all cases the largest reduction in the storey displacements have been obtained for the hybrid system which consists of an active mass damper and base isolation. Active mass damper has also reduced the displacement of the base isolation. Adding passive mass damper to the structure with base isolation has also reduced the storey displacements for the cases of El Centro and Synthetic earthquakes. But, for Erzincan earthquake the displacements are approximately the same. This can be because of the stronger effect of Erzincan earthquake than the other ones. Moreover implementing base isolation to the uncontrolled structure has reduced the displacements.

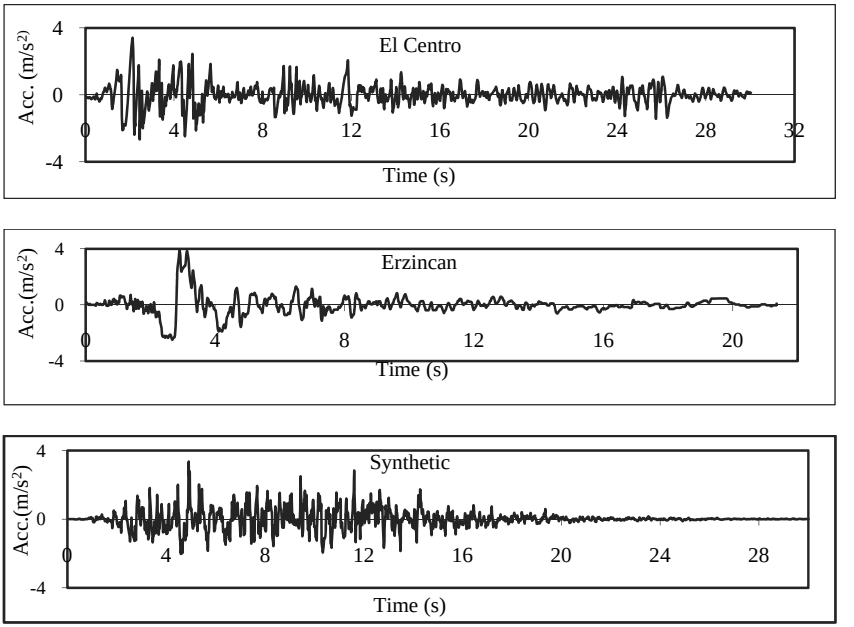

Figure 2: Earthquake time history.

Table 1: Maximum storey displacements (m).

Earthquake	Storey No.	Control Cases			
		1	2	3	4
El Centro	Mass Damper	-	-	0.0649	0.0516
	Base Isolation	-	0.2039	0.2144	0.1868
	1	0.0670	0.0846	0.0592	0.0552
	2	0.0371	0.0198	0.0180	0.0177
	3	0.0188	0.0109	0.0097	0.0109
Erzincan	Mass Damper	-	-	0.1401	0.1491
	Base Isolation	-	0.3306	0.3649	0.3410
	1	0.2801	0.2700	0.3018	0.2391
	2	0.1510	0.1713	0.2031	0.1527
	3	0.0229	0.0236	0.0267	0.0226
Synthetic	Mass Damper	-	-	0.0315	0.0637
	Base Isolation	-	0.1641	0.1714	0.1695
	1	0.0387	0.0200	0.0191	0.0245
	2	0.0291	0.0141	0.0131	0.0147
	3	0.0176	0.0077	0.0068	0.0088

The hysteretic curves for the second storey of the structure under El Centro earthquake are given in fig. 3 for all cases. In fig. 3, the numbers (1) to (4) represent the control cases defined above. Implementing base isolation to the system makes the structural behavior elastic for El Centro earthquake.

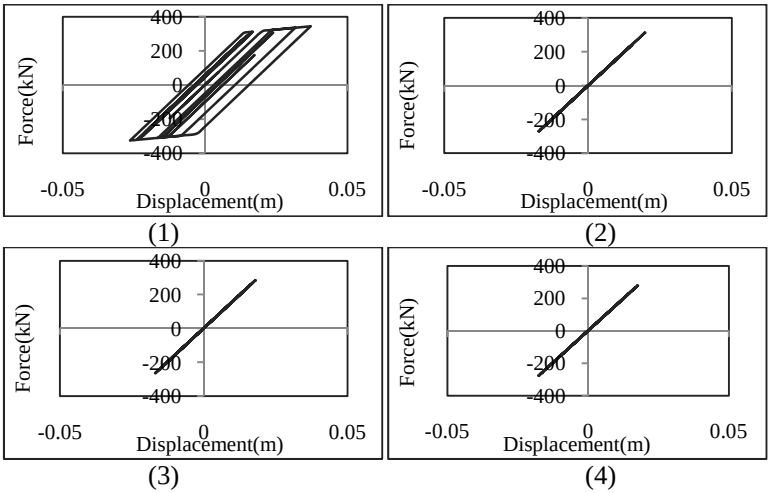

Figure 3: Hysteretic curve for El Centro earthquake.

It is known that the sum of kinetic energy, damping energy, strain energy and control energy is equal to earthquake energy. For passive control cases control energy is zero for all the earthquake duration. In addition; the increase in the control forces result in the increase in the control energy consumption. For this reason appropriate numerical values are assigned to the elements of **Q** and **R** matrices. For the uncontrolled, passive and active control cases, energy distributions are given in fig. 4 for synthetic earthquake. It can be seen from fig.4 that for uncontrolled case the strain energy curve oscillated between the values of

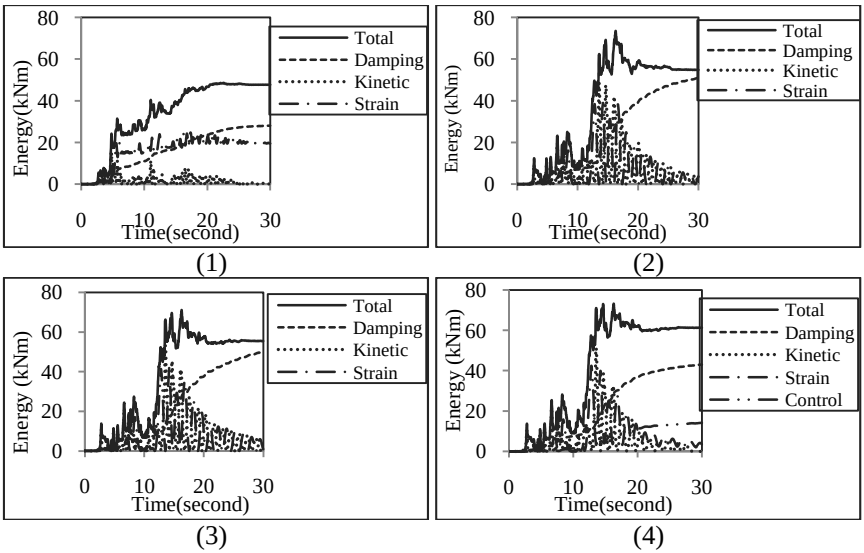

Figure 4: Seismic energy distributions for synthetic earthquake.

14-21 (kNm), this is because of the plastic strains of the structure. Implementing passive or active devices to the structure makes the structural behavior elastic. For active control case maximum damping energy has decreased nearly %14 and the maximum control energy for providing control forces is 13.95 kNm.

The energy distributions of the structure subjected to El Centro earthquake are given in fig. 5. For El Centro earthquake, the largest reduction in the strain energy has been obtained for the hybrid system, while the maximum control energy for this system is 29.11 kNm . In fig. 5 it can be seen that strain energy oscillates between 70kNm and 92 kNm. This is because of the plastical behavior of the structure under El Centro earthquake. The energy distributions for Erzincan earthquake is given in fig.6.

Under Erzincan earthquake for active control case, the maximum control energy is 38.15 kNm. For three different earthquakes, adding base isolation and mass damper to structure has increased the total energy consumption of the structure.

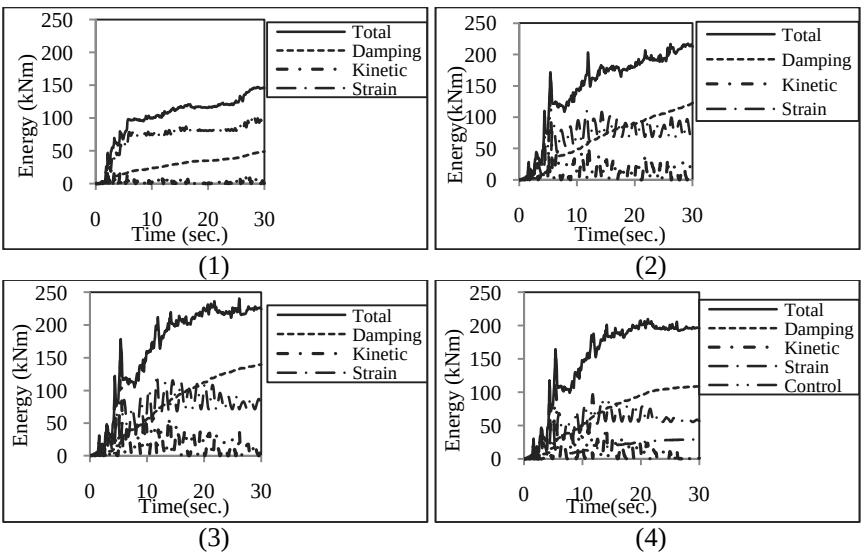

Figure 5: Seismic energy distributions for El Centro earthquake.

5 Conclusion

In this study dynamic behavior and the energy distributions in structures with passive and active control elements are investigated. It has been found that implementing control devices to structures reduces significantly the displacement responses. Applying passive or active control to uncontrolled structure, increases

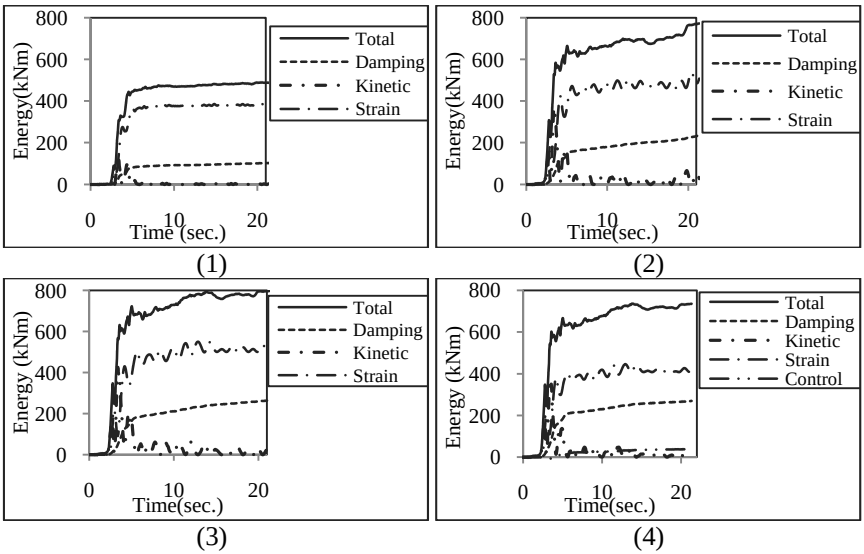

Figure 6: Seismic energy distributions for Erzincan earthquake.

the total energy consumption. Structure with base isolation and passive mass damper and structure with base isolation and active mass damper at the top of the building are the most effective control systems. Implementing two different control elements to a structure may be more feasible than a single active or passive device.

References

[1] Yao, J.T.P., Concept of structural control. *Journal of Structural Division ASCE*, **98**, pp.1567-1574, 1972.

[2] Housner, G.W., Bergman, L.A., Caughey, T.K., Chassiakos, A.G., Claus, R.O., Masri, S.F., Skelton, R.E., Soong, T.T., Spencer, B.F. & Yao, J.T.P., Structural Control: Past, Present, and Future. *Journal of Engineering Mechanics, ASCE*, **123(2)**, pp.897-958, 1997.

[3] Wong, K.K.F. & Wang, Y. Probabilistic structural damage assessment and control based on energy approach. *The Structural Design of Tall Buildings*, **10**,pp. 283-308, 2001.

[4] Wong, K.K.F. & Zhao, D., Effectiveness of inelastic structural control based on elastic displacement and energy. *Structural Control and Health Monitoring*, **12**,pp. 47-64, 2005.

[5] Wong, K.K.F. & Yang, R., Effectiveness of structural control based on control energy perspectives. *Earthquake Engineering and Structural Dynamics*, **30**, pp.1747-1768, 2001.

[6] Wong, K.K.F. & Pang, M., "Energy density spectra in actively controlled inelastic structures-theory". *Structural Control and Health Monitoring*, **14**, pp.261-278, 2007.
[7] Wong, K.K.F. & Pang, M., Energy density spectra in actively controlled inelastic structures-application. *Structural Control and Health Monitoring*, pp.**14**, 279-300, 2007.
[8] Lu, L.Y., Lin, G.L. & Lin,C.,C., Absolute-energy-based active control strategies for linear seismic isolation systems. *Structural Control and Health Monitoring*, **DOI:10.1002/stc.373** 2010.
[9] Aldemir, U., Bakioglu, M. & Akhiev S.S.,Optimal control of linear buildings under seismic excitations. *Earthquake Engineering and Structural Dynamics*, **30**,pp.835-851, 2001.
[10] Aldemir, U. & Bakioglu, M., Active structural control based on prediction and degree of stability. *Journal of Sound and Vibration*, **247(4)** 561-576, 2001.
[11] Aldemir, U., Predictive suboptimal semiactive control of earthquake response. *Structural Control and Health Monitoring*, **17** , 654-674, 2010.
[12] Aldemir, U., A simple active control algorithm for earthquake excited structures. *Computer-Aided Civil and Infrastructure Engineering*, **25,** 218-225, 2010.
[13] Yang, J.N., Akbarpour, A. & Ghaemmaghami, P., New Optimal Control Algoritms for Structural Control. *J.Eng. Mech. ASME*, **113,9** pp. 1369-1386, 1987.
[14] Akhiev, S. S., Aldemir, U. & Bakioglu, M., Multipoint Instantaneous Optimal Control of Structures. Computers and Structures, **80**, pp.909-917, 2002.
[15] Shinozuka, M. & Deodatis, G., Simulasyon of Stochastic Processes by Spectral Representation *Appl. Mec. Rev***. 44(4)**, pp.191-203, 1991.

Vibrobase insulation of a building excited by the technical seismicity effect of tube railway operation

D. Makovička[1] & D. Makovička Jr[2]
[1]*Czech Technical University in Prague, Klokner Institute, Czech Republic*
[2]*Static and Dynamic Consulting, Czech Republic*

Abstract

This paper deals with the application of an elastic elastomer layer at foundation base level in order to eliminate excessive vibrations propagating to the assessed building through the geological environment from an underground railway station structure. The dominant vibrations propagate as non-stationary vibrations through the subsoil from the tube structure in the close vicinity of the analysed building structure. For response analysis, the measured time histories in the construction area were selected and then the typical response was used as an input for a dynamic analysis of the structure. The solution of vibration transfer from the subsoil to the structure is demonstrated using the example of a multi-storey reinforced concrete building, founded on a dual foundation plate. An anti-vibration layer of rubber has been designed between the two plates. Two 3-D numerical models of the building take into account the individual storeys, firstly together with the lay-out of the rubber distribution in the foundation part and secondly without this rubber part.
Keywords: technical seismicity, vibro-base insulation, elastomer, dynamic analysis, response prognosis.

1 Introduction

The dynamic effects of subsurface traffic propagating through the ground environment into the ambient buildings of urban agglomerations have been acquiring ever increasing importance. Construction firms try to use the areas in the proximity of underground lines because of their lucrative location, usually for residential construction. It is these structures erected in the proximity of

WIT Transactions on The Built Environment, Vol 120, © 2011 WIT Press
www.witpress.com, ISSN 1743-3509 (on-line)
doi:10.2495/ERES110071

underground tunnels or directly above them in the case of shallow tunnels that are threatened by vibrations from underground traffic.

Trains running through underground tunnels produce vibrations which, together with the vibrations from a wide range of constituents of the underground railway, such as ventilation fans and escalator drives, propagate from the source to more distant structures. As a rule, these vibrations propagate into building foundations at the foundations/subsoil interface. Vibrations produced by subsurface traffic usually do not threaten the safety of structures. Nevertheless, they may be significant because of their undesirable impacts on people living or working in the residential or office parts of the building, especially due to their tuning.

2 Loading effect of underground traffic

The character of vibrations depends on their parameters at their source, i.e. the character of the train motion, the structure and occupancy of the rolling stock, the geometry and characteristics of the permanent way (above all, the fastening of the rails, etc.), the structure of the tunnel or station, the parameters of the equipment of the tunnel or station, etc. The magnitude of the vibrations is influenced not only by the vibration parameters at the source, but also by the composition of the geological environment in the proximity of the underground railway, i.e. the route from the source to the threatened structure. Last but not least, the magnitude of these vibrations may be increased or damped by the actual execution of the structure loaded by them.

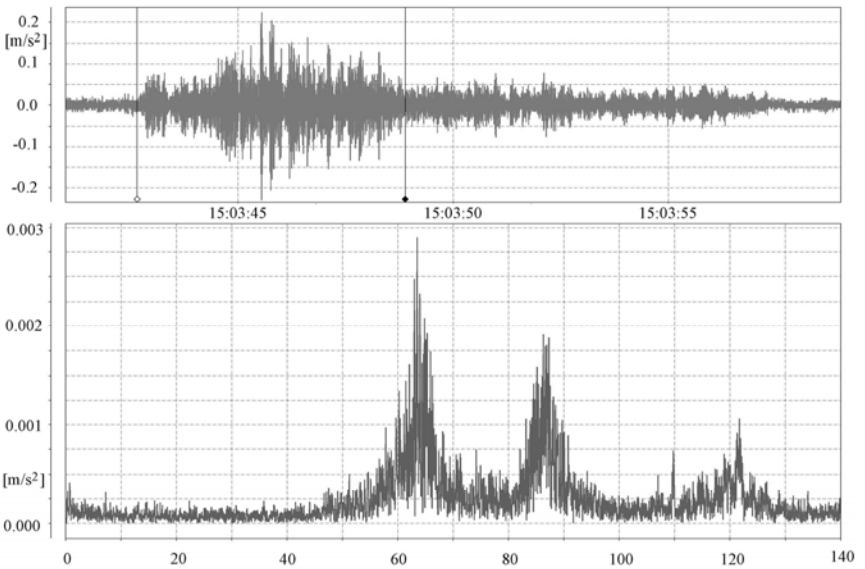

Figure 1: Measured vertical of the underground station excited by a train pass (the whole course, FFT spectrum).

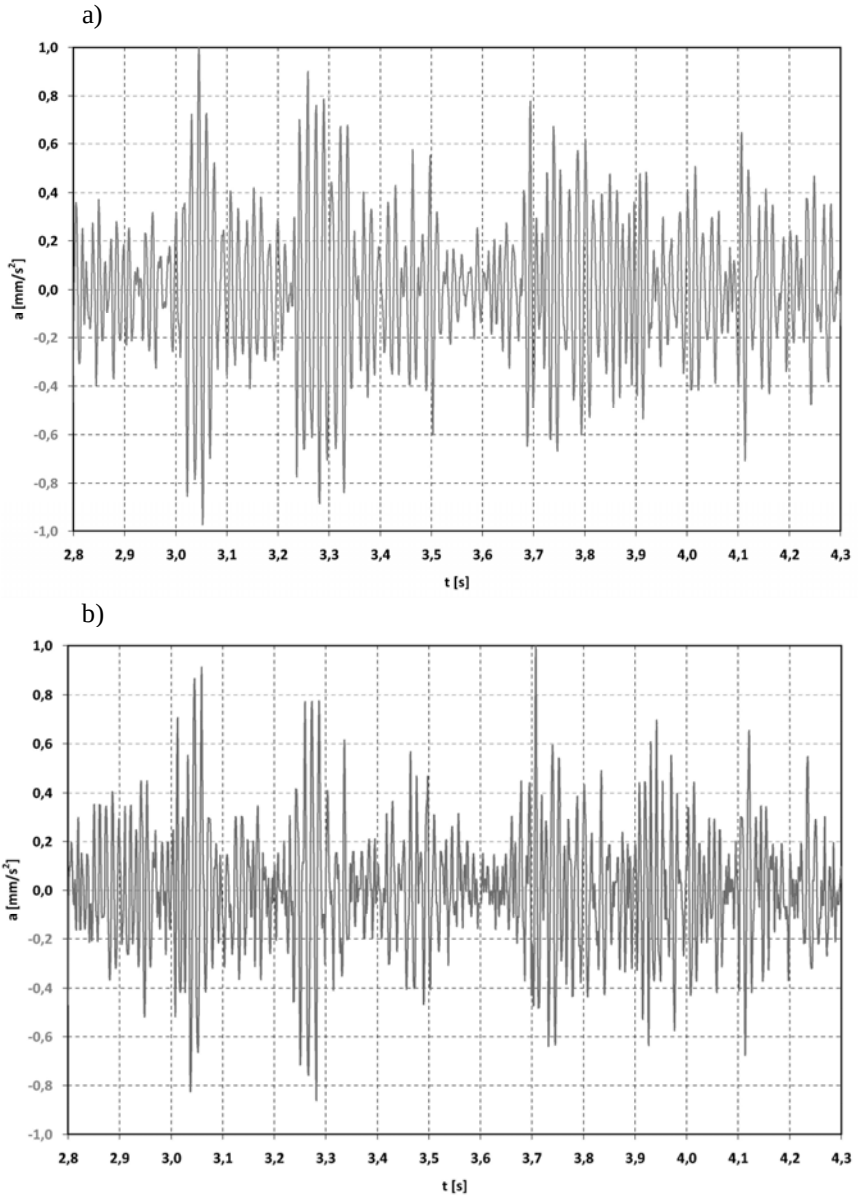

Figure 2: Selected parts of vibration excitation, a) vertical direction, b) horizontal direction.

When planning the correct measures for a structure that we intend to protect against excessive vibrations, we therefore need to know the amplitude level and the frequency structure of the vibrations which will propagate from the underground into the building. However, the measured real characteristics of the

vibrations may show considerable mutual differences, because the magnitude of the vibrations and their frequency structure depend not only on the general parameters (train design, permanent way, structures of stations and tunnels, etc.) but also on the local parameters on the site (particularly the composition of the geological environment, foundation design, etc.) A responsible designer of measures for reducing vibration transfer into the structure to be protected therefore needs, first of all, to perform vibration measurements on site, and to evaluate them, preferably at the foundation base level. These measurements produce typical histories of vibrations affecting selected parts of the structure (Fig. 1 and Fig. 2), which can be considered as the dynamic load of the future or existing structure at its foundation level. This vibration load has a non-stationary character.

3 Elastic support of the structure at its foundation level

An effective method for reducing the vibration level of the protected structure (Fig. 3) as a whole with reference to its foundation structures (plate, piles, strips, etc.) is to spring it from the foundations. In our case, the multistorey reinforced concrete building (Fig. 3) is founded on the base plate. On top of this plate an antivibration layer of rubber has been designed. Above the rubber there is an upper foundation plate in which the cast-in-place skeleton building structure is constrained. The principle involves consistent separation of the upper part of the structure from the foundation structure by an elastic layer. The thickness of this continuous elastic layer or of blocks of several strata of this material, and their distribution, must be determined from the mechanical properties of the rubber (particularly its stiffness) and its static prestress on the basis of a static and dynamic analysis of the whole building.

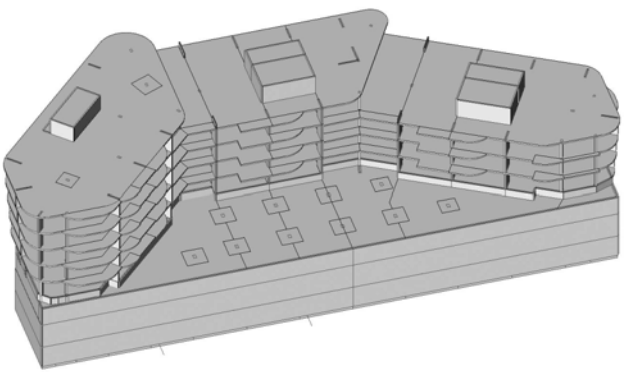

Figure 3: Calculation model.

The mechanical characteristics of the antivibration rubber layer were determined by laboratory tests of 500×500×30 mm samples that were used to form the vibration-resistant layer. The rubber blocks (slabs) are butt-jointed (not interlocked) in a single layer with 3 – 5 mm joints enabling the rubber to buckle, thus assuring identical conditions of deformability and, consequently, stiffness corresponding to the conditions at the foundation base.

The advantage of rubber layers is that they provide sufficient damping to reduce the resonance peaks of the vibrations of the elastic supported structure.

4 Structure analysis

The calculation model takes into account the individual storeys, broken down into the floor, foundation and roof slabs, columns, load-bearing walls and peripheral and interior girders. The layer of rubber was considered as the elastic subsoil of the Winkler-Pasternak model below the whole area of the upper part of the foundation plate. The rubber stiffness in the theoretical model takes into account the results of experimental tests on these materials. The mass of the floor and the foundation plates includes the masses of the non-load-bearing components (thin partitions, floorings, etc.) as well as the equivalent of the live loads of floors, roof and terraces.

The natural vibrations were computed for the analyzed building structure. For the dynamic response to the effects of external actions (traffic), the lowest possible tuning of the rubber-mounted structure is decisive. This manifests itself, on the one hand, by flexural vibrations of the vibroinsulated building in the environs of 1.75 Hz, and, on the other hand, by vertical and horizontal translative vibrations of the building as a whole or by torsional vibrations. The lowest six vibration modes are shown in Fig. 4. Not only the basic natural vibration modes but also the higher natural vibration frequencies of the individual storeys, possibly columns and walls, balconies, etc., appear in the computation, which makes the response of the building on each storey slightly different (higher, lower, possibly with antinodes on different sites).

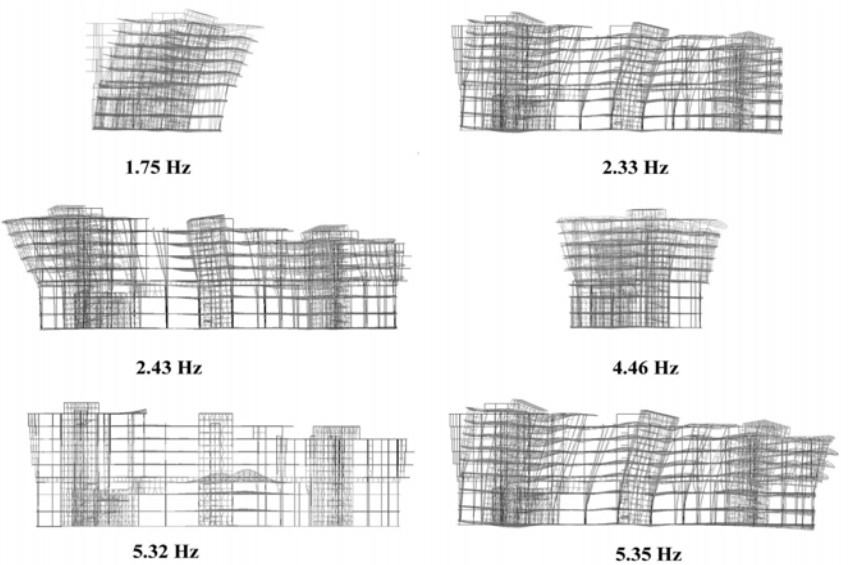

Figure 4: The lowest six natural vibration modes of a vibroinsulated structure.

The difference between the calculated natural frequencies for the structure with and without vibroinsulation is very small (Table 1).

Table 1: Effect of vibroinsulation on natural frequency [Hz] values.

Natural frequency [Hz]		Character of natural mode
with vibroinsulation	without vibroinsulation	
1.75	1.91	Bending of the whole structure in perpendicular direction
2.33	2.53	Bending of floor plates and bending of the whole structure in longitudinal direction
2.43	2.54	Rotation of the whole structure round the vertical axis
4.46	4.56	Rotation of the whole structure round the vertical axis and floor slab bending of the higher storeys
5.32	5.53	Higher modes of floor slab bending
5.35	5.57	Bending of some floor plates of the lower storeys and roof
5.43	5.76	Bending of some floor plates of the middle storey
5.56	5.82	Higher modes of floor slab bending
5.87	6.00	
5.99	6.19	

The dynamic load, i.e., the vibrations (Fig. 2), was introduced into the model independently for both directions as a normalized load and with the identical phase all over the foundation plate. The vibrations of the building produced by underground traffic were predicted by the response analysis of the whole system. Extremes of relative displacements in all the storeys are shown in the Tab. 2. The time histories for selected points on all the floors located on the chosen vertical line on the margin of the left highest structure part on its rear side are shown in Fig. 5. The most intensive vibrations can be observed in the proximity of columns, balconies, terraces and structural parts situated on the underground side. With increasing height, this excitation mode will manifest itself by vibrations of the building in one of the natural frequencies of the structure. More significant influence of vibration is in most cases limited to the lowest two or three storeys. In the higher storeys, the time characteristic of the vibrations is divided into lower frequencies. Another element reducing the vibration level in the individual storeys may be the non-load-bearing partitions, floating floors, carpet floorings, etc.

Table 2: Extremes of relative floor displacements under vertical excitation.

Floor level	Insulated structure				Noninsulated structure			
	Vertical excitation		Horizontal excitation		Vertical excitation		Horizontal excitation	
	u_z		u_y		u_z		u_y	
	Max	Min	Max	Min	Max	Min	Max	Min
-3rd Floor	1.00	-0.76	1.00	-0.83	1.00	-1.00	1.00	-1.00
-2nd Floor	1.22	-1.29	0.96	-1.07	**1.43**	-1.00	**1.28**	**-1.89**
-1st Floor	**1.24**	-0.97	0.89	-0.89	1.00	-1.00	**1.12**	**-1.23**
+1st Floor	**0.87**	-0.92	0.70	-0.59	0.85	-0.82	**1.18**	**-1.49**
+1st Floor, balconies	**1.25**	-1.22	0.90	-1.05	0.85	-1.09	**1.12**	**-1.56**
+2nd Floor	**0.74**	-0.64	**1.00**	**-1.02**	0.70	-0.53	0.85	-0.91
+2nd Floor, balconies	0.84	-0.92	**1.05**	**-1.07**	**1.02**	-0.91	0.96	-0.91
+3rd Floor	**0.70**	-0.69	0.85	-0.76	0.54	-0.72	**0.91**	**-0.95**
+3rd Floor, balconies	0.92	-0.79	**0.95**	-0.76	**1.02**	-0.72	0.76	**-0.84**
+4th Floor	**0.73**	-0.72	**1.08**	**-1.13**	0.63	-0.51	0.81	-1.04
+4th Floor, balconies	**0.96**	-0.95	0.57	-0.53	0.81	-0.84	**0.65**	**-0.88**
+5th Floor	**0.66**	-0.66	**1.08**	-0.93	0.63	-0.56	0.81	**-1.19**
+5th Floor, balconies	1.24	-1.21	**0.55**	-0.44	**1.33**	-1.35	0.38	**-0.70**
+6th Floor	**0.69**	-0.71	0.85	-1.04	0.52	-0.47	**1.09**	**-1.32**
+6th Floor, balconies	**1.44**	-1.32	0.72	-0.81	1.02	-1.05	**0.84**	**-1.14**

An observation of the response computation during vertical versus horizontal excitation reveals that the horizontal excitation level (non-normalised) is lower than the vertical excitation level - according to the measurements, approximately twice as low. Moreover, the response to horizontal excitation is, as a rule, of very low frequency, and it is also damped faster than in the case of vertical excitation.

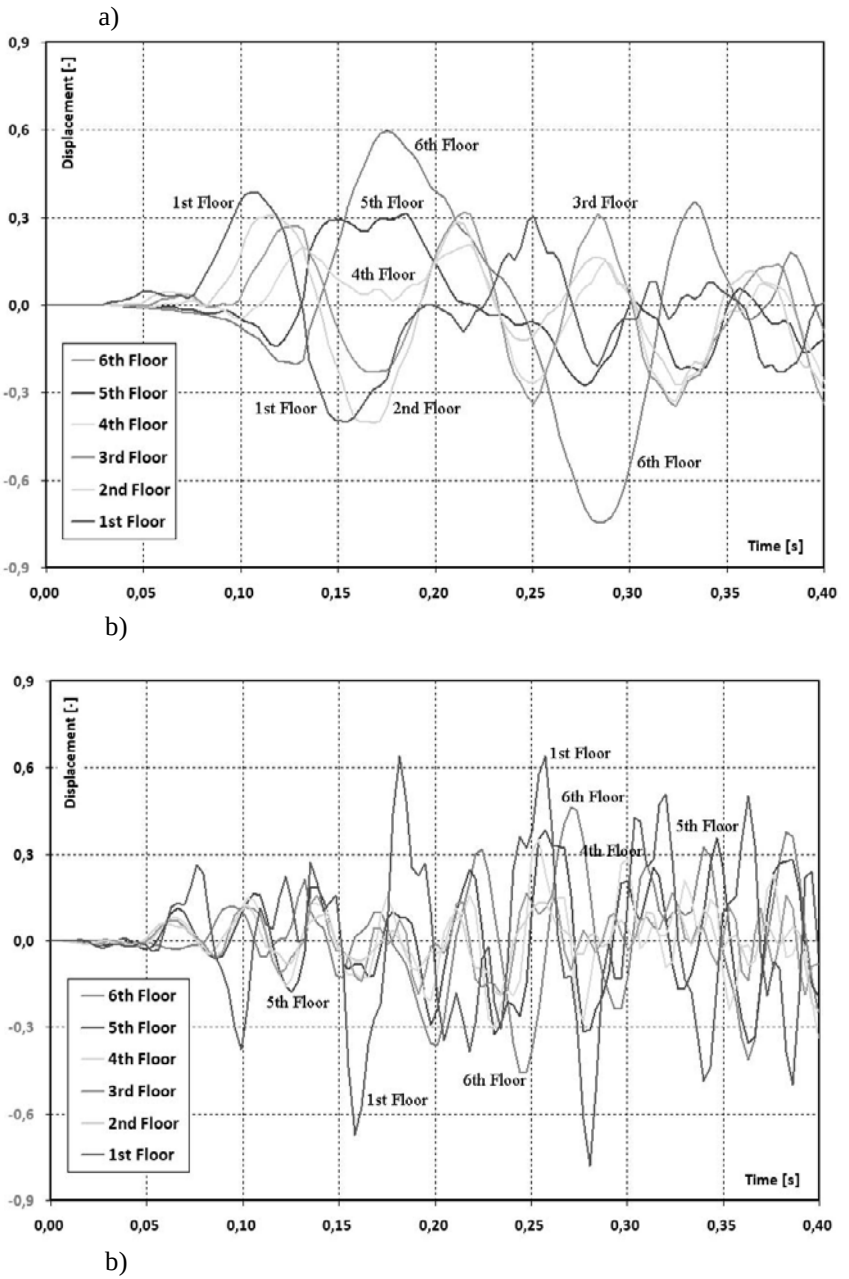

Figure 5: Time histories of relative displacements on line B, a) vertical direction, b) horizontal direction.

5 An assessment of the effectiveness of springing

An assessment of the effectiveness of the sprung system can be based on a comparison between the measured vibrations (Fig. 1) and the vibration level of the individual storeys in the sprung building.

The measured dominant excitation frequencies of underground train traffic are 63 Hz and 87 Hz on the frequency peaks (Fig. 1). The springing of the building will shift its dominant vibrations into the range of the lowest natural frequencies (from 1,7 Hz to about 20 Hz, see Fig. 5) of the sliding or flexural vibrations of the building as a whole. For frequencies of up to 20 Hz, this maximum response acceleration value corresponds approximately to the effective acceleration a_{RMS} according to Table 3.

Table 3: Prognosis of maximum floor vibration.

Excitation a_{RMS} [mm/s^2]	Vertical excitation		Horizontal excitation	
	Middle part of floors	Balconies	Middle part of floors	Balconies
Amplification	0.92	1.44	1.08	1.07
	Response a_{RMS} [mm/s^2]			
0.80-0.84	0.736-0.773	1.152-1.210		
0.22-0.24			0.238-0.259	0.235-0.257

The above results (Tables and Fig. 5) show that the influence of springing will manifest itself by redistribution of the dominant vibrations into the low frequency range of the springing and by the practically negligible amplitude range of the vibration level in comparison with the initially dominant excitation frequencies (Fig. 1).

6 Conclusion

This paper deals with the application of an elastic antivibration layer at foundation base level in order to eliminate excessive vibrations propagating to the assessed building through the geological environment from an underground railway structure. When the train is in motion, the dominant vibrations are transferred to the environs in the form of non-stationary vibrations produced by the pass of the train and of the tunnel station structure vibration (in our case).

The histories of the measured vibrations were used as loads applied to a modelled building structure at the foundation base of which, as an alternative, a separating elastic rubber layer had been designed. The response of the vibroinsulated structure is compared with the non-isolated structure. The computed vibration histories reveal that the vibrations of the sprung structure are

decreased in almost all the above-ground storeys. The effectiveness of the springing is determined by the frequency tuning of the sprung structure. The lower the tuning of the structure based on springs (the lower the dominant natural frequencies), the greater the decrease in the higher vibration frequencies and acoustic frequency effects propagating into the structure from its geological environment.

More significant influence of vibration is in most cases limited to the lowest two or three storeys. The predicted vibrations in the individual storeys were shown for a model with and without insulation, and were compared with the level of excitation vibrations at the foundation base. In the case of hard inelastic placing of the building on subsoil without springing, the vibrations would propagate from the subsoil in the whole frequency interval directly into the building structure, practically without decreasing. The applied springing is, consequently, a very efficient instrument for reducing the transfer of vibration from the soil to the interior parts of the building.

Acknowledgement

This research was supported as a part of the research projects in GAČR 103/08/0859 "Structure response under static and dynamic loads caused by natural and man induced activity", for which the authors would like to thank the Agency.

References

[1] Makovička, D. & Makovička, D., Jr., Response analysis and vibroinsulation of buildings subject to technical seismicity, *Earthquake Resistant Engineering Structures VII*, WIT Press, Southampton, UK, pp. 197-205, 2009.
[2] Makovička, D. & Makovička, D., Jr., Structure insulation exposed to excessive vibration of underground traffic (in Czech), *Stavební obzor*, 14/1, 2005.
[3] Jacquet, T. & Heiland, D., *Tieffrequente Bauwerken-Kopplungen als Schutz gegen Erschütterungen*, Gerb Berlin, 2002.
[4] Kay, H., Nachträgliche Schwingungsisolierungen von Gebäuden, *Spezialtiefbau*, TIS 2001, No. 4.

Behaviour of steel reinforced concrete beam-column joints

I. Montava, A. Gonzalez, R. Irles & J. C. Pomares
Universidad de Alicante,
Departamento de Ingeniería de la Construcción, Spain

Abstract

A composite structure with steel reinforced concrete, SRC, has the strength of reinforced concrete and the ductility of steel, meaning that appropriate design can achieve high seismic resistance capacity.

The present investigation shows the results and conclusions obtained from analyzing the strength and ductility of three different joints of a structural frame tested with increasing loading and unloading cycles, one with Reinforced Concrete, RC, another with Steel reinforced concrete, SRC, and a third with only reinforced concrete with the same strength capacity as the SRC section.

We are able to give hyperstatic and isostatic structures sufficient failure warning capacity, significant ability to dissipate energy and adequate protection against fire.

Keywords: reinforced concrete structures, steel reinforced concrete, ductility, structures, SRC, HAA, joint, earthquake resistant structure, steel.

1 Introduction

In recent decades there have been numerous studies aimed at determining the seismic behaviour of reinforced concrete structures, metal structures and composite structures.

Composite structures achieve similar rigidity to concrete structures and similar ductility to steel structures, [1], with metal sections being necessary to protect against fire. Reinforced concrete structures with completely embedded profiles significantly increase energy dissipation with adequate fire protection [2] This study attempts to understand the behaviour of reinforced concrete structures with embedded metal profiles, known in English as SRC (steel reinforced

WIT Transactions on The Built Environment, Vol 120, © 2011 WIT Press
www.witpress.com, ISSN 1743-3509 (on-line)
doi:10.2495/ERES110081

concrete). SRC is a structural system able to combine the strength and stiffness advantages of reinforced concrete structures with the high ductility of steel structures, high fire resistance, high energy absorption capacity and simple, cost-effective implementation acceptable to most builders and developers in the sector.

Since the Kanto earthquake (1923), which caused most fatalities of those known in Japan until the last Hounsu Coast earthquake (2011), the largest known magnitude at 8.9 degrees on the Richter scale, a type of composite construction system has been used in Japan for most of the structures of buildings over seven stories high [3].

The surprising seismic resilience of buildings in Japan is mainly due to the systematic use of profiles embedded in concrete structures and the use of energy dissipation by applying the Japanese seismic regulations [4]. The earthquake off the Japanese Hounsu coast on March 11th 2011 showed the excellent seismic behaviour of buildings built in recent years compared with the destruction caused by the tsunami provoked by the earthquake. Also surprising is the scant acceptance and diffusion of the structural system of metal sections embedded in reinforced concrete structures in European buildings up to now. Eurocode 4 refers to the calculation of this structural system [5].

It is true that the seismic forces are much higher in Japan, where structures must withstand earthquakes of magnitude seven or greater, but in certain unique buildings and especially those used by the public, it is essential to ensure the structural resistance to seismic action not covered by our current regulations. Hospitals, emergency centres, buildings, fire-stations, ambulance parks, power stations, schools and other buildings, should be designed to withstand disasters of varying magnitude, taking into account return periods higher than normally considered.

This structural system can increase little the overall cost of the work, compared with the importance of ensuring the structural strength demanded by severe earthquake activity.

2 Study procedure

A number of preliminary tests of the material used for the manufacture of prototypes were carried out to identify the real strength of the material. The ultimate resistance is much greater than expected resistance. The elastic limit was used to calculate resistance (Table 1).

Table 1: Material properties used in prototype 4 - SRC.

Concrete	HA-25/F/20/I	Ac	Fck=25 N/mm^2	Fce=31,58 N/mm^2
Steel reinf.	B-500-SD	As	Fsk=500 N/mm^2	Fse=511 N/mm^2
Structural Steel	HEB-100-S275	Aa	Fak=275 N/mm^2	Fae=335 N/mm^2

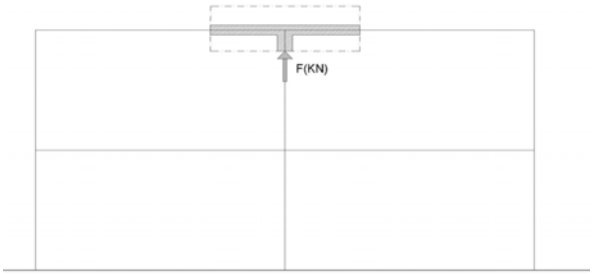

Figure 1: Single beam-column joint.

Loading and unloading tests with movement control were carried out (Fig. 2) on each of the prototype to breakage, using the laboratory test rig in the Department of Construction Engineering at the University of Alicante (Fig. 3).

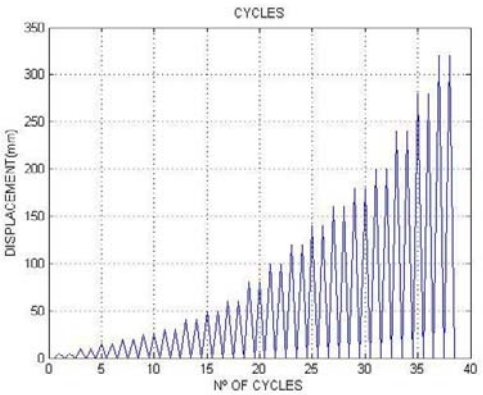

Figure 2: Loading-unloading cycles.

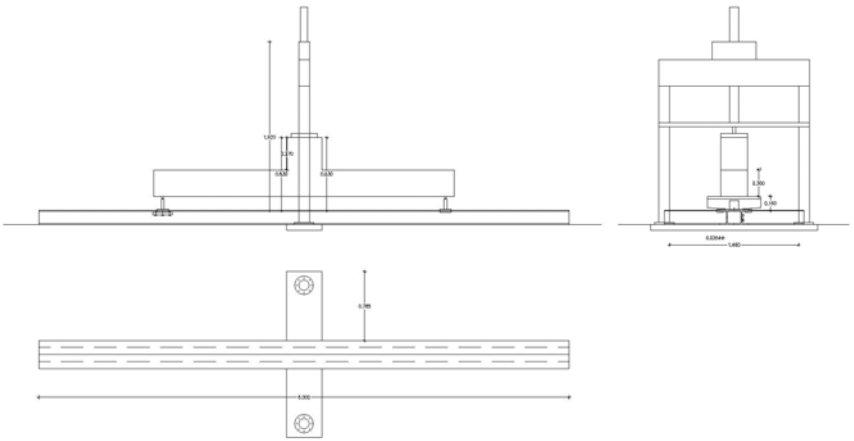

Figure 3: Laboratory test rig.

The initial prototypes 1 and 2 were used to adjust the following prototypes to improve the design and calibrate the tests. The budget of the SRC joints is higher but the estimated budget on a 100 m^2 rig (Table 2) is equalled by reducing the proportion of metal profiles in the structure as a whole and using mass-produced metal joints.

Table 2: Summary of the prototypes tested and data obtained.

Prototype		Cross-section	Steel	Steel section	Joint Price	Estimated 100 m^2 cost
P03	RC	300x250	4 ø 12	-	90 E.	75 E/m^2
P04	SRC	300x250	4 ø 12	HEB-100	150 E.	85 E/m^2
P05	RC	300x250	2 ø 16 2 ø 20	-	120 E.	80 E/m^2

This is a simple 3-bar joint (Fig. 1). RC prototype 3 is made with conventional reinforcement, SRC prototype 4 (Fig. 4), keeps the same reinforcement and cross-section and concrete, with the metal profile added to identify the increase in ductility and strength. RC prototype 5 is designed with the ultimate strength of prototype 3.

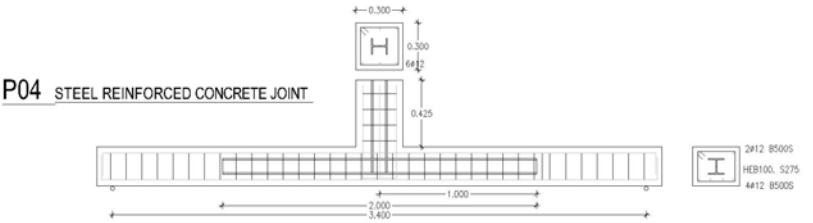

Figure 4: SRC prototype 4 tested.

The test results show the hysteretic behaviour in the load-deflection diagrams, and are analyzed in detail below.

3 Analysis of results

3.1 Overview

Figures 5 and 6 show the results for the three prototypes in a time-deflection diagram, already showing the increased strength and ductility between RC Prototype 3 and SRC Prototype 4.

They also show the different slopes and elastic and permanent deflections.

The RC prototype 3 is in domain 2 of deformation [6], and with little reinforcement obtains a cross-section with ductile failure. The final rupture of prototype 3 is a quick break, with the reinforcement under stress finally breaking and destroying the structure (Fig. 7).

Ultimate deformation is reached with total rupture of the steel.

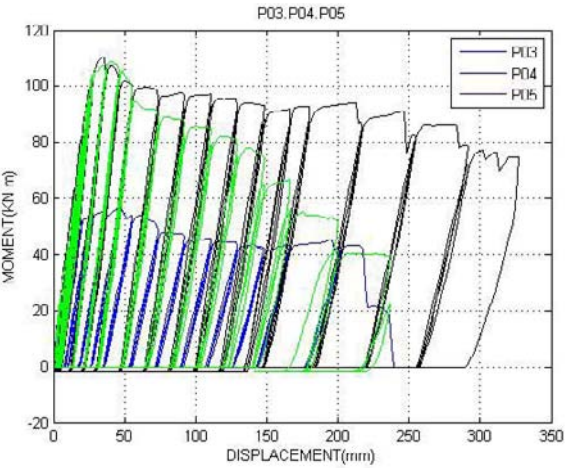

Figure 5: M-D complete graph of P03-P04-P05.

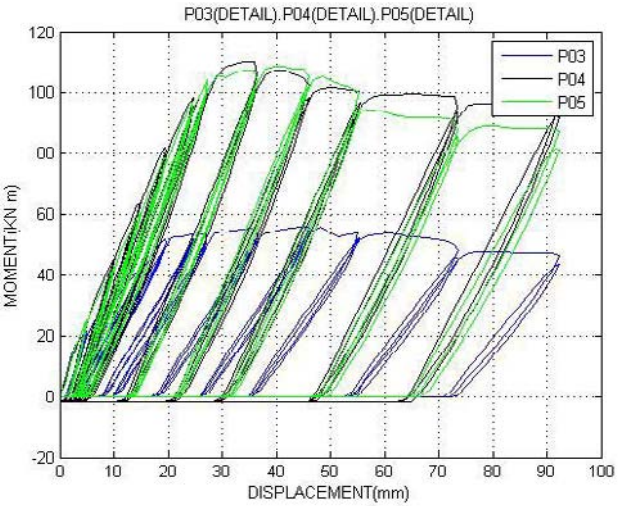

Figure 6: M-D details of P03-P04-P05.

With the SRC prototype 4 there is a break with much higher deformations. Once the concrete ruptures, the structure continues being deformed as if it were a metal frame, so very high deformations can be obtained, given the high ductility of steel metal profiles and the general confinement of the profile, which only disappears locally at the cross-section break (Fig. 8). Given the deformations achieved, the test was stopped with the cross-section maintaining high resistance, so that the ultimate deformation achieved occurred with the partial rupture of the cross-section in the plastic hinge stage, still with significant resistance capacity.

Figure 7: Photograph of the ultimate rupture of prototype 3.

Figure 8: Photograph of the ultimate rupture of prototype 4.

Steel reinforced concrete Structures consist of three different materials. By progressively increasing the load, we find different stages of resistance of the cross-section. In structures, joint ductility allows the redistribution of loads and the dissipation of seismic energy. The high ductility that steel gives to reinforced concrete joints allows the structure to offer a capacity for plastic adaptation that prevents the appearance of excessive stress states, not explicitly calculated in general.

RC prototype 5 is designed with the ultimate strength of SRC prototype 4, but without the metal profile, so as to compare the difference in ductility between the two structures (Fig. 9).

The rupture occurs in domain 3, corresponding to the total compression fracture of concrete. The reinforcement broke by compressive buckling.

Figure 9: Photograph of the ultimate rupture of prototype 5.

3.2 Calculation of the resistance of the SRC section

With reinforced concrete structures, the following stress states can be identified as the loads applied are progressively increased: (Fig. 10).

1. – Elastic phase. The concrete has not been fully cracked and the section is behaving correctly. The sections are arranged according to the classical linear-elastic behaviour and, in this case, the neutral axis passes through the centre of gravity of the homogenised section of the concrete and steel.

2. – Crack phase. The concrete most under stress reaches its tensile strength limit. The crack propagates and the stresses that the concrete stops resisting are absorbed by the structural steel and reinforcement, whose stress increases sharply. The neutral axis shifts towards the top flange of the metal profile, with the metal profile under stress. [7].

3. – Pre-break phase. The metal section still retains deformation capacity at this stage, meaning that the structure can continue to absorb energy before rupture.

4. – Metal profile break phase. Once the concrete loses all its strength, and the reinforcement under stress breaks, the section only resists with the metal profile.

With SRC structures, the most widely used and convenient method for calculating the ultimate strength is the method of superimposition of resistances, including the resistance capacity of three different materials, concrete, steel reinforcements and metal profiles, each with their own deformations.
Eurocode 4 describes a simplified method for calculating embedded steel sections completely covered by concrete to calculate the strength of sections subjected to flexion and compression. The calculation process consists of situating the neutral axis by force equilibrium equations and assessing the last moment the section resists.

With Prototype 4 the neutral axis in the flange of the profile (Fig. 11).

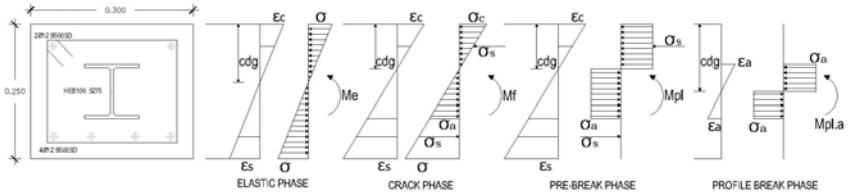

Figure 10: Stress states in concrete and steel under increasing load.

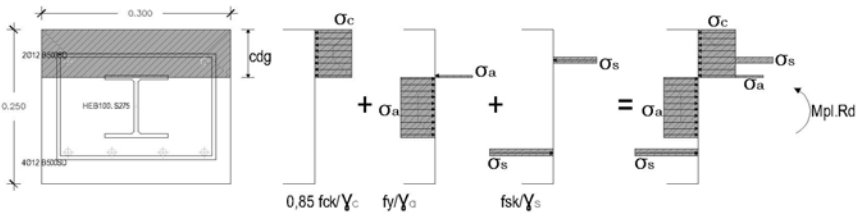

Figure 11: Stress state in pre-break for concrete and steel.

3.3 Energy aspects

The following chart summarizes the experimental results:

Defining the energy absorbed by deformation as the energy absorbed by the structure in the loading process and evaluating it as the area beneath the load-deflection curve [8], we have:

$$\text{Absorbed energy: } U=W=\int_0^{\Delta u} F(\Delta)d\Delta \tag{1}$$

The elastic deformation energy is recovered in the process of loading and unloading when we are in the elastic range (Fig. 6). In the plastic phase most of the energy dissipates, with Table 3 showing the values for the final deflection of each prototype.

From the deflections obtained in the elastic regime we can identify the inertia of the sections (2), whose results are also shown in Table 3:

$$flecha = f = \frac{PL^3}{48EI} \tag{2}$$

Table 3: Summary of the prototypes tested and data obtained.

Prototype		KN	KN m	Defor. mm	Elastic Energy	Energy absorbed
P03	RC	73	55	220	10,863 cm^4	10.31 KN m
P04	SCR	146	110	330	14.557 cm^4	42,46 KN m
P05	RC	146	110	230	14.557 cm^4	17,41 KN m

From the results we can deduce that the inertia of the SRC sections with metal embedded increases by 34% compared to the inertia of reinforced concrete sections in elastic range, with the increase in the slopes in Graph 11 being in elastic range.

The use of these joints in conventional reinforced concrete structures reduces the reinforced concrete sections by increasing the ductility of the structure, reducing labour demands by using less reinforcement, being easier to concrete and significantly increasing seismic safety. If the joints are produced industrially, their cost is greatly reduced, meaning that we estimate there to be almost no increase in cost over reinforced concrete structures.

4 Conclusions

The following conclusions are drawn from the experimental results presented:

1. – The absorbed energy to rupture in the SRC prototype is triple that for RC to equal strength, and equal reinforcement increases four times with the embedded metal profile added. (Table 4)

2. – The resistance of Steel reinforced concrete sections, SRC, is nearly twice the tensile strength of the reinforced concrete section, RC, without the metal profile (Fig.12).

3. – The successive slopes of the loading-unloading graph are higher and more consistent in the prototype in the SRC prototype than in the RC prototype, which is less rigid (Fig. 6).

4. – The successive slopes of the loading-unloading graph, measuring stiffness, than are greater in the elastic zone in the plastic zone (Fig. 6)

5. – The inertia of the SRC sections is greater than that of the RC sections, the increase being greater than that due to the principal inertia of the metal profile. (Table 3).

6. – The ultimate deformation is much higher in SRC structures, which behave like metal structures with near fracture deformations, compared to RC structures, which have a fragile ultimate rupture. This means that the ductility of the SRC structure can be nearly double that of the RC structure (Fig. 12)

7. – Steel reinforced concrete Structures, SRC, significantly improve ductility and resistance and can dissipate a lot of energy, making them safer and more resistant to seismic activity than reinforced concrete, RC.

8. – In the light of these results, it would be interesting to consider generalising the reinforcement with metal profiles embedded in the joints of Reinforced Concrete structures to obtain more earthquake resistant structures with adequate fire resistance, especially in public and emergency service buildings in which high-seismic safety should be guaranteed.

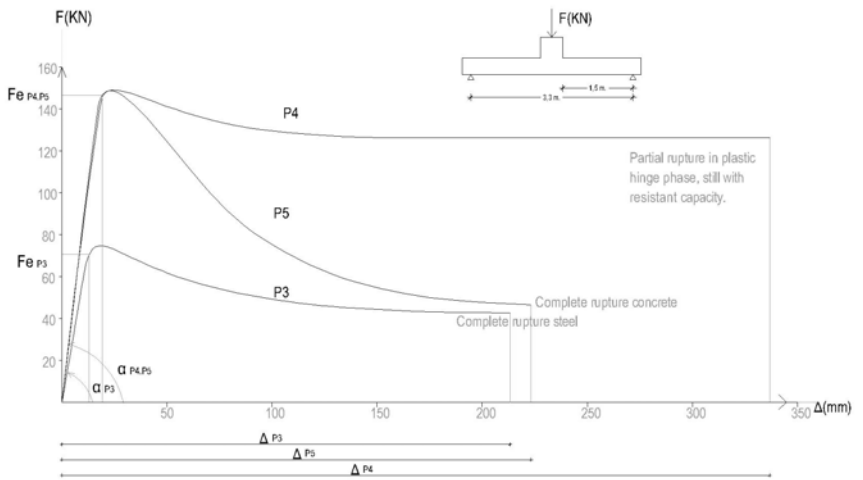

Figure 12: Graph summarising the test results.

Acknowledgements

The studies presented in this paper were made possible thanks to the financial support of the Department of Construction Engineering at the University of Alicante. The authors gratefully acknowledge this support.

References

[1] Beatriz Gil Rodriguez, *Metodología práctica para el diseño de pórticos de estructura mixta con uniones semi-rígidas.* Tesis Doctoral. Universidad de Navarra, 2006.
[2] Cheng-Cheng Chen, Keng-Ta Lin, Behaviour and strength of Steel reinforced concrete beam–column joints with two-side force inputs, *Journal of Constructional Steel Research*, 65.pp. 641-649, 2009.
[3] Hiroshi Kuramoto, *Seismic Design Codes for Buildings in Japan*, Journal of Disaster ResearchVol.1No.3, 2006.
[4] Wakabayashi, Minoru. Martinez Romero, Enrique, *Diseño de estructuras sismorresistentes*, McGraw-Hill, pp.180-189, 1988.
[5] Eurocode 4. *Proyecto de estructuras mixtas de hormigón y acero*, 1994.
[6] EHE-08-. *Instrucción de Hormigón Estructural*, 2008.
[7] Benito Hernández, C., *Nociones de cálculo plástico*, Editorial Rugarte, S.L., Madrid, pp 24-25, 1975.
[8] Hiroshi Akiyama, *Metodología de proyecto sismorresistente de edificios basada en el balance energético.* Editorial Reverté. S.A., 2003.

Section 3
Ground motion

This page intentionally left blank

Developing a 7.5-sec site-condition map for Japan based on geomorphologic classification

K. Wakamatsu[1] & M. Matsuoka[2]
[1]*Department of Civil and Environmental Engineering, Kanto Gakuin University, Japan*
[2]*Geoinformation Center, Geological Survey of Japan, National Institute of Advanced Industrial Science and Technology, Japan*

Abstract

In a seismic hazard assessment, local geologic and ground conditions play important roles in characterizing and estimating hazards. The authors created a systematically standardized GIS-based ground-condition map containing the attributes of geomorphologic classification in grid cells of 7.5 arc-seconds latitude × 11.25 arc-seconds longitude for all of Japan. This paper introduces the concept of developing the 7.5-arc-second JEGM, and presents sample images of the JEGM. As an example of the database's application to estimating the hazards—the average shear velocity of the ground in the upper 30 m–Vs30 is estimated and mapped for all of Japan. As the other examples of the database's application being released by public agencies, presents prefectural seismic risk analyses, Seismic Hazard Maps for Japan, Quick Estimation System for Earthquake Maps triggered by observation records (QuiQuake) are presented.
Keywords: GIS database, geomorphologic land classification, seismic hazard mapping, Vs30, seismic risk analyses.

1 Introduction

A number of ocean-trench earthquakes including the Tokai, Tonankai and Nankai earthquakes and inland earthquakes hit the Tokyo metropolitan area are expected to occur with high probabilities in the near future in Japan. Local ground conditions play important roles in characterizing and assessing their hazards. However, neither a digital database nor paper maps of ground conditions throughout Japan had been available in a unified form.

WIT Transactions on The Built Environment, Vol 120, © 2011 WIT Press
www.witpress.com, ISSN 1743-3509 (on-line)
doi:10.2495/ERES11091

Therefore, the authors have created a systematically standardized GIS-based ground-condition map covering all of Japan, the "Japan Engineering Geomorphologic Classification Map (JEGM)" and released on CD-ROM (Wakamatsu et al. [1]). The database covers all of Japan with a Japanese standard size grid, which is 30 arc-seconds latitude x 45 arc-seconds longitude (approximately 1 x 1 km^2) and includes five sets of major attributes—geomorphologic classification, geologic age, slope angle, elevation, and relative relief—in approximately 380,000 grid cells. Among its attributes, the geomorphologic classification database was based on a new engineering-based geomorphologic classification scheme for identifying and classifying subsurface ground conditions.

The JEGM was employed for the following types of nationwide hazard mapping: liquefaction potential (Wakamatsu et al. [1]), average shear velocity of ground in the upper 30 m, Vs30, for estimating the site amplification factors (Matsuoka et al. [2]), flood potential (Wakamatsu et al. [1]), and erosion rate potential in mountainous area (Hasegawa et al. [3]).

To perform more accurate hazard zoning, we had been developed a 7.5-arc-second Japan Engineering Geomorphologic Classification Map (7.5-arc-second JEGM) for all of Japan, which is a high spatial-resolution version of the above-mentioned 30-arc-second JEGM. In this paper, we present the concept behind the development of the 7.5-arc-second engineering geomorphologic classification database (the 7.5-arc-second JEGM) and its application for seismic hazard estimation.

2 7.5-arc-second JEGM

2.1 Concept of mapping

The map contains an attribute of geomorphologic land classification in grid cells that are 7.5 arc-seconds latitude × 11.25 arc-seconds longitude (approximately 250 × 250 m^2) in size. The criteria for 30 arc-second JEGM were used to develop the 7.5-arc-second JEGM, with some additional classifications such as "lowland between coastal dunes and/or bars," "rock shore, rock reef," "dry river bed," which are negligible areas in the 1-km square grid cell. A description of geomorphologic map units is presented in Table 1, together with the corresponding general ground conditions and general depth of groundwater. These criteria were based on the purpose of the mapping project: identification and classification of subsurface ground conditions, through standard geomorphologic classification. The geomorphologic factors presented in table 1 are known to be correlated with subsurface ground and hydrologic conditions (e.g. Zuidam et al. [4]).

Table 1: Description of geomorphologic map units in the 7.5-arc-second JEGM.

Geomorphologic map unit	Definition and general characteristics	Subsurface soil condition	General depth of groundwater*
Mountain	Steeply to very steeply sloping topography with highest elevation and relative relief within a grid cell of more than approximately 200 m. Moderately to severely dissected.	Pre-Quaternary hard to soft rock.	Deep
Mountain footslope	Gently sloping topography adjoining mountains and composed of material sourced from the mountains such as colluvium, talus, landslide, and debris flow deposits.	Loose debris and soils consisting of colluvium, talus, landslide, and debris flow deposits.	Deep
Hill	Steeply to moderately sloping topography with higher elevation and relative relief within a grid cell of approximately 200 m or less. Moderately dissected.	Pre- Quaternary and Quaternary hard to soft rock.	Deep
Volcano	Steeply to moderately sloping topography with higher elevation and larger relative relief, composed of Quaternary volcanic rocks and deposits.	Quaternary hard to soft volcanic rock and/or deposits.	Deep
Volcanic footslope	Gently sloping topography located around skirt of volcano including pyroclastic-, mud- and lava-flow fields, and volcanic fan produced by dissection of volcanic body. Slightly dissected.	Quaternary loose to dense volcanic deposits consisting of ash, scoria, pumice, pyroclastic flow, lava, debris avalanche, etc.	Deep
Volcanic hill	Moderately sloping topography composed of pyroclastic flow deposits. Moderately to severely dissected.	Loose to moderately loose pyroclastic flow deposits such as ash, scoria, and pumice.	Deep
Rocky strath terrace	Fluvial or marine terrace with flat surface and step-like form, including limestone terrace of emerged coral reef. Thickness of subsurface soil deposits is less than 5 m.	Hard to soft rock.	Deep
Gravelly terrace	Fluvial or marine terrace with flat surface and step-like form. Covered with subsurface deposits (gravel or sandy soils) more than 5 m thick.	Dense gravelly soil.	Deep
Terrace covered with volcanic ash soil	Fluvial or marine terrace with flat surface and step-like form. Covered with cohesive volcanic ash soil to more than 5 m thick.	Stiff volcanic ash (cohesive soil).	Deep
Valley bottom lowland	Long and narrow lowland formed by river or stream between steep to extremely steep slopes of mountain, hill, volcano, and terrace.	Moderately dense to dense gravel or boulders in mountain, but loose sandy soil to very soft cohesive soil in plain.	Shallow
Alluvial fan	Semi-cone-like form composed of coarse materials, which is formed at the boundary between mountains and lowland. Slope gradient is more than 1/1000.	Dense gravel with boulders to moderately dense sandy gravel.	Deep in the central part of fan but shallow in the distal part of fan

2.2 Procedure of mapping

First, the preliminary map was compiled; the major geomorphologic units were evaluated and classified on the basis of the 30-arc-second JEGM and interpretation of topographic maps. The detailed geomorphologic surveys of local geomorphologic features at scales of 1: 50,000 were subsequently performed to delineate units on the basis of the criteria listed in table 1, based on interpretation and compilation of existing information, which is available from published reports, papers, topographical maps, and other available maps and boring exploration data, in addition to our expertise in geomorphology and geotechnical engineering. Finally, a detailed map was drawn up, and digitized and stored in cells using GIS software. Each cell is assigned to the single geomorphologic unit that occupies the greatest area of the cell when multiple units exist within the cell.

Figure 1 shows a sample image of the 7.5-arc-second JEGM for all of Japan. The total number of cells of the map is approximately 6 million.

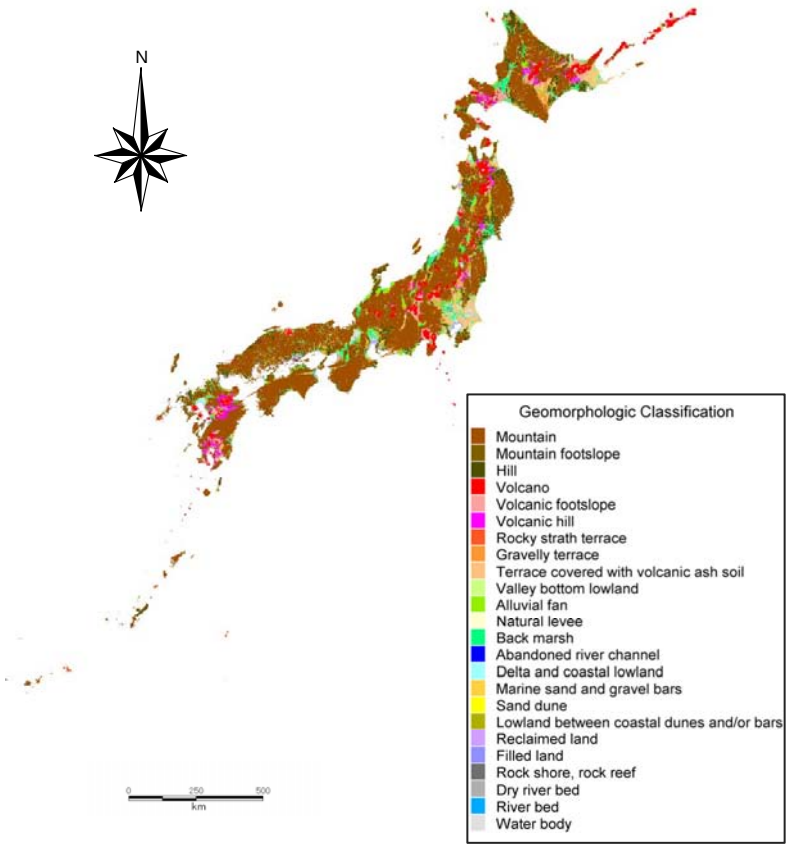

Figure 1: 7.5 arc-second JEGM for all of Japan.

3 Average shear-wave velocity (Vs30) mapping using the 7.5-arc-second JEGM

Shear-wave velocity in the upper 30 meters, Vs30 is observed or estimated using borehole data and it is important parameter for evaluating the seismic micro zoning with consideration of site effect during ground motion (Borcherdt [5]).

In a previous study (Matsuoka et al. [2]), we calculated the Vs30, covering approximately 2,000 sites all over Japan where shear-wave velocity has been measured. Geomorphologic units for all PS logging data sites were interpreted using the original data of the 30-second JEGM. Next, we examined the correlation between not only geomorphologic units but also geographical information derived from the JEGM and the Vs30 values. We found that the Vs30s showed some dependency on altitudes, slopes, and distances from mountains or hills formed during older periods (Pre-Tertiary or Tertiary). Multiple linear regression formulae for each geomorphologic unit was developed to estimate the Vs30 using elevation (*Ev*), slope (*Sp*), and distance (*Dm*) from a mountain or a hill as explanatory variables. The basic regression formula is the following equation:

$$\log \mathrm{Vs30} = a + b \log Ev + c \log Sp + d \log Dm \pm \sigma \qquad (1)$$

where *a*, *b*, *c*, and *d* represent regression coefficients, and σ is the standard deviation. The units of *Ev*, *Sp*, and *Dm* are meters, 1000 times tangent values, and kilometers, respectively. When the value of the explanatory variable is less than 1, we fixed the value as "1".

Table 2 shows the regression coefficients and standard deviation of each geomorphologic unit obtained by regression analysis. The regression coefficients show that the higher the elevation, the steeper the slope, and the shorter the distance from the mountain or the hill, Vs30 values become larger. As for the logarithmic standard deviation for the overall estimation, the estimation formula shown in Equation 1 has a higher accuracy than previous empirical estimations.

Using Equation 1 and the attributes of the geomorphologic classification in the 7.5-arc-second JEGM, geologic age, elevation, and slope contained in the 30-arc-second JEGM, we were able to compute the Vs30 distribution with 250 m spatial resolution. Figure 2 shows the Vs30 map for all of Japan. The Vs30 values are approximately 150 m/s on delta and coastal lowland, reclaimed land, and back marsh. The areas of valley bottom lowland also show a rather small Vs30 in the range from 180 to 200 m/s.

To draw an amplification capability map, the Vs30 was converted into the amplification factor for PGV with respect to stiff soil, which corresponds to ground with Vs30 of 600 m/s, through an empirical relationship (Fujimoto and Midorikawa [6]). The amplification map for all of Japan is shown in fig. 3.

Table 2: Description of geomorphologic map units in the 7.5-arc-second JEGM (Cont.).

Geomorphologic map unit	Definition and general characteristics	Subsurface soil condition	General depth of groundwater*
Natural levee	Slightly elevated area formed along the riverbank caused by fluvial deposition during floods.	Loose sandy soil.	Shallow
Back marsh	Swampy lowland formed behind natural levees and lowlands surrounded by mountains, hills, and terraces.	Very soft cohesive soil containing peat or humus.	Very shallow
Abandoned river channels	Swampy shallow depression along former river course with elongated shape.	Very loose sandy soil occasionally covered with soft cohesive soil.	Very shallow
Delta and coastal lowland	Delta: flat lowland formed at the river mouth by fluvial accumulation. Coastal lowland: flat lowland formed along shoreline by emergence of shallow submarine deposits, including discontinuous lowlands along sea- or lake- shore.	Loose fluvial sandy soil over-lying very soft cohesive soil.	Shallow
Marine sand and gravel bars	Slightly elevated topography formed along shoreline, composed of sand and gravel, which was washed ashore by ocean wave and/or current action.	Moderately dense to dense marine sand or gravel occasionally with boulder.	Shallow
Sand dune	Wavy topography usually formed along shoreline or river, comprised of fine to moderately aeolian sand; generally overlies sandy lowland.	Very loose to loose fine to medium sand.	Deep at crest of dune but shallow near base of dune
Lowland between coastal dunes and/or bars	Swampy lowland formed behind dunes or bars	Very soft cohesive soil containing peat or humus.	Very shallow
Reclaimed land	Former bottom flat of sea, lake, lagoon, or river that has been reclaimed as land by drainage.	Loose sand overlying very soft cohesive soil, sometimes covered with loose sandy fill.	Very shallow
Filled land	Former water body such as sea, lake, lagoon, or river reclaimed as land by filling.	Very loose to loose sandy fill, overlying very soft cohesive soil or loose sandy soils.	Very shallow to shallow
Rock shore, Rock reef	Irregular topography of rock or coral around beach zone.	Pre- Quaternary and Quaternary hard to soft rock	Near sea level
Dry riverbed	Nearly flat, irregular topography without water in normal time.	Loose sandy to gravelly alluvial soil, occasionally with boulders.	Very shallow
River bed	Nearly flat, irregular topography with varying water cover and having erosion and accumulation parts.	Loose sandy to gravelly alluvial soil, occasionally with boulders	
Lake	Inland water body.		
Nearshore waters	Nearshore water body.		

*Deep: deeper than 3 m below the ground surface, Shallow: within 3 m of the ground surface, Very shallow: within 1 m of the ground surface.

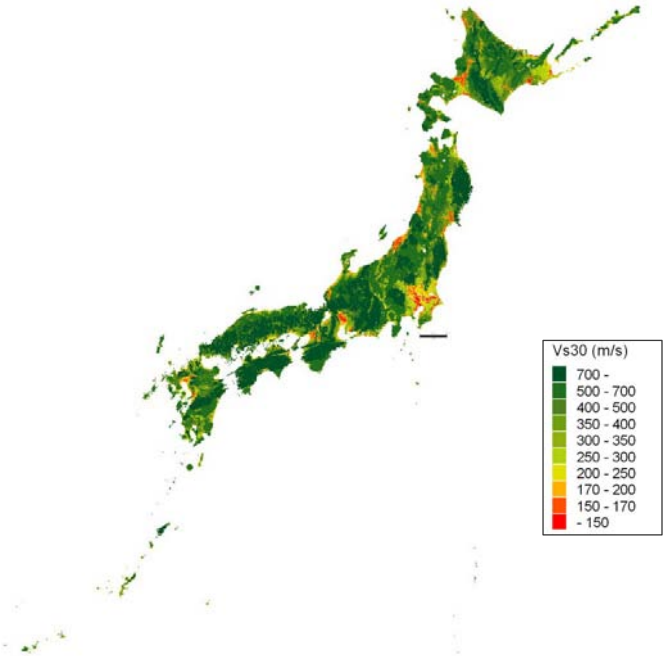

Figure 2: Vs30 map calculated from the 7.5-arc- second JEGM.

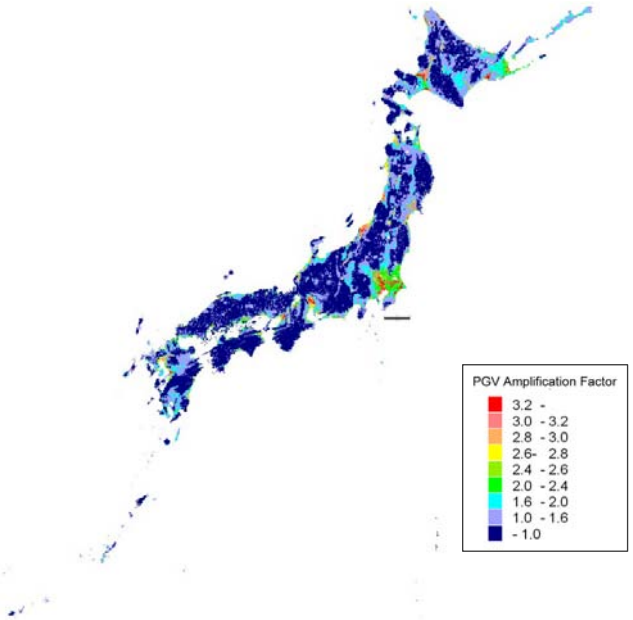

Figure 3: PGV site amplification map converted from Vs30 map.

Table 3: Regression coefficient (Matsuoka et al. [2]).

Geomorphologic map unit	Regression coefficient				s.d.
	a	*b*	*c*	*d*	s
Mountain (Pre-Tertiary)	2.900	0	0	0	0.139
Mountain (Tertiary)	2.807	0	0	0	0.117
Mountain footslope	2.602	0	0	0	0.092
Hill	2.349	0	0.152	0	0.175
Volcano	2.708	0	0	0	0.162
Volcanic footslope	2.315	0	0.094	0	0.100
Volcanic hill	2.608	0	0	0	0.059
Rocky strath terrace	2.546	0	0	0	0.094
Gravelly terrace	2.493	0.072	0.027	-0.164	0.122
Terrace covered with volcanic ash soil	2.206	0.093	0.065	0	0.115
Valley bottom lowland	2.266	0.144	0.016	-0.113	0.158
Alluvial fan	2.350	0.085	0.015	0	0.116
Natural levee	2.204	0.100	0	0	0.124
Back marsh	2.190	0.038	0	-0.041	0.116
Abandoned river channel	2.264	0	0	0	0.091
Delta and coastal lowland	2.317	0	0	-0.103	0.107
Marine sand and gravel bars	2.415	0	0	0	0.114
Sand dune	2.289	0	0	0	0.123
Reclaimed land	2.373	0	0	-0.124	0.123
Filled land	2.404	0	0	-0.139	0.120

4 Utilization of 7.5-arc-second JEGM and Vs30 map

In recent years, the 7.5-arc-second JEGM and the JEGM based Vs30 map have been employed various kinds of seismic hazard mappings in Japan. We introduce several examples of utilization of the both maps.

4.1 Prefectural seismic risk analyses

The Basic Law on Natural Disasters [7] obliges concerned government bodies and local governments to work out plans to prepare for disasters based on central government measures. Seismic risk analyses have been carried out to develop regional disaster prevention planning. In these analyses, the 7.5-arc-second JEGM has been used to develop the subsurface ground model for seismic intensity mapping and liquefaction hazard mapping for scenario earthquakes; target area is divided into 250 m size grid cell and representative soil profile in each cell is evaluated from the borehole data in the cell; it is estimated considering the geomorphologic classification of the 7.5-arc-second JEGM when there is no borehole data in the cell (Saitama Prefecture [8]; Chiba Prefecture [9]; Kanagawa Prefecture [10]). In some cases the JEGM based Vs 30 map is directly used to evaluate the site amplification for seismic intensity (Tokyo metropolitan government [11]). Figure 4 shows seismic intensity map of Tokyo metropolitan for a 7.3-JMA magnitude scenario earthquake centered in northern Tokyo Bay.

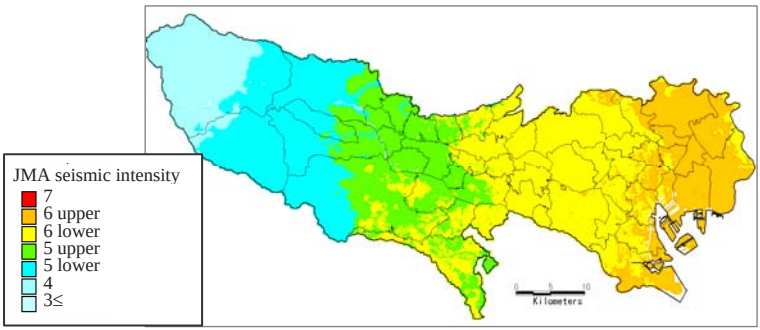

Figure 4: Seismic intensity map of Tokyo metropolitan for 7.3-JMA magnitude scenario earthquake centered in northern Tokyo Bay [11].

4.2 National Seismic Hazard Maps for Japan

The Headquarters for Earthquake Research Promotion, Ministry of Education, Culture, Sports, Science and Technology have been prepared and released the National Seismic Hazard Maps for Japan every January 1st shince 2005 [12]. This work is initiated by the earthquake research committee (ERC) on a basis of a long-term evaluation of seismic activity, and evaluation of strong ground motion. The hazard map consists of two kinds of maps; one is a probabilistic seismic hazard map (PSHM) that shows the relation between seismic intensity value and its probability of exceedance within a certain time period. Another one is a scenario earthquake shaking map (SESM). The national seismic hazard maps for the PSHM, an empirical attenuation formula is used following the seismic activity modeling by ERC, and peak ground velocity for sites is evaluated.

The 7.5-arc-second JEGM based Vs 30 map was employed from 2009 version to evaluate site amplification in every 7.5-arc-second grid-cell of the PSHM. The hazard maps and various information to produce the maps, such as data on seismic activities, seismic source models and underground structures are released by Web-GIS at the Japan Seismic Hazard Information Station (J-SHIS) [13]. 2011 version of the PSHM is presented in fig. 5.

4.3 Quick estimation system for earthquake maps triggered by observation records (QuiQuake)

The Quick Estimation System for Earthquake Maps Triggered by Observation Records (QuiQuake) is a system which provides wide-ranging and detailed strong motion ground motion maps, based on information such as peak ground velocity and JMA instrumental seismic intensity, soon after an earthquake occurs. The website [14] has been published by the National Institute of Advanced Industrial Science and Technology (AIST) since October 13, 2009. The system uses combinations of the 7.5-arc-second JEGM based amplification capability and observed seismic records. In this system, automatic calculation of spatial interpolation, including consideration of attenuation characteristics from

the seismic source, is immediately activated by harvesting the seismic data recorded at strong ground motion observation stations (K-NET and KiK-net) operated by the National Research Institute for Earth Science and Disaster Prevention (NIED).

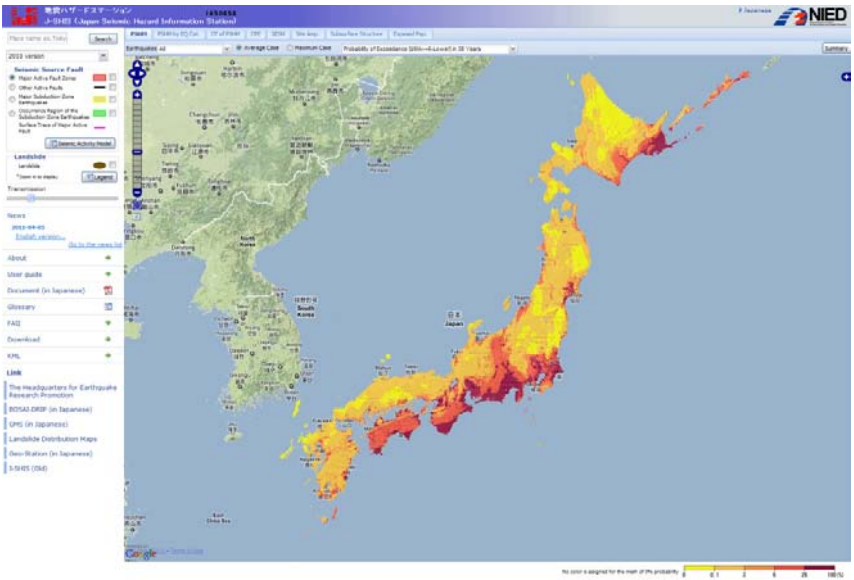

Figure 5: Probability of exceedance of seismic intensity 6 lower of PSHM within 30 years for average case considering all earthquakes.

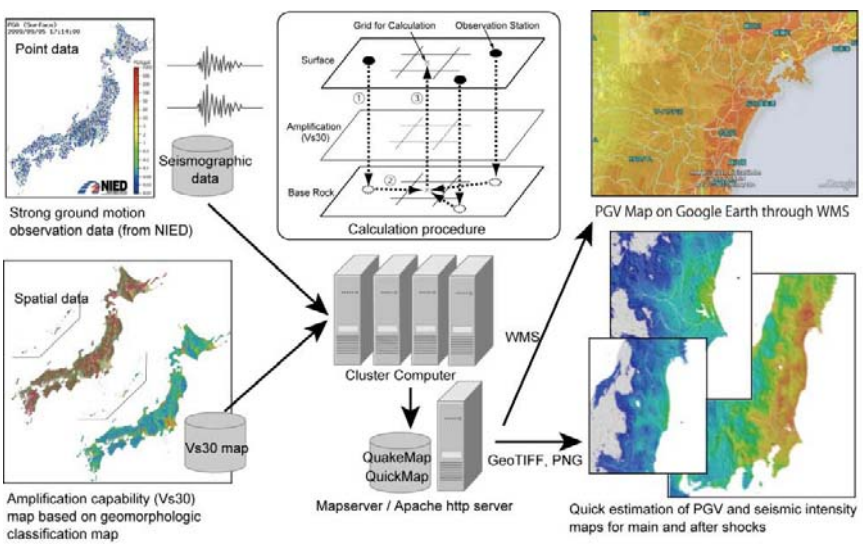

Figure 6: System overview and calculation procedure of QuiQuake.

Furthermore, ground motion maps for more than 5,000 major earthquakes after June 1996 have been computed and archived such that they chronologically represent the seismic motions over the last 15 years. The strong motion maps are also published through an OGC (Open Geospatial Consortium) standard web service interface. It is expected that these maps will be used as fundamental information for municipalities and private companies to develop business continuity plans (BCPs) and to take effective countermeasures against seismic disasters. The schematic overview of QuiQuake is shown in fig. 6.

5 Concluding remarks

In this paper, we introduce the 7.5-arc-second "Japan Engineering Geomorphologic Classification Map (JEGM)," the high spatial-resolution version of 30-arc-second JEGM, which was based on engineering-based geomorphologic classification standards; the concept and procedure of mapping are described, and the image samples of 7.5-arc-second JEGM for major urban areas in Japan are presented. As an example of the database's application to detailed and accurate hazard zoning, we estimated and mapped the average shear-wave velocity of the ground in the upper 30 m, Vs30 for all of Japan and introduce some other utilization for seismic hazard mapping released by public organization. The digital data of the 7.5-arc-second JEGM, Vs30 map and PGV site amplification map converted from Vs30 map are released on line: http://www.j-shis.bosai.go.jp/JSHIS2/download.html?lang=en

Acknowledgements

The developing the 7.5-arc-second JEGM was done as a part of the project 'Development of Integrated Geophysical and Geological Information Database' sponsored by the Special Coordination Fund for Science and Technology Promotion of Japan. QuiQuake is supported by strong ground motion observation stations operated by National Research Institute for Earth Science and Disaster Prevention (NIED). The authors gratefully acknowledge these supports.

References

[1] Wakamatsu, K., Kubo, S., Matsuoka, M., Hasegawa, K. & Sugiura, M., Japan Engineering Geomorphologic Classification Map with CD-ROM Database, University of Tokyo Press, Tokyo, 2005. (in Japanese with English abstract and manual)

[2] Matsuoka, M., Wakamatsu, K., Fujimoto K., & Midorikawa, S., Average shear-wave velocity mapping using Japan Engineering Geomorphologic Classification Map, Journal of Structural Engineering and Earthquake Engineering, 23-1, 57s-68s, 2006.

[3] Hasegawa, K., Wakamatsu, K. & Matsuoka, M., GIS-based Nationwide Evaluation of Erosion Rate Potential in Japan, Proc. 2nd Japan-Taiwan Joint Workshop on Geotechnical Hazards from Large Earthquakes and Heavy Rainfall, ATC3-ISSMGE, pp.108-113, 2006.
[4] Zuidam R. A et al., Aerial Photo-Interpretation in Terrain Analysis and Geomorphologic Mapping, Smits Publishers, Hague, 1986.
[5] Borcherdt, R.D., Effects of local geology on ground motion near sanFrancisco Bay, Bulletion of Seismological Society of America, pp.29-61, 1970.
[6] Fujimoto, K. & Midorikawa, S., Average shear-wave velocity mapping throughout Japan using the Digital National Land Information, J. Japan Association for Earthquake Engineering, Vol.3, No.3, pp.13-27, 2003. (in Japanese with English abstract)
[7] Ministry of Internal Affairs and Communications, The Basic Law on Natural Disasters, 1961, http://law.e-gov.go.jp/htmldata/S36/S36HO223.html
[8] Saitama Prefecture, Report on Seismic Damage against Scenario Earthquakes in Saitama Prefecture, http://www.pref.saitama.lg.jp/page/h19higaisoutei.html (in Japanese), cited in 2007 (in Japanese).
[9] Chiba Prefecture, Report on Seismic Damage against Scenario Earthquakes in Chiba Prefecture, https://www.pref.chiba.lg.jp/bousai/jishin/higaichousa/houkokusho.html (in Japanese) cited in 2008 (in Japanese).
[10] Kanagawa Prefecture, Report on Seismic Damage against Scenario Earthquakes in Kanagawa Prefecture, http://www.pref.kanagawa.jp/osirase/saigai/chousakekka/soutei21.htm cited in 2009 (in Japanese)
[11] Tokyo metropolitan government, Report on Seismic Damage against Scenario Earthquakes in Tokyo metropolitan, http://www.bousai.metro.tokyo.jp/japanese/tmg/research.html cited in 2006 (in Japanese)
[12] The Headquarters for Earthquake Research Promotion, National Seismic Hazard Maps for Japan, http://www.jishin.go.jp/main/index-e.html
[13] National Research Institute for Earth Science and Disaster Prevention, Japan Seismic Hazard Information Station (J-SHIS), http://www.j-shis.bosai.go.jp/?lang=en
[14] National Institute of Advanced Industrial Science and Technology, Quick Estimation System for Earthquake Maps triggered by observation records (QuiQuake), http://qq.ghz.geogrid.org/QuakeMap/index.en.html

Coherency between ground motions synthesized for analysis input of a large span structure

X. Tao[1,2], H. Liu[3], J. Lu[1], X. Sun[2] & H. Wang[1]
[1]*Institute of Engineering Mechanics, China Earthquake Administration, China*
[2]*School of Civil Engineering, Harbin Institute of Technology, China*
[3]*State Key Laboratory of Bridge Structural Dynamics, Chongqing Communication Research and Design Institute, China*

Abstract

In order to fit the requirement of non-consistent input for seismic analysis of a large span structure with multi-supports, coherency of a synthesized ground motion field is validated in this paper. The result shows that the correlation between motions close to each other on rock site is strong, the mean values of coherencies are from 0.7 to 0.8, and the maximum is up to 1.0. The coherency decreases with the distance between the motion points. Correlation between low frequency motions close to each other on soil site is very strong, the mean of coherencies is larger than 0.8. The correlation of low frequency motions decreases also with the distance. The correlation between high frequency motions (>5Hz) is weak, the coherencies corresponding to various distances are all less than 0.5, and the mean is mostly less than 0.25. The result is consistent with the conclusion from the statistics of the observed data on some dense arrays like SMART-1 during the past earthquakes.
Keywords: non-consistent input, ground motion, synthesis, coherency, multi-support.

1 Introduction

Seismic risk of a large span structure is generally evaluated from response analysis, since there are very few experiences of this kind of structure during past earthquakes. Non-consistent input for seismic analysis of a large span structure with multi-supports is emphasized in the last decades, from the spatial variation

WIT Transactions on The Built Environment, Vol 120, © 2011 WIT Press
www.witpress.com, ISSN 1743-3509 (on-line)
doi:10.2495/ERES110101

of ground motions observed at dense arrays (Berrah and Kausel [5]; Der Kiureghian and Neuenhofer [6]; Wang and Wang [26]). The simplest one is travelling wave, the waveforms are same, and the difference is just a time lag between the time histories. In order to describe the complicated nature of ground motion and reduce the risk from the input simplification, many improvements were suggested (Loh [13]; Harichandran and Vanmarke [7], Qu et al. [16]). The authors and their co-workers developed a set of approaches for synthesis for near field ground motion (Tao and Wang [21, 22]; Wang and Tao [25]; Zhang et al. [27]). It emphasized the predominant effect of source on the motion, took the no-homogeneous slip on the source rupture plane into account, the high frequency motion was randomly synthesized, the low frequency motion was calculated by means of a simplified numerical Green Function method, and the two were superposed in time domain after low and high pass filtered. For the validation of the approaches, the synthesized result was compared with some observed data during the past earthquakes. The distribution of peak values, response spectra of motions on the observation sites are quite similar, while the hanging wall effect and rupture directivity effect are described clearly (Liu et al. [12]; Sun [19]). This paper is going to validate if the approaches express the spatial structure of the real ground motion field, i.e. the spatial correlation between motions close to each other, in other words, the coherency in frequency domain. Obviously, this is very significant for the non-consistent input.

2 Synthesis of ground motion field

A hybrid source model is generated for the synthesis (Wang and TAO [23, 25]), to describe the slip distribution of on the faulting plane of the earthquake with magnitude 6.5, as shown in figure 1.

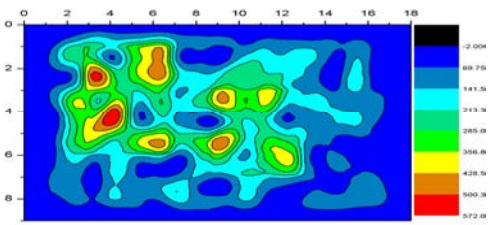

Figure 1: The adopted source model.

High frequency motion at ground surface is synthesized by a random approach (Atkinson and Silva [2]; Beresnev and Atkinson [3]). Fourier spectrum of ground motion from one sub-source is described in that approach as following (Boore [4]; Atkinson and Silva [2])

$$FA(M_0, f, R) = S\left(M_0, f\right) \cdot G(R) \cdot D(R, f) \cdot A(f) \cdot P(f) \qquad (1)$$

where S(M0, f) is source spectrum, G(R) is geometry attenuation term, D(R, f) is energy dissipation term, A(f) is near surface amplification factor, and P(f) if high frequency truncated function. A dynamic corner frequency is adopted in S(M0, f)

so that the motion amplitude at near field and the received energy at far-field don't depend on the sub-source size (Motazedian and Atkinson [15]).

The motion at that ground point can be obtained by superposition of motions from all sub-sources with time lags according to the triggering time differences and the differences of distances from the sub-sources to the point, as follows (Tao and Wang [22]).

$$a(t) = \sum_{i=1}^{N_L} \sum_{j=1}^{N_W} a_{ij}(t - \Delta t_{ij}) \tag{2}$$

where N_L, N_W are the number of the sub-sources along the strike and dip directions respectively, $a_{ij}(t)$ is the ground motion from the i, j th sub-source, Δt_{ij} is the corresponding time lag.

Low frequency ground motions are calculated by a simplified numerical Green function method where the regional media and 3D velocity structure of the crust in the volume containing the source and its surroundings are taken into account (Zhang et al. [27]). The whole region under consideration is divided into two parts, a deep homogenous zone with the source in it and a shallow inhomogeneous zone from the ground surface to bottom of the upper crust. The latter is divided further into finite element network. The displacement time history at each node on the bottom of the second part is from analytical solution of the first part. The ground motion at surface are calculated by a space-time decoupling explicit finite element analysis with a second-order local artificial transmitting boundary with displacement field input from the first step.

The wide band ground motion is superposed by corresponding high and low frequency motions in time domain at the every point filtered low and high pass respectively.

The site condition is taken into account by 1D equivalent linearization approach. In frequency domain, the ground motion at surface can be described as the multiple of the input at the bottom of soil layer and the transfer function of the soil layer.

$$A(\omega) = R(\omega) \cdot U(\omega) \tag{3}$$

where $A(\omega)$ is Fourier spectrum of motion at ground surface, $R(\omega)$ is the transfer function of soil layer, $U(\omega)$ is the spectrum of the input motion.

3 Coherency coefficients

Coherency function is considered as the best descriptor of the similarity and cross-variation between two ground motions. It is defined as following (Lu [14])

$$\gamma_{ij}(\omega) = \begin{cases} \dfrac{S_{ij}(\omega)}{\sqrt{S_{ii}(\omega) S_{jj}(\omega)}} & S_{ii}(\omega) S_{jj}(\omega) \neq 0 \\ 0 & S_{ii}(\omega) S_{jj}(\omega) = 0 \end{cases} \tag{4}$$

where $S_{ij}(\omega)$ is cross-power spectrum of motions at the i, j th points, $S_{ii}(\omega)$ and $S_{jj}(\omega)$ are the auto-power spectra of motions at the two points respectively. $|\gamma_{ij}(\omega)|$ is generally called as lag coherency, or coherency coefficient, $0 \le |\gamma_{ij}(\omega)| \le 1.0$. The bigger coherency coefficient, the stronger relativity is between the motions at the two points. When the value of the coefficient is 1.0, the motions are the same completely.

Let $a_i(t)$ and $a_j(t)$ are the acceleration time histories at the i, j th points, the coherency coefficient is calculated by the following process:

(1) To calculate the Fourier spectra $A_i(\omega)$ and $A_j(\omega)$ of $a_i(t)$ and $a_j(t)$ respectively by Fast Fourier Transfer (FFT).

(2) To calculate the corresponding cross power spectrum and auto-power spectra by

$$S_{ii}(\omega) = A_i^*(\omega)A_i(\omega) \tag{5}$$

$$S_{jj}(\omega) = A_j^*(\omega)A_j(\omega) \tag{6}$$

$$S_{ij}(\omega) = A_i^*(\omega)A_j(\omega) \tag{7}$$

where $A_i^*(\omega)$ and $A_j^*(\omega)$ represent the conjugation of $A_i(\omega)$ and $A_j(\omega)$, respectively.

(3) To smooth the spectra in frequency domain by

$$\overline{S}(\omega) = \int_{-\infty}^{+\infty} S(\Omega)w(\omega - \Omega)d\Omega \tag{8}$$

where $\overline{S}(\omega)$ represents $S_{ii}(\omega)$, $S_{jj}(\omega)$ or $S_{ij}(\omega)$ respectively, $w(\omega)$ is spectrum window that is to restrain the leak in FFT. The Parzzen window is adopted here

$$w(\omega) = \frac{3}{4}u\left(\frac{\sin\frac{u\omega}{4}}{\frac{u\omega}{4}}\right)^4 \tag{9}$$

where u is a parameter of band width of the spectrum window, it can be determined from the equivalent band width b as follows

$$u = \frac{280}{151b} \tag{10}$$

The bigger band width b is the smoother is the spectrum.

(4) To calculate the coherency by

$$|\gamma_{ij}(\omega)| = \frac{|\overline{S}_{ij}(\omega)|}{\sqrt{\overline{S}_{ii}(\omega)\overline{S}_{jj}(\omega)}} \tag{11}$$

4 Coherency between ground motions in the synthesized field

4.1 Coherency coefficient from ground motion field on rock site

A line is selected from the area of the synthesized motion field motioned in section 2 of this paper, and then a set of points with 200 meter intervals on the line are chosen. The coherencies are calculated for motions at point pairs with various distances, by means of the procedure introduced in section 3. Figure 2 shows two examples of coherencies between motions at points with distance 200m to each other on rock site.

From the figure, one can see that the coherency coefficient between motions at points with 200 meter distance on rock surface varies with frequency with a

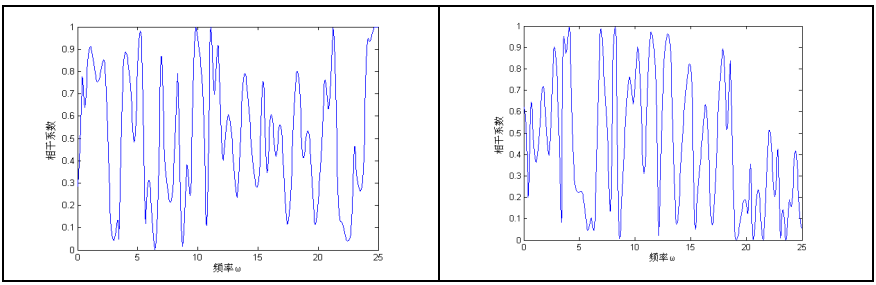

Figure 2: Two examples of coherencies between motions at points with distance 200m on rock site.

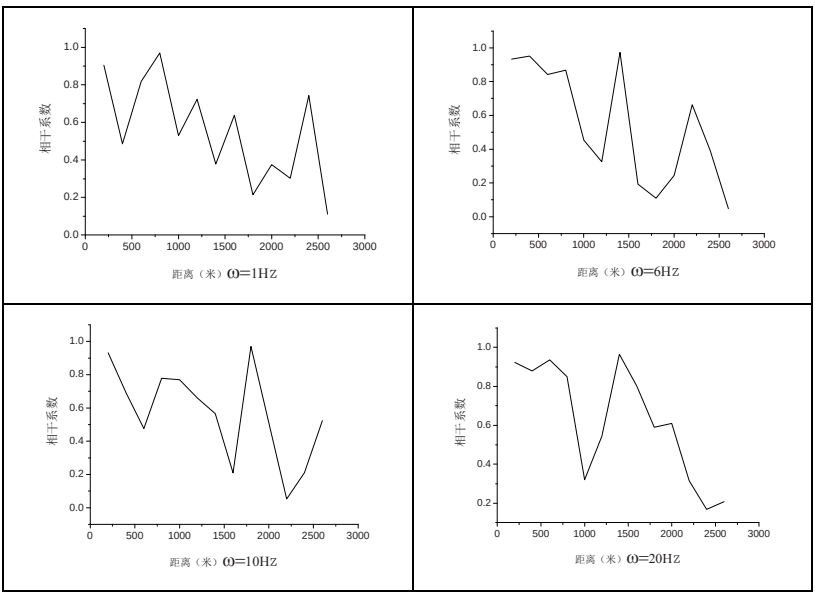

Figure 3: Variation of the coherency with distance at 4 frequencies on rock site.

fluctuation and without a certain trend, and the mean value is from 0.7 to 0.8, maximum is up to 1.0. It means the spatial correlation is strong.

Figure 3 shows the coherency coefficients between the points with distance from 200 to 2800 meters at 4 frequencies 1.0, 6.0, 10.0 and 20.0 Hz. One can see from the figure that the coefficient decreases while the distance increases. The statistic result shows that coherencies of the motions at point pairs with distance no larger than 400 meters are almost more than 0.8 and those correlations are small for distance thousand meters.

4.2 Coherency coefficient from ground motion field on soil site

Figure 4 shows two examples of coherencies between motions at points with distance 200m to each other on soil site, for North-South, East-West and Up-Down directions respectively, from up to down.

From the figure one can see that the coherency is quite strong in the range of frequency less than 5 Hz, the coefficient values are more than 0.8 in average. For the range of frequency larger than 5 Hz, coherency decreases quickly, the mean of coefficient is from 0.2 to 0.3. It means the correlation in that rage is weak.

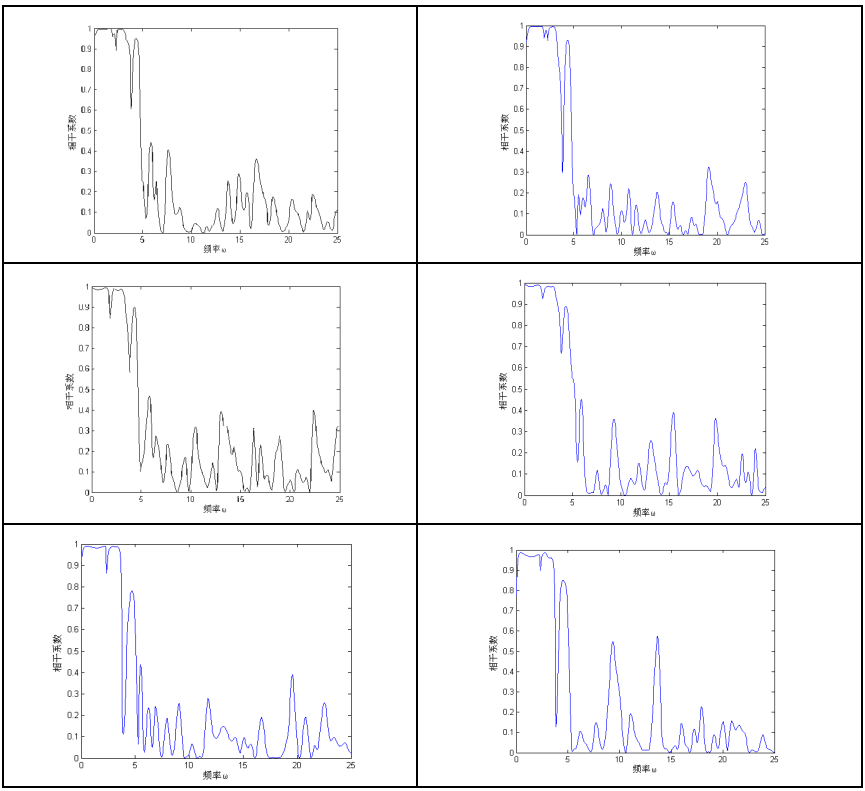

Figure 4: Two examples of coherencies between motions at points with distance 200m on soil site.

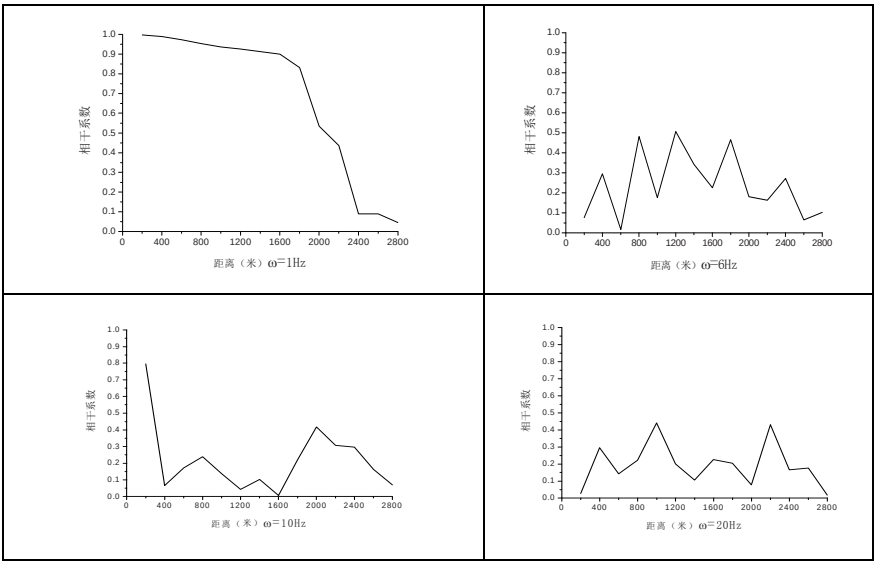

Figure 5: Variation of the coherency with distance at 4 frequencies on soil site (NS).

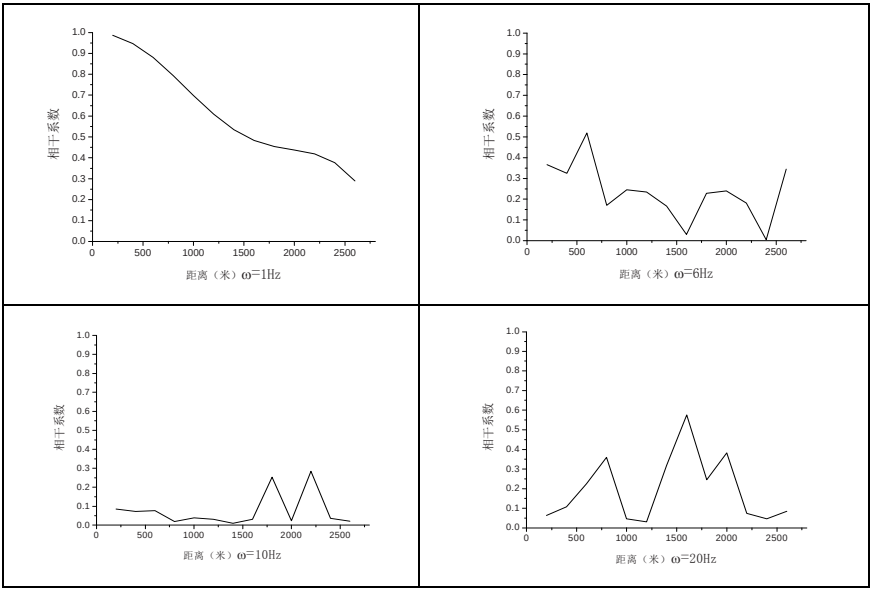

Figure 6: Variation of the coherency with distance at 4 frequencies on soil site (EW).

Figure 5, figure 6 and figure 7 show the coherency coefficients between the points with distance from 200 to 2800 meters at the 4 frequencies, for North-

South, East-West and Up-Down directions respectively, from up to down. One can see from those that the correlation is large for low frequency (1.0Hz and less) motions with distance 400 meters and less, the coefficients are all more than 0.8, and it decreases with frequency quickly. Similarly, it also decreases with distance. Coherency of high frequency motions is weak, the coefficients are all less than 0.5, and the mean values are almost less than 0.25.

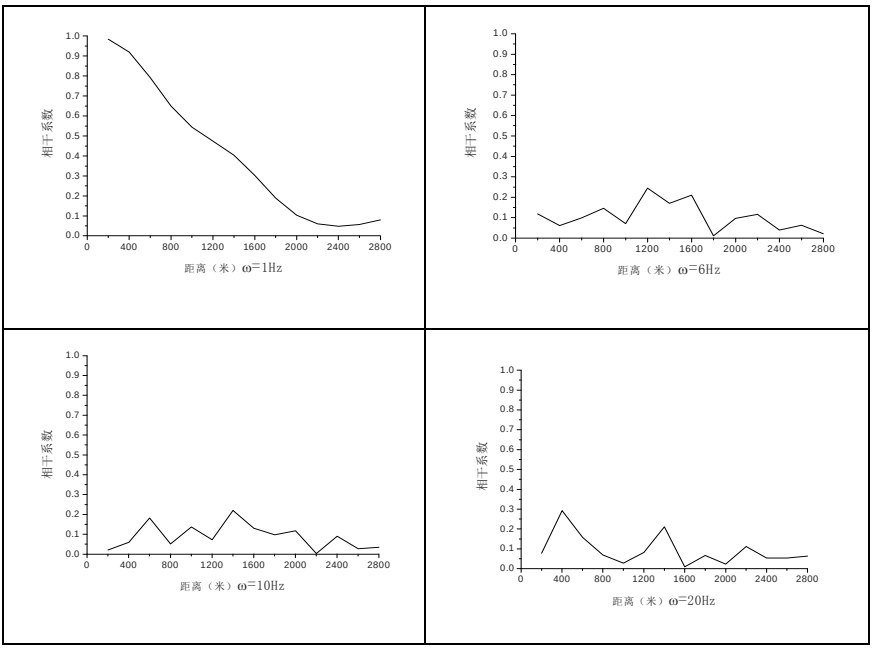

Figure 7: Variation of the coherency with distance at 4 frequencies on soil site (UD).

5 Conclusions

Spatial structure of a synthesized ground motion field is validated by means of the coherency coefficients between motion pairs with various distances. The result shows that the correlation between motions with distance 200 meters on rock site is strong, the mean values of coherencies are from 0.7 to 0.8, and the maximum is up to 1.0. There is a trend that coherency decreases with the distance, the coefficient between motions with distance 400 meters and less are almost more than 0.8 and it gets small for thousand meter distance. Correlation between low frequency motions with distance 200 meters on soil site is very strong, the mean of coherencies is larger than 0.8. The correlation of low frequency motions decreases also with the distance. The correlation between high frequency motions (>5Hz) is weak, the coherencies corresponding to various distances are all less than 0.5, and the mean is mostly less than 0.25.

The result of this paper is consistent with the conclusion from the statistics of the observed data on some dense arrays like SMART-1 during the past earthquakes, the spatial correlation of ground motions at two surface points depends on the distance and frequency components of the motions, decreases while distance increases and/or frequency is getting high (Jin and Liao [9]).

Acknowledgements

This work was supported by National Natural Science Foundation of China under Contract No. 50778058 and 90715038, and the Fund of Key Laboratory of Bridge Earthquake Resistance Technology, Ministry of Communications, P. R. C. under Contract No. 200802.

References

[1] Aki. K, An overview and issues: review of simulation procedures, Strong ground motion simulation and earthquake engineering applications, EERI, 1985

[2] Atkinson G. and W. Silva. Stochastic modeling of California ground motions. Bulletin of the Seismological Society of America, 90(2): 255-274. 2000

[3] Beresnev, I. and G. Atkinson. Source parameters of earthquakes in eastern and western North America based on finite-fault modeling. Bulletin of the Seismological Society of America, 92:695-710. 2002

[4] Boore, D. M. (1983). Stochastic simulation of high-frequency ground motions based on seismological models of the radiated spectra. Bulletin of the Seismological Society of America 73(6): 1865-1894

[5] Berrah M., Kausel E. Response spectrum analysis of structures subjected to spatially varying motions. EESD, 21(6):461-470. 1992

[6] Der Kiureghian A., Neuenhofer A. Response spectrum method for multi - support seismic excitations. EESD, 21 (8):713-740. 1992

[7] Harichandran R., E. Vanmarke. Stochastic Variation of Earthquake Ground in Space and Time. ASCE. J. EM. 112(2):154-174. 1986

[8] Irikura, K., Prediction of strong motions from future earthquakes caused by active faults-case of the Osaka basin, Proc. of 12WCEE, Auckland, 2000

[9] Jin X. and Z. Liao. Physical simulation of random field of ground motion. Earthquake engineering and engineering vibration, 14(3):11-19. 1994

[10] Kakehi, Y. and K. Irikura, Estimation of high-frequency wave radiation areas on the fault plane by the envelope inversion of acceleration seismograms, Geophys. J. Int., 125, 892-900. 1996

[11] Liu Haiming, Tao Xiaxin, Sun Xiaodan, and Li Ping. Forecast of strong ground motion field near the fault for earthquake disaster reduction in urban areas. Proc. of the 7th International Conference on Earthquake Resistant Engineering Structures, Cyprus, 2009

[12] Liu H. M., X. X. Tao, X. D. Sun, P. Li, Forecasting of the strong ground motion field in Lanzhou city and its vicinity caused by an earthquake with magnitude 6.5 on the western segment of Maxianshan-beiyuan fault, Northwestern Seismological Journal, 30(3): 227-231 (in Chinese). 2008

[13] Loh C. H., Analysis of the spatial variation of seismic waves and ground movements from SMART-1 Array data, EESD, 13(5): 561-581, 1985
[14] Lu Jianbo. Spatial correlation of synthesized ground motion field. Dissertation for Master Degree, Institute of Engineering Mechanics, 2008 (in Chinese)
[15] Motazedian D. and G. M. Atkinson. Stochastic finite-fault modeling based on a dynamic corner frequency. Bulletin of the Seismological Society of America, 95(3): 995-1010. 2005
[16] Qu Tiejun, Wang Junjie, Wang Qianxin. A practical model for the power spectrum of spatial variant ground motion. ACTA Seismologica Sinica, 18(1):55-62. 1996
[17] Somerville, P.G., R.W. Graves, Strong ground motions of the Kobe, Japan earthquake of Jan. 17, 1995, and development of a model of forward rupture directivity effects applicable in California. Proc. of the Western Regional Technica; Seminar on earthquake engineering for dams, Association of State Dam Safety Officials, Sacramento, 1996
[18] Somerville P., Seismic hazard evaluation, Proc. 12WCEE, Auckland, 2000
[19] Sun Xiaodan, Some issues on estimation of strong ground motion field. Dissertation for Doctor Degree, Harbin Institute of Technology (in Chinese), 2010
[20] Tao Xiaxin, Sun Xiaodan, Liu Haiming and Li Ping. Some issues on forecast of strong ground motion field. Proc. of the 7th International Conference on Earthquake Resistant Engineering Structures, Cyprus, 2009
[21] Tao Xiaxin and Wang Haiyun, A random source model for near filed strong ground motion prediction, Proc. of 13WCEE, Vancouver. Paper No.1945. 2004
[22] Tao Xiaxin, Wang Guoxin. Rupture directivity and hanging wall effect in near field strong ground motion simulation, ACTA Seismologica Sinica, 16(2): 205-212. 2003
[23] Wang Haiyun and Tao Xiaxin, Relationships between moment magnitude and fault parameters: theoretical and semi-empirical relations, Earthquake Engineering and Engineering Vibration, 2(2):201-211. 2003
[24] Wang Haiyun, Tao Xiaxin, Li Jie, Global source parameters of finite fault model for strong ground motion predictions, Proc. of 13WCEE, Vancouver. Paper No.2743. 2004
[25] Wang H. Y. and X. X. Tao, Charactering a shallow earthquake asperity model for predicting near field strong ground motion, Journal of Harbin Institute of Technology, 37(11): 1533-1539 (in Chinese). 2005
[26] Wang Junjie, Wang Qianxin. Response of large spam arc bridge under ground motion with spatial variation. Journal of Vibration Engineering, 8(2):119-126. 1995
[27] Zhang D. L., X. X. Tao, Z. H. Zhou, Study on Finite Fault Model for Calculation–Considering Slip-Time Function of Heterogeneous Displacement Distribution in Temporal and Spatial Domain. Northwestern Seismological Journal, 27(3):193-198 (in Chinese). 2005

Role of hysteretic damping in the earthquake response of ground

N. Yoshida
Tohoku Gakuin University, Japan

Abstract

Parametric studies are carried out to investigate the role of the hysteretic damping in earthquake response analysis. The maximum acceleration is found to have an upper bound under very large earthquakes and hysteretic damping does not affect it. On the other hand, response acceleration becomes large in the shorter period as the hysteretic damping increases. It comes because stiffness after the unloading becomes large so as to increase the hysteretic damping ratio, which is a quite different feature that viscous damping has although they are usually understood to have the same mechanical nature.
Keywords: earthquake, hysteretic damping, shear strength, upper bound acceleration.

1 Introduction

Nonlinear behaviour of soils for the earthquake response analysis of ground is usually defined by strain dependent shear modulus and damping ratio. As such, damping ratio is supposed to be an important mechanical property. It has been supposed to supress the earthquake response; earthquake motion becomes smaller as the damping ratio increases.

On the other hand, the authors showed a different point of view [1]. Maximum acceleration does not exceed the upper bound acceleration under the large ground motion. It means that damping ratio does not work so as to supress the ground acceleration at the ground surface. Instead, another aspect is found; response at high frequency is excited as the damping ratio.

In the previous study, however, only one example was shown. A series of parametric study is carried out in this paper in order to see what happens when the hysteretic damping changes.

WIT Transactions on The Built Environment, Vol 120, © 2011 WIT Press
www.witpress.com, ISSN 1743-3509 (on-line)
doi:10.2495/ERES110111

2 Constitutive models

Three stress-strain models were used in this study, which are called Hyperbolic, H-D, and H-D/w E. All models use the same hyperbolic model for the skeleton or backbone curve,

$$\tau = \frac{G_0 \gamma}{1 + \gamma / \gamma_r} \tag{1}$$

where τ and γ denote shear stress and shear strain, respectively, G_0 denotes elastic shear modulus, and γ_r denotes reference strain. The hysteresis curves are defined differently as follows

1) Hyperbolic: ordinary hyperbolic model whose hysteresis loop is developed by applying the Masing's rule to a skeleton curve.

2) H-D: damping characteristics is evaluated from the proposal by Hardin and Drnevich [2],

$$h = h_{max}\left(1 - G / G_0\right) \tag{2}$$

where G denotes shear modulus and h_{max} is maximum damping ratio. The hysteresis curve that satisfies this equation can be made by using the method proposed by the authors [3]. The hyperbolic equation same with Eq. (1) is used for the hysteresis curve in this method, but two parameters G_0 and γ_r do not have mechanical meaning because they are automatically evaluated in order to get damping ratio defined as Eq. (2).

3) H-D/w E: many constitutive models assume that stiffness at unload is same with the initial or elastic modulus, but, as shown in Figure 1, it decreases with strain amplitude as

$$\frac{G_0}{G_{max}} = \frac{1 - G_{min} / G_0}{1 + \gamma / \gamma_{r0}} + \frac{G_{min}}{G_0} \tag{3}$$

where G_{min} denotes minimum stiffness at unloading. The hysteresis curve that satisfy Eq. (3) is obtained by the previous method, but the Ramberg-Osgood model is used in order to add the new condition, Eq. (3).

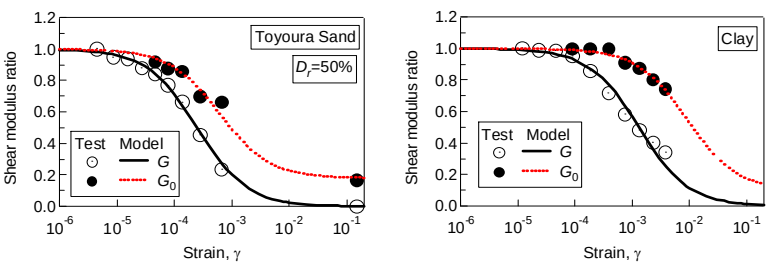

Figure 1: Shear modulus and stiffness at unloading as a function with respect to strain.

3 Brief review of previous calculation

3.1 Soil profiles and material

Soil in the Tokyo city area [4] shown in Figure 2 was analysed. Here, V_s denotes S wave velocity, ρ denotes density, c denotes cohesion, and ϕ denotes internal friction angle. Model parameters are set as in Table 1.

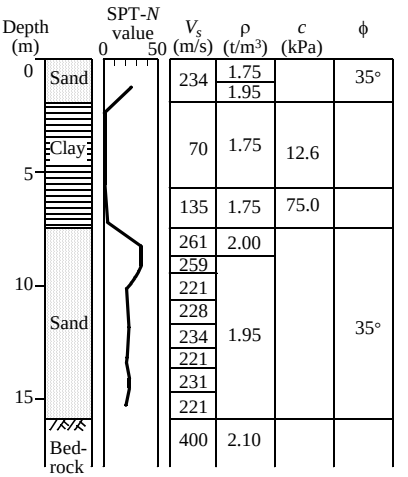

Figure 2: Soil profiles.

Table 1: Model parameters.

Material	γ_r	h_{max}	γ_{r0}	G_{min}/G_0
Sand	8.63×10^{-4}	0.22	0.002	0.4
Clay	1.42×10^{-3}	0.22	0.013	0.1

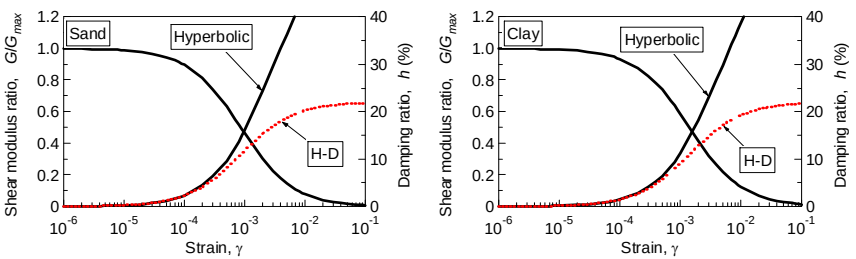

Figure 3: Dynamic deformation characteristics of sand and clay.

Cyclic deformation characteristics are shown in Figure 3. Here, both H-D and H-D/E show the same damping characteristics and, as well known, the hyperbolic model shows larger damping ratio at large strains. Stress-strain curve

is shown in Figure 4 with shear strain amplitude of 0.6 % and 4 %, respectively. Curves are quite different between the hyperbolic model and two H-D type models, but those by the two H-D type models are similar to each other.

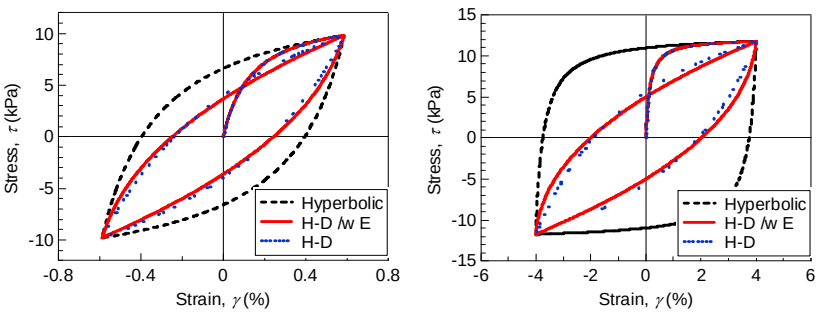

Figure 4: Stress-strain curve of clay.

3.2 Earthquake motions

Two earthquake motions are chosen among the earthquake motions shown in ref. [4]. The one has limited number of large amplitude waves and the other large number of large amplitude waves; they are called the shock wave and the vibration wave, respectively. Among them, only the result by using the shock wave is shown in this paper. Since large strain behavior is interested, the acceleration is increased so that the peak acceleration becomes 8 m/s^2 at the outcrop base layer. The waveform is shown in Figure 5.

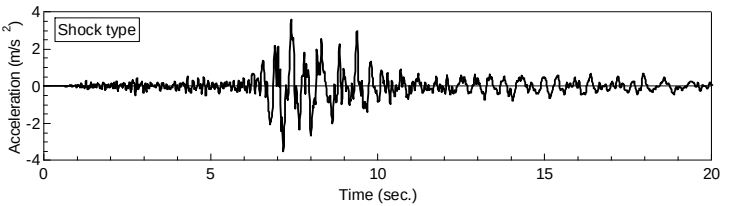

Figure 5: Earthquake motions to the engineering seismic base layer.

3.3 Response under shock wave and discussion

Maximum response is shown in Figure 6. The maximum acceleration decreases rapidly from GL-5.8 m, resulting in about 2 m/s^2 at the ground surface. Since the layer between GL-2.8 and 5.8 m (clay layer) shows large strains up to several percent, shear stress in these layer reaches nearly the shear strength, which can be confirmed through the chained line (shear strength) in Figure 6. If a layer reaches shear strength, acceleration above this layer reaches limit acceleration

α_{ult} [5] because of the equilibrium condition between the shear stress in this layer and the inertia force above this layer, as

$$\alpha_{ult} = \tau_f G / \sigma_v \tag{4}$$

where τ_f denotes shear strength of the key layer, G denotes acceleration of gravity and σ_v denotes overburden stress. Applying this equilibrium condition into the 4th layer (GL-2.8 to 3.8 m), expected upper bound acceleration becomes 2.08 m/s, which agrees with the maximum acceleration at the ground surface in Figure 6. It is emphasized that damping ratios are quite different in these three cases, but the difference cannot be seen in the maximum acceleration.

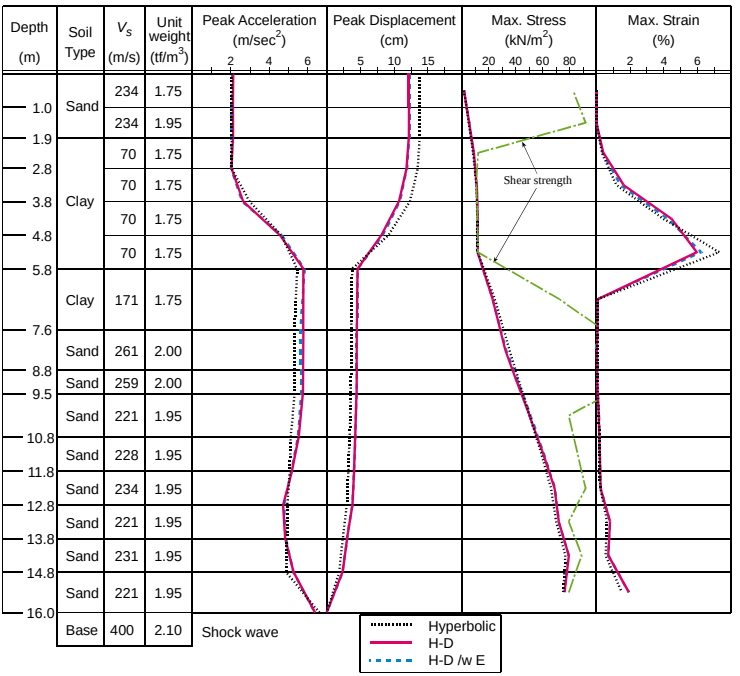

Figure 6: Maximum response under shock wave.

Response spectra are computed from the acceleration at the ground surface, which is shown in Figure 7. There is no significant difference at the period longer than about 0.5 s, but the hyperbolic model shows much larger accelerations than the other two cases in the shorter period. It is emphasized that the damping ratio is the largest in the hyperbolic model. If large damping ratio suppresses the vibration, response acceleration by the hyperbolic model must be smaller than other two cases.

It is also noted that two H-D models (H-D and H-D/ E) shows almost similar response. It indicates that stiffness at unload is not a big issue. The hysteresis loops essentially become similar shape because they are spindle shape with the same area.

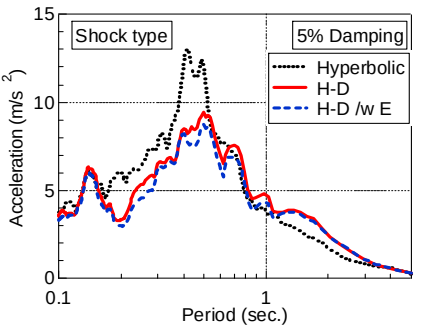

Figure 7: Response spectrum under shock wave.

The stress-strain curves at the 6th layer where shear strain becomes largest are shown in Figure 8. Apparent stiffness after the unloading seems much larger in the hyperbolic model than those in the two H-D models. As seen in Figure 4, stiffness after unloading should be kept large so as to keep large damping ratio in the hyperbolic model. On the other hand, as damping ratio is small in the two H-D models, stiffness after the unloading is smaller than that of the hyperbolic model. Therefore, apparent stiffness is larger in the hyperbolic model than in the two H-D models. This is the reason why the hyperbolic model shows larger response acceleration than the two H-D models.

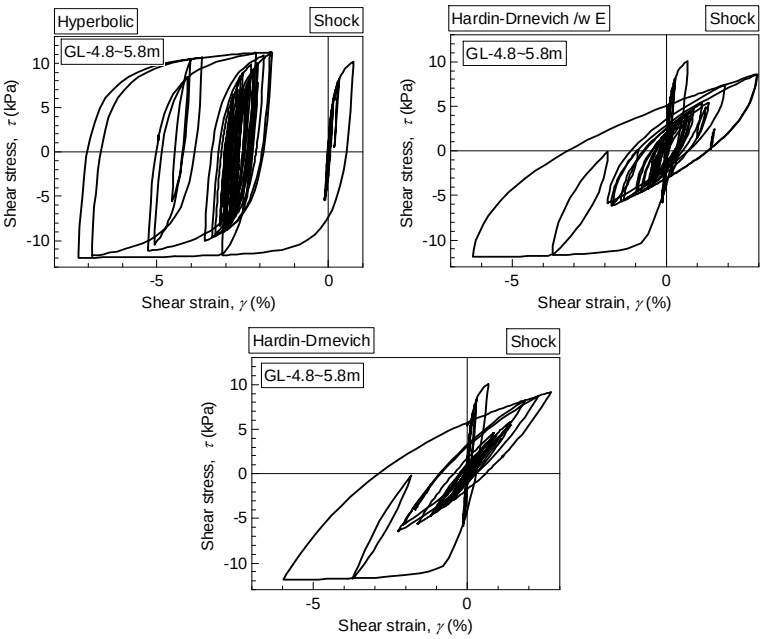

Figure 8: Stress-strain curves at 6th layer under shock wave.

Although result under shock type acceleration is introduced here, the result under the vibration type earthquake also shows similar behaviour.

4 Effect of input acceleration

If upper bound acceleration associated with the small shear strength of soil, amplification depends on the input acceleration. Then, a parametric study is carried out to see the effect of the magnitude of the input motion to the earthquake response. The same soil profile and the input earthquake motion are used in the parametric study except that the maximum damping ratio h_{max} is set 25 %. The magnitude of the input earthquake is scaled and applied. The input motion used in the previous section is used as standard value; magnification factor is the ratio from this input motion.

Figure 9 shows maximum response under the magnification factors 0.01, 0.1, 0.5, 1.0, 1.5, and 2.0. When the input acceleration is very small, maximum acceleration increases upward. As the input acceleration increases, however, it becomes constant in certain thickness. For example, maximum acceleration is nearly constant between GL and GL-3.8 m and between GL-5.8 m and 12.8 m. Just below these layers, maximum acceleration decrease rapidly. Shear strains in these layers are more than 1%, which indicates that shear stresses reach near the shear strength (see Figure 8). It means that these constant maximum accelerations are upper bound acceleration. There are two key layers defining the

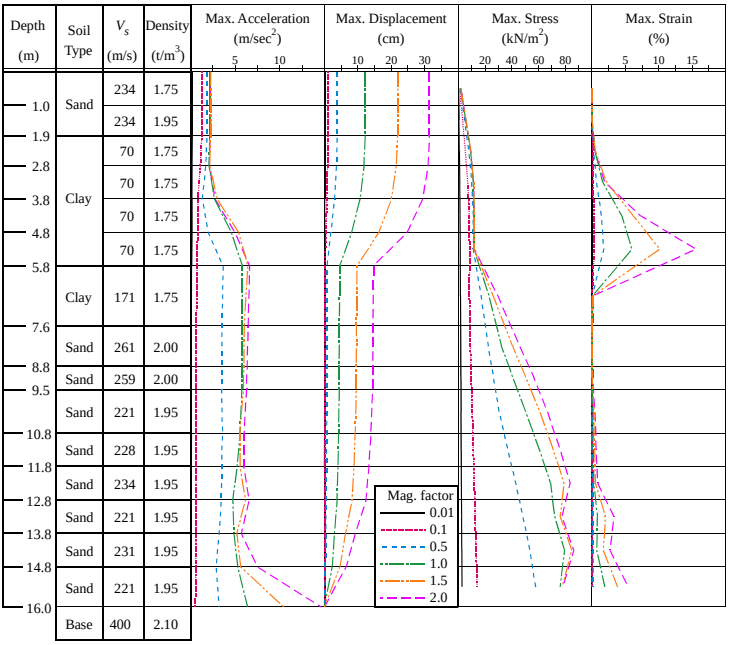

Figure 9: Maximum response.

upper bound acceleration, both of which control maximum accelerations above these layers. The shear strength of the upper layer is smaller than that of the lower layer.

Figure 10 shows change of the maximum acceleration at the ground surface when different magnitude of the earthquake works, and Figure 11 shows amplification factor (maximum acceleration at the ground surface / maximum acceleration of the input motion). Maximum acceleration increases as the input motion becomes large, but rate of the increase gradually decreases, resulting in constant maximum acceleration or upper bound acceleration. This feature is same with the one by Idriss [6] and Suetomi and Yoshida [7]. In the same manner, the amplification factor is 2.35 under the very small input or elastic response, but it decreases quickly as nonlinear behaviour becomes significant. It is noted that the upper bound acceleration depends on the shear strength of the weakest layer and its depth, relationship in Figure 10 is not a unique curve but depends on the site.

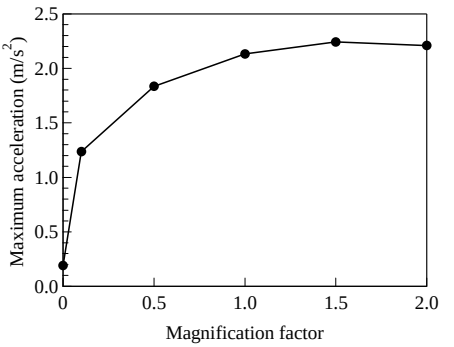

Figure 10: Maximum acceleration vs. input motion.

As described above, this behaviour is first found by Idriss [6], but the mechanism is not known at that time. Through this study, it becomes clear that it is caused because there is upper bound acceleration.

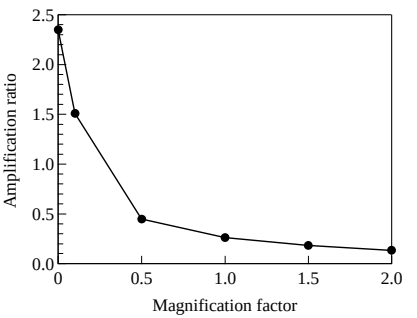

Figure 11: Amplification ratio vs. input motion.

5 Effect of hysteretic damping

The maximum damping ratio h_{max} is chosen a parameter in this section. The theoretical maximum value of h_{max} is $2/\pi$. Then h_{max} is varied from 10 % to 60 %.

Figure 12 shows maximum response. The maximum acceleration at the ground surface is nearly constant regardless of the h_{max}. Therefore, it is clear that the damping ratio does not work to suppress the earthquake motion.

Figure 13 shows maximum acceleration vs. h_{max} relationships. The maximum acceleration at the ground surface seems constant in Figure 12, but it decreases

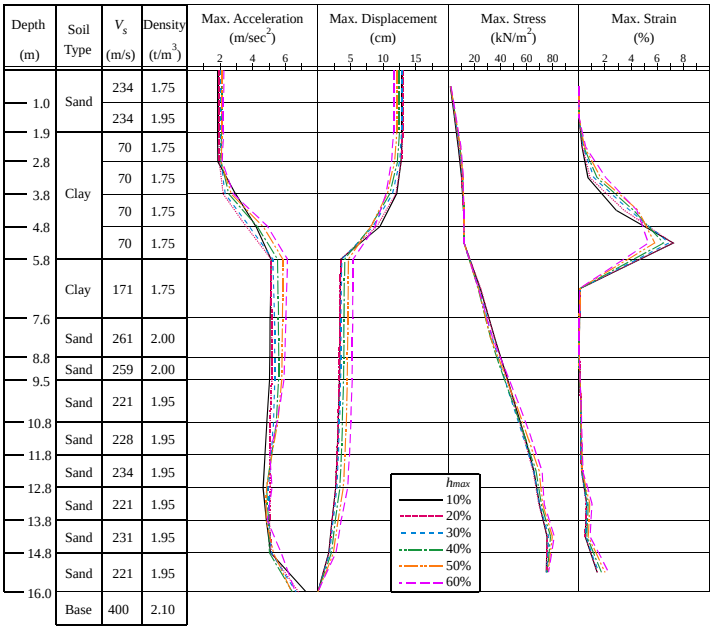

Figure 12: Maximum response.

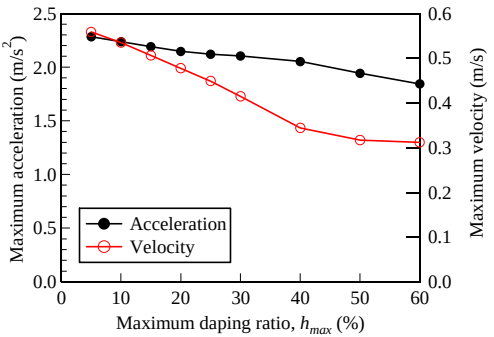

Figure 13: Maximum responses vs. maximum damping ratio.

as h_{max}. Then, it seems that h_{max} works to suppress the response of the ground. However, when looking at Figure 12 in detail, different feature can be seen.

Maximum strains below GL-2.8 m increases as h_{max} increases. In indicates that key layer that controls the upper bound acceleration goes downward. As can be seen from Eq. (4), the upper bound acceleration decreases as the depth of the key layer increases or σ_v increases.

Maximum damping ratio h_{max} is usually between 15 and 25 degrees in the actual soil. In this damping ratio, change of the maximum acceleration is not large. In this meaning, damping ratio is said not to affect the maximum acceleration at the ground surface.

Figure 14 shows acceleration response spectra under the damping ratio of 5%. The response acceleration becomes larger in shorter period as h_{max} increases. On the other hand, it becomes smaller in longer period. The boundary is around 0.5 s. It is noted that shorter period less than 0.5 s is very important period in many building or civil engineering structures. From the discussion above, it is clear that this large response acceleration occur as the stiffness after the unloading becomes larger as h_{max} increases. This is quite different feature that the word “damping” has.

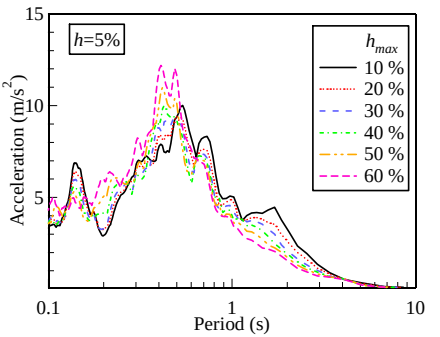

Figure 14: Acceleration response spectra.

6 Conclusion

Parametric study is carried out in order to see the mechanism how hysteretic damping works in the earthquake response of the ground. The following conclusions are obtained.

1) Large hysteretic damping does not imply small response or amplification under the large earthquake motion because maximum acceleration has upper bound associated from the failure of the weak layers.
2) Stiffness after the unloading becomes large as the damping ratio increase because area of the hysteresis loop must be large. This large stiffness excites high frequency or small period ground shaking, resulting in large response acceleration in the small period range.

The second conclusion is quite different feature that the term “damping” has. In this sense, hysteresis damping does not have the same mechanical property with the viscous damping.

References

[1] Yoshida, N. (2009): Effect of hysteretic damping and stiffness at unloading on response of ground during earthquake, Proc., 3rd Greece-Japan Workshop on seismic design, observation, retrofit of foundations, Santorini, Greece, pp. 573-583
[2] Hardin, B. O. and Drnevich, V. P. (1972): Shear modulus and damping in soils: design equations and curves, Proc. of the American Society of civil engineers, Vol. 98, No. SM7, pp. 667-692
[3] Ishihara, K., Yoshida, N. and Tsujino, S. (1985): Modelling of stress-strain relations of soils in cyclic loading, Proc. 5th International Conference for Numerical Method in Geomechanics, Nagoya, Vol. 1, pp. 373-380, 1985
[4] Sato, M., Yasuda, S., Yoshida, N. and Masuda, T. (1998): Simplified method for estimating maximum shear stress in the ground during earthquakes, Journal of Geotechnical Engineering, Proc. JSCE, No. 610/III-45, pp. 83-96 (in Japanese)
[5] Suetomi, I., Sawada, S., Yoshida, N. and Toki, K. (2000): Relation between shear strength of soil and upper limit of earthquake ground motion, Jour. of Structural Mechanics and Earthquake Engineering, Proc. JSCE, No. 654/I-52, pp. 195-206 (in Japanese)
[6] Idriss, I. M. (1990): Response of Soft Soil Sites during Earthquakes, Proceedings, H. Bolton Seed Memorial Symposium, Berkeley, California, Vol. 2, pp. 273-289
[7] Suetomi, I. and Yoshida, N. (1998): Nonlinear behavior of surface deposit during the 1995 Hyogoken-nambu earthquake, Soils and Foundations, Special Issue on Geotechnical Aspects of the January 17 1995 Hyogoken-Nambu earthquake, No. 2, pp. 11-22

This page intentionally left blank

Ground-motion simulation for the eastern province of Saudi Arabia using a stochastic model

M. S. Fnais
Geology & Geophysics Department, Faculty of Science, King Saud University, Riyadh, Saudi Arabia

Abstract

The eastern Arabian Peninsula lies close to Zagros fold-thrust fault belt that has been considered as one of the most active seismotectonic regions in the Middle East, where the occurrences of large earthquakes ($M_w \geq 5.0$) are in abundance. The southern Kuwait seismic zone is the nearest source to the study area. Hence, a wide spread damage can be expected in this region due to the presence of thick section of soft sediments. Here earthquake catalogue is compiled, reviewed precisely and compared with the international seismological data. The affected seismotectonic zones are modeled and their seismicity parameters and maximum moment magnitude are estimated. Peak Ground Acceleration values for earthquakes with magnitudes $4.0 \leq M_w \leq 7.5$ have been simulated at distances up to 300 km from the source using a stochastic model. The predicted attenuation for Peak Ground Acceleration (PGA) at bedrock is estimated as: log (PGA) = $-0.94 + 0.249\ M_w - \log r - 0.00233r + 0.19\ P$. With the help of this equation, the potential seismic hazard for the eastern part of the Arabian Peninsula can be assessed.
Keywords: ground motion simulation, stochastic, seismicity, seismotectonic zones, eastern province.

1 Introduction

The Eastern province of Saudi Arabia becomes one of the important zones throughout Saudi Arabia where important commercial and densely populated cities are located. In addition, the strategic petroleum industries are of utmost importance to national and international interest. The area has experienced (June

WIT Transactions on The Built Environment, Vol 120, © 2011 WIT Press
www.witpress.com, ISSN 1743-3509 (on-line)
doi:10.2495/ERES110121

2, 1993) an earthquake of magnitude 4.8, which occurred in the Minagish oil field (southwest of Kuwait) and was widely felt with panic in the city of Kuwait. This area was struck again by earthquakes on September 1997 (M 3.9) and December 30, 1997 (M 4.2). While in January 2002 a moderate earthquake (M 5.2) shook the Musandam Peninsula at the border between Oman and the United Arab Emirates. In November 1945, a significant earthquake of M = 8.1 originated from Makran subduction zone, (located at the southeastern end of the Arabian plate boundary) and affected the eastern province of Saudi Arabia. Convergence between the Arabian and Eurasian tectonic plates commonly originates damaging earthquakes, where the events instigated by the subduction zone are the most destructive (Kanamori [1]). This historical background reveals that a potential for wide-spread damage as a result of future destructive earthquakes cannot be noted ruled out in the tangent area.

2 Geologic setting of Eastern Saudi Arabia

A sequence of continental and shallow marine sediments extends along the Arabian Gulf with relatively low-relief terrain in which Tertiary and younger deposits cover the older units. The Upper Cretaceous and Eocene rocks represented by limestone and dolomite, while Quaternary sequences are made from sandstone, sandy marl, and sandy limestone of non-marine origin (Fig. 1).

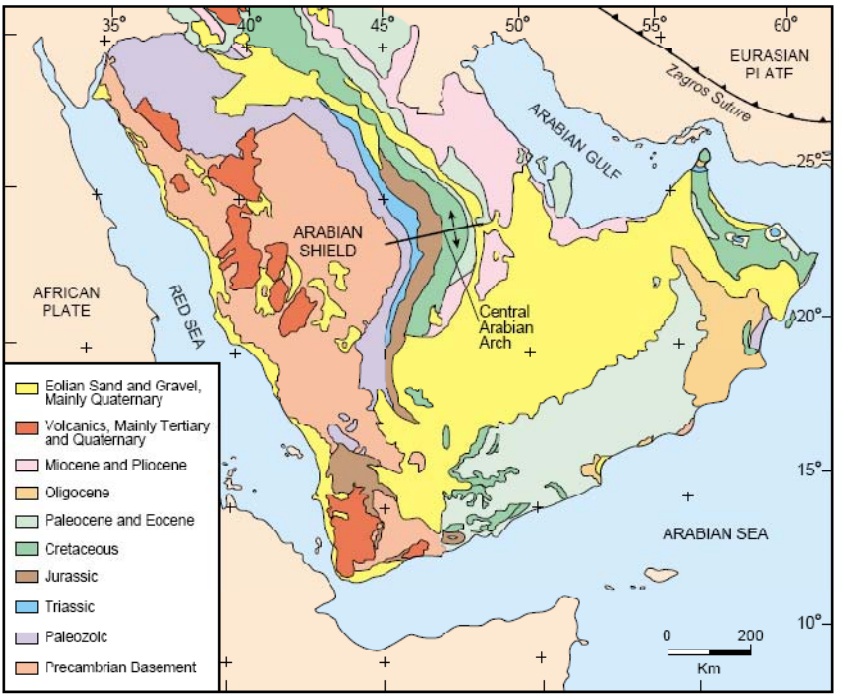

Figure 1: Generalized geology of the Arabian Peninsula (USGS [3]).

These sequences dip gently towards the east and northeast below the thrusting of the Zagros Mountains (Al-Sayari and Zoetl [2]). The Umm er Radhuma Formation of Paleocene and lower Eocene age forms a wide belt extending ~1200 km from south to north with a width of 60-120 km. The middle part of the belt is covered with eolian sand. The exposures of the Umm er Radhuma Formation forms a gently undulating but rough surface with low altitude isolated hills and benches. Outcrops of the Dammam Formation of lower and middle Eocene age are restricted to the Arabian Gulf coastal region.

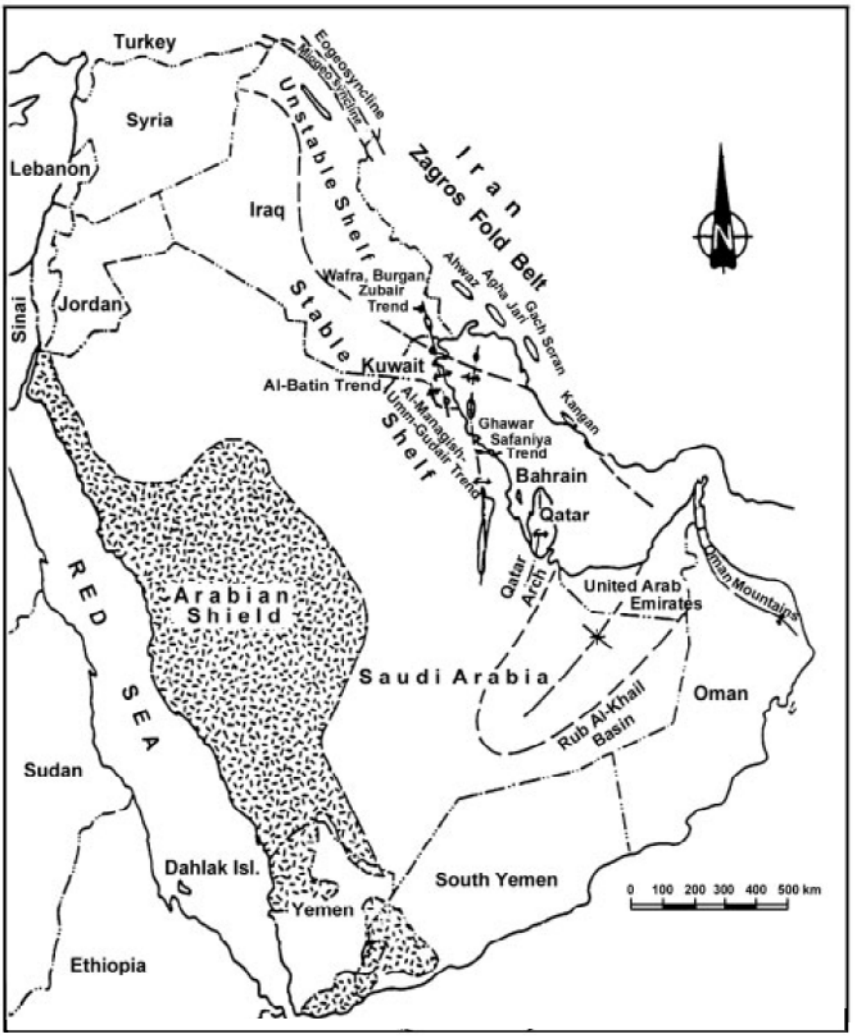

Figure 2: Major tectonic units of the Arabian Gulf Region (Clarke [4]).

Tectonics of the eastern province is dominated by a collision between the Arabian Plate and the Eurasian Plate along Zagros and Bitlis Thrust belt. Five major tectonic episodes controlled the tectonostratigraphy of the Upper Cambrian and Phanerozoic sedimentary successions in the Arabian Plate. Clarke [4] stated that number of N-S trending fault terrains, such as the Summan Platform, the Khurais-Burgan trend, the Ghawar trend and the Qatar Arch trend are distributed through the area of interest. These great anticlines are bounded by the orthogonal NE-SW trending (Wadi Batin) and NW-SE trending (Abu Jifan) strike-slip faults (Fig. 2).

3 Seismicity of Saudi Arabia

Number of low to moderate magnitude events originated from the eastern province of Saudi Arabia and the Zagros Thrust Fault belt have been recorded through the recently deployed seismic stations. Most earthquakes occurred in the crustal part of the Arabian Plate beneath the Zagros Belt. Large earthquakes (M ≥ 5) are quite common along this fault and a potential for destructive earthquakes with wide-spread damage cannot be ruled out in future. The Zagros Belt is a prolific source for number of earthquakes with magnitude (M ≥ 7) occurred in the past decades. According to Al-Shaabi [5], about 69 instrumentally recorded earthquakes (2.4 < Ml < 5.8) have been occurred during the period between 1990 and 1998, which clustered around the southeastern flank of Ghawar anticlinal structure.

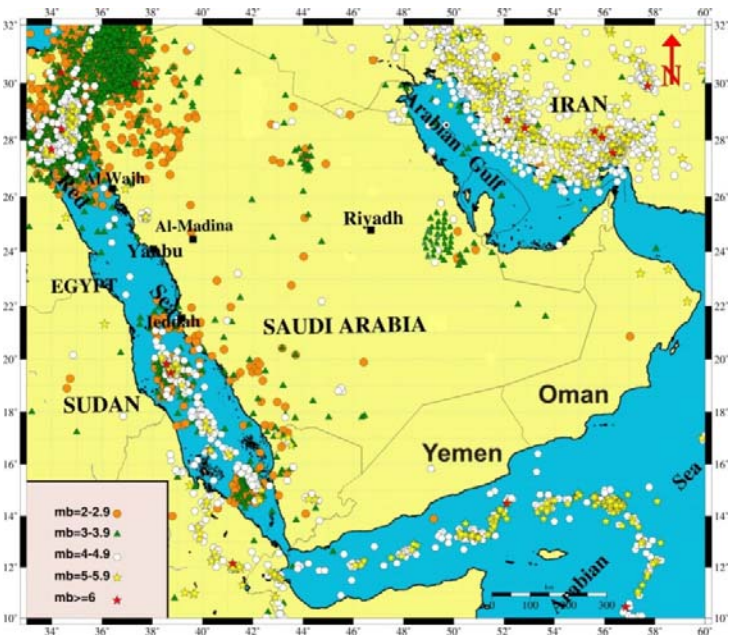

Figure 3: Seismicity map for the Arabian Peninsula (1900 up to Dec. 2010).

3.1 Earthquakes data resources

For present study, the earthquake data have been obtained from different sources, i.e., Seismic Studies Center (SSC) of King Saud University, Saudi Geological Survey (SGS); Kuwait National Seismological Network (KNSN). The collected data are merged, precisely reviewed, re-analyzed and refined from duplicated events through the International Seismological Center (ISC); United States Geological Survey (USGS); and the European Mediterranean Seismological Center (EMSC). Different magnitude scales are unified and converted into moment magnitude using Scordilis [6] relation. Finally, spatial distribution of the compiled seismicity catalogue is plotted to construct new seismicity map for the Arabian Plate and adjacent area (Fig.3). The reliability and quality of earthquake data sources have been investigated before their use for the catalogue compilation. Foreshock and aftershock sequences have been removed from the catalogue using the windowing procedure proposed by Gardner and Knopoff [7].

3.2 Identification of seismotectonic source zones

Depending on the distribution of earthquakes, geological structures and previous seismotectonic studies (Al-Amri, [8]; Tavakoli, [9] and Pascucci et al. [10]), seven of seismogenic source zones can be differentiated (Fig. 4 and table 1).

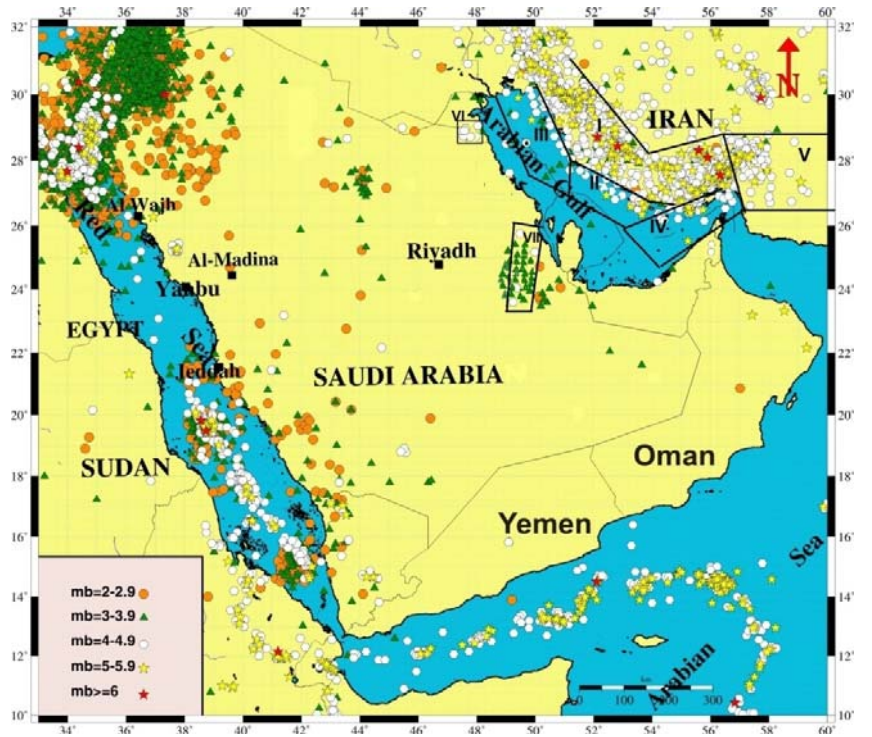

Figure 4: Seismic source zones affected the eastern province of Saudi Arabia.

Table 1: Seismtectonis source zones affecting the eastern province.

Zone	Source Zone Name	M_{max}	b-values
I	Zagros fold and thrust Belt	7.4	1.00
II	Zagros Foredeep zone	7.2	0.85
III	Zagros Mesopotamian Foredeep	6.9	0.85
IV	Dibba Fault Line zone	6.7	0.8
V	Makran subduction zone	8.5	1.00
VI	Southwestern Kuwait (Minagish-Umm Qudair) zone	6.5	0.74
VII	Al-Ghawar uplifting zone	5.5	0.63

Makran subduction zone located away of the eastern province and there is no direct damaging effects can be affected the buildings and industrial compounds in the area. Some of the identified seismic source zones described in the following paragraphs;

3.2.1 Zagros Fold and thrust zone (ZFTZ)

The Zagros mountain belt is a NW-trending fold-and-thrust belt, consisting of a 6-15-km thick sedimentary section which overlies Precambrian metamorphic basement while, the sedimentary cover can be divided into three successive sequences. The earthquake locations in this folded belt define a zone of about 200 km wide that runs parallel to its central axis. The present faulting activities beneath the Zagros fold belt as due to re-activation of pre-existing normal faults as reverse faults in the Arabian continental margin.

The historical data indicates that an earthquake of magnitude 5.7 has occurred in March 21 1875. One of earthquakes with magnitude of 5.5 occurred on Feb 4, 1934, and 3 events have magnitudes of 5.4 in 1925, 1939, and 1958 have occurred in this source zone. In 1972, a magnitude 6.1 has occurred which was followed by a magnitude 6 in 1976 over a period of 4 years. Magnitude range through this zone is seen to be frequented many times with magnitude 5 and above has been recorded. These earthquakes could indeed cause a significant ground shaking in the eastern province of Saudi Arabia. The M_{max} of this zone is 7.4.

3.2.2 Zagros foredeep zone

Zagros fold-thrust belt can be divided into three tectonic zones from NE to the SW into; Zagros fold-thrust belt, Zagros Foredeep zone and Zagros Mesopotamian Foredeep zone. The Zagros Foredeep Fault separates the alluvial basin of the Zagros Belt from the simply Folded Belt. It partly controls the morphology of the Arabian Gulf and is marked by relatively long linear anticlines. Seismically, the Foredeep fault is active but less than the Fold-thrust belt (Talebian and Jackson [11]). The foredeep Zagros system is limited to the coastal Plain and Arabian Gulf. The Coastal Plain is narrow feature that slopes gently to the south with an area of about 226.000 km^2; the Arabian Gulf is a

shallow epicontinental sea with a tectonic origin (foreland depression) which covers the Arabian shelf platform with water depths less than 100 m. The evolution of the area can be subdivided into 3 main steps; The first step is characterized by a rifted continental shelf phase (Permian and Triassic) with thick marine deposition followed by thinning due to uplift and pre-Jurassic truncation associated to drift separation of the Arabian Plate. In the second step (Jurassic to Mid Cretaceous), thin sequences of arid climates were deposited. The third step concerns the collision and Zagros orogeny; at first a regional uplift is recognized in the whole area while in the Palaeocene-Eocene the subsidence starts and the first flysch sediment are deposited in an elongate foredeep with NW/SE direction.

3.2.3 Dibba fault line zone (DFLZ)

The tectonic activities through this source zone are comes from the Dibba fault and the Hormuz salt basin south of the Arabian Gulf. This seismic source is active through both of historically and instrumentally periods. Two of earthquakes (magnitude 6.4 occurring in Jan 10, 1897 and in July 9, 1902) were documented. Furthermore, two of earthquakes with magnitude of 6.2 have also occurred in March 21, 1977 and Apr 1, 1977. It is revealed that this seismogenic source zone has earthquakes of above magnitude 6 and some seismic events above magnitude 5. The maximum earthquake of this zone is 6.7 based on the statistical analysis of the historical and instrumental data.

3.2.4 Eastern province (Al-Ghawar) zone

The Ghawar anticlinal structure has two of subparallel and north-south trending structural crests separated by a saddle with about 174 miles long and 12 miles wide. The general trend of this zone is oriented almost NNE-SSW. To the north there are N–S trending Kuwait Arch of basement horst. Al-Ghawar and Qatar arch area was subjected with some earthquakes with magnitudes greater than 5.0. Most of these seismic events are located south to southeast of the Ghawar anticlinal structure while others occurred to the west of Qatar peninsula. The most prominent joint set strikes northwest, and another set of less prominent oriented northeast. The growth of the Al-Ghawar anticlinal structure was active in the Pleistocene and Quaternary. The average growth rate, indicated by tilting of the flanks, is 0.06^{o} per one million years. The origin of these earthquakes is the extraction of oil and/or recent tectonic activities of the area.

3.2.5 Southwestern Kuwait (Minagish-Umm Qudair) zone

Recent seismicity studies for the State of Kuwait, reveals two main clusters of events. The first one is located around the Minagish-Umm Qudair oil fields in the south whereas, the second is concentrated at the Raudhatain-Sabriya oil fields in the north. The spatial distribution of earthquakes around the oil fields suggests that, these seismic events are of induced-tectonic origin. The magnitude of these earthquakes ranges from 0.3 to 4.8 and originated at depth levels ranged from 3.3 to 28 km. The maximum expected magnitude of the southwestern Kuwait zone is 6.5 (El-Enezi et al. [12, 13]).

4 Ground motion attenuation characteristics

Peak Ground Acceleration (PGA) and response spectra represent the main parameters for seismic hazard assessment and designing earthquake resistant structures. Due to the absence of strong ground motion records for the eastern province of Saudi Arabia and even for the countries of the Arabian Peninsula, the previous hazard studies in Saudi Arabia (Al-Haddad et al. [14] and Al-Amri et al. [15]); Kuwait (Sadek [16]); United Arab of Emirates (Abdalla and Al-Homoud [17, 18]) and for the Arabian Peninsula region (Peiris et al. [19]) borrowed attenuation models from abroad to calculate the ground motion parameters. This work has been oriented to have a simple approach for estimation of the ground motion attenuation relation for the considered area. This will be achieved throughout selection of an adapted seismological model for synthetic generation of PGA based on the stochastic approach taking into account the effect of probable variability in stress drop, radiation coefficient, cut-off frequency and focal depth.

4.1 Seismological model

Seismological model of Boore [20] have been applied worldwide for ground motion prediction. Fourier amplitude spectrum of ground acceleration at the bedrock is expressed as:

$$A(f) = CS(f)D(f)P(f)$$

where S(f) represents the source spectral function, D(f) is the path function characterizing the attenuation, P(f) is a filter to shape acceleration amplitudes beyond a high cut-off frequency (f_m) to correspond the particular ground motion measure of interest, and **C** is a scaling factor. The single corner frequency model of Brune [21] is used in this study in the form of;

$$S(f) = (2\pi f)^2 M_0 / \left[1 + (f / f_c)^2\right]$$

where $\mathbf{M_0}$, is the seismic moment and $\mathbf{f_c}$ is the corner frequency which can be calculated throughout the following equation;

$$f_c = 4.9 \times 10^6 V_s (\Delta\sigma / M_0)^{1/3}$$

where **Vs** is the shear wave velocity at the source region that depends on the depth of the earthquake and the used crustal structure and $\mathbf{\Delta\sigma}$ is the stress drop. The diminution function D(f) of Boore [20] can be defined as:

$$D(f) = G \exp\left[-\pi f R / V_s Q(f)\right]$$

where **G** represents the geometric attenuation while, the other term expresses anelastic attenuation and **Q** is the quality factor of the region. The high-cut filter in the seismological model is given by:

$$P(f, f_m) = \left[1 + (f / f_m)^8\right]^{-1/2}$$

where $\mathbf{f_m}$ controls the high frequency fall of the spectrum. The scaling factor **C** can be estimated as;

$$C = R_{\theta\varphi} KF / \left(4\pi\rho V_s^{\,3}\right)$$

where $\mathbf{R_{\theta\varphi}}$ is the average radiation coefficient for range of azimuths and take-off angles, **K** is a factor for the partition onto two horizontal components, **F** is the free surface effect for the shear wave, **ρ** is the density at the source. The three segments geometrical spreading operator of Atkinson and Boore [22] has been used in this study. The geometrical attenuation term **G** for the eastern province is taken to be equal to R−1 for R<70 km and equal to R0.0 for distances from 70 to 130 km. The simulation procedure consists of three steps. First, a Gaussian stationary random process sample of strong ground motion duration that can be simulated as;

$$T = 1/\, f_c + 0.05R$$

Second, the sample is windowed by multiplying it with the modulating function of and is Fourier transformed into frequency domain. The Fourier amplitude spectrum is normalized by the square root of the mean square amplitude spectrum and multiplied by the target spectrum A(f) that was derived from the seismological model. Third, the transformed amplitude back into the time domain to generate a sample of acceleration time history.

4.2 Ground motion attenuation model

The attenuation model is generally expressed as a mathematical function connecting the strong ground motion to parameters characterizing the earthquake source, propagation medium, and local site response. The model should be simple as the available data and usually do not warrant excessive statistical analysis. Number of attenuation models is used for predicting strong ground motion in terms of magnitude, distance, and local site geology. The proposed model of Joyner and Boore [23] has been selected for this study where, the basic form of this model can be expressed as:

$$\log(A) = \alpha + \beta M - \log R + bR + P\sigma$$

where A represents the peak ground acceleration in gal (cm/s^2); M is the earthquake magnitude; R is the distance; and α, β, and b are the model parameters. σ is the standard deviation of log (A). The factor P is a dummy variable that represents the normal distribution: a value of P =0 implies mean (50-percentile) values of PGA, while the value of P =1 implies mean plus one standard deviation (84-percentile) values. The above-mentioned equation is a linear function of magnitude and of distance dependent terms. The first term represents the geometric losses, and it is constrained to spherical spreading from a point source while the second term accounts for anelastic losses. Joyner and

Boore [23] performed the regression analyses on the attenuation model in two stages; the first regression is on distance as:

$$\log(A) = \sum_{i=1}^{n} a_i E_i - \log R + br$$

where $E_i = 1$ for earthquake I and 0 otherwise.

A is the peak horizontal acceleration, n is the number of earthquakes included in the data set; d is the closest distance between the recording site and the surface projection of the fault rupture and values of α_i and b are determined by linear regression with average depth. Once the α_i values are determined, they are used to calculate the first order polynomial regression representing the magnitude dependence. The second regression is then performed to determine the magnitude dependence:

$$a_i = \alpha + \beta M_i$$

The employing of dummy variable E_i has the advantage that it decouples the determination of magnitude dependence from the determination of distance dependence.

Through this work, the essential model parameters of stress drop, focal depth, corner frequency (f_m), and the radiation coefficient are treated as random variables but were distributed uniformly around the mean value. The stress drop is taken to vary between 20 and 60 bars. The average focal depth for the affected zones (Zagros Foredeep, Zagros Mesopotamian Foredeep seismic source zones) has been estimated to be 25 km while, the focal depth of southwestern Kuwait seismic source (the closest seismic source to the eastern province of Saudi Arabia) ranges from 3.3 to 28 km. Accordingly, the used focal depth through this study is taken as a uniform random variable in the range of 3.0–28 km. The cut-off frequency is taken in the interval 20–30 Hz. The range of the S-wave radiation coefficient is taken as 0.48–0.64 (Boore and Boatwright [24]). Q value has been calculated by Mokhtar et al. [25] for the eastern part of the Arabian platform.

PGA values for the eastern province of Saudi Arabia are simulated for moment magnitudes ranging from 4.0 to 6.5 with 0.5 magnitude unit increments (Fig. 5). The upper bound of magnitude range is selected to be 6.5 representing the maximum magnitude that can be produced from southern Kuwait seismogenic source. The distance is varied from 0 to 300 km (at 18 values of fault distances ranging from 1 to 300 km as follows: 1, 2, 5, 10, 15, 20, 30, 40, 50, 60, 70, 80, 100, 120, 150, 200, 250 and 300 km) representing the shortest distance between the projection of the rupture and the site of interest. The parameters of the attenuation equation for bed rock as follows;

$$\log (A) = -0.94 + 0.249\ M - \log r - 0.00233r + 0.19\ P$$

The local geology and topography effects control the distribution of damages due to strong earthquakes. The amplification of earthquake ground motion by local site conditions must be estimated in areas characterized by soft sediments.

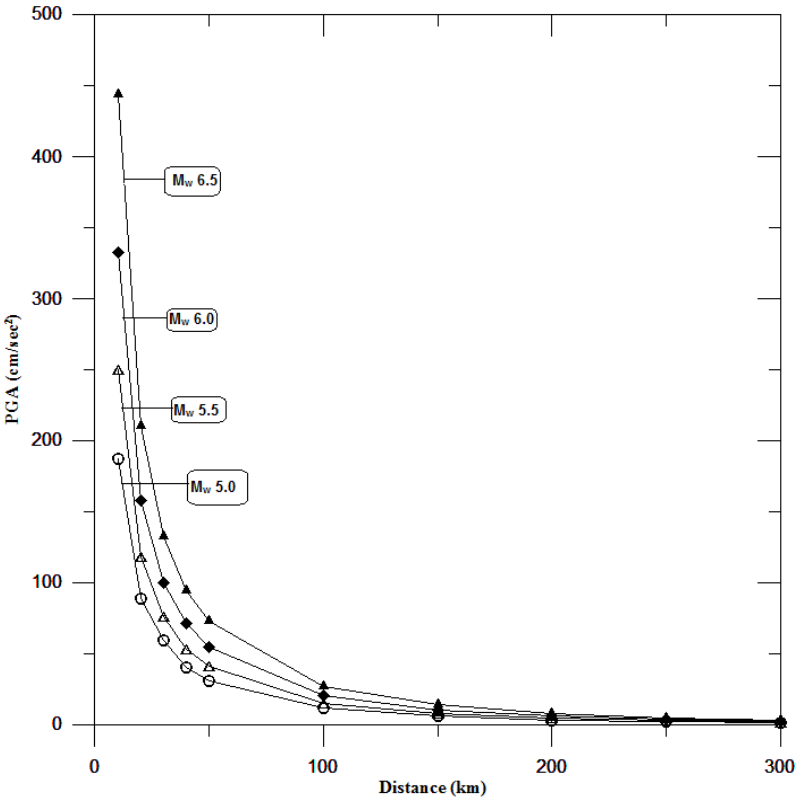

Figure 5: The estimated PGA through the eastern province of Saudi Arabia.

5 Conclusions

Eastern province of Saudi Arabia attracted the attention recently of multinational companies working in the development of petroleum industries however number of earthquake prone zones surrounded the area. Hence, there is a wide-spread potentiality of seismic hazard due to these earthquakes are expected. Accordingly, the estimation of ground motion attenuation relation that represents the essential element to quantify the seismic hazard for the considered area is of national importance. The present study acts as step through the national plan aims to sustain development through all ways of life. The results of this work must be taken into consideration through the National building Code committee and following-up of implementation of these results are highly recommended.

References

[1] Kanamori, H. (1986): Rupture process of subduction-zone earthquakes. Ann. Rev. Earth. Planet. Sci., 14, pp. 293-322.

[2] Al-Sayari, S. S. & Zoetl, J. G. (eds) (1978): Quaternary Period in Saudi Arabia. Sedimentological, Hydrogeological Hydrochemical, Geomorphologicaland Climatological Investigations in Central and Eastern Saudi Arabia. Springer-Verlag, Vienna.
[3] United States Geological Survey (USGS) (1963): Geologic Map of the Arabian Peninsula (Scale 1:2,000,000) and Geologic Quadrangle Maps (Scale 1:500,000).
[4] Clarke, H. W. M. (1988): Stratigraphy and rock unit nomenclature in the oil-producing area of interior Oman. Journal of Petroleum Geology, II(1): 5-60.
[5] Al-Shaabi, S. F. (2004): Induced seismicity at Ghawar hydrocarbon reservoir, eastern Saudi Arabia. Annals Geol. Surv. Egypt, V. XXVII, pp. 335-342.
[6] Scordilis, E.M. (2006): Empirical global relations converting M_s and M_b to moment magnitude. Journal of Seismology, 19, 225-236.
[7] Gardner, J.K. and Knopoff, L. (1974): Is the sequence of earthquake in Southern California, with aftershocks removed, Poissonian? Bull. Seism. Soc. Am., 64: 1363-1367.
[8] Al-Amri, A. M. (2004): Seismic zones in the Arabian Peninsula. Seismic Studies Center, King Saud University, Riyadh, Saudi Arabia, p.215
[9] Tavakoli, B. (1996): Major Seismotectonic Provinces of Iran. International Institute of Earthquake Engineering and Seismology, Internal Document, Tehran, Iran.
[10] Pascucci, V., Free, M.W., and Lubkowski, Z.A. (2008): Seismic hazard and seismic design requirements for the Arabian Peninsula. The 14th World Conference on earthquake engineering, October 12-17, Beijing, China.
[11] Talebian, M.; Jackson, G. (2004): A reappraisal of earthquake Focal mechanisms and active shortening in Zagros mountain of Iran. Geophys. J. Int., 156, 506-526.
[12] Al-Enezi, A., Abdul Fatah and Safak E. (2005): Assessment of the seismic hazard for the state of Kuwait. Abstracts of the Gulf Seismic Forum, UAE University, Al-Ain, U. A. E.
[13] El-Enezi, A., Petrat, L., and Abdel-Fattah, R. (2008): Induced seismicity and surface deformation within Kuwait's oil fields. 2nd IASME/WSEAS International conference on geology and seismology (GES'08), Cambridge, UK, February 23-25.
[14] Al-Haddad, M. Siddiqi, G. H., Al-Zaid, R., Arafa, A., Necioglu, A., and Turkelli, N. (1994): A basis for evaluation of seismic hazard and design criteria for Saudi Arabia. Earthquake Spectra 10 (2), 231-258
[15] Al-Amri, A., Rodgers, A., and Al-khalifah, T. (2008): Improving the Level of Seismic Hazard Parameter in Saudi Arabia Using Earthquake Location. Arabian J. of Geosciences, 1, DOI 10.1007/s12517-008-0001-5, 1-15.
[16] Sadek, A. W. (2004): Seismic map for the state of Kuwait. Emirates Journal for Engineering Research, 9 (2), pp. 53-58.

[17] Abdalla, J.A & A.S. Al-Homoud (2004a): Seismic hazard assessment of United Arab Emirates and its surroundings. Journal of Earthquake Engineering, Vol. 8, No. 6, 817-837.
[18] Abdalla, J.A. and Al-Homoud, A. (2004b): Earthquake hazard zonation of eastern Arabia. Proceedings of the 13th World Conference on Earthquake Engineering, Vancouver, Canada, August 1-6, 2004, Paper No. 1008.
[19] Peiris, N.; Free, M.; Lubkowski; Z. and Hussein, A.T. (2006): Seismic hazard and seismic design requirements for the Arabian Gulf region. Proceedings of the 1st European Conference on Earthquake Engineering and Seismology, Geneva, September 2006, Paper No. 1121.
[20] Boore, D.M. (2003): Simulation of ground motion using the stochastic method. Pure & Appl. Geophys., 160:635-675.
[21] Brune, J. (1970): Tectonic stress and the spectra of seismic shear waves from earthquakes. J Geophys Res 75:4997-5009.
[22] Atkinson G.M., Boore D.M. (1995): Ground-motion relations for eastern North America. Bull Seism Soc Am 85:17-30.
[23] Joyner, W.B. and Boore, D.M. (1981): Peak horizontal acceleration and velocity from strong motion records including records from the 1979, Imperial valley, California earthquake. Bull Seism Soc Am 71:2011-2038.
[24] Boore, D.M. and Boatwright, J. (1984): Average body-wave radiation coefficients. Bull Seism Soc Am 74:1615-1621.
[25] Mokhtar, T. A., C. J. Ammon, R. B. Herrman, and H. A. A. Ghalib (2001): Surface-wave velocities across Arabia, Pure Appl. Geophys., 158, 1425-1444.

This page intentionally left blank

Section 4
Soil structure interaction

This page intentionally left blank

Nonlinear vibrations of piles in viscoelastic foundations

E. J. Sapountzakis & A. E. Kampitsis
School of Civil Engineering,
National Technical University of Athens, Greece

Abstract

In this paper, a boundary element method is developed for the nonlinear dynamic analysis of piles of arbitrary doubly symmetric simply or multiply connected constant cross section, partially embedded in viscoelastic foundations, undergoing moderate large deflections under general boundary conditions, taking into account the effects of shear deformation and rotary inertia. The pile is subjected to the combined action of arbitrarily distributed or concentrated transverse loading and bending moments in both directions as well as to axial loading. To account for shear deformations, the concept of shear deformation coefficients is used. Five boundary value problems are formulated with respect to the transverse displacements, to the axial displacement and to two stress functions and solved using the Analog Equation Method, a BEM based method. Application of the boundary element technique yields a nonlinear coupled system of equations of motion. The solution of this system is accomplished iteratively by employing the average acceleration method in combination with the modified Newton Raphson method. The evaluation of the shear deformation coefficients is accomplished from the aforementioned stress functions using only boundary integration. The proposed model takes into account the coupling effects of bending and shear deformations along the member as well as the shear forces along the span induced by the applied axial loading. Numerical examples are worked out to illustrate the efficiency, wherever possible the accuracy and the range of applications of the developed method.
Keywords: piles, nonlinear vibrations, large deflections, Timoshenko beam, shear deformation coefficients, boundary element method, viscoelastic foundation.


WIT Transactions on The Built Environment, Vol 120, © 2011 WIT Press
www.witpress.com, ISSN 1743-3509 (on-line)
doi:10.2495/ERES110131

1 Introduction

Many problems related to soil-structure interaction can be modelled by means of a beam or a beam-column on an elastic foundation. Practical examples of these are railroad tracks, highway pavements, continuously supported pipelines, and strip foundations. Moreover, piles are frequently employed for the foundation of structures such as buildings, quay walls, bridges and offshore structures. These piles, which are subjected to lateral forces that result from loading on supported structures, during earthquake excitation, develop a nonlinear dynamic response. Thus, the study of nonlinear effects on the dynamic analysis of structural elements is essential in civil engineering applications, wherein weight saving is of paramount importance. This non-linearity results from retaining the square of the slope in the strain–displacement relations (intermediate non-linear theory), avoiding in this way the inaccuracies arising from a linearized second-order analysis. Thus, the aforementioned study takes into account the influence of the action of axial, lateral forces and end moments on the deformed shape of the structural element. Moreover, due to the intensive use of materials having relatively high transverse shear modulus and the need for beam members with high natural frequencies the error incurred from the ignorance of the effect of shear deformation may be substantial, particularly in the case of heavy lateral loading. The Timoshenko-Rayleigh beam theory, which includes shear deformation and rotary inertia effects has an extended range of applications as it allows treatment of deep beam (depth is large relative to length), short and thin-webbed beams and beams where higher modes are excited.

When the beam-column deflections of the structure are small, a wide range of linear analysis tools, such as modal analysis, can be used, and some analytical results are possible. During the past few years, the linear dynamic analysis of beams on elastic foundation has received a good amount of attention in the literature with pioneer the work of Hetenyi [1] who studied the elementary Bernoulli-Euler beams on elastic Winkler foundation. Rades [2] presented the steady-state response of a finite rigid beam resting on a foundation defined by one inertial and three elastic parameters in the assumption of a permanent and smooth contact between beam and foundation considering only uncoupled modes. Wang and Stephens [3] studied the natural vibrations of a Timoshenko beam on a Pasternak-type foundation showing the effects of rotary inertia, shear deformation and foundation constants of the beam employing general analytic solutions for simple cases of boundary conditions. De Rosa [4] and El-Mously [5] derived explicit formulae for the fundamental natural frequencies of finite Timoshenko-beams mounted on finite Pasternak foundation.

Moreover, El Naggar and Novak [6] studied the lateral response of singe piles and pile groups accounting the nonlinear behaviour of the soil adjacent to the pile and discontinuity conditions at the pile-soil interface. Padron et. al. [7] studied a BEM–FEM coupling model for the time harmonic dynamic analysis of piles and pile groups embedded in an elastic half-space where piles are modelled using finite elements as a beam according to the Bernoulli hypothesis, while the soil is modelled using boundary elements as a continuum, semi-infinite,

isotropic, homogeneous or zoned homogeneous, linear, viscoelastic medium. Hu et al. [8] presented the nonlinear partial differential equation governing the nonlinear transverse vibration of pile under the assumption that both the materials of the pile and the soil obey nonlinear elastic and linear viscoelastic constitutive relations while the frequency and the response of the system have been obtained by the complex mode method and the method of multiple time scales.

As the deflections become larger, the induced geometric nonlinearities result in effects that are not observed in linear systems. Contrary to the good amount of attention in the literature concerning the linear dynamic analysis of beam-columns supported on elastic foundation, little work has been done on the corresponding nonlinear problem, such as the nonlinear free vibration analysis of multispan beams on elastic supports presented by Lewandowski [9], employing the dynamic finite element method, neglecting the horizontally and rotary inertia forces and considering the beams as distributed mass systems.

In this paper, a boundary element method is developed for the nonlinear dynamic analysis of piles of arbitrary doubly symmetric simply or multiply connected constant cross section, partially embedded in viscoelastic foundation, undergoing moderate large deflections under general boundary conditions, taking into account the effects of shear deformation and rotary inertia. The pile is subjected to the combined action of arbitrarily distributed or concentrated transverse loading and bending moments in both directions as well as to axial loading. To account for shear deformations, the concept of shear deformation coefficients is used. Five boundary value problems are formulated with respect to the transverse displacements, to the axial displacement and to two stress functions and solved using the Analog Equation Method [10], a BEM based method. Application of the boundary element technique yields a nonlinear coupled system of equations of motion. The solution of this system is accomplished iteratively by employing the average acceleration method in combination with the modified Newton Raphson method [11, 12]. The evaluation of the shear deformation coefficients is accomplished from the aforementioned stress functions using only boundary integration. The essential features and novel aspects of the present formulation compared with previous ones are summarized as follows.

i. Shear deformation effect and rotary inertia are taken into account on the nonlinear dynamic analysis of piles subjected to arbitrary loading (distributed or concentrated transverse loading and bending moments in both directions, as well as axial loading).
ii. The homogeneous linear half-space is approximated by a viscoelastic foundation.
iii. The pile is supported by the most general nonlinear boundary conditions including elastic support or restrain, while its cross section is an arbitrary doubly symmetric one.
iv. The proposed model takes into account the coupling effects of bending and shear deformations along the member as well as shear forces along the span induced by the applied axial loading.

v. The shear deformation coefficients are evaluated using an energy approach, instead of Timoshenko and Goodier's [13] and Cowper's [14].
vi. The effect of the material's Poisson ratio v is taken into account.
vii. The proposed method employs a BEM approach (requiring boundary discretization) resulting in line or parabolic elements instead of area elements of the FEM solutions (requiring the whole cross section to be discretized into triangular or quadrilateral area elements), while a small number of line elements are required to achieve high accuracy.

2 Statement of the problem

Let us consider a prismatic pile of length l, of constant arbitrary doubly symmetric cross-section of area A. The homogeneous isotropic and linearly elastic material of the pile cross-section, with modulus of elasticity E, shear modulus G and Poisson's ratio v occupies the two dimensional multiply connected region Ω of the y,z plane and is bounded by the $\Gamma_j\left(j=1,2,...,K\right)$ boundary curves, which are piecewise smooth, i.e. they may have a finite number of corners. Consider Cyz to be the principal bending coordinate system through the cross section's centroid. The pile is partially embedded in a homogeneous viscoelastic soil. The foundation model is characterized by the Winkler moduli k_y, k_z and the damping coefficients c_y, c_z corresponding to the directions *y*, *z* respectively. Thus, the foundation reaction is written as

$$p_{sy}\left(x,t\right)=k_y v\left(x,t\right)+c_y\frac{\partial v\left(x,t\right)}{\partial t} \tag{1}$$

$$p_{sz}\left(x,t\right)=k_z w\left(x,t\right)+c_z\frac{\partial w\left(x,t\right)}{\partial t} \tag{2}$$

The pile is subjected to the combined action of the arbitrarily distributed or concentrated time dependent axial loading $p_x=p_x\left(x,t\right)$, transverse loading $p_y=p_y\left(x,t\right)$, $p_z=p_z\left(x,t\right)$ acting in the y, z directions, respectively and bending moments $m_y=m_y\left(x,t\right)$, $m_z=m_z\left(x,t\right)$ along y, z axes, respectively.

Under the action of the aforementioned loading, the displacement field of the pile taking into account shear deformation effect is given as

$$\bar{u}\left(x,y,z,t\right)=u\left(x,t\right)-y\theta_z\left(x,t\right)+z\theta_y\left(x,t\right) \tag{3}$$

$$\bar{v}\left(x,t\right)=v\left(x,t\right) \tag{4}$$

$$\bar{w}\left(x,t\right)=w\left(x,t\right) \tag{5}$$

where $\bar{u}$, $\bar{v}$, $\bar{w}$ are the axial and transverse pile displacement components with respect to the Cyz system of axes; $u\left(x,t\right)$, $v\left(x,t\right)$, $w\left(x,t\right)$ are the

corresponding components of the centroid C and $\theta_y(x,t)$, $\theta_z(x,t)$ are the angles of rotation due to bending of the cross-section with respect to its centroid.

Employing the strain-displacement relations of the three-dimensional elasticity for moderate displacements, the following strain components can be easily obtained

$$\varepsilon_{xx} = \frac{\partial \overline{u}}{\partial x} + \frac{1}{2}\left[\left(\frac{\partial \overline{v}}{\partial x}\right)^2 + \left(\frac{\partial \overline{w}}{\partial x}\right)^2\right] \tag{6}$$

$$\gamma_{xz} = \frac{\partial \overline{w}}{\partial x} + \frac{\partial \overline{u}}{\partial z} + \left(\frac{\partial \overline{v}}{\partial x}\frac{\partial \overline{v}}{\partial z} + \frac{\partial \overline{w}}{\partial x}\frac{\partial \overline{w}}{\partial z}\right) \tag{7}$$

$$\gamma_{xy} = \frac{\partial \overline{v}}{\partial x} + \frac{\partial \overline{u}}{\partial y} + \left(\frac{\partial \overline{v}}{\partial x}\frac{\partial \overline{v}}{\partial y} + \frac{\partial \overline{w}}{\partial x}\frac{\partial \overline{w}}{\partial y}\right) \tag{8}$$

$$\varepsilon_{yy} = \varepsilon_{zz} = \gamma_{yz} = 0 \tag{9}$$

where it has been assumed that for moderate displacements $\left(\partial \overline{u}/\partial x\right)^2 << \partial \overline{u}/\partial x$, $\left(\partial \overline{u}/\partial x\right)\left(\partial \overline{u}/\partial z\right) << \left(\partial \overline{u}/\partial x\right) + \left(\partial \overline{u}/\partial z\right)$, $\left(\partial \overline{u}/\partial x\right)\left(\partial \overline{u}/\partial y\right) << \left(\partial \overline{u}/\partial x\right) + \left(\partial \overline{u}/\partial y\right)$. Substituting the displacement components to the strain-displacement relations, the strain components can be written as

$$\varepsilon_{xx}(x,y,z,t) = u' + z\theta_y{}' - y\theta_z{}' + \frac{1}{2}\left(v'^2 + w'^2\right) \tag{10}$$

$$\gamma_{xy} = v' - \theta_z \tag{11}$$

$$\gamma_{xz} = w' + \theta_y \tag{12}$$

where γ_{xy}, γ_{xz} are the additional angles of rotation of the cross-section due to shear deformation .

Considering strains to be small, employing the second Piola – Kirchhoff stress tensor and assuming an isotropic and homogeneous material, the stress components are defined in terms of the displacement ones as

$$S_{xx} = E\left[u' + z\theta_y{}' - y\theta_z{}' + \frac{1}{2}\left(v'^2 + w'^2\right)\right] \tag{13}$$

$$S_{xy} = G\cdot\left(v' - \theta_z\right) \tag{14}$$

$$S_{xz} = G\cdot\left(w' + \theta_y\right) \tag{15}$$

On the basis of Hamilton's principle, the variations of the Lagrangian equation defined as

$$\delta\int_{t_1}^{t_2}\left(U - K - W_{ext}\right)dt = 0 \tag{16}$$

and expressed as a function of the stress resultants acting on the cross section of the pile in the deformed state provide the governing equations and the boundary conditions of the pile subjected to nonlinear vibrations. In eqn. (16), $\delta(\cdot)$ denotes variation of quantities while U, K, W_{ext} are the strain energy, the kinetic energy and the external load work. Moreover, the stress resultants of the pile using the expressions of the stress components are given as

$$N = EA\left[u' + \frac{1}{2}\left(v'^2 + w'^2\right)\right] \tag{17}$$

$$M_y = EI_y\theta_y' \tag{18}$$

$$M_z = EI_z\theta_z' \tag{19}$$

$$Q_y = GA_y\gamma_{xy} \tag{20}$$

$$Q_z = GA_z\gamma_{xz} \tag{21}$$

where A is the cross section area, I_y, I_z the moments of inertia with respect to the principle bending axes and GA_y, GA_z are its shear rigidities of the Timoshenko's beam theory, where

$$A_z = \kappa_z A = \frac{1}{a_z}A \qquad A_y = \kappa_y A = \frac{1}{a_y}A \tag{22}$$

are the shear areas with respect to y, z axes, respectively with κ_y, κ_z the shear correction factors and a_y, a_z the shear deformation coefficients. Substituting the stress components and the strain resultants to the strain energy variation and employing eqn. (16), the equilibrium equations of the pile are derived as

$$-EA\left(u'' + w'w'' + v'v''\right) + \rho A\ddot{u} = p_x \tag{23}$$

$$\begin{aligned} &EI_z v'''' + \rho A\ddot{v} + p_{sy} + \frac{EI_z}{GA_y}\left(\left(Nv'\right)'' - \rho A\frac{\partial^2\ddot{v}}{\partial x^2} - p_{sy}'' + p_y''\right) - \left(Nv'\right)' \\ &-\rho I_z\frac{\partial^2\ddot{v}}{\partial x^2} - \frac{\rho I_z}{GA_y}\left(\frac{\partial^2\left(Nv'\right)'}{\partial t^2} - \rho A\ddot{v}'' - \ddot{p}_{sy} + \ddot{p}_y\right) = p_y - m_z' \end{aligned} \tag{24}$$

$$\begin{aligned} &EI_y w'''' + \rho A\ddot{w} + p_{sz} + \frac{EI_y}{GA_z}\left(\left(Nw'\right)'' - \rho A\frac{\partial^2\ddot{w}}{\partial x^2} - p_{sz}'' + p_z''\right) - \left(Nw'\right)' \\ &-\rho I_z\frac{\partial^2\ddot{w}}{\partial x^2} - \frac{\rho I_y}{GA_z}\left(\frac{\partial^2\left(Nw'\right)'}{\partial t^2} - \rho A\ddot{w}'' - \ddot{p}_{sz} + \ddot{p}_z\right) = p_z + m_y' \end{aligned} \tag{25}$$

Eqns. (23)-(25) constitute the governing differential equations of a Timoshenko-Rayleigh pile, partially embedded in viscoelastic foundation, subjected to nonlinear vibrations due to the combined action of time dependent axial and transverse loading. These equations are also subjected to the pertinent boundary conditions of the problem, which are given as

$$a_1 u(x,t) + \alpha_2 N(x,t) = \alpha_3 \tag{26}$$

$$\beta_1 v(x,t) + \beta_2 V_y(x,t) = \beta_3 \qquad \bar{\beta}_1 \theta_z(x,t) + \bar{\beta}_2 M_z(x,t) = \bar{\beta}_3 \tag{27}$$

$$\gamma_1 w(x,t) + \gamma_2 V_z(x,t) = \gamma_3 \qquad \bar{\gamma}_1 \theta_y(x,t) + \bar{\gamma}_2 M_y(x,t) = \bar{\gamma}_3 \tag{28}$$

at the pile ends $x = 0,l$, together with the initial conditions

$$u(x,0) = \bar{u}_0(x) \qquad \dot{u}(x,0) = \dot{\bar{u}}_0(x) \tag{29}$$

$$v(x,0) = \bar{v}_0(x) \qquad \dot{v}(x,0) = \dot{\bar{v}}_0(x) \tag{30}$$

$$w(x,0) = \bar{w}_0(x) \qquad \dot{w}(x,0) = \dot{\bar{w}}_0(x) \tag{31}$$

where $\bar{u}_0(x), \bar{v}_0(x), \bar{w}_0(x), \dot{\bar{u}}_0(x), \dot{\bar{v}}_0(x)$ and $\dot{\bar{w}}_0(x)$ are prescribed functions. In eqns. (27), (28) V_y, V_z, M_z, M_y and θ_y, θ_z are the reactions, the bending moments and the angles of rotation due to bending with respect to *y*, *z*, respectively.

Finally, $\alpha_k, \beta_k, \bar{\beta}_k, \gamma_k, \bar{\gamma}_k$ ($k = 1,2,3$) are functions specified at the pile ends $x = 0,l$. Eqs. (26)-(28) describe the most general nonlinear boundary conditions associated with the problem at hand and can include elastic support or restraint. It is apparent that all types of the conventional boundary conditions (clamped, simply supported, free or guided edge) can be derived from these equations by specifying appropriately these functions (e.g. for a clamped edge it is $\alpha_2 = \alpha_3 = \beta_2 = \beta_3 = \gamma_2 = \gamma_3 = \bar{\beta}_2 = \bar{\beta}_3 = \bar{\gamma}_2 = \bar{\gamma}_3 = 0$, $\alpha_1 = \beta_1 = \gamma_1 = 1$, $\bar{\beta}_1 = \bar{\gamma}_1 = 1$).

The solution of the initial boundary value problem given from eqns. (23)-(25), subjected to the boundary conditions (26)-(28) and the initial conditions (29)-(31) which represents the nonlinear flexural dynamic analysis of a Timoshenko-Rayleigh pile, partially embedded in viscoelastic foundation, presumes the evaluation of the shear deformation coefficients a_y, a_z, corresponding to the principal coordinate system *Cyz*. These coefficients are established equating the approximate formula of the shear strain energy per unit

length [15] $U_{appr.}=\dfrac{a_y Q_y^2}{2AG}+\dfrac{a_z Q_z^2}{2AG}$ with the exact one given from $U_{exact}=\int_{\Omega}\dfrac{(\tau_{xz})^2+(\tau_{xy})^2}{2G}d\Omega$ and are obtained as [16]

$$a_y=\frac{1}{\kappa_y}=\frac{A}{\Delta^2}\int_{\Omega}\left[(\nabla\Theta)-\boldsymbol{e}\right]\cdot\left[(\nabla\Theta)-\boldsymbol{e}\right]d\Omega \tag{32}$$

$$a_z=\frac{1}{\kappa_z}=\frac{A}{\Delta^2}\int_{\Omega}\left[(\nabla\Phi)-\boldsymbol{d}\right]\cdot\left[(\nabla\Phi)-\boldsymbol{d}\right]d\Omega \tag{33}$$

where $(\tau_{xz})_j,(\tau_{xy})_j$ are the transverse (direct) shear stress components, $(\nabla)\equiv\boldsymbol{i_y}(\partial/\partial y)+\boldsymbol{i_z}(\partial/\partial z)$ is a symbolic vector with $\boldsymbol{i_y},\boldsymbol{i_z}$ the unit vectors along y and z axes, respectively. Moreover, $\Delta=2(1+\nu)I_yI_z$ where ν is the Poisson ratio of the cross section material, $\boldsymbol{e}=\left(\nu I_y\dfrac{y^2-z^2}{2}\right)\boldsymbol{i_y}+\nu I_y yz\boldsymbol{i_z}$ and $\boldsymbol{d}=\nu I_z yz\boldsymbol{i_y}-\left(\nu I_z\dfrac{y^2-z^2}{2}\right)\boldsymbol{i_z}$ while $\Theta(y,z)$ and $\Phi(y,z)$ are stress functions which are evaluated from the solution of the following Neumann type boundary value problems [16]

$$\nabla^2\Theta=-2I_y y \quad \text{in } \Omega \tag{34}$$

$$\frac{\partial\Theta}{\partial n}=\boldsymbol{n}\cdot\boldsymbol{e} \text{ on } \Gamma=\bigcup_{j=1}^{K+1}\Gamma_j \tag{35}$$

$$\nabla^2\Phi=-2I_z z \quad \text{in } \Omega \tag{36}$$

$$\frac{\partial\Phi}{\partial n}=\boldsymbol{n}\cdot\boldsymbol{d} \text{ on } \Gamma=\bigcup_{j=1}^{K+1}\Gamma_j \tag{37}$$

where $\boldsymbol{n}$ is the outward normal vector to the boundary Γ. In the case of negligible shear deformations $a_z=a_y=0$. It is also worth here noting that the boundary conditions (37), (39) have been derived from the physical consideration that the traction vector in the direction of the normal vector $\boldsymbol{n}$ vanishes on the free surface of the pile.

3 Integral representations – numerical solution

According to the precedent analysis, the nonlinear flexural dynamic analysis of Timoshenko-Rayleigh pile, partially embedded in viscoelastic foundation, undergoing moderate large deflections reduces in establishing the displacement components $u(x,t)$ and $v(x,t)$, $w(x,t)$ having continuous derivatives up to the second order and up to the fourth order with respect to x, respectively, and also having derivatives up to the second order with respect to *t* (ignoring the inertia terms of the fourth order [17]). These displacement components must satisfy the coupled governing differential eqns. (23)-(25) inside the pile, the boundary conditions (26)-(28) at the pile ends $x = 0,l$ and the initial conditions (29)-(31). Eqns. (23)-(25) are solved using the Analog Equation Method [10] as it is developed for hyperbolic differential equations [18].

4 Numerical examples

On the basis of the analytical and numerical procedures presented, a computer program has been written and a representative example has been studied to demonstrate the efficiency of the developed method. In this example, the results have been obtained using $L = 41$ nodal points along the pile and a time step of $\Delta t = 1.0\ \mu sec$.

4.1 Example

A partially embedded pile of total length $l = 10m$ ($l_{free} = 3.0m$, $l_{embed} = 7m$), of circular cross section of diameter $D = 0.5m$ ($E = 29GPa$, $v = 0.2$, $A = 0.196m^2$, $I_y = I_z = 3.066 \cdot 10^{-3} m^4$) is studied. The foundation model is characterized by the Winkler modulus $k = 17.4MN/m^2$ and the damping coefficient $c = 12kNs/m^2$. According to its boundary conditions, the embedded pile end is free, while the other end is free according to its displacements and blocked according to its rotations. The pile is subjected to a concentrated compressive axial load $P_x(0,t) = 1500kN$, $(t \geq 0.0)$ and to a concentrated transverse force $P_z(0,t) = 1000kN$, $(t \geq 0.0)$ acting at its top.

In fig. 1 the time histories of the head displacement $w_{top}(0,t)$ of the pile embedded in a viscoelastic foundation are presented taking into account the rotary inertia and the shear deformation effect, for two values of the damping coefficient ($c = 0kNs/m^2$, $c = 12kNs/m^2$) and performing either a linear or a nonlinear analysis. Moreover, in table 1 the maximum values of the head displacement $(w_{top})_{max}$ and the periods T_z of the first-cycle of motion are presented for the aforementioned viscous cases of analysis.

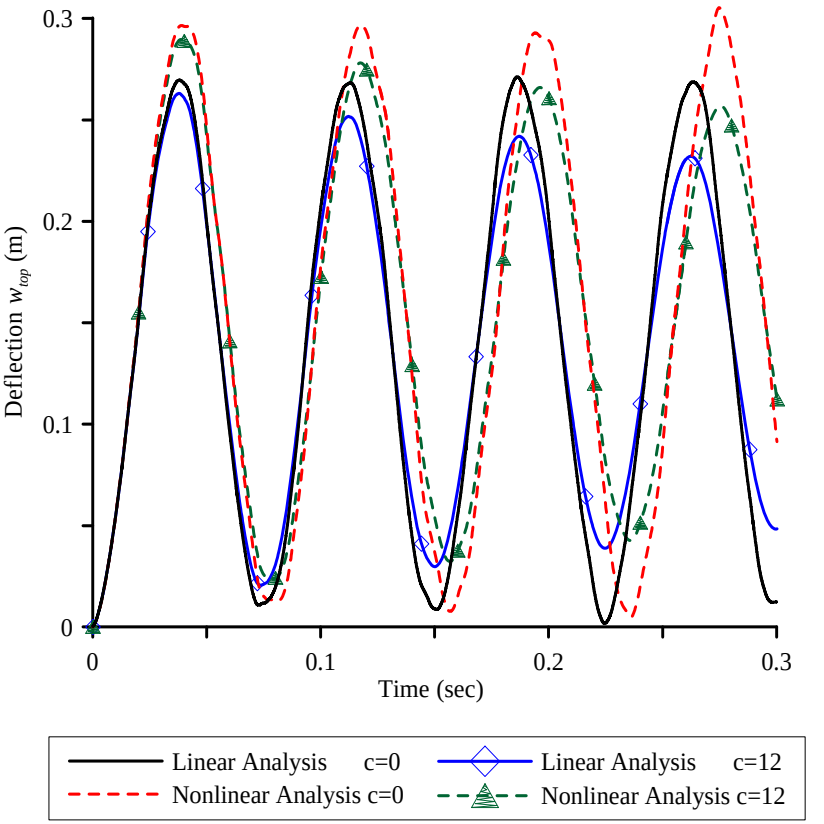

Figure 1: Time history of the transverse displacement $w_{top}(0,t)$ of the pile head.

Table 1: Maximum head displacement $\left(w_{top} \times 10^{-2} m\right)_{max}$ and period $T_z\left(10^{-2} sec\right)$ of the first cycle of motion of the pile.

Nonlinear Analysis		Linear Analysis	
$\left(w_{top}\right)_{max}$	T_z	$\left(w_{top}\right)_{max}$	T_z
29.662	8.10	26.956	7.28

Finally, in order to demonstrate the coupling effect of the transverse displacements in both directions in the nonlinear analysis, as a variant of the above application, the examined pile additionally to the already described

loading is also subjected to a concentrated transverse force $P_y(0,t) = 2000kN$, acting also at its top. In table 2 the maximum values of the head transverse displacements $(w_{top})_{max}$, $(v_{top})_{max}$ are presented performing either a linear or a nonlinear analysis. The difference in the elements of the first columns of tables 1, 2 is due to the coupling effect of the transverse displacements.

Table 2: Maximum head transverse displacements $(w_{top})_{max}$, $(v_{top})_{max}$ $(\times 10^{-2})m$ of the pile.

Nonlinear Analysis		Linear Analysis	
$(w_{top})_{max}$	$(v_{top})_{max}$	$(w_{top})_{max}$	$(v_{top})_{max}$
29.671	59.343	26.956	53.912

5 Concluding remarks

The main conclusions that can be drawn from this investigation are

a. The numerical technique presented in this investigation is well suited for computer aided analysis for piles of arbitrary simply or multiply connected doubly symmetric cross section.
b. The proposed method is developed for general dynamic analysis, while the pile is subjected to the most general boundary conditions and is embedded in viscoelastic foundation.
c. In some cases, the effect of shear deformation is significant, increasing the transverse displacements and decreasing the bending moments in both linear and nonlinear analysis.
d. The discrepancy between the results of the linear and the nonlinear analysis is remarkable.
e. The damping coefficient is of paramount importance for piles in viscoelastic foundations, as it reduces the vibration amplitude and the consequences of the dynamic response.

Acknowledgements

The work of this paper was conducted from the “DARE” project, financially supported by a European Research Council (ERC) Advanced Grant under the “Ideas” Programme in Support of Frontier Research [Grant Agreement 228254].

References

[1] Hetenyi, M., Beams and plates on elastic foundations and related problems, *Applied Mechanics Reviews*, **19**, pp. 95-102, 1966.

[2] Rades, M., Dynamic analysis of an inertial foundation model, *International Journal Solids Structures*, **8**, pp. 1353-1372, 1972.

[3] Wang, T.M. & Stephens, J. E., Natural frequencies of Timoshenko beams on Pasternak foundation. *Journal of Sound and Vibration*, **51**(2), pp. 149-155, 1977.

[4] De Rosa, M.A., Free vibrations of Timoshenko beams on two-parameter elastic foundation, *Computers & Structures*, **57**(1). pp. 151-156, 1995.

[5] El-Mously, M., Fundamental frequencies of Timoshenko beams mounted on Pasternak foundation, *Journal of Sound and Vibration*, **228**(2), pp. 452-457, 1999.

[6] El Naggar, M.H. & Novak, M., Nonlinear analysis for dynamic lateral pile response, *Soil Dynamics and Earthquake Engineering*, **15**, pp. 233-244, 1996.

[7] Padron, L.A., Aznarez, J.J. & Maeso, O., BEM-FEM coupling model for the dynamic analysis of piles and pile groups, *Engineering Analysis with Boundary Elements*, **31**, pp. 473-484, 2007.

[8] Hu, C.L., Cheng, C.J. &Chen, Z.X., Nonlinear transverse free vibrations of piles, *Journal of Sound and Vibration*, **317**, pp. 937-954, 2008.

[9] Lewandowski, R., Nonlinear free vibrations of multispan beams on elastic supports, Computers & Structures, 32(2), pp. 305-312, 1989.

[10] Katsikadelis, J.T., The analog equation method. A boundary-only integral equation method for nonlinear static and dynamic problems in general bodies, Theoretical and Applied Mechanics, 27, pp. 13-38, 2002.

[11] Chang, S. Y. Studies of Newmark method for solving nonlinear systems: (I) basic analysis, *Journal of the Chinese Institute of Engineers*, 27(5), pp. 651-662, 2004.

[12] Isaacson, E. & Keller, H.B., *Analysis of Numerical Methods*, John Wiley and Sons: New York: 1966.

[13] Timoshenko, S.P. & Goodier, J.N., *Theory of Elasticity*, 3rd edn: McGraw-Hill: New York, 1984.

[14] Cowper, G.R., the shear coefficient in Timoshenko's beam theory. *Journal of Applied Mechanics*, ASME, **33**(2), pp. 335-340, 1966.

[15] Stephen, N.G., Timoshenko's shear coefficient from a beam subjected to gravity loading, *ASME Journal of Applied Mechanics*, **47**, pp. 121–127, 1980.

[16] Sapountzakis, E.J. & Mokos, V.G., A BEM solution to transverse shear loading of beams, *Computational Mechanics*, **36**, pp. 384-397, 2005.

[17] Thomson, W. T., *Theory of vibration with applications*, Englewood Cliffs Prentice Hall, 1981.

[18] Sapountzakis E.J. & Katsikadelis J.T., Elastic deformation of ribbed plates under static, transverse and inplane loading, *Computers and Structures*, **74**, pp. 571-581, 2000.

Evaluation of response characteristics of buried pipelines during earthquakes

K. Fuchida
Department of Architecture & Civil Engineering,
Kumamoto National College of Technology, Kunamoto, Japan

Abstract

This paper presents an evaluating method for seismic behaviour of pipelines during earthquakes and studies the response characteristics of them for various conditions of ground displacements and pipelines. The proposed method consists of mainly two analytical methods which are the seismic response analysis of surface ground layers and the pseudo static response analysis of buried pipelines. The seismic response analysis method for surface ground layers is 2-dimensional effective stress analysis based on Biot's two phase mixture theory and Iai's constitutive equation. The pipeline analysis is based on a beam theory on an elastic foundation and modified transfer matrix method. Numerical computations are performed for various models with changing conditions of ground and pipes. As a result, axial and lateral response characteristics of pipelines are shown and evaluated by relating with earthquakes, grounds and pipelines conditions.
Keywords: response analysis, buried pipeline, surface layers, modified transfer matrix method.

1 Introduction

Severe damages of lifeline systems during earthquakes much affect the social activity and urban life of citizens. It is very important that aseismic investment for lifeline systems is performed in view of fast recovery of economical and social works in urban area after earthquakes.

This research aims to propose an evaluating method for seismic responses of buried pipelines and study the response characteristics of buried pipelines which are subjected to various seismic ground displacements with many conditions of pipelines and joints during earthquakes.

WIT Transactions on The Built Environment, Vol 120, © 2011 WIT Press
www.witpress.com, ISSN 1743-3509 (on-line)
doi:10.2495/ERES110141

The proposed method consists of two analytical methods. Firstly the responses of surface ground layers, in which a weak pipeline is buried, are investigated. Then detailed responses of pipelines are evaluated based on input soil displacements which are determined by referring to above responses of surface ground layers. The proposed method is briefly introduced as follows and some investigated examples of analyses are shown here.

2 Evaluation method for pipeline responses

The evaluating method for buried pipeline responses during earthquakes consists of two main analytical methods. The first method is the seismic response analysis for the surface ground layers. The analysis is performed by the existing computer program which is the effective stress analysis program "NUW2" [1–3]. The program "NUW2" is based on Biot's two phase mixture theory and Iai's constitutive equation [4]. The second method is the pseudo static response analysis for the buried pipeline. This method is based on the beam theory on an elastic foundation and modified transfer matrix method [5, 6]. The flow of this synthetic method is shown in Figure 1.

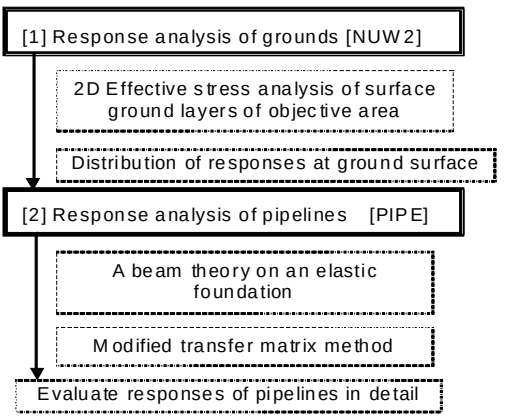

Figure 1: Flow of the evaluating method.

2.1 Seismic response analysis for surface ground layers

The analytical method for response of surface ground layers used in this study adopts the two-dimensional dynamic equilibrium equations for the soil-water phase and generalized Darcy law for the pore water based on Biot's two-phase mixture theory as in references [1–3]. To treat non-linearity (liquefaction) of the soil in the near field, the constitutive model for the plain condition is introduced. This constitutive model is constructed based on the 2-D strain-space multimechanism model for cyclic mobility of sandy soil first proposed by Iai *et al*. [4]. For the far field condition, the absorbing boundary condition is prepared.

Above dynamic equilibrium equations are formulated to the finite element equation by considering the irreducible weak Galerkin formulation. The matrix form of finite element equation for a saturated porous medium with compressible pore water including the absorbing boundary condition may be written as:

$$\begin{pmatrix} m_{uu} & m_{uw} \\ m_{uw}^T & m_{ww} \end{pmatrix} \begin{Bmatrix} \ddot{\bar{u}} \\ \ddot{\bar{w}} \end{Bmatrix} + \begin{pmatrix} 0 & 0 \\ 0 & c_{ww} \end{pmatrix} \begin{Bmatrix} \dot{\bar{u}} \\ \dot{\bar{w}} \end{Bmatrix} + \begin{pmatrix} K_{uu} & K_{uw} \\ K_{uw}^T & K_{ww} \end{pmatrix} \begin{Bmatrix} \bar{u} \\ \bar{w} \end{Bmatrix} + \begin{Bmatrix} \int_\Omega B_u^T \sigma' d\Omega \\ 0 \end{Bmatrix} \quad (1)$$
$$= \begin{Bmatrix} \bar{f}_u + \bar{f}_u^f \\ \bar{f}_w + \bar{f}_w^f \end{Bmatrix} - \begin{pmatrix} c'_{uu} & c'_{uw} \\ c'^T_{uw} & c'_{ww} \end{pmatrix} \begin{Bmatrix} \dot{\bar{u}} - \dot{\bar{u}}^f \\ \dot{\bar{w}} - \dot{\bar{w}}^f \end{Bmatrix}$$

where u and w are the nodal displacement vectors and other notations can be seen in reference [2]. Equation (1) is coded as the 2D-FE effective stress analysis program of the name "NUW2".

2.2 Response analysis for pipelines

The responses of pipelines subjected to the ground displacement induced by liquefaction or seismic wave are analyzed by the program "PIPE" [5, 6], which is based on the beam theory on an elastic foundation. Replacing the stiffness of liquefied or non-liquefied ground around the pipeline with a coefficient of subgrade reaction, the pipeline is modeled as pipeline-soil spring system as shown in Figure 2. The pipeline segments are connected by the axial and rotational joint spring k_t and k_r, respectively. The joint and soil springs are assumed to be bi-linearly elastic and the inertia and damping forces are neglected under the static load assumption. Based on these assumptions, when a ground motion is transmitted to a pipeline directly by soil spring, the governing axial and lateral equations of the pipeline are written by

a) axial direction

$$-EA\frac{d^2u}{dx^2} + k_{sx}u = k_{sx}u_s \quad (2)$$

b) lateral direction

$$EI\frac{d^4v}{dx^4} + k_{sy}v = k_{sy}v_s \quad (3)$$

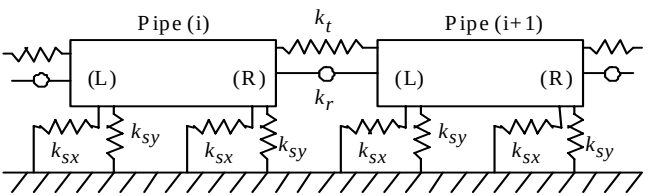

Figure 2: Modelling of pipeline-soil system.

where u, v = axial and lateral displacements of the pipeline respectively, E, A and I = Young's modulus, cross sectional area and geometrical moment of inertia of the pipeline respectively, u_s, v_s = axial and lateral displacements of input ground motion respectively, k_{sx}, k_{sy} = axial and lateral soil spring constants respectively.

In this study axial deformation of eq. (2) and bending deformation of eq. (3) are uncoupled. For prevention of numerical error accumulation, modified transfer matrix method is adopted. According to this method, the vector y for the displacements and the vector z for the forces are correlated as follows;

$$\vec{a}y + \vec{b}z = \vec{c} \tag{4}$$

$$\overleftarrow{a}y + \overleftarrow{b}z = \vec{c} \tag{5}$$

where a, b are square matrices, and the symbol → , ← mean the transfer from left to right and from right to left, respectively. Here the state vector V at the pipeline element is defined as

$$V = [y, z] \tag{6}$$

where y=[u, v, ϕ], z=[N, M, Q], ϕ, N, M, Q =deflection angle, axial force, bending moment and shear force at the end of pipeline segment. Then the eqs. (2) and (3) are also represented by the system equation as

$$\frac{dV}{dx} = AV + f(x) \tag{7}$$

where

$$A = \begin{bmatrix} 0 & 0 & 0 & -1/EA & 0 & 0 \\ 0 & 0 & -1 & 0 & 0 & 0 \\ 0 & 0 & 0 & 0 & -1/EI & 0 \\ -k_{sx} & 0 & 0 & 0 & 0 & 0 \\ 0 & 0 & 0 & 0 & 0 & 1 \\ 0 & -k_{sy} & 0 & 0 & 0 & 0 \end{bmatrix}, \quad f(x) = \begin{bmatrix} 0 \\ 0 \\ q(x) \\ 0 \\ 0 \\ p(x) \end{bmatrix}$$

$q(x)=k_{sx}u_s$=distributed axial load
$p(x)=k_{sy}v_s$=distributed lateral load

A general solution of eq. (7) is given by

$$V(x) = e^{Ax}V(0) + e^{Ax}\int_0^x e^{-As} f(s)ds \tag{8}$$

where e^{Ax} =transfer matrix.

The governing axial and lateral equations (2) and (3) are written as same as eq. (7);

$$\frac{d}{dx}\begin{Bmatrix} u \\ u' \end{Bmatrix} = \begin{bmatrix} 0 & 1 \\ \beta_1^2 & 0 \end{bmatrix}\begin{Bmatrix} u \\ u' \end{Bmatrix} + \begin{Bmatrix} 0 \\ -\beta_1^2 u_s \end{Bmatrix} \tag{9}$$

$$\frac{d}{dx}\begin{Bmatrix} v \\ v' \\ v'' \\ v''' \end{Bmatrix} = \begin{bmatrix} 0 & 1 & 0 & 0 \\ 0 & 0 & 1 & 0 \\ 0 & 0 & 0 & 1 \\ -4\beta_2^4 & 0 & 0 & 0 \end{bmatrix} \begin{Bmatrix} v \\ v' \\ v'' \\ v''' \end{Bmatrix} + \begin{Bmatrix} 0 \\ 0 \\ 0 \\ 4\beta_2^4 v_s \end{Bmatrix} \tag{10}$$

where $\beta_1 = \sqrt{k_{sx}/EA}$, $\beta_2 = \sqrt[4]{k_{sx}/EI}$, ' means the differential *d/dx*.

Using the vector *V*, the field transfer matrix e^{Ax} can be obtained. At the joint between the pipe segments i and i+1, the following relations are obtained by considering the conditions of displacements and equilibrium;

$$\begin{aligned} &u_{i+1}^L = u_i^R - N_i^R/k_T\,, \quad v_{i+1}^L = v_i^R\,, \quad \phi_{i+1}^L = \phi_i^R - M_i^R/k_R\,, \\ &N_{i+1}^L = N_i^R\,, \quad M_{i+1}^L = M_i^R\,, \quad Q_{i+1}^L = Q_i^R \end{aligned} \tag{11}$$

where k_T, k_R = spring constant of joint for translation and rotation, respectively.

3 Results and considerations

Numerical computations for the seismic response of surface ground layers are conducted for the Kobe ground models [3]. An example of surface layers model of Kobe ground by 2D-FE is shown in Figure 3. This cross section of the width of 2,250m and the depth of 20m to 30m are divided into 100 and 6 finite elements, respectively. The ground models rest on the rigid base rock surface and have absorbing (viscous) boundaries (A. B.) at both sides. The left and right sides of the diagrams are toward mountain and sea sides, respectively. In the diagrams N denotes the standard penetration test N-value which is converted to the initial soil stiffness (shear modulus) in the analysis. The geological parameters in Figure 5 are given as; A1 denotes the diluvial sandy gravel, A2 the alluvial sandy gravel, A3 the reclaimed soft soil, A5 the alluvial clay. Kobe earthquake recorded at GL-32m in Port Island is used as input seismic acceleration waves. The NS and UD components of this input waves are impinged simultaneously upward from horizontal base surface of the ground models with the maximum acceleration amplitude A_{max} of 0.1, 1.0, 5.4 and 10.0m/s^2. Figure 4 shows the distribution of maximum ground strain along cross section for four cases of the maximum acceleration amplitude A_{max}. Large ground strain appears near the coastal areas where may refer to heavily damaged areas of pipelines.

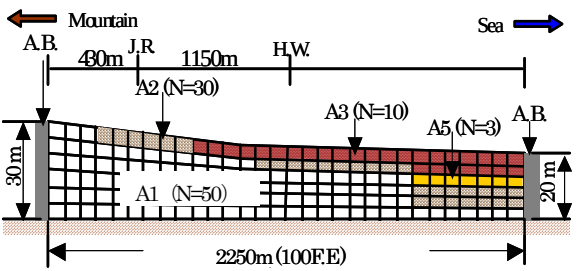

Figure 3: Example of surface ground layers model.

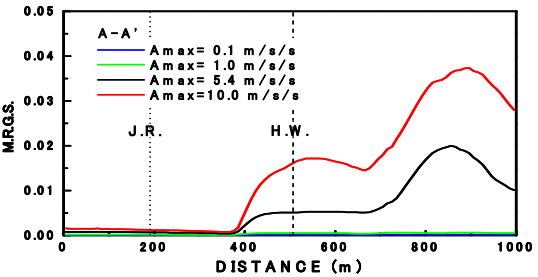

Figure 4: Maximum response ground strain near the surface (G.L.-2m).

Numerical computations are carried out for the responses of axial and lateral displacements and internal forces of pipelines. The input ground displacement is assumed to be uniformly distributed over the pipeline length. The reference pipeline dimensions are shown in Table 1. The reference soil spring characteristic is assumed to be represented by bi-linear coefficient of subgrade reaction as shown in Figure 5. The GM-type and S-type joint which resistant characteristic are shown in Figure 6 and 7, respectively, are used as the reference joints for segmented pipelines. The pipeline cases of the both ends fixed type and the cantilever type are evaluated subjected to lateral and longitudinal ground input, respectively.

Table 1: Reference pipe parameters.

Physical items	Values(unit)
Material of segment	Ductile cast iron
Nominal diameter	500 (mm)
Thickness	9.5 (mm)
Total length	100 (m)
Young modulus	1.57×10^8 (kN/m^2)
Specific gravity	7.15
Tensile strength	3.92×10^5 (kN/m^2)
Bending strength	5.59×10^5 (kN/m^2)
Allowable joint expansion	50 (mm)
Allowable joint rot. angle	5 (degree)

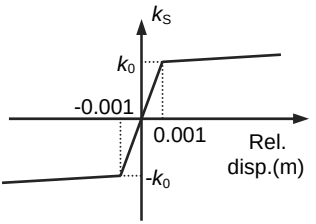

Figure 5: Characteristics of soil spring.

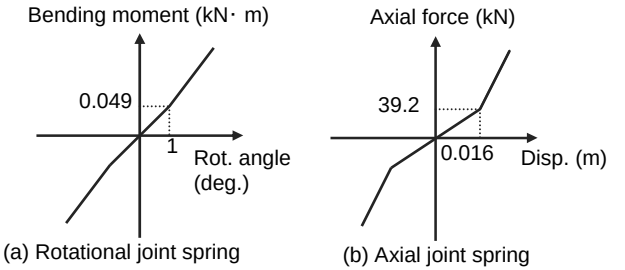

Figure 6: Characteristics of GM-type joint.

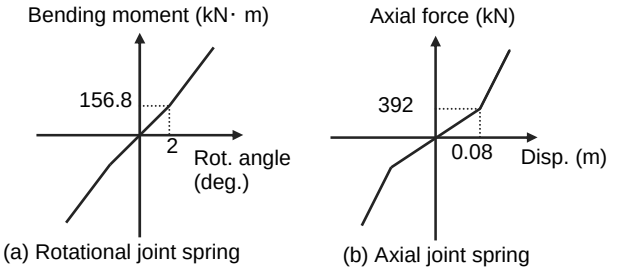

Figure 7: Characteristics of S-type joint.

Figure 8 (a), (b) show the distribution of the responses of displacement and axial force of pipelines with S-type joint, respectively. Axial input soil displacement 0.01m per unit length 1m is almost accumulated at the joint as the expansion displacement. Maximum axial force 850kN which means maximum axial stress about 15600 kN/m^2 is below tensile strength but maximum joint expansion 72.0mm is larger than allowable one 50mm.

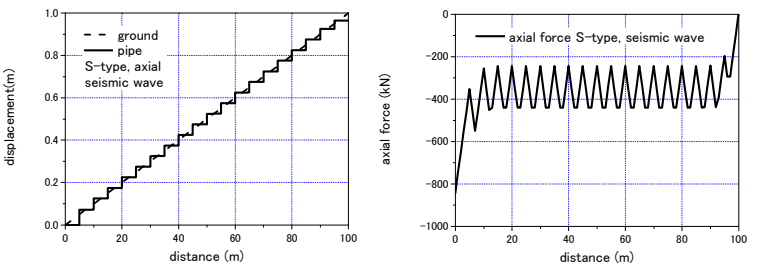

(a) Displacements (b) Axial forces

Figure 8: Distribution of responses of pipelines.

Figure 9 (a), (b) show the distribution of the responses of lateral displacement and bending moment of pipelines with S-type joint, respectively. Maximum lateral displacement of pipeline is 0.8m as for 0.1m input of soil. Maximum bending moment 2734kNm which means bending stress about 190000kN/m^2 is below tensile strength.

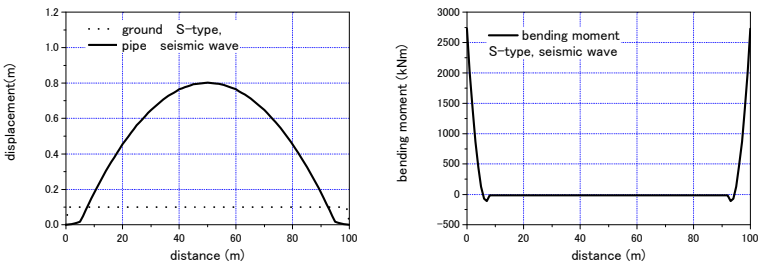

(a) Displacements (b) Bending moments

Figure 9: Distribution of responses of pipelines.

Figure 10 (a), (b) show the same distributions of responses as Figure 9. In Figure 10 the responses in the case of liquefaction are shown in which the pipeline with S-type joint is subjected to 5m lateral flow displacement of soil. Maximum lateral displacement and bending moment of pipeline are about 1m and 80kNm, respectively. Maximum joint rotational angle reaches to about 1.6 degree which is less than the allowable value 5 degree. This means breakage of joint does not occur.

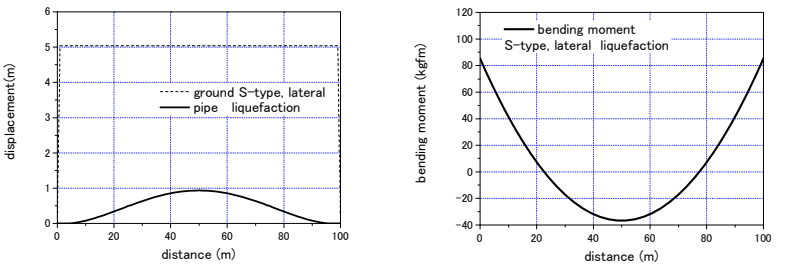

(a) Displacements (b) Bending moments

Figure 10: Distribution of responses of pipelines.

Figure 11 (a), (b) show the same distributions of pipeline responses with GM-type joint as Figure 10. In Figure 11 the responses in the case of liquefaction are shown in which the pipeline is subjected to 5m lateral flow displacement of soil. Maximum lateral displacement is about 9.6m, which is larger than that of pipeline with S-type joint because GM-type joint is more flexible than S-type

one. In GM-type joint, maximum joint rotational angle for lateral input case reaches to about 19 degree which is larger than the allowable value 5 degree. This means breakage of joint.

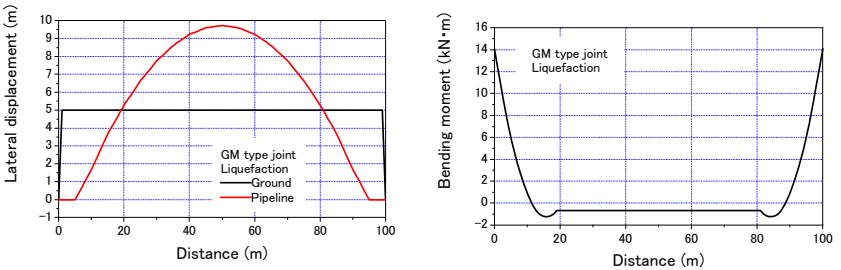

(a) Displacements (b) Bending moments

Figure 11: Distribution of responses of pipelines (GM-type joint).

Figure 12(a), (b) show the distributions of responses of pipeline joint, in axial and lateral seismic wave input case, respectively. In Figure 12 the responses of joint expansions are shown in which the pipeline is subjected to 0.01m axial and 0.1m lateral displacement of soil, respectively. Maximum axial joint expansion in the case of axial input and lateral one are 72mm and 113mm, respectively, which are over the allowable value 50mm.

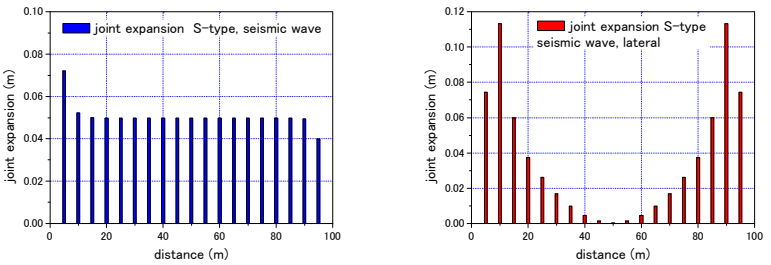

(a) Axial input (b) Lateral input

Figure 12: Distribution of responses of pipeline joints.

Figure 13 shows the distributions of responses of joint rotational angle for lateral seismic wave input case. Maximum joint rotational angle reaches to about 1.6 degree which is smaller than the allowable value 5 degree. This means breakage of joint does not occur.

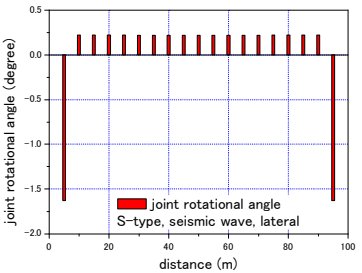

Figure 13: Distribution of responses of rotational angles.

4 Conclusions

In this study, the evaluation method for seismic responses of pipelines is proposed and response characteristics of pipelines are evaluated. The method consists of two different kinds of analyses which are the seismic response analysis of surface ground layers and the pseudo static response analysis of pipelines. Some numerical computational examples of pipeline responses are investigated. The proposed method is effective on evaluating the situation of whole conditions of pipelines and surface ground layers in perspective and the detailed pipeline responses including the response characteristics of surface ground layers.

References

[1] Akiyoshi, T., Fuchida, K. & Fang, H. L., “Absorbing boundary conditions for dynamic analysis of fluid-saturated porous media”, Soil Dynamics and Earthquake Engineering, 1994, **13(4)**, 387-397.

[2] Akiyoshi, T., Fuchida, K. et al., A Nonlinear Seismic Response Analysis Method for Saturated Soil-Structure System with Absorbing Boundary, *Int. J. Numeric. and Analytic. Methods in Geomaech.*, **20(5)**, pp.307-329, 1996.

[3] Akiyoshi, T., Fuchida, K. & Shirinashihama, S., Local site effects of transient dynamic characteristics of irregularly layered grounds, Proc. Fourth Int. Conf. on Recent Advances in Geotech. Earthq. Eng. And Soil Dynamics, Paper No.3.11, 2001.

[4] Iai, S. et al., Strain space plasticity model for cyclic mobility, *Soils and Foundations*, JSSMFE, Vol.32, No.2, pp.1-15, 1992.

[5] Fuchida, K., Wang, L.R.L. & Akiyoshi, T., Parametric Analysis of Buried Pipelines Subjected to Liquefied Ground Movements, Proc. of 5th U.S. National Conference on Earthquake Engineering, pp.959-968, 1994.

[6] Fuchida, K., Akiyoshi, T., Sun, X., Preventive effect of ground improvement on liquefaction and destructive deformation of pipelines, Proc. of Third China-Japan-US Trilateral Symposium on Lifeline Earthquake Engineering, pp.141-148, 1998.

Dynamic interaction of adjacent tall building structures on deep foundations

M. A. Rahgozar & M. Ghandil
Department of Civil Engineering, University of Isfahan, Isfahan, Iran

Abstract

In design of low rise structures the effects of soil-structure interaction are often ignored. However, these effects are considerable for heavy structures such as skyscrapers or multi-level highway structures. The existence of this interaction phenomenon can also be extended to the adjacent buildings. For example, in an area congested with many nearby tall buildings, to account for the proximity effects of adjacent buildings will become critical. Previous few studies conducted in this area, were limited to 2D finite element plain-strain models. Assuming plain-strain for foundation soil may be valid, however, for a building structure which has limited dimensions in plan, this assumption could be erroneous.

In the current study, in order to capture the proximity effects on the response of adjacent buildings under earthquake motions, 3D models of 15 and 30 storey building structures on group piles are used. The foundation soils considered are clay and sand. Dynamic analyses are performed under horizontal components of several actual earthquakes. Three different combinations of two adjacent buildings are considered, 1) two 15-stories, 2) two 30-stories, and 3) one 15- and one 30-stories. Seismic soil-structure interaction analyses in this study are based on direct method. Foundation soil behavior is assumed to be equivalent linear while structures are assumed to behave in elastic range. Results show that the interaction of adjacent buildings depends on structural heights, type and depth of the foundation soil, frequency content of the earthquake records, the type of proximity and the distance between the adjacent buildings.

Keywords: dynamic time history analysis, equivalent linear method, soil-structure interaction, adjacent structures, tall buildings, group piles, frequency content, high amplitude record, low amplitude record, global response of structures.

WIT Transactions on The Built Environment, Vol 120,
www.witpress.com, ISSN 1743-3509 (on-line)
doi:10.2495/ERES110151

1 Introduction

In the design of ordinary structures the effects of soil-structure interaction (SSI) are often ignored. However, these effects are considerable for heavy structures. The existence of this interaction phenomenon can also be extended to the adjacent buildings on same foundation soil. Damages due to earthquakes, such as Kobe earthquake in 1995, show that structural response depends on its foundation and foundation soil. SSI is reported to be one the main reasons for these damages [1]. Behnamfar and Shugimura [2] conducted a comprehensive study on the dynamic responses of 1, 2, 10 and 20 story building structures, both individually and as pairs of adjacent structures. They found that, as the structures are closer, the amplification frequency increases and in some cases, the structural response increases too. Kermani et al. [3] modelled two adjacent buildings located on soft soils (foundation soil and the two structures modelled as one soil-structure system) in order to determine the natural frequencies of the system. They found that if the distance between two adjacent structures is less than 50% of the building dimension in plan, the effects of structural adjacency on seismic response of the structures are considerable and must be considered. Nateghi et al. [4] studied the effects of structure-soil-Structure interaction (SSSI) on seismic response of 2D tall building structures. Their model was in plane-strain. They observed that if site period is far from fundamental period of the structure, the buildings adjacency has minor effects on seismic response of structures.

In all aforementioned studies, the FE model was 2D with the assumption of plain-strain behaviour for the whole soil-structure system. Nonetheless, all arrived at this conclusion that the structural adjacency in many seismic cases cannot be ignored. However, in order to have a more realistic view of the seismic interaction of adjacent structures, one must use 3D FE models without simplifying assumption of plain-strain behaviour. In this research, full 3D Structure-Soil-Structure models are developed and used. In order to capture the effects of earthquake frequency content on this building adjacency study, the final results are illustrated in two main earthquake types, High amplitude records and Low amplitude records.

2 Modelling methods of accounting for SSI

In general, two methods are considered for a SSI studies: the substructure and direct methods. The substructure method although simpler, for real soil-structure systems with different soil layers, group piles, non-circular or flexible footings, etc., may lead to very approximate results. In this method, the soil layer under the building foundation is represented by spring and dashpot elements. Direct method, however, is based on FE modeling of the whole soil-structure system and accounts for radiation of seismic waves in an unbounded medium, by implementing transmitting boundaries. The distance between the artificial soil boundaries and the building is usually several times the width of the structure [5]. A significant part of the FE mesh and the degrees of freedoms in this method belongs to the foundation soil. One may use as many soil layers and soil types as

required in this method. For a 3D adjacency study, the substructure method is far less accurate than the direct method. In order to study the seismic SSSI in this research, the direct method is used.

3 Description of structural models

Two 15 story and 30 story building structures representing mid-rise and high-rise Buildings are considered. The structures have 4 bays in each direction in plan. Each bay is 5 meters. Height of stories is 3 meters. The building site is assumed to be in Tehran/Iran, with high seismic hazard risk where design earthquake acceleration is 0.35g. Design gravity floor loads of DL=760 kg/m² and LL=200 kg/m² are used [6]. Lateral load resisting system is considered to be special moment resisting frame and designed according to ASCE7 2010 code with ETABS software [7]. All steel design provisions such as weak beam – strong column for these systems according to that code are considered. Site classification in structural design is assumed as type D.

4 Description of foundation and soil properties

Both structures rest on piles. Pile groups are designed for soil type D [8]. For 30 story structure, pile group includes 25 piles and for the 15 story structure, pile group has 16 piles. Each pile is 20 meter long. Piles are of reinforced concrete with reinforcements differing in the top 8 meter of the piles compared to its lower part. They are circular with a radius of 0.5 m for the 15-story and 0.8 m for the 30-story buildings. The pile caps are one meter deep and all design criteria including punching shear controls are performed.

Two building sites are considered in this study. Site 1 includes 20 m of sandy soil in two layers, as per Table 1. Site 2 consists of 45 m of clay soil in three layers as per Table 2. Other relevant properties of these soil profiles are also shown in Tables 1 and 2. Figure 1 illustrates the soil nonlinearity curves (Soil shear modulus vs. Shear strain) for Sites 1 and 2.

Table 1: Soil properties at site 1.

Sand (OCR<1)			
Z (m)	E (Kpa)	G (Kpa)	Vs (m/s)
[0 - 10]	107315	92121	224
[10 - 25]	168206	150303	277

Table 2: Soil properties at site 2.

Clay (OCR<1)				
Z (m)	Cu (Kpa)	G (Kpa)	ρ (kg/m3)	Vs (m/s)
[0 - 10]	148	61190	1936	178
[10 - 25]	206	85172	2178	197
[25 - 45]	365	150957	2470	246

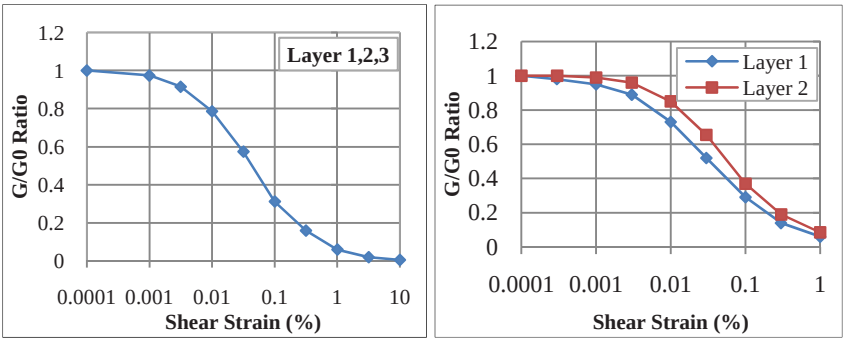

Figure 1: Variation of shear modulus vs. Shear strain for different soils [9]. (Right diagram is for Site 1 and Left diagram is for site 2).

5 Description of selected earthquake records

According to ASCE7- 2010 code, at least 7 seismic records must be considered for seismic analysis and design of structures. The criteria for selection of right earthquake records are given in Table 3.

Table 3: Criteria for selection of earthquake records.

Accelerator Location	Free Field	Magnitude (Richter)	6.0 - 7.0
Frequency Bandwidth (Hz)	0.2 - 10.0	Fault Distance (km)	20.0 - 50.0
Strong Ground Motion Duration (sec)	more than 12	Site Classification (ASCE 2010)	D

A thorough search according to the above criteria lead to the selection of seven records listed in Table 4. Figure 2 depicts 5% damped response acceleration of these records in unit of g. It is clear that the strong motions in

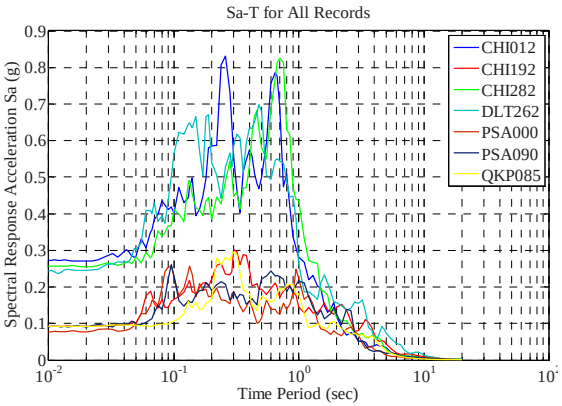

Figure 2: Spectral response acceleration in unit of g (5% damping).

these spectra happen almost in the same frequency/period range, while the amplitude in one group is high and in the other is low. Therefore, these records are classified as Low amplitude records shown in blue and High amplitude records in red. The final results of this research are also illustrated in these two formats/colours: High amplitude (in Red) and Low amplitude (in Blue). So, one can see the effects of earthquake frequency contents on the response of different soil-structure systems, more clearly.

To achieve more realistic results, these records are scaled according to ASCE7-2010. The scaling width is $0.2T_1$-$1.5T_1$ for each structure (T_1 is the first mode period of the structure). Final Scale Factors and PGA of the scaled records are presented in Table 4.

Table 4: Earthquakes scale factors and scaled PGAs per ASCE7-2010.

Selected Records Properties (Scaling Method : ASCE 2010 Code)				
			Scaled PGA (g)	
ID	*Earthquake*	*Component*	*15 Story*	*30 Story*
P0166	Imperial Valley	H-CHI012	0.38	0.57
		H-CHI282	0.35	0.53
P0169	Imperial Valley	QKP085	0.29	0.44
P0170	Imperial Valley	H-DLT262	0.34	0.50
P0267	Victoria, Mexico	H-CHI192	0.27	0.40
P0819	Landers	PSA000	0.25	0.38
		PSA090	0.27	0.40

Blue : Low Amplitude Record
Red : High Amplitude Record

6 Dynamic analysis of Soil-Structure Interaction (SSI) and Structure-Soil-Structure Interaction (SSSI) systems

SAP2000 software is used to conduct time history dynamic analyses of seismic SSI and SSSI responses of 3D soil-structure systems [10]. These analyses are carried out for three different conditions: 1) one single structure (15 or 30 story) based on rigid support/bedrock, 2) one single structure on piles and on Site1 or Site 2, 3) Two adjacent structures on piles and on Site 1 or 2. Figure 3, for example, shows 3D view of FE model of two 30-story adjacent structures used in this research.

For structural modelling, beam element is used for frame members and piles. Shell elements are used for rigid diaphragm and pile caps. Solid 3D element with 8 nodes is selected for soils. Structural elements assumed to behave linearly. To account for soil nonlinearities, an equivalent linear approach is assumed for soil behaviour. This method is effective, fast and sufficiently accurate for analysis of large scale soil media [11].

One of the main issues in SSI is the determination of the location of transmitting boundaries in plan. These boundaries should be considered far enough from the structure to ensure the earthquake energy dissipation conditions, and at the same time not considered too far so that the FE model becomes very

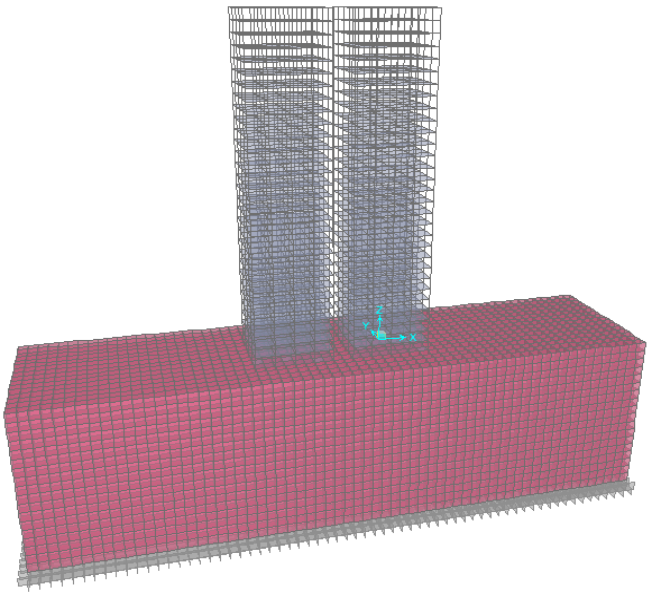

Figure 3: A typical 3D FE model of two 30-story adjacent buildings.

large to handle. Therefore, to find optimum locations, a sensitivity study on the location of these boundaries is run in this work. Where a two adjacent 30-story buildings on Site 2 in two different site plan dimensions of 40 x 160m and 60 x 180 m were analyzed under H-DLT262 record which is the most critical seismic excitation among the seven records. It was observed that the variation of for example the story lateral displacement in these two models were less than 3% (figure 4). Therefore, the site dimension used for all dynamic analyses in this research is considered 40 x 160 m in plan.

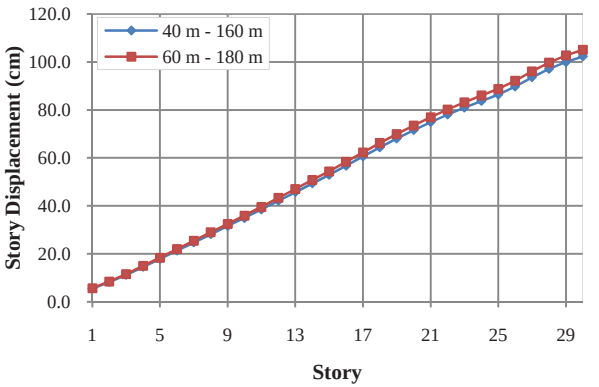

Figure 4: Variation of story displacements for two 30 story adjacent structures on Site 2, with two different site plan dimensions.

The nonlinear behaviour of soil must be considered during dynamic SSI analysis. Among the two common methods of Equivalent linear method and nonlinear visco-elastic method, the former is used in this study. In both methods shear strain as well as shear modulus of the soil are determined through an iteration procedure using the Seed and Idriss diagrams in Figure 1. In Equivalent linear method, however, the stiffness matrix is kept constant during each run and the shear strain and modulus are updated only at the end of each run until with a 5% error, convergence is achieved, while in nonlinear visco-elastic method, shear strain and modulus are updated for each element and at each time step. Equivalent linear method is fast and has acceptable accuracy whereas nonlinear visco-elastic method is time consuming and not with much higher accuracy [11]. Figure 5 compares story displacements for a 30 story adjacent to a 15 story on Site 2 under H-DLT262 record using different nonlinear analyses methods. Neglegible difference in the results justify the use of Equivalent linear method in this work.

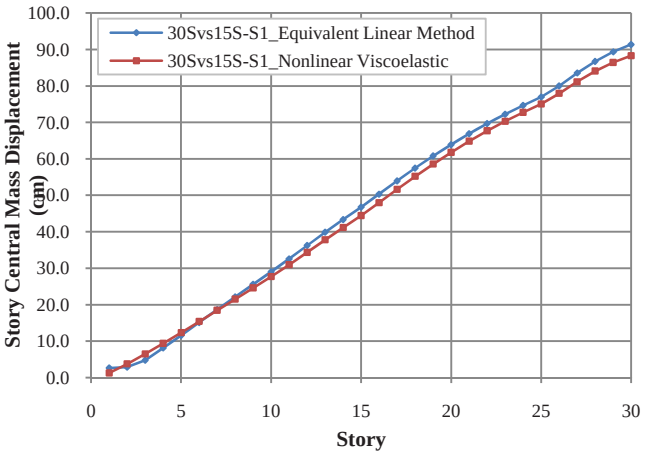

Figure 5: Story displacements for a 30 story adjacent to a 15 story on Site 1 under H-DLT262 record using different nonlinear analyses methods.

It is expected that for two adjacent buildings, as they are closer, the interaction response of the structures is higher. This response becomes higher as the buildings are taller. To determine the critical distance of two adjacent buildings, one free standing single 30 story as well as two adjacent 30 story buildings, with variable distances, on site 2 were analyzed under H-DLT262 record. The adjacent building distances varies between 0.125a to 3a, where a is the lateral building dimension in plan (20m). By comparison of the lateral story displacements for these models, the following conclusions were made: 1) for building distances more than 0.5a, SSSI need not be considered. 2) The highest responses occur where building distances are between 0.125a to 0.25a. 0.125a

corresponds to 2.5 m, and no pounding happened at this distance. Therefore, in this study only these two distances, 0.125a and 0.25a are considered.

7 Results and discussions

Three main objectives are pursued by the seismic SSSI analyses in the research: 1) study local structural responses such as story lateral displacements, 2) study global structural responses such as base shears, 3) study the effects of frequency and amplitude of earthquake records on structural responses. All results are presented in two colors: High amplitude records in Red and Low amplitude records in Blue.

7.1 The effects of SSSI on story displacements

Figure 7 shows variation of story displacements for all adjacency cases for a 30 story. It is clear the highest response for a 30 story is when it is adjacent to another 30 story. If the adjacent building is 15 story, its response is less. It must be noted that "30S" stands for a single 30 story on rigid support, and "30S-S1" means a single 30 story on Site 1. According to Figure 6, the least response for a 15 story happens when it is next to a 30 story. According to the results, a taller building increases the response of a shorter adjacent building, and a shorter building decreases the response of a taller adjacent building.

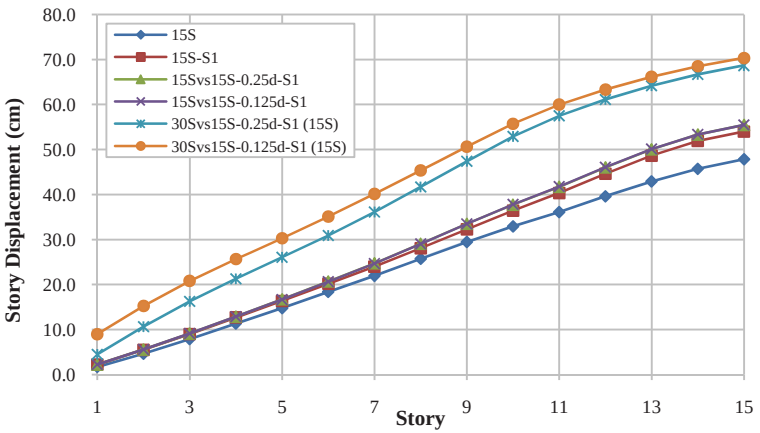

Figure 6: Maximum story displacements for a 15 story structure on Site 1 in different adjacency cases, under High amplitude record (H-DLT262).

7.2 The effects of SSSI on structural base shear

According to the results in Figure 9, base shear in 30 story is higher when it is next to a 15 story. Also the base shear in 15 story is least when it is next to a 30 story. In this figure "Sin" stands for a single 30 story.

7.3 The effects of earthquake frequency content on structural response

By comparing the story displacements (in Figures 7 and 8) and base shears (in Figure 9) for a 30 story in all adjacency cases, it is clear that high amplitude values (in Red) are higher than the Low amplitude values (in Blue) up to 200%.

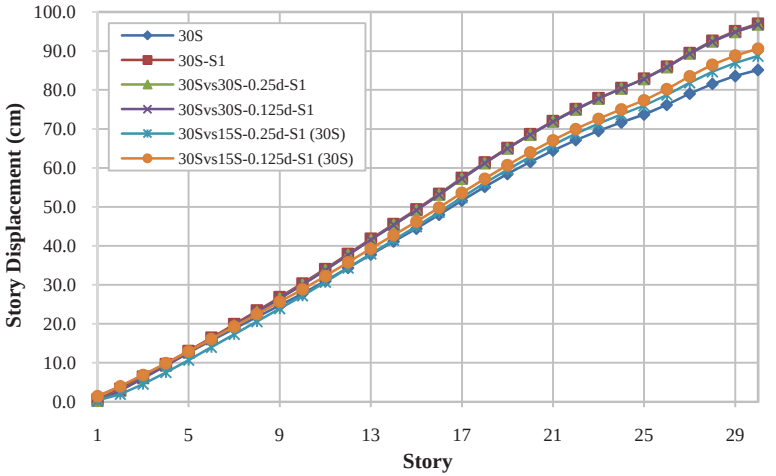

Figure 7: Maximum story displacements for a 30 story structure on Site 1 in different adjacency cases, under High amplitude record (H-DLT262).

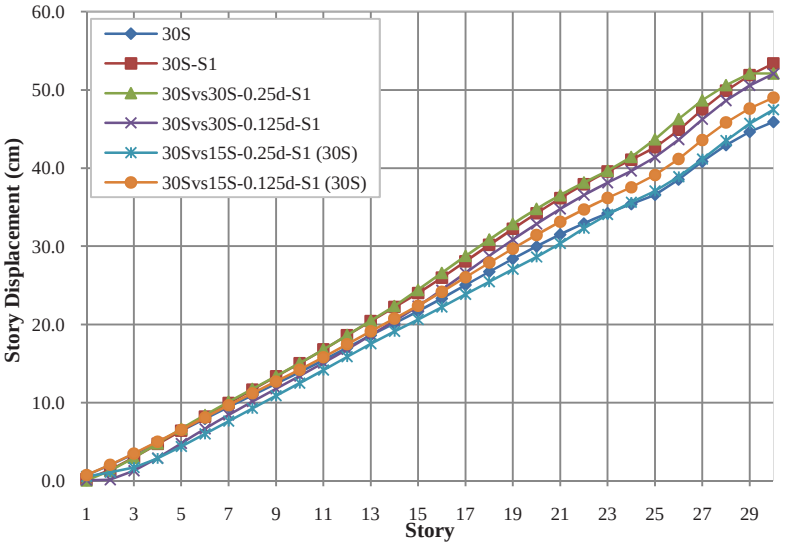

Figure 8: Maximum story displacements for a 30 story structure on Site 1 in different adjacency cases, under Low amplitude record (H-DLT262).

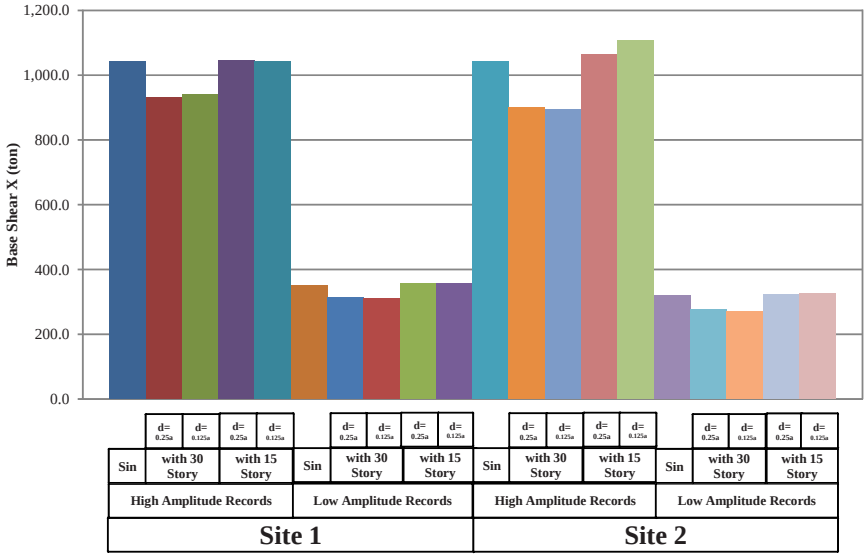

Figure 9: Structural base shears in all 30 story structure adjacency cases.

8 Conclusions

In the current study, in order to study the adjacency effects on the response of structures under earthquakes with different frequency contents, 3D models of 15 and 30 storey structures on group piles and on different sites were analyzed. The results obtained are:

1) For a 30 story the highest story displacement occurs when it is adjacent to another 30 story. If the adjacent building is 15 story, its response is less. The least response for a 15 story happens when it is next to a 30 story. According to the results, a taller building increases the response of a shorter adjacent building, and a shorter building decreases the response of a taller adjacent building.

2) Base shear in 30 story is higher when it is next to a 15 story. Also the base shear in 15 story is least when it is next to a 30 story.

3) Earthquake frequency content influences the results significantly, for example, responses to High amplitude records are higher than to Low amplitude ones, up to 200%.

References

[1] Dynamic soil structure interaction analysis via coupled finite-element-boundary-element method, http://en.wikipedia.org/~soil-structure interaction.htm Shimomura, Y., 2006.

[2] Behnamfar, F. & Sugimura, Y., Dynamic response of adjacent structures under spatially variable seismic waves, *Probabilistic Engineering Mechanics*, (14), pp 33–44. 1999.
[3] Kermani, M., Saadatpour, M. & Behnamfar, F., Study of Natural Frequency of Adjacent Structures on Flexible Soil, *6th Int. Conf. of Civil Engineering*. Isfahan University of Technology, Isfahan, Iran, 2001.
[4] Nateghi, F., Tabrizi, A. & Behnamfar, F., Structure-soil-structure effects on nonlinear response of tall buildings, *First European Conf. Earthquake Engineering. and Seism*. (13), pp 206–215, 2006.
[5] John P. Wolf., Dynamic soil structure interaction, Prentice-Hall, Inc., Englewood Cliffs, New Jersey, 07632, 1985.
[6] American society of civil engineers, Minimum design loads for buildings and other structures, American Society of Civil Engineers, 1801 Alexander Bell Drive, Reston, Virginia 20191, 2010.
[7] Computers & Structures, Inc., ETABS, Integrated building design software, User Manual, Version 9, 1995 University Avenue Berkeley, California 94704 USA, 2005.
[8] M. G. Tomlinson., Pile design and construction practice, FN Spon, London 9966, 2004.
[9] Seed HB & Idriss IM., Soil moduli and damping factors for dynamic response analysis, University of California, Berkeley, CA, 1970.
[10] Computers & Structures, Inc., SAP2000, Linear and nonlinear static and dynamic analysis and design of three-dimensional structures, User Manual, Version 11, 1995 University Avenue Berkeley, California 94704 USA, 2006.
[11] Steven L. Kramer., Geotechnical Earthquake Engineering, Prentice-Hall, Inc., Englewood Cliffs, New Jersey 07458, 1996.

This page intentionally left blank

Moment formulation for random eigenvalue problems in beams

B. W. Yeigh[1] & J. A. Hoffman[2]
[1]*State University of New York Institute of Technology, USA*
[2]*Engineering Solutions, LLC, USA*

Abstract

This paper proposes a moment formulation model to handle eccentric load imperfections in beams on elastic foundation taking into consideration the randomness of imperfections. An alternative approach to the secant formula to capture the effects of load imperfections is described. The study demonstrates eccentricity is the most detrimental form of structural imperfections and that it aggressively and adversely interacts with other imperfections.
Keywords: stability, load imperfections, beam on elastic foundation, regular perturbation, eigenvalue, energy method, stochastic, spectral representation.

1 Introduction

One fundamental problem still remains to be explored in structural engineering are the stability of imperfection sensitive structures. Unlike tension and flexural members that fail when the applied loads cause stresses that exceed material limitations, slender columns most often fail by buckling. Furthermore, column buckling does not depend on the proportional limit of the member. Buckling is a complex failure mechanism that is often catastrophic with little or no warning. It depends not only on the material and section properties of the column, but also on the contributions and interactions of its length, end support conditions, lateral supports, and location of the applied load.

The classical stability analysis [5, 7], is actually developed largely from the work of Leonhard Euler who first analytically investigated the column buckling phenomenon in 1744. Over the years, much has been done to extend and refine Euler's work. Buckling formulations based on the Euler equation had some rational consideration for the behavior of the material in question. They all


WIT Transactions on The Built Environment, Vol 120, © 2011 WIT Press
www.witpress.com, ISSN 1743-3509 (on-line)
doi:10.2495/ERES110161

perform empirically well for ideal columns with concentric loads, and models that are not unusually sensitive to imperfections. However, imperfections exist and are common in real structures. In this study, the authors define structural imperfections as any small, unavoidable deviations from the perfect structure. These deviations include those of shape (i.e., initial curvature), material properties, section properties, support mechanisms, and the geometric configuration of the applied load such as accidental eccentricity.

While not all structures are sensitive to imperfections, experience and experimentation have shown that some structures including the beam on elastic foundation and cylindrical shells are quite sensitive to structural imperfections [8]. One way to address imperfections is to design structures by increasing factors of safety. For the most part, engineers approach imperfections by using some rational means to determine the stresses in a column that are caused by the imperfection, and then checking this against the Euler load, possibly with an added safety factor. In an attempt to more accurately analyze the effect of shape imperfections, the secant formula is used to capture the effects of the imperfection [6]. While the secant formula will give good results for the stresses in a column with imperfections, it is not a buckling formula. It is a strength formula. The formula gives an excellent estimate of the stress in the column, but it does not and can not predict whether or not the column has survived up to the classical buckling load, nor does it say anything about imperfection sensitivity.

However, if a structure is sensitive to imperfections, an unstable equilibrium exists at the critical load, and it is possible for neighboring equilibria to exist at loads less than the critical load. The structure may experience structural "softening" as it nears the critical load and consequently less load is required to produce more deflection [1]. Examples of structures that are sensitive to structural imperfections are thin shells, space frames, thin-walled beams, arches, and laterally supported columns such as the beam on elastic foundation (BEF). This paper considers eccentricities in the applied loads in BEF.

2 Numerical method

Introduced first by Palassopoulos [3], the Critical Imperfection Magnitude Method (CIM) is a robust regular perturbation method that addresses limitations of Koiter's method [2]. CIM considers all types of imperfections and not just shape imperfections. Yeigh [9] provided a stochastic interpretation of the method. CIM takes the potential energy to the second-order expansion and kinematically admissible set of generalized coordinates to the fourth-order expansion. The general method is outlined in Palassoupoulos [3], and stochastic formulation is presented in Yeigh [9]. The potential energy of the "perfect" structure (i.e., no imperfections), V_0, is expanded in terms of the generalized coordinates q_j, where j = 1, 2, ..., M.

$$V_0 = v_0 + a_{0j}q_j + b_{0jk}q_jq_k + c_{0jkl}q_jq_kq_l + d_{0jklm}q_jq_kq_lq_m + \ldots \quad (1)$$

Then the potential energy of the "actual" structure (i.e., with imperfections), V is discretized and expanded:

$$V = V_0 + \varepsilon V_1 + \varepsilon^2 V_2 + \ldots \tag{2}$$

$$V_1 = v_1 + a_{1j}q_j + b_{1jk}q_jq_k + c_{1jkl}q_jq_kq_l + \ldots \tag{3}$$

$$V_2 = v_2 + a_{2j}q_j + b_{2jk}q_jq_k + c_{2jkl}q_jq_kq_l + \ldots \tag{4}$$

where the coefficients $a_{(.)}$, $b_{(.)}$, $c_{(.)}$ and $d_{(.)}$ are chosen to be symmetric with respect to permutation of their indices. The universal imperfection magnitude parameter ε is a measure of the magnitude of deviation in material and structural properties from the perfect structure. In general, any property S can be modeled as $S(x) = S_0[1 + \varepsilon s(x)]$ with a mean value of S_0 and an imperfection pattern s(x). When $\varepsilon = 0$, the structure is reduced to the perfect structure. However, the product of the imperfection being considered and the critical imperfection magnitude ε_{cr} must be sufficiently small (<0.35) in order for the power series expansion to converge. The potential energy can be rewritten in more general form:

$$\begin{aligned} V = {} & (v_0 + \varepsilon v_1 + \varepsilon^2 v_2 + \ldots) + (a_{0j} + \varepsilon a_{1j} + \varepsilon^2 a_{2j} + \ldots)q_j \\ & + (b_{ojk} + \varepsilon b_{1jk} + \varepsilon^2 b_{2jk} + \ldots)q_jq_k \\ & + (c_{0jkl} + \varepsilon c_{1jkl} + \varepsilon^2 c_{2jkl} + \ldots)q_jq_kq_l + \ldots \end{aligned} \tag{5}$$

The first and second variations offer equilibrium and stability conditions:

$$\begin{aligned} \delta V = {} & \{(a_{0j} + \varepsilon a_{1j} + \varepsilon^2 a_{2j} + \ldots) \\ & + 2(b_{0jk} + \varepsilon b_{1jk} + \varepsilon^2 b_{2jk} + \ldots)q_k \\ & + 3(c_{ojkl} + \varepsilon c_{1jkl} + \varepsilon^2 c_{2jkl} + \ldots)q_kq_l \end{aligned} \tag{6}$$

$$\begin{aligned} \delta^2 V = {} & \{2(b_{ojk} + \varepsilon b_{1jk} + \varepsilon^2 b_{2jk} + \ldots) \\ & + 6(c_{ojkl} + \varepsilon c_{1jkl} + \varepsilon^2 c_{2jkl} + \ldots)q_l \end{aligned} \tag{7}$$

Then the eigenvalue problem can be formulated:

$$\begin{bmatrix} \gamma_1 & \gamma_2 \\ I & 0 \end{bmatrix} \begin{Bmatrix} \delta q \\ \varepsilon \delta q \end{Bmatrix} = \frac{1}{\varepsilon} \begin{Bmatrix} \delta q \\ \varepsilon \delta q \end{Bmatrix} \tag{8}$$

where I and 0 represent identity and zero submatrices.

$$\gamma_{1jk} = \frac{1}{\sqrt{b_{0jj}b_{0kk}}} \left[-b_{1jk} + \frac{3c_{0jkl}a_{1l}}{2b_{0ll}} \right] \tag{9}$$

$$\begin{aligned} \gamma_{2jk} = {} & \frac{1}{\sqrt{b_{0jj}b_{0kk}}} \left[-b_{2jk} + \frac{3c_{1jkl}a_{1l}}{2b_{0ll}} + \frac{3c_{0jkl}a_{2l}}{2b_{0ll}} - \frac{3c_{0jkl}b_{1lm}a_{1m}}{2b_{0ll}b_{0mm}} \right. \\ & \left. - \frac{3c_{0jkl}b_{1lm}a_{1m}}{2b_{0ll}b_{0mm}} + \frac{9c_{0jkl}c_{0lmm}a_{1m}a_{1n}}{8b_{0ll}b_{0mm}b_{0nn}} - \frac{3d_{0jklm}a_{1l}a_{1m}}{2b_{0ll}b_{0mm}} \right] \end{aligned} \tag{10}$$

3 Beam on elastic foundation (BEF) formulation with random load imperfections (eccentricity)

Eccentricity in the applied load can be modeled as a shape imperfection because the resulting end moments induce curvature into the beam. The eccentricity imperfections η_1 and η_2 will be modeled as single-value random variables. The imperfection patterns are assumed to be one-dimensional, homogenous, Gaussian random fields. The cosine series formula [4] will be used to simulate random imperfection patterns. The function s(x) represents the imperfection pattern which is a 1D-1V, homogeneous, Gaussian stochastic field with a zero mean. In terms of the cosine series with deterministic amplitude A_n, and a random phase angle φ_n, the pattern is written as:

$$s(x) = \sqrt{2} \sum_{n=1}^{N} A_n \cos(\kappa_n x + \varphi_n) \tag{11}$$

$$A_n = \left(G_{ff}\left(\kappa_n\right)\Delta\kappa\right)^{\frac{1}{2}} \tag{12}$$

$$\kappa_n = n\Delta\kappa = n\frac{\kappa_u}{N},\ \text{n = 1, 2, ..., N} \tag{13}$$

where κ is the wave number and κ_u is the fixed upper cut-off wave number. The value of κ_u is chosen such that above it, the corresponding one-sided power spectral density $G_{ff}(\kappa)$ is zero or negligibly small. The following power spectral density (PSD) function and corresponding autocorrelation function $R_{ff}(\xi)$ are used:

$$G_{fofo}(\kappa_0) = \frac{1}{2}\sigma_{fo}^2 b_{fo}^3 \kappa_o^2 \exp\left[-b_{fo}\left|\kappa_o\right|\right] \tag{14}$$

$$R_{fofo}(\xi_0) = \sigma_{fo}^2 \frac{1-3\left(\frac{\xi_o}{b_{fo}}\right)^2}{\left[1+\left(\frac{\xi_o}{b_{fo}}\right)^2\right]^3} \tag{15}$$

The correlation distance, b_{fo}, is chosen to best match the PSD to the expected degree of fluctuation in the imperfections. Long values of b_{fo}, the PSD undulates slowly. Short values of b_{fo}, the PSD varies sharply. The correlation distance used in this study is 1.50, a reasonable and realistic choice that reflects an actual beam with imperfections.

BEF with imperfections in initial shape, bending rigidity, foundation stiffness, load and eccentric end loads were considered in this study. The beam also has a depth, d_e. The variable d_e does not explicitly enter the potential energy formulation. However, in order to model the distribution of the end

eccentricities, the depth must be physically defined. This can be achieved by relating d_e to length, L by means of a span-to-depth ratio. For this study, a commonly used engineering span-to-depth ratio of 20 is used.

For generality, non-dimensional variables were used throughout. For this problem, the most convenient approach to a non-dimensional form is to divide the length variables by the modified span length, $L_P=L/\pi$.

$$x=\frac{X}{L_P}=\frac{\pi X}{L},\ w=\frac{W}{L_P}=\frac{\pi W}{L},\ \varphi=\frac{L_P^4}{(EI)_0}K=\frac{L^4}{\pi^4(EI)_0}K \tag{16}$$

$$z_1=\frac{Z_1}{L_P}=\frac{\pi Z_1}{L},\ z_2=\frac{Z_2}{L_P}=\frac{\pi Z_2}{L},\ \rho=\frac{L^2}{\pi^2(EI)_0}P,\ v=\frac{L}{\pi(EI)_0}V \tag{17}$$

Imperfections in bending rigidity (EI), foundation stiffness (K), load (P), and eccentricity (Z) are described as zero mean stochastic fields:

$$EI(x) = (EI)_0[1 + \varepsilon e(x)],\ \varphi(x) = \varphi_0[1+ \varepsilon k(x)],\ w_0 = \varepsilon h(x) \tag{18}$$

$$z_1 = \varepsilon\eta_1,\ z_2 = \varepsilon\eta_2,\ K(x) = K_0[1 + \varepsilon k(x)] \tag{19}$$

$$\varphi_0=\frac{L_P^4}{(EI)_0}K_0=\frac{L^4}{\pi^4(EI)_0}K_0 \tag{20}$$

The functions e(x), k(x), and h(x) are the imperfection patterns (stochastic fields) for the beam to be used on the bending rigidity, foundation stiffness, and initial shape respectively. The terms η_1 and η_2 are independent random variables. For the case of a Gaussian distribution, η is distributed normally with zero mean and standard deviation σ_η. For physical reasons, the distributions for η are truncated at the top and bottom edges of the beam. It is desired to have positively defined end moments M_1 and M_2 in the formulation of V_M. In order for M_1 to be positive, Z_1 must be negative. ($M_1 = -PZ1$) The reverse is true for M_2. Here, a positive Z_2 gives a positive M_2. ($M_2 = PZ_2$)

There are four contributing components to the potential energy of the BEF: the strain energy of bending due to change in curvature (V_B), the strain energy of the foundation (V_K), the potential energy of the applied load (V_P), and the potential energy of the moments resulting from the accidental eccentricities (V_M): $V = V_B + V_K + V_P + V_M$. Before proceeding with the development of the coefficients in the characteristic equation, the spectral representations for e(x), k(x), and h(x) must be developed.

$$e(x)=\sum_{j=1}^{N}e_j\cos(\kappa_j^e x+\Phi_j^e) \qquad k(x)=\sum_{j=1}^{N}k_j\cos(\kappa_j^k x+\Phi_j^k) \tag{21}$$

A direct representation for h(x) similar to eqn. (21) is not possible. The cosine series does not work because the forced end conditions require zero end displacements. Addressing the incompatibility question requires first generating the shape imperfection field using the spectral representation method, and then

rotating and translating the field to meet the required boundary conditions. This fitting procedure is described as follows:

$$h^*(x) = \left[\sqrt{2}\sum_{i=1}^{N} h_i \cos(\kappa_j^h x + \Phi_j^h)\right] - cx + h_0 \tag{22}$$

and, realizing that $h^*(0) = h^*(\pi) = 0$, $h^*(x) = \sum_{j=1}^{N} h_j^* \sin(jx)$ and $c = \dfrac{h(\pi) - h(0)}{\pi}$

where $h_j^* = \dfrac{2}{\pi}\left[-\int_0^{\pi} cx\sin(jx)\,dx - \int_0^{\pi} h(0)\sin(jx)\,dx + \int_0^{\pi} \sqrt{2}\sum_{i=1}^{N} h_i \cos(\kappa_j^h x + \Phi_j^h)\sin(jx)\,dx\right]$ (23)

4 Numerical results

The solution of the eigenvalue problem for the i^{th} sample imperfection pattern yields the critical imperfection magnitude. For each imperfection parameter, the root mean square (rms) magnitude was then combined with the critical imperfection magnitude, $\varepsilon_{cr}^{(i)}$ to yield the rms imperfection magnitudes, $\varepsilon_{RMS}^{(i)\eta}$, $\varepsilon_{RMS}^{(i)e}$, $\varepsilon_{RMS}^{(i)k}$, and $\varepsilon_{RMS}^{(i)h^*}$:

$$\varepsilon_{RMS}^{(i)\eta} = \varepsilon_{cr}^{(i)}\sqrt{\frac{(\eta_1^{(i)})^2 + (\eta_2^{(i)})^2}{2}} \text{ and } \quad \varepsilon_{RMS}^{(i)[\bullet]} = \varepsilon_{cr}^{(i)}\sqrt{\frac{1}{\pi}\int_0^{\pi} [\bullet(x)]^2\,dx} \tag{24}$$

where [●] is e, k, or h* and i = 1, 2, …, M. The product of the imperfection magnitude ε_{cr} and RMS imperfection patterns should not be greater than 0.35 since it violates the nature of the perturbation approximation and are physically meaningless. Finally, the rms imperfection magnitudes are averaged over the sample size and the results tabulated. The following input parameters are used:

Sample size = 50

Foundation stiffness: $\varphi_0 = 225$

Eccentricity standard deviation: $\sigma_\eta = 0.05$

Imperfections simulated: $\kappa_{uo} = 7.449$, $b_{f0} = 1.50$, $\sigma_{f0} = 0.05$

Power spectral density function: $G_{fofo}(\kappa_0) = \frac{1}{2}\sigma_{fo}^2 b_{fo}^3 \kappa_o^2 \exp\left[-b_{fo}|\kappa_o|\right]$

Figure 1 shows the direct comparison of ε_{RMS} for η alone, e alone, k alone, and h alone. Combined effects of shape and non-shape imperfections are presented in Figure 2. The first and most important observation is that the eccentricity in the applied loads is an even more dominant imperfection than that of initial shape. It was expected that eccentricity would have a similar effect upon the BEF as does initial shape since the moment it creates is a form of shape

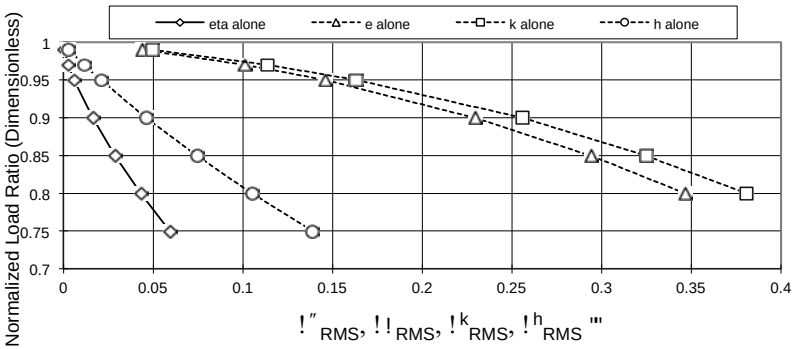

Figure 1: Direct comparison of e, k, and h.

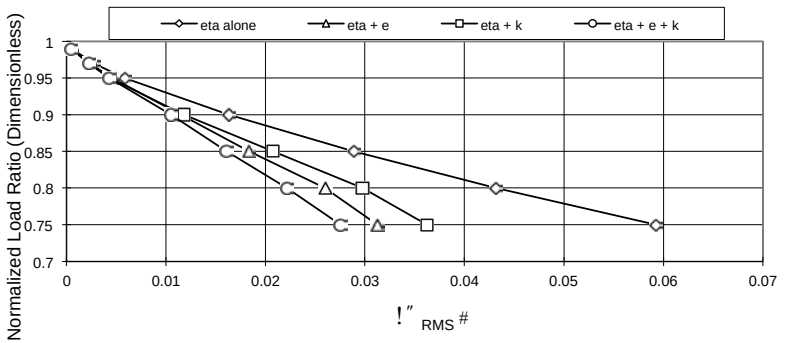

Figure 2: Effects of eccentricity on ε^{η}_{RMS} with other imperfections.

imperfection. Shape imperfections become more and more dominant as the correlation distance decreases [9].

The effects on eccentricity imperfection sensitivity will be most pronounced when it is modeled as a random variable, as it is in this case. Thus, the model used in this study maximizes the dominance of the eccentricity imperfection; while holding the dominance of shape imperfections back to an average. Eccentricity is indeed a shape imperfection. The ε_{RMS} for η are similar in shape, orientation (i.e., concave up), and location as those for h. This result was expected, given that the entry point of the ηs into the characteristic equation was in the a_{1j} term.

Figures 3 and 4 show, in the case of ε_{RMS} for η there is a remarkable twentyfold increase in sensitivity when shape imperfections are present. In the case of h, when eccentric loads are present, the sensitivity is increased even more, by about 50 times. It is also obvious from these plots that any detrimental effects from the addition of e and k imperfections are so minor as to be almost inconsequential in the face of the overwhelming dominance of the two shape imperfections working in conjunction.

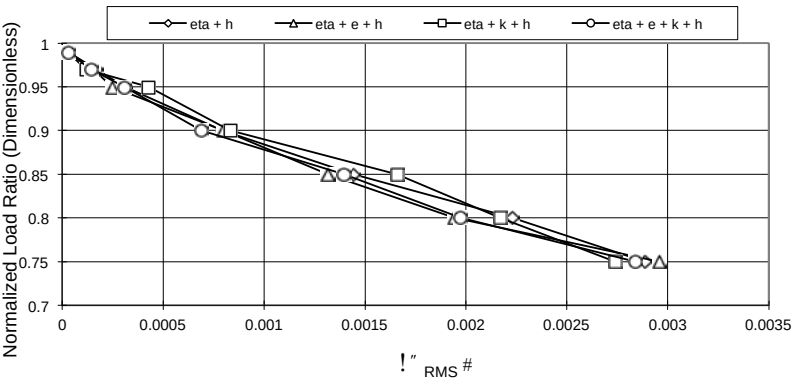

Figure 3: Effects of initial shape imperfections on eccentricity.

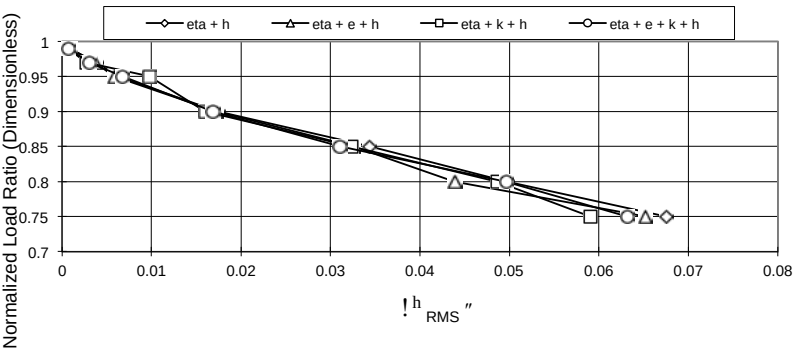

Figure 4: Effects of eccentricity on initial shape imperfections.

5 Conclusions

Eccentricity in the applied load is the most dominant of all imperfections for a correlation distance of 1.50. Also, the buckling sensitivity of the BEF to all other imperfections is extremely degraded in the presence of eccentricity in the applied loads. This is especially true in the case of imperfections in the initial shape of the beam. This study also proved that eccentricity in the applied load is in fact a shape imperfection. Furthermore, this study concluded that the buckling sensitivity of the beam did not depend on the sign of the product of the eccentricities on each end of the beam.

References

[1] Bazant, Z. & Cedolin, L., *Stability of Structures*. Oxford, 1991.
[2] Koiter, W.T., *On the Stability of Elastic Equilibrium*. Ph.D. thesis. Delft, Holland, 1967.

[3] Palassopoulos, G.V., A New approach to the Buckling of Imperfection-Sensitive Structures. *Journal of Engineering Mechanics*, 119, pp. 850-869, 1993.
[4] Shinozuka, M. & Deodatis, G., Simulation of Stochastic Processes by Spectral Representation. *Applied Mechanics Reviews*, 44(4), 1991.
[5] Thompson, J.M.T. & Hunt, G.W., *Elastic Instability Phenomena*. Wiley, New York, 1984.
[6] Timoshenko, S . & Gere, J. *Mechanics of Materials*, PWS-KENT, 1984.
[7] Timoshenko, S.P. & Gere, J.M., *Theory of Elastic Stability*. McGraw-Hill: New York, 1961.
[8] Wilson, W.M. & Newmark, N.M., The Strength of Thin Cylindrical Shells as Columns. *Engineering Experiments Station Bulletin*, U. of Ill., Urbana, Ill., 1933.
[9] Yeigh, B.W. *Imperfections and Instabilities. Dissertation*, Princeton, 1995.

This page intentionally left blank

Section 5
Structural performance

This page intentionally left blank

Safety evaluation for dams against different modes of surface faults induced by earthquakes

Y. Ariga
Graduate School of Science and Technology, Hirosaki University, Japan

Abstract

Safety evaluation against surface earthquake faults is an important subject for long and large structures such as railways, highways, tunnels, banks, dams, and so forth. Normal faults, reverse faults, strike-slip faults and rotational faults, for instance, can be supposed in regard to the modes of surface faults. However, an analytical method for evaluating the safety against surface earthquake faults has not yet been established. So, I devised an evaluation method for safety against various modes of surface earthquake fault by applying a 3-D dynamic analysis method. Applicability of the method proposed was examined by the case study in regard to a concrete gravity dam. As a result, the discontinuous behavior of dam-fault-foundation system can be simulated by the method proposed. Vertical behavior of a dam by the normal fault or a reverse fault can be analyzed by inputting an acceleration wave in the vertical direction from the half of the rigid base of the 3-D FEM model. Horizontal behavior of the dam by a strike-slip fault can be analyzed by inputting an acceleration wave in the horizontal direction. Discontinuous behavior of the dam against various modes of surface faults can be simulated by combining a horizontal input and a vertical input of acceleration wave.
Keywords: safety evaluation, surface fault, 3-D dynamic analysis, concrete dam.

1 Introduction

The Upper Crystal Dam, the Upper Howell Dam, and the Old San Andreas were damaged by the surface displacement of the San Andreas Fault during the San Francisco Earthquake in 1906 [1, 2]. The Shih-Kang Dam was destroyed by the vertical relative displacement of about 7.6m during the Taiwan Chi-chi Earthquake in 1999 [3]. These historical cases show clearly that the safety

WIT Transactions on The Built Environment, Vol 120, © 2011 WIT Press
www.witpress.com, ISSN 1743-3509 (on-line)
doi:10.2495/ERES110171

evaluation against surface displacement induced by an earthquake fault is an important subject for such long and large structures. However, the analytical method for evaluating safety against surface fault displacement has not been practically developed. So, I studied and devised an evaluation method by applying 3-D dynamic analysis in order to simulate the discontinuous behavior of the dam against various modes of surface earthquake faults.

2 Safety evaluation method

2.1 Necessity for safety evaluation against surface fault

Normal faults, reverse faults, strike-slip faults, and rotational faults can be supposed in regard to the modes of surface faults, as shown in fig. 1. After the Chi-chi Earthquake, some studies on the analytical method in regard to the surface earthquake fault were reported. The analytical methods, such as the applied element method [4], the non-linear stochastic finite element method [5], the Lagrangian particle finite difference method [6], and so forth were reported for evaluating the deformation of ground and the behaviour of structures. But, the analytical method for evaluating the discontinuous behaviour of long and large structure induced by a surface earthquake fault has not been established yet. By such a necessity, I studied the analytical method in order to evaluate the seismic safety of long and large structures against surface earthquake faults.

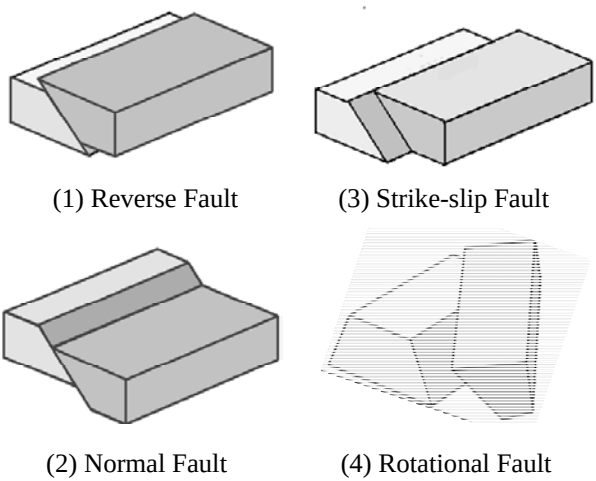

Figure 1: Modes of surface fault.

2.2 FEM model for safety evaluation

A safety evaluation method was devised by applying 3-D dynamic analysis for a coupled dam-joint-foundation-reservoir system [7]. The boundary condition of the FEM model and the way for inputting earthquake action were especially

contrived in this study. 3-D dynamic analysis model for a coupled dam-foundation-fault system is shown in fig. 2 (the wide range model), which was made by assuming that the surface earthquake fault is distributed just below the dam. The width and the depth of the wide range model are 1335m and 1094m, respectively. Fig. 3 shows the narrow range model around the dam, whose width and the depth of the narrow range model are 445m and 218.88m. The analytical results are indicated by using the narrow analytical model around the dam body.

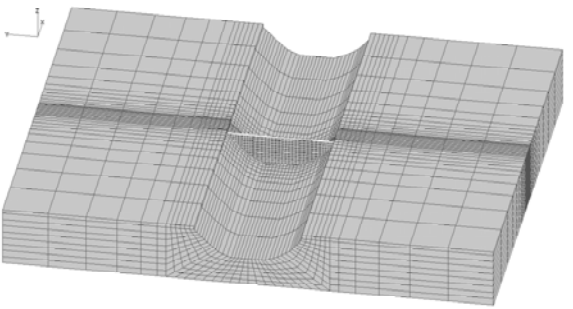

Width:1335.0m, Depth:1094.4m, Height:162.0m

Figure 2: Wide range model.

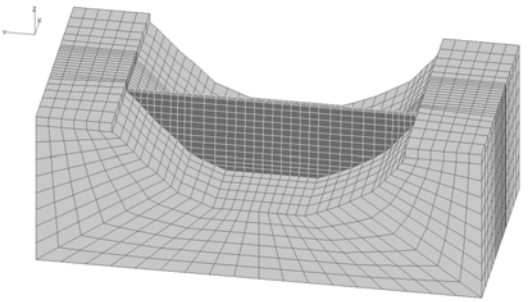

Width:445.0m, Depth:218.88m, Height:162.0m

Figure 3: Narrow range model.

Table 1: Dynamic property values of dam and foundation.

Items	Dynamic shear modulus	Density	Poisson's ratio	Damping factor
Rock foundation	9380 N/mm^2	2.6 t/m^3	0.3	5%
Dam concrete	11032 N/mm^2	2.4 t/m^3	0.2	5%

The dynamic property values of the dam and foundation are shown in Table 1. These property values were identified by the 3-D dynamic simulation analysis for the actual earthquake behaviour of the existing concrete dam based on the earthquake motions recorded during the 1993 Kushiro-oki Earthquake [8].

2.3 Joint element for modeling of fault and joints

Fig. 4 shows the distribution of the fault just below the dam, the contraction joints within the dam body, and the peripheral joint along the dam base. These fault and joints are modeled by using 3-D joint elements. The structural and mechanical characteristics of the 3-D joint element are shown in fig. 5 and fig. 6. In fig. 4, the contact plane of the joint element-1 is composed of foundation rock. The contact plane of the joint element-2 and element-3 is composed of dam concrete. The contact plane of the joint element-4 is composed of foundation rock and dam concrete. The dynamic property values of these 4 kinds of joint elements can be set according to the structural material and the condition of contact plane.

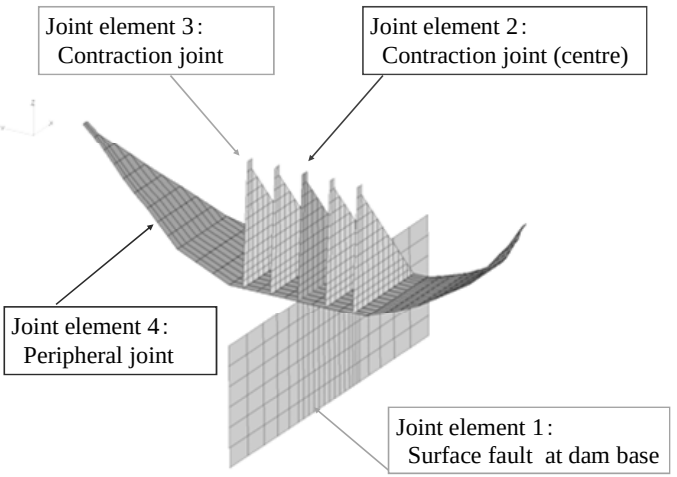

Figure 4: Distribution of fault, contraction joints, and peripheral joint.

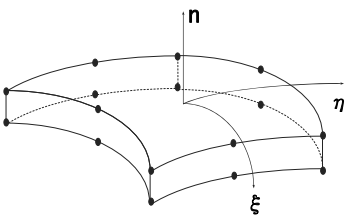

Figure 5: Structure of joint element.

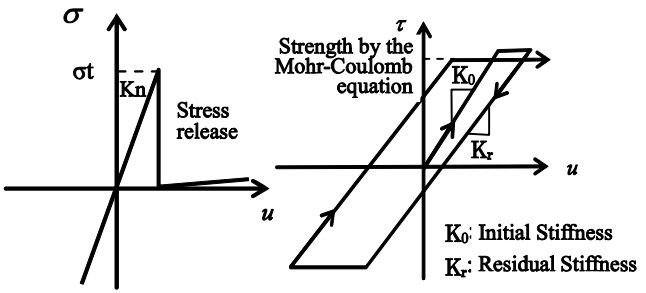

(1) Opening (2) Sliding

Figure 6: Mechanical characteristics of joint element.

The dynamic property values of the fault, the contraction joints, and the peripheral joint are assumed as shown in table 2. Kn is the dynamic shear modulus of joint plane in the normal direction. Ko is the dynamic shear modulus of joint plane in the tangential direction. C is the shear strength of joint plane. φ is the friction angle of joint. Kr is the dynamic shear modulus after opening or sliding. C' is the residual shear strength of joint plane after opening or sliding. φ` is the residual friction angle of joint plane after opening or sliding. H_j is the damping factor of joint. And, σ_t is the initial tensile strength of joint. As for Kn and Ko, the values 10 times as much as the ordinal values are assumed in order to suppress the deformation at the contact plane of joint elements.

Table 2: Dynamic property values of fault and joints.

Fault & Joints	Kn N/mm^2	K_0 N/mm^2	C N/mm^2	φ °	σt N/mm^2	Hj %
Surface Fault	243000	93000	0	45	0.01	5
Contraction Joint(centre)	264000	110000	0	45	0.01	5
Contraction Joint	264000	110000	0	45	0.01	5
Peripheral joint	243000	93000	4.5	45	3.00	5

Kr=1 N/mm^2 C'=0 N/mm^2 φ`=45°

2.4 Boundary condition

The boundary condition of the 3-D analytical model is shown in fig. 7. Free boundary is set at the right half of bottom boundary in order to generate a discontinuous displacement along the fault. Acceleration wave is input from the left half of bottom boundary, which is set to be rigid base. The right and left lateral boundaries are set to be a roller support in the vertical plane. The front

and rear lateral boundaries are set as a free boundary. By setting such boundary conditions, the right half of the 3-D analytical model moves by inertia force, and the discontinuous displacements occur along the fault. Consequently, the behavior of dam against the surface fault displacement, the opening and sliding of the contraction joints and the peripheral joint, and the discontinuous relative displacement can be simulated.

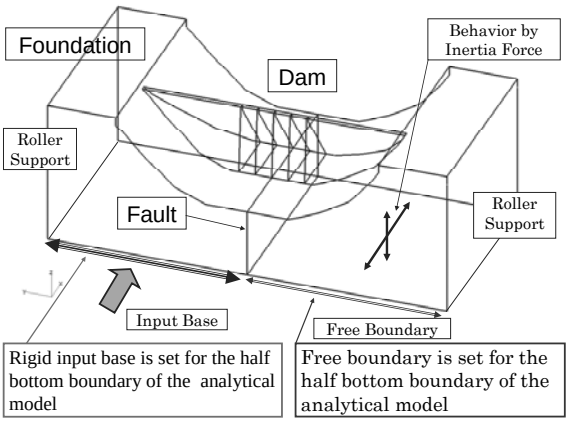

Figure 7: Boundary condition of 3-D FEM model.

2.5 Acceleration input

The acceleration wave form shown in fig. 8 is input as a seismic action by the surface fault from the bottom of 3-D FEM model, because it is necessary to input very strong acceleration toward one direction in order to simulate the large discontinuous displacement along the fault, and incidentally to simulate the discontinuous behaviours at the contraction joints and the peripheral joint. The acceleration wave form can be expressed by the curve of second degree, which is convex down ward. The maximum amplitude of acceleration wave is assumed to be 1G, and the duration time is 3 seconds.

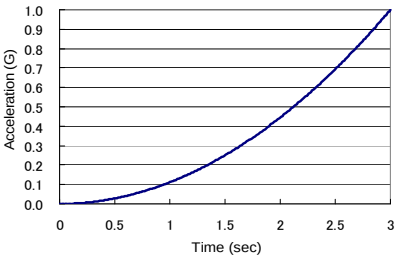

Figure 8: Acceleration input at the bottom boundary.

3 Results of analyses

3.1 Analytical result in regard to strike-slip fault

The analytical result in regard to the discontinuous behaviour of the dam when the acceleration wave was input in the horizontal up-down stream direction by using the wide analytical model is shown in fig. 9. The mode of strike-slip fault can be simulated by inputting the acceleration wave in the horizontal direction. In this case, the maximum residual displacement of joints at the centre of dam base was approximately 0.18m.

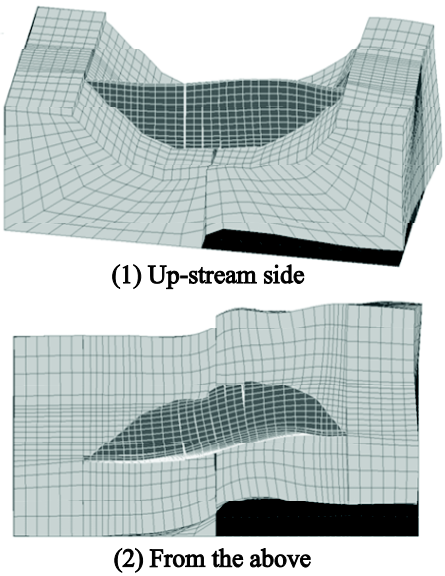

Figure 9: Analytical result in regard to discontinuous behaviour of dam caused by strike-slip fault.

3.2 Analytical result in regard to reverse fault

The analytical result in regard to the discontinuous behaviour of the dam when the acceleration wave was input in the vertical direction by using the wide analytical model is shown in fig. 10. Discontinuous behaviour of the dam caused by reverse fault, or the mode of reverse fault can be simulated by inputting the acceleration wave in the vertical direction. In this case, the maximum residual displacement of joints at the centre of dam base was approximately 2.4m.

3.3 Analytical result in regard to rotational fault

The result when the acceleration wave was input in the vertical direction by using the narrow analytical model is shown in fig. 11. The mode of rotational

fault can be simulated by inputting the acceleration wave in the horizontal direction and using the narrow model. In this case, the maximum residual displacement of joints at the centre of dam base was approximately 1.9m.

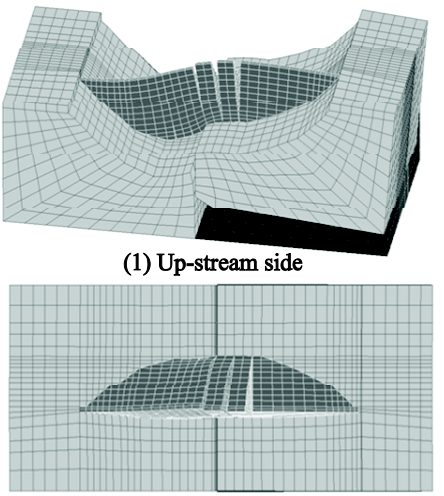

Figure 10: Analytical result in regard to discontinuous behaviour of dam caused by reverse fault.

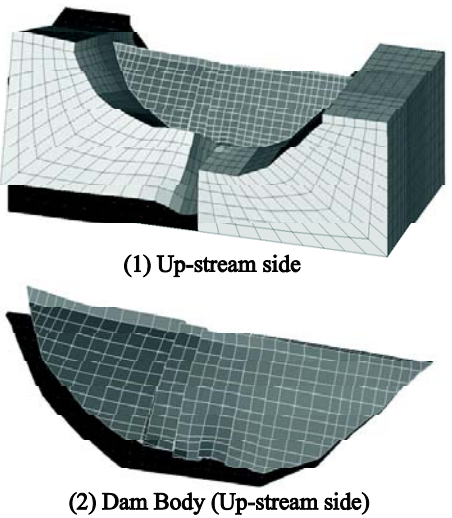

Figure 11: Analytical result in regard to discontinuous behaviour of dam caused by rotational fault.

4 Conclusions

Safety evaluation against a surface earthquake fault is an important subject for long and large structures. Therefore, I devised a safety evaluation method against surface fault displacement induced by an earthquake.

The method proposed was developed by applying 3-D dynamic analysis for a coupled dam-joint-foundation-reservoir system.

Applicability of the method proposed was examined by the case study under the assumption that the fault is distributed just below the concrete gravity dam, by taking the actual case of the Shih-Kang Dam.

The discontinuous behavior and the residual displacement of dam-fault-foundation system against various modes of faults can be simulated by the method proposed.

A vertical fault displacement in connection with a reverse fault can be analyzed by inputting an acceleration wave in the vertical direction from the half of the rigid base of 3-D model.

A horizontal fault displacement in connection with a strike-slip fault can be analyzed by inputting an acceleration wave in the horizontal up-down stream direction.

A rotational fault displacement can be simulated by combining a horizontal input and a vertical input.

The residual displacements along the fault and joints will be changed according to the conditions of the input wave and the boundary condition of analytical model. Quantitative evaluation for dynamic property values of contact plane of fault and joints, the frequency and amplitude of input wave, and the verification of validity of the method proposed are the subjects for future study.

The method proposed is effective for evaluating discontinuous behaviors of the coupled dam and surface earthquake fault system. The proposed method can be broadly applied for various kinds of structure-foundation-fault system.

The prediction of earthquake occurrence and the estimation of earthquake motion have been a main theme in the conventional studies on active faults, up to now. If it will be possible to predict the movement of a surface earthquake fault and to forecast a displacement along the surface earthquake fault, more rational safety evaluation will be realized.

References

[1] Sherard, J. L., Cluff, L. S. and Allen, C. R., Potentially active faults in dam foundations, *Geotechnique* 24, No.3, 367-428, 1974

[2] Leps, T.M., The influence of possible fault offsets on dam design, *Water Power & Dam Construction*, 36-43, 1989

[3] Lee, J. C., Chu, H.T., Angelier, J., Chan, Y. C., Hu, J. C., Lu, C. Y. and Rau, R. J., Geometry and structure of northern surface ruptures of the 1999 Mw=7.6 Chi-Chi Taiwan Earthquake: influence from inherited fold belt structures, *Journal of Structural Geology* 24, 173-192, 2002

[4] Meguro, K. and Ramancharla, P. K., Numerical study on the Characteristics of the ground responses in the Near-Fault regions, *Proceedings of 11th Japan Earthquake Engineering Symposium*, Japanese Geotechnical Society, 397-400, 2002
[5] Hori, M., Anders, M and Gotoh, H., Model experiment and numerical simulation of surface earthquake fault induced by lateral strike slip, *Structural Eng./Earthquake Eng.*, JSCE, Vol.19, No.2, 227-236, 2002
[6] Konagai, K. and Johansson, J., Two dimensional Lagrangian Particle Finite Difference Method for modeling large soil deformation, *Structural Eng./Earthquake Eng.*, JSCE, Vol.18, No.2, 105-110, 2001
[7] Ariga, Y., Cao, Z., Watanabe, H., Seismic stability assessment of an existing arch dam considering the effects of joints, *Proceedings of the 21st International Congress on Large Dams*, Q.83-R.33, 553-576, 2003
[8] Ariga, Y., 3-D reproduction analyses for actual earthquake behaviours and quantitative evaluation of dynamic property values of existing concrete dams, *The Ninth Canadian Conference on Earthquake Engineering*, No.1043, p.238-247, 2007

Garigliano nuclear power plant: seismic evaluation of the turbine building

P. Palumbo[1], L. Gramiccia[2], S. Cardellicchio[1], E. Faccioli[3] & M. Villani[3]
[1]*Sogin spa, Italy*
[2]*SRS Group, Italy*
[3]*Studio Geotecnico Italiano, Italy*

Abstract

The Italian Garigliano Nuclear Power Plant (NPP) started its energy production in 1963. At present it is in the decommissioning stage. In order to get a proper management of the radioactive waste that will be produced during the dismantling operations it has been considered convenient to convert the turbine building of the plant into a temporary waste repository. This decision posed a remarkable seismic safety assessment issue. As a matter of fact, the challenge was to extend, in satisfactory safety conditions, the use of an important facility that has reached the end of its designed lifetime and to have this extended use approved by nuclear safety agencies. In this context many tasks have been accomplished, of which the most important are: (a) a new appraisal of site seismic hazard; (b) the execution of many investigations and testing on the construction materials; (c) the set up of a detailed 3D finite element model including the explicit representation of foundation piles and soil; (d) consideration of soil structure kinematic and dynamic interaction effects. This paper describes the adopted seismic safety assessment criteria which are based on a performance objectives design approach. While performance based design is the approach currently recommended by European Regulations to manage seismic risk and it is fully incorporated in the Italian code for conventional buildings, bridges and plants, NPP are not explicitly considered. Therefore it was necessary to delineate a consistent interpretation of prescribed rules in order to properly select the maximum and operating design earthquakes on one side and corresponding acceptable limit states on the other side. The paper further

WIT Transactions on The Built Environment, Vol 120, © 2011 WIT Press
www.witpress.com, ISSN 1743-3509 (on-line)
doi:10.2495/ERES110181

provides an outline of the numerical analyses carried out, of the main results obtained and of the principal retrofitting actions that will be realized.
Keywords: nuclear power plant, radioactive waste, repository, seismic hazard, existing building.

1 Introduction

The Italian NPP (Caorso, Trino, Garigliano, Latina) are all in the decommissioning phase. SOGIN is the Italian public company that is in charge of the whole process. In the current phase, all different nuclear sites have a significant need of radioactive waste storage capabilities. These needs are typically characterized by a remarkable demand of protected volumes and by the imperative requirement of high safety standards to store materials with a wide typology of radiological hazard. The realization of new repositories is difficult due to scarcity of land areas free from constraints and suitable for construction, and also because of the difficulty in obtaining permits for the realization of new buildings. This situation suggests investigations on the convenience of using existing buildings. For existing structures, beyond the check of the availability of useful volume, the assessment of structural and seismic safety condition is essential. In this regard it should be stressed that nuclear sites in Italy are a very heterogeneous reality not only in terms of seismic hazard but also due to the wide differences of building vulnerability. In order to ensure, throughout the national territory, equal levels of protection against earthquakes and radiation, it is therefore necessary to establish general design criteria. In this context, studies carried out for the Garigliano NPP constitute a significant step in the complex process of unification of the design criteria. The evaluation activities of the turbine building at Garigliano were aimed at:

1. ascertaining the seismic safety of the structures;
2. defining the possible intervention strategies to upgrade structures in view of future uses;
3. designing of the upgrading work.

The safety of an existing structure is an unknown entity whose appraisal is affected by uncertainties related to limited knowledge about materials properties, geometries, construction details, and workmanship. No hidden defects can be excluded a priori. Moreover one should keep in mind that:

1. the aging of structures, even when assisted by regular maintenance, never brings an improvement of safety;
2. the progress of numerical and experimental investigation techniques enables engineers to obtain ever more reliable safety estimates; it follows that the collection of original project documents is necessary but not sufficient for the best assessment of the actual level of safety;
3. the knowledge of intensity and frequency of environmental phenomena (e.g. earthquakes) that interact with structures is constantly evolving.

On these bases it is clear that the role of numerical simulation is of paramount importance and that, to attain reliable estimates of safety margins, numerical models have to be very accurate.

2 Description of the Garigliano turbine building

2.1 Main features of the building and foundation

The turbine building is a reinforced concrete structure. In Figure 1(a) a shot of the whole building is shown. It is composed of three parts, as shown in the scheme in Figure 1(b): a main part (which is taller than the others), an office area (low and lateral) and a workshop area (low and located at the head of the building). The waste storage will be realized in the main part of the building. Due to preliminary considerations on seismic regularity requirements of the building, some necessary civil works have been identified: the main building will be made structurally independent from the other two parts through the realization of separation vertical joints, as shown in Figure 2.

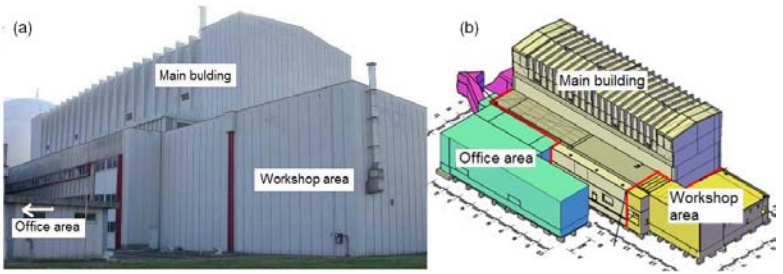

Figure 1: Garigliano turbine building: (a) main view, (b) general scheme.

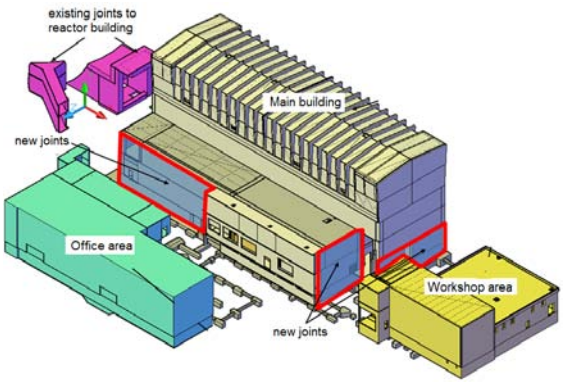

Figure 2: Hypothesis of new separation joints.

The main building is about 70x30m in plant and 30m high. The gross area is about 2000 m^2 and the gross volume is about 60000 m^3; the weight of structures is about 38000 t.

The ground floor is located at an elevation of 10.00 m.a.s.l. (Figure 3); the turbine operating floor is located at 21.45 m.a.s.l; rooftop at 39.5 m.a.s.l.

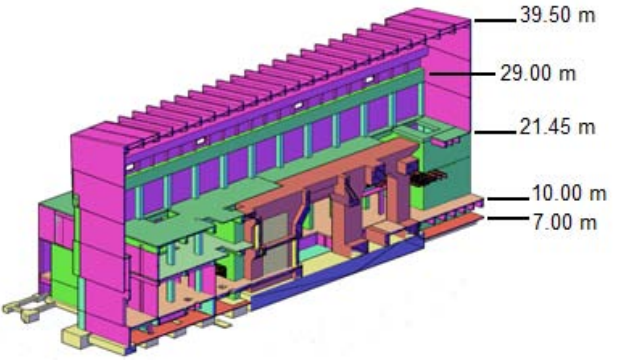

Figure 3: Building longitudinal section.

The building structure presents a strong discontinuity in stiffness at the turbine operating floor level. Below this floor we find shear walls of great thickness and above this floor we find very slender frames which form great portals 20 m high and 20 m wide. These portals present a certain discontinuity in stiffness: between elevation 21.45 and 29.00 m columns spacing is equal to 5 m; above 29.00 m columns spacing is halved. Support for columns with variable cross sections of the upper part is provided by a longitudinal beam of large cross section.

The foundation system is shown in Figure 4: it consists of independent mats laid on the ground at elevations varying between 3 and 5 m. The mats are supported by about 900 weakly reinforced concrete piles having a diameter of 50 cm.

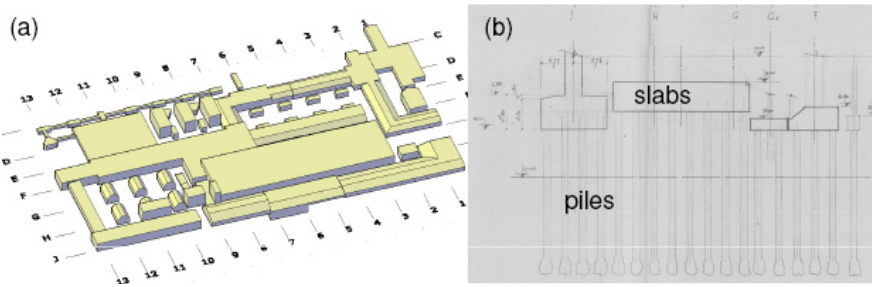

Figure 4: Foundation: (a) mats system, (b) typical foundation section.

2.2 Data collection and supplemental investigations

A significant effort has been dedicated to gathering all the information useful to acquire an adequate knowledge of the physical condition of the structure and of its level of deterioration. In fact, a high level of knowledge is necessary in order to obtain valid estimates of the mechanical parameters of materials required for numerical analysis.

The amount of information gathered through the survey of available drawings, specifications, and other documents was not sufficient to the task. These data have been therefore supplemented and verified by means of nondestructive and destructive on-site investigations and laboratory testing on material specimens. Key locations and parameters have been accurately selected to obtain sufficient knowledge of construction features, materials properties and soil characteristics. The lower bound estimates of material properties have been based on mean values of test results minus one standard deviation. Test results have shown a perfect matching with available data.

A specific soil characterization has been performed through field measurements (cross hole testing) to obtain shear wave velocity profile down to 60 m depth.

3 Seismic hazard and inelastic capacity

3.1 Seismic demand requirements

To highlight the criteria adopted in the selection of the seismic input used in the analyses, let us introduce the "categorization" concept. This concept is synthetically illustrated making reference to Table 1.

Table 1: Design class related to facility hazard category and safety class. (Source: [1]).

DESIGN CLASS SELECTION				
Hazard Category / Safety class	High 1	Moderate 2	Low 3	Conventional 4
Safety class 1	Design class 1	Design class 2	Design class 3	Design class 4
Safety class 2	Design class 2	Design class 3	Design class 3	Design class 4
NNS class	Design class 4	Design class 4	Design class 4	Design class 4

For structures, systems and components (SSC) in the nuclear fuel cycle facilities the International Atomic Energy Agency (IAEA) identifies four "hazard categories": high, moderate, low and conventional. To select the proper category for storage facilities, the quantity, form and isotopes in the storage inventory and therefore the magnitude of the radiological hazard have to be taken into account. Waste storage facilities are usually located in the range between low and moderate hazard category. Furthermore, to assign the so called "design class" (DC), which is related to the level of protection or performance objective to be

ensured, the importance of the SSC under design in providing protection against radiation has to be considered. Since structural integrity has a dominant importance to contain radiation, safety class 1 is generally assigned to civil structures. It follows that DC 2 or DC 3 could be both appropriate for a radioactive temporary waste storage facility. The design classes can be briefly described as follows: DC 1 ensures the level of protection used for NPP; DC 2 ensures an intermediate level of protection (above building code criteria for essential facilities and below NPP criteria); DC 3 ensures the level of protection used in the building code for essential facilities; DC 4 ensures the level of protection used in building code for conventional facilities. DC 2 has been considered appropriate for safety assessment in the present work.

Levels of protection (performance objectives) are defined by associating different threshold limit states (LS) of the structure to earthquake exceedance probabilities. According to EC8 - Part 3 [2], for the protection of ordinary buildings, the approach to be adopted is as follows: LS of Damage Limitation (DL) associated with exceedance probability of 20% in the nominal design life; LS of Significant Damage (SD) associated with exceedance probability of 10% in the nominal design life; LS of Near Collapse (NC) associated with exceedance probability of 2% in the nominal design life. A comparative prospect of limit states as defined in EC8, Italian Code NTC 2008 [3] and FEMA 356 [4] is shown in Table 2.

Table 2: Performance objectives.

FEMA 356	OP	Operational Performance
	IO	Immediate Occupancy
	LS	Life Safety
	CP	Collapse Prevention
EC8	DL	Damage Limitation
	SD	Significant Damage
	NC	Near Collapse
NTC 2008	SLO	Stato Limite di Operatività
	SLD	Stato Limite di Danno
	SLV	Stato Limite di Salvaguardia della Vita
	SLC	Stato Limite di Collasso

Comparison		
FEMA 356	EC8	NTC 2008
OP	DL	SLO
IO		SLD
LS	SD	SLV
CP	NC	SLC

According to NTC 2008 the appropriate levels of protection for essential non nuclear facilities are considered to be achieved by selecting exceedance probabilities (PVR) and return periods (RP) indicated in Table 3 for nominal design life V_n equal to 25 and 50 years. For the temporary waste storage facility of Garigliano NPP V_n = 25 yr. has been chosen. Therefore, to comply with DC 2 criteria, the performance objectives adopted for this facility are as follows:

- the performance objective SLD has to be ensured under the earthquake with return period RP = 500 yr. (see arrows in Table 3);
- the performance objective SLV has to be ensured under the earthquake with return period RP = 1000 yr.

Table 3: Performance objectives and return periods (NTC 2008).

NTC 2008					
Cu=2		coefficient of importance	Cu=2		coefficient of importance
Vn=25 yr		nominal design life	**Vn=50** yr		nominal design life
Vr=50 yr		reference design life	Vr=100 yr		reference design life
performance objective	PVR (exceedance probability)	RP (return period)	performance objective	PVR (exceedance probability)	RP (return period)
SLO	64%	48 yr	SLO	64%	96 yr
SLD	53%	66 yr	SLD	53%	132 yr
SLV	10%	487.5 yr	SLV	10%	975 yr
SLC	5%	987.5 yr	SLC	5%	1975 yr

SLD in NTC 2008 is equivalent to the EC8 Damage Limitation (DL). The structure is only slightly damaged, with structural elements prevented from significant yielding and retaining their strength and stiffness properties. Non-structural components, such as partitions and infills, may show distributed cracking, but the damage could be economically repaired. Permanent drifts are negligible. The structure does not need any repair measures.

SLV in NTC 2008 is equivalent to the EC8 Significant Damage (SD). The structure is significantly damaged, with some residual lateral strength and stiffness, and vertical elements are capable of sustaining vertical loads. Non-structural components are damaged, although partitions and infill panels have not failed out-of-plane. Moderate permanent drifts are present. The structure can sustain after-shocks of moderate intensity. The structure is likely to be uneconomic to repair.

3.2 Hazard evaluation: site response spectrum

The reference response spectrum on free field conditions at the site has been evaluated through probabilistic seismic hazard analysis (PSHA). The results can be expressed either as “hazard curves” (annual probability of exceedance vs. ground motion parameter) for different spectral ordinates or, equivalently, as uniform hazard (UH) response spectra, which indicate, for a fixed annual probability of exceedance, the value of the ground motion parameter vs. the structural period. In a PSHA, the uncertainties are generally divided into aleatory uncertainties, related to the unpredictable nature of future earthquakes and, typically, included in the standard error of the ground motion predictive equations (GMPEs), and epistemic uncertainties, stemming from incomplete data and imperfect knowledge regarding the earthquake process. The latter are accounted for by adopting different models in a logic tree approach. Each branch of this tree represents a different choice regarding a specific step of the analysis, and a normalized weight is assigned to it. The final result derives from the combination of the hazard curves calculated by following all the possible branches of the logic tree.

For the region at study, different representations of the seismogenic zones that govern hazard are possible. The first representation is the seismotectonic model

ZS9 [5], basis of the hazard zonation included in the present Italian seismic code [3]. For this model, the parameters of the Gutenberg Richter relationship have been computed by fitting the earthquake rates derived from the Italian earthquake catalogue CPTI04 (http://emidius.mi.ingv.it/CPTI). The slope *b* of the relationship has been derived both for each source and at a regional level. The second representation is the so-called "smoothed seismicity", [6] in which each point of a grid is considered as a possible source and the rates are computed only on the basis of the earthquake catalogue. To this end, the results obtained in the DPC-INGV national project S2 (http://nuovoprogettoesse2.stru.polimi.it/, 2007-2009) have been used. The third option is a fault model. The basic reference for the description of seismically active faults was taken to be the database of the Italian seismic sources DISS3 (http://diss.rm.ingv.it/diss/). Moreover, since the Italian earthquake catalogue CPTI04 includes an event of magnitude 6.6 (occurred in 1349) at a distance of about 30 km from the NPP, the information derived from the DBMI04 (http://emidius.mi.ingv.it/DBMI04/) the previous version of DISS3.0.4 and the study by [7] have been combined. Thus, a new source for the 1349 earthquake has been defined (red rectangle in Figure 5). All the faults, shown in Figure 5, are considered capable of exhibiting a "characteristic earthquake" [8], modelled through a Brownian Passage Time (BPT) distribution [9], [10]. A background seismicity (for magnitudes $M_w \leq 6.5$) has been associated to the ZS9 sources (green polygons in Figure 5).

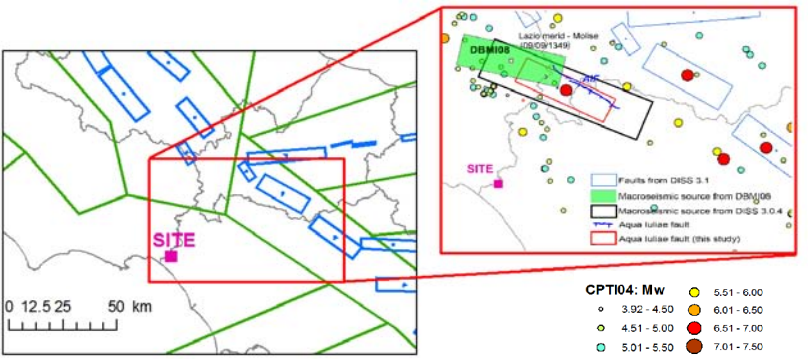

Figure 5: Seismotectonic context of the region at study: SSZs of the ZS9 model (green), faults of DISS3.1.0 (in blue). The zoom on the rhs displays the different reconstructions of the macroseismic source of the 1349 event, according to DBMI04 (green rectangle), DISS3.0.4 (black) and Galli e Naso (2009) (blue line), as well as the source adopted in this analysis (red). (See online for colour version.)

The attenuation equations (GMPEs) adopted for the analysis are: Boore and Atkinson [11], BA08, Cauzzi and Faccioli [12], CF08, Bindi et al. [13], BIEA09 and Akkar and Bommer [14], AB10. Since the models used different definition of the predicted motions, the conversion factors proposed by [15] have been

applied and the results are given in terms of geometric mean of the horizontal components.

As mentioned, the different choices regarding the seismotectonic context, the hazard parameters and the GMPEs have been combined into a logic tree (shown in Figure 6). All the hazard computations were carried out with CRISIS2008 code an enlarged version of the well-known CRISIS2007 code ([16]).

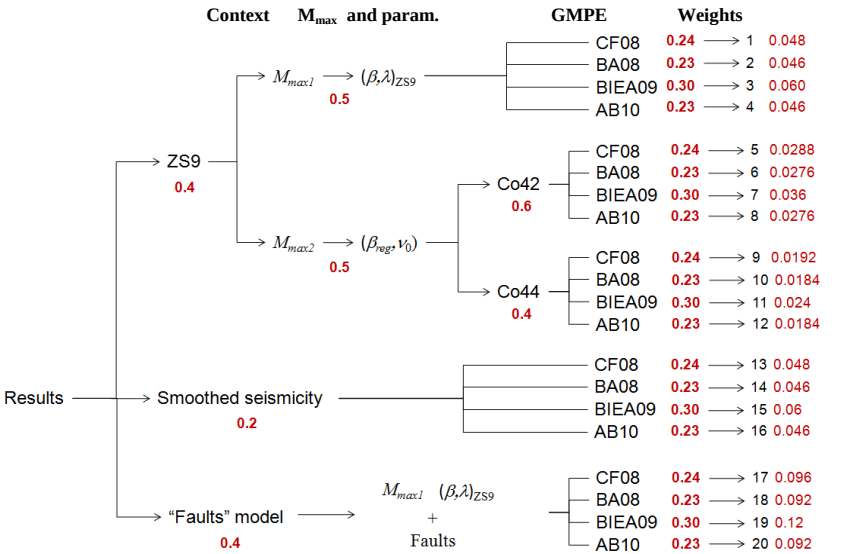

Figure 6: Logic tree adopted in the PSHA. The weights associated with each branch are shown in red. (See online for colour version.)

The resulting UH response spectrum (soil type C, V_{s30}=266 m/s) for a return period (RP) of 975 yr. is shown in Figure 7 in terms of mean and band of dispersion (dotted curves). For the sake of comparison the elastic response spectrum provided by the Italian seismic code NTC2008 is also displayed in the

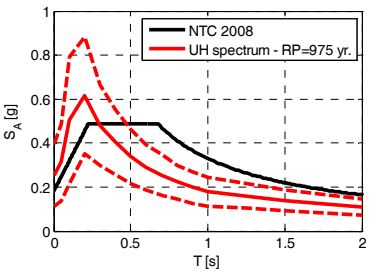

Figure 7: Comparison between the mean UH spectrum for RP=975 yr. And band of dispersion resulting from the analysis and the elastic response spectrum from NTC 2008.

same figure. Note that for a wide range of vibration periods (T>0.4-0.5 s) the UH spectra are lower than the NTC2008 spectrum [3], while for short periods the spectral ordinates of the mean UH spectrum are higher.

3.3 Structure inelastic capacity

Concerning the energy absorption capacity of the structure beyond the elastic limit, it is of interest to summarize the main concepts underlying the adopted approach. In seismic analyses of Single Degree of Freedom (SDOF) systems the relationship between the peak deformation of the inelastic system, U_m, and the corresponding linear system, U_0, is expressed by defining three non dimensional ratios:

- the inelastic deformation ratio: $C = U_m/U_0$;
- the displacement ductility ratio. $\mu = U_m/U_y$;
- the yield strength reduction factor or ductility factor: $R_y = \mu/C = U_0/U_y$ = (strength required for the structure to remain elastic) / (yield strength of the structure);

U_y is the displacement corresponding to the yield strength. The inelastic deformation ratio C and the ductility factor R_y can be expressed as functions of the elastic vibration period $T_n = 1/f_n$ and the ductility ratio μ. The wide variety of investigations aimed at defining reliable relationships among R_y, μ, and T_n is documented in [17] and [18].

The inelastic deformation capacity of existing reinforced concrete structural elements is not known and cannot be identified with precision. To overcome the uncertainties inherent in estimating the ductility of these elements, the performance requirements in the elastic field have to be increased, thereby limiting the demand of ductility resources. At the same time, however, the presence of a sufficient safety margin must be ensured in order to minimize the risk of brittle fracture. In this respect, international standards have the following positions.

IAEA [19] defines the "inelastic energy absorption factor" F_μ, for each system, structure member or component. These factors express the amount by which the elastically computed seismic demand for the specific system, structure member or component is to be reduced to determine the inelastic seismic demand.

In Annex III of [19] the coincidence of F_μ with the R_y factor is established with the addition of a questionable note which states that, to simplify the approach, F_μ is assumed to be independent on frequency.

With regard to the same issue, EC8 - Part 3 [2] provides the following indications: "In the q-factor approach the design spectrum for linear analysis is obtained from EN 1998-1: 2004, 3.2.2.5. A value of q = 1,5 and 2,0 for reinforced concrete and steel structures, respectively, may be adopted regardless of the structural type. Higher values of q may be adopted if suitably justified with reference to the local and global available ductility, evaluated in accordance

with the relevant provisions of EN 1998-1: 2004". The q factor even in this case is equivalent to the above defined reduction factor R_y and is considered independent of frequency. The q-factor approach is also adopted by the Italian code NTC 2008 [3].

The U.S. Electric Power Research Institute (EPRI) [20] defines the so called "ductility reduction factor", $k = 1/R_y$. The reduced earthquake forces are obtained by multiplying the elastically calculated forces by the reduction factor, k. EPRI suggests: "for all but the most brittle failure modes, one can very conservatively choose k = 0.8", which means $R_y = 1.25$.

In this work, the assessment of SLV performance objective has been carried out by means of linear analyses. The inelastic deformation capacity of reinforced concrete structural elements has been taken into account by considering the dependency of R_y on frequency and by conservatively assuming the R_y-μ-T_n Newmark's relationship with $\mu = 1.5$. It follows that, in the range of frequencies between 2 and 8 Hz, R_y is equal to 1.4.

4 Seismic response analysis

4.1 Finite element model

The finite element model adopted for the structure is shown in Figure 8. A portion of soil and the piles have been explicitly represented in the model to reproduce the effects of soil structure interaction. The volume of soil considered in the model has no mass, is sufficiently broad as to make irrelevant the influence on response of the boundary constraints and takes into account the soil layering profile of the site.

The model of the superstructures is made of beam, plates and massive finite elements and reproduces in great detail the geometry and stiffness of all structural components. In addition to masses resulting from dead loads, the mass of auxiliary systems (i.e. cranes), radioactive material and containers to be stored is properly distributed at different levels. The total weight due to these overloads is approximately 10.000 t; therefore the total mass of the model is about 38.000+10.000 = 48.000 t.

4.2 Dynamic and seismic response of the structure

The earthquake response of the turbine building has been evaluated through linear dynamic and response spectrum analyses. Soil-structure interaction (SSI) causes an increase in the fundamental natural period of the structure and in damping values with respect to the theoretical assumption of rigid soil. As known, an increased period due to SSI may lead, as a result of soil or seismological factors, to higher response of the superstructure [21]. As far as the change in damping is concerned, it is the result of energy dissipation in the soil due to radiation and material damping.

In the modal analysis procedure, SSI mainly affects the fundamental vibration modes only, i.e. modes with higher participation factors, whereas the higher

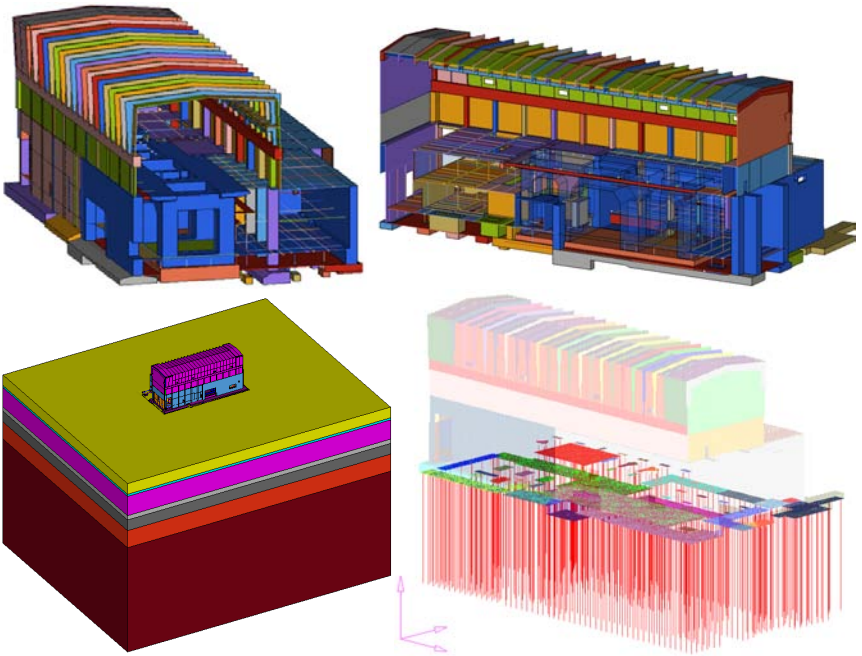

Figure 8: Finite element model of the turbine building – different views.

modes are relatively unaffected. SSI effects have been therefore taken into account in the analyses by adopting empirical findings [22] and by properly modifying the elastic response spectrum ordinates according to the criteria described in Appendix E of [23]. The expected shear modulus at small strain levels for the soils beneath the foundations have been estimated from shear wave velocity profile obtained by cross-hole testing. The shear modulus value at large strain levels, compatible with the adopted seismic excitation, has been determined in accordance with [4].

The fundamental modes of the building involve mainly the large portal above 21.45 m elevation. The fundamental transverse mode (Figure 9, left) presents a flexional shape both in horizontal and vertical planes, with maximum deflections located in the middle vertical plane of the building; the mode is associated with a frequency of 2.3 Hz and involves about 80% of the total mass. The fundamental longitudinal mode (Figure 9, right) presents local peaks of deformation in the head walls; it is associated with a frequency of 2.5 Hz and involves up to 95% of the total mass. The first fundamental vertical mode is at 4.3 Hz and involves about 75% of total mass.

As previously mentioned, the temporary waste storage facility should ensure the performance objective SLD against the earthquake with RP = 475 yr and the performance objective SLV against the earthquake with RP = 1000 yr.

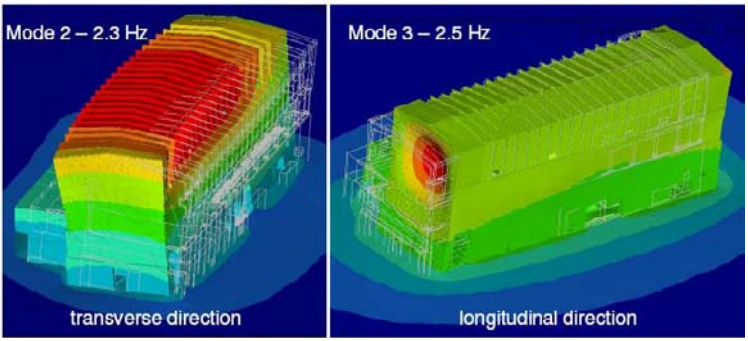

Figure 9: Horizontal fundamental modes – displacement contours.

In the response spectrum analyses the simultaneous occurrence of horizontal and vertical seismic motions has been taken into account by using the SRSS combination rule.

The results obtained reveal the negative effects produced by the existing structural irregularities along the height of the building. The most important of these irregularities is related to the disappearance of the shear walls in the upper part of the structure starting from the turbine operating floor. These deficiencies cause excessive lateral flexibility in the upper part of the building with consequent large displacements of portals and head walls. Some sections in the portal and in the head walls (i.e. the base sections of columns and the middle sections of roof beams) are subjected to excessive stress levels.

4.3 Safety assessment of foundations

4.3.1 Main assumptions

The resisting capacity of the foundation soil subjected to static and seismic actions has been assessed considering a shallow foundation system; piles have been solely regarded as a means to improve soil strength.

This approach is dictated primarily by the fact that piles, with diameter of 50 cm and length not accurately known but variable according to the soil local profile, are reinforced only in the uppermost 5 m, with a very limited presence of steel reinforcement. It follows that any attempt to treat piles as structural elements leads to a conflict with the minimum code requirements of strength for deep foundation systems, especially in seismic conditions.

Such an approach, i.e. shallow foundations on improved soil, allowed us to consider less restrictively the following issues. First, the actual state of integrity and quality of piles is not known. The behavior of the “shallow foundations on improved soil” may be satisfactory in the presence of column elements with mechanical properties inferior to those of reinforced concrete piles and in the presence of force levels higher than those normally allowed for piles.

The second issue concerns the uncertainties associated with the actual length of the piles, varying roughly between 13 and 18 m. In fact, it is not possible to know the true length of each pile or to state that the sandy and gravel layers have

been actually reached by all piles, or to exclude the presence of lenses or layers of silty-clay below the base of piles clamped in the sandy and gravel layers. Even from this point of view, the behavior of the "shallow foundations on treated soil" may result satisfactory in situations where, locally, the minimum safety requirements for bearing capacity of foundation piles cannot be met.

4.3.2 Bearing capacity assessment

As seen previously, the dynamic analysis has been carried out using a finite element model of the structure-foundation system in which the soil is modeled as an elastic medium. A set of equivalent static forces has been derived from the response spectrum analysis and, subsequently, the bearing capacity and safety margins of the foundations have been assessed by means of non linear static analysis involving advanced modeling of the soil behavior [24]. Concepts underlying the displacement based "pushover" analyses, commonly used for superstructures, have been extended to the supporting foundation and soil. The "pushover" analyses have been carried out considering separately each single mat-piles system and consequently, neglecting the stiffness provided by the presence of superstructures. In Figure 10 a typical pushover curve obtained for a foundation mat, pile and soil system under vertical and horizontal loads is shown. The bearing capacity and the safety against sliding of the foundation have been assessed through the identification of a displacement threshold representing the required performance limit. In the present example the limit has been attained for a load multiplier equal to 1.5, whereas the required load multiplier, according to [3], should be 2.3.

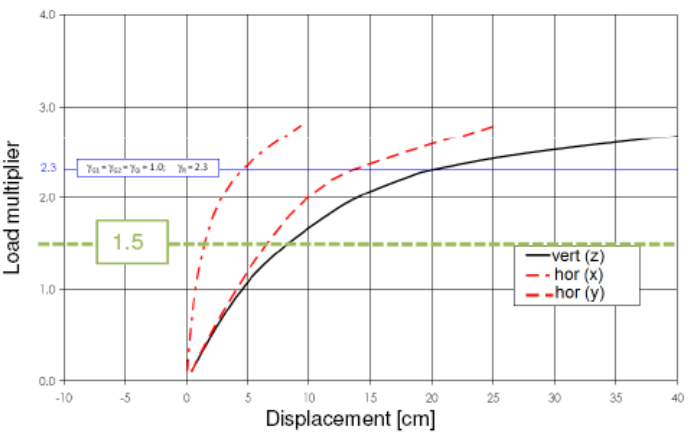

Figure 10: Pushover curve for a foundation mat (bearing capacity).

Pushover analyses pointed out that, for the bearing capacity against the strongest earthquake (RP=1000 yr), in the worst cases, foundations have capacities equal to 0.65÷0.8 times the required one. On the contrary, on the side

of the sliding capacity assessment, the analyses have shown sufficient safety margins.

5 Planned retrofitting actions

According to FEMA [4, 25] four main retrofitting strategies can be conceived: (a) local strengthening of components; (b) removal of existing irregularities; (c) global structural stiffening; (d) global structural strengthening.

The turbine building upgrading requires the simultaneous use of all these strategies. The local strengthening will increase the capacity of single structural elements without affecting the overall response of the structure. The removal of existing irregularities will reduce the demand predicted by the analysis. Construction of new braced frames or shear walls within the structure is an effective measure for adding stiffness in places where it is lacking.

The main planned actions for seismic rehabilitation of the Garigliano turbine building consist of: (1) the strengthening of the upper part of the building starting from the turbine operating floor, and (2) the upgrading of foundations.

To attain the first aim, braced frames or shear walls in cross direction will be built. Furthermore, beams to reduce the flexional deformability of the head wall will be added. It is worth noting that these new structures should not disturb the normal radioactive waste handling in the storage.

Local strengthening actions are limited to few columns at the 21.45 m elevation that will be strengthened by means of steel jacketing. A further local strengthening will be designed for the existing steel connections between the turbine pedestal and the main body of the building at the 21.45 m elevation.

On the foundation side, the upgrading actions should improve both the uniformity of the distribution onto the soil of the actions coming from the superstructure and the soil bearing capacity.

To comply with the first aim, new stiffened slabs will be poured at ground level; these new structures will have the twofold effect of connecting the existing mats and of providing the proper increment of bending stiffness. To achieve the second goal, grouting operations in the soil will be carried out.

6 Conclusions

In the near future the turbine building of the Garigliano NPP could be used as a temporary radioactive waste storage facility. In this paper the method and design criteria adopted to achieve a reliable estimate of the building capacity to withstand the design earthquake have been briefly described. Numerical safety assessment and critical issues in the superstructure and in the foundations are described. An overview of strengthening interventions to be implemented to achieve the required level of seismic safety has been also provided.

The seismic safety assessment of the turbine building is clearly a very significant component of the complex evaluation of costs and benefits associated with a safe extension of the structure life. In this regard, it is worth to bear in mind that the resistance against earthquake of old reinforced concrete structures

strongly depends on the chemical and physical effects of aging, the careful conception of construction details and the quality of execution.

The information that can be retrieved in regard to these aspects has a mostly qualitative nature. It is therefore difficult to translate it into numerical parameters even of the most appropriate and accurate mathematical model. This observation inevitably suggests the belief that even the most extensive investigations about construction materials and the highest level of accuracy and completeness of the mathematical simulation should in any case be accompanied by a mature and expert engineering judgment.

References

[1] IAEA-TECDOC-1250, *Seismic design considerations of nuclear cycle facilities*, October 2011.
[2] EN 1998-3, Eurocode 8 (EC8), *Design of structure for earthquake resistance. Part 3: Assessment and retrofitting of buildings*, August 2005.
[3] D.M. 14 gennaio 2008, *Norme tecniche per le costruzioni* (NTC 2008), 2008.
[4] FEMA 356, *Prestandard and commentary for the seismic rehabilitation of building*, November 2000
[5] Gruppo di Lavoro, 2004a per la redazione della mappa di pericolosità sismica. INGV, Final Report, (http://esse1.mi.ingv.it) with Appendices.
[6] Frankel, A., 1995. *Mapping seismic hazard in the central and eastern United States*, Seism. Res. Lett. 66, 8–21.
[7] Galli, P.A., Naso, J.A., *Unmasking the 1349 earthquake source (southern Italy): paleoseismological and archaeoseismological indications from the Aquae Iuliae fault*, Journal of Structural Geology, 31, 128–149, 2009.
[8] Youngs, R.R., Coppersmith, K.J. *Implications of fault slip rates and earthquake recurrence models to probabilistic seismic hazard estimates, Bulletin of the Seismological Society of America*, Vol. 75, No. 4, pp. 939–964, 1985
[9] Matthews, M.V., Ellsworth, W.L., Reasenberg, P.A. *A Brownian Model for Recurrent Earthquakes*, Bulletin of the Seismological Society of America, Vol. 92, No. 6, pp. 2233–2250, 2002
[10] Peruzza, L., Pace, B., Cavallini, F. *Error propagation in time-dependent probability of occurrence for characteristic earthquakes in Italy*, Journal of Seismology, DOI 10.1007/s10950-008-9131-1, 2010.
[11] Boore, D.M., and Atkinson, G.M. *Ground-motion prediction equations for the average horizontal component of PGA, PGV, and 5%-damped PSA at spectral periods between 0.01 s and 10.0 s*, Earthquake Spectra, 24(1), 99-138, 2008.
[12] Cauzzi, C., and Faccioli, E., *Broad band (0.05 s to 20s) prediction equations for displacement response spectra calibrated on a worldwide digital database*, Journal of Seismology 12, 453-475, 2008.
[13] Bindi D., Luzi L., Massa M., Pacor F., *Horizontal and vertical ground motion prediction equations derived from the Italian Accelerometric*

Archive (ITACA). Bulletin of Earthquake Engineering. In press. doi: 10.1007/s10518-009-9130-9, 2009.
[14] Akkar, S., and Bommer, J.J. *Empirical equations for the prediction of PGA, PGV and spectral acceleration in Europe, the Mediterranean region and the Middle East*. Seismological Research Letters, vol. 81(2) pp. 195-206, 2010.
[15] Beyer K., Bommer J.J., *Relationships between Median Values and between Aleatory Variabilities for Different Definitions of the Horizontal Component of Motion,* Bulletin of the Seismological Society of America, Vol. 96, No. 4A, pp. 1512–1522, 2006.
[16] Ordaz M., Jara J.M., Singh S.K. *Riesgo sísmico y espectros de diseño en el estado de Guerrero*. Technical Report, Instituto de Ingenieria, UNAM, Mexico City, 1991.
[17] E. Miranda, V. Bertero, *Evaluation of strength reduction factors for earthquake-resistant design*, Earthquake Spectra, Vol. 10, No 2, 1994.
[18] A.K. Chopra, R.K. Goel, *Capacity-demand-Diagram for estimating seismic deformation of inelastic structures. SDOF systems*, Report PEER-1999/0.
[19] IAEA - Safety Reports Series No. 28, *Seismic evaluation of existing Nuclear Power Plant*, 2003
[20] Electric Power Research Institute (EPRI), *A methodology for assessment of Nuclear Power Plant Seismic Margin*, EPRI NP-6041, October 1988.
[21] G. Gazetas, *Seismic design of foundations and soil-structure interaction*, First ECEES, 2-8 September 2006.
[22] J.P. Stewart, J.P. Seed, G.L. Fenves, *Seismic soil structure interaction in buildings. II: empirical findings*, ASCE Journal of geotechnical engineering, 1999.
[23] FEMA 440, *Improvement of nonlinear static seismic analysis procedures*, June 2005.
[24] SGI – Studio Geotecnico Italiano - *Servizio di valutazione sismica dell'edificio turbina della centrale del Garigliano – Verifica delle fondazioni in condizioni sismiche*, SGI Report n. 08073-060RO1E01, November 2010.
[25] FEMA 547 *Techniques for the Seismic Rehabilitation of Existing Buildings*, October 2006.

This page intentionally left blank

Seismic history analysis of asymmetrical adjacent buildings with soil-structure interaction consideration

M. E. Uz & M. N. S. Hadi
School of Civil, Mining and Environmental Engineering, University of Wollongong, NSW, Australia

Abstract

The seismic response history analysis of multi-storey asymmetric adjacent buildings with soil-structure interaction (SSI) during impact is investigated in this study. The coupled multi-degree of freedom modal differential equations of motion for the two way asymmetric shear buildings are derived and solved using a step by step solution by the fourth-order Runge-Kutta method with impact and without impact. The SSI forces are modelled in the form of the frequency-independent soil springs and dashpots. A numerical example of two-way asymmetric four-storey adjacent buildings under the variation of the important SSI system parameters such as the large and small SSI effects is investigated under the excitation of the 1940 El Centro Earthquake. This study shows that the lateral torsion response of both buildings is affected when impact takes place with the adjacent buildings. The first three modal response histories of each building are significantly reduced due to the effect of the small SSI. Further, it is also observed that the roof twist of the lighter buildings is decreased for the large SSI effect compared to the small SSI effect. Finally, in increased eccentricities, the impact response of buildings is significantly severe.
Keywords: earthquake engineering, impact effects, soil-structure interaction, asymmetry.

1 Introduction

Providing the required separation distance is not always possible. Many researchers have investigated the pounding problem of seismic analysis of two way asymmetric buildings with soil-structure interaction under the two


WIT Transactions on The Built Environment, Vol 120, © 2011 WIT Press
www.witpress.com, ISSN 1743-3509 (on-line)
doi:10.2495/ERES110191

directional ground motions [1–5]. In these studies, to deal with the non-proportional damping of the SSI systems, equivalent modal damping was calculated to facilitate the modal response history analysis. The equivalent modal damping was estimated by either quantifying the dissipated energy in the soil [6] or matching the approximation approaches normal mode solution with the rigorous solution for a certain structural location [3]. For engineering applications without the need for calculating the complicated equivalent modal damping, a simple and real valued modal response history analysis has been developed [7]. Moreover, the effects of both the SSI systems and pounding on the coupled buildings under strong earthquakes have not been investigated fully. The aim of this study is to conduct a comparative study in order to investigate the SSI effect onto adjacent buildings considering the effect of pounding. Based on the fourth order Runge-Kutta method, a MATLAB program is developed to solve the equations of motion for the SSI systems of coupled buildings subjected to pounding effects under the excitations of earthquake ground acceleration and numerical simulations presented are used. The issue of the pounding of bidirectional asymmetric adjacent buildings with the SSI systems is not familiar with the complex-valued seismic analysis procedures in the frequency domain [8, 9]. A response history analysis procedure considering of both effects is proposed using the MDOF modal equations of the motion by watching the solutions of equations of motions for the whole SSI systems and pounding on the adjacent buildings in the following numerical examples.

2 Theoretical background of system model

In order to consider the effects of the large and small SSI systems, two-way asymmetric coupled buildings are modelled in this study. To validate the equation of motion for the whole SSI system comparing to the multi-degrees of freedom modal equations of the motion, a modal analysis study is conducted herein. The interaction forces at the soil-structure interface are simulated using frequency-independent spring and dashpot set in parallel [10]. The rectangular dimensions of foundations for both buildings are converted as circular footings in order to adopt the frequency independent spring and dashpot set. The simplified model of N- and S- storey coupled buildings resting on the surface of an elastic half-space is shown in Figure 1. For i= (1,2,.,N) and j=(1,2,.,S), $m_i, k_{xi}, c_{xi}, k_{yi}, c_{yi}, I_{xi}$ and I_{yi} are the mass, the elastic structural stiffness, damping coefficients and moments of inertia of the related floor about the axes through the centre of mass (CM) and parallel to the x and y axes for Building A and Building B, respectively. The subscripts i and j in Figure 1 are the storey number of the buildings that denote 1, 2,., N for Building A and 1, 2,.,S for Building B. Moreover, the subscripts and superscripts of a and b symbolize Building A and Building B, respectively. For the horizontal component of ground motion assumed to be uniform over the base of the buildings, the total number of degrees of freedom is 3N+5 for N-storey building and therefore 3N+5 and 3S+5 equations are required for both Building A and Building B,

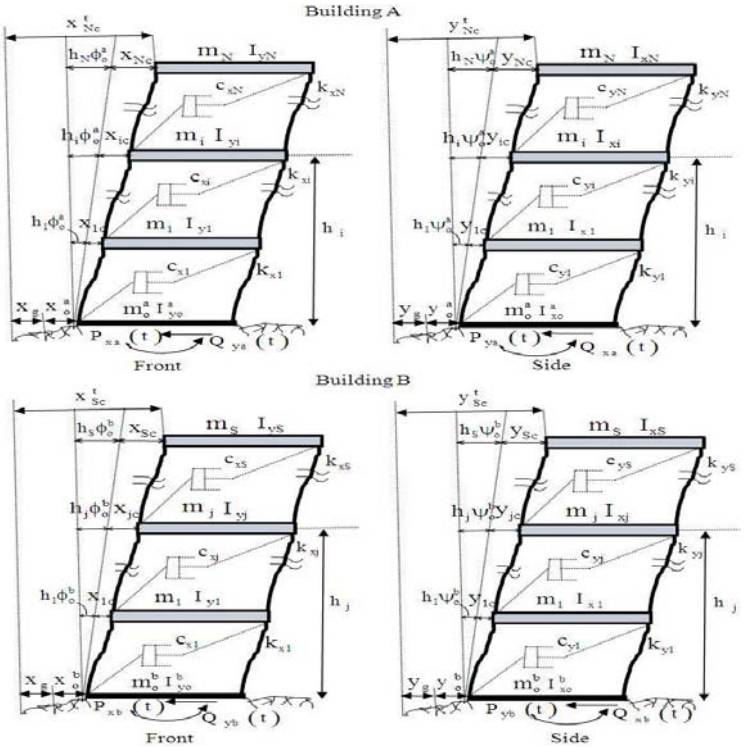

Figure 1: Elevation of dynamic model for asymmetric adjacent shear buildings.

respectively. Equations for Building B are the same as shown below for Building A associated with the number of storey (j) of Building B.

Hence, only the equations of Building A are expressed here. Translation in the longitudinal (x) and transverse (y) directions and rotation about the CM of these equations may be expressed as shown in Eqn. (1). As an example, for N-storey Building A, the total number of degrees of freedom, 3N+5 are obtained as 3N equations of dynamic equilibrium of each floor of the superstructure for the translation in the x and y directions and rotation about the centre of mass and 5 degrees of freedom due to interaction at the foundation. The 3N equations of dynamic equilibrium of each floor of Building A may be expressed as

$$
\begin{aligned}
&[M_a]\{\ddot{x}^t_{ic}\}+[C_{ax}]\{\dot{x}_i\}+[K_{ax}]\{x_i\}+\left[F^p_{xij}(t)\right]=\{0\}\\
&[M_a]\{\ddot{y}^t_{ic}\}+[C_{ay}]\{\dot{y}_i\}+[K_{ay}]\{y_i\}+\left[F^p_{yij}(t)\right]=\{0\}\\
&r_a^2[M_a]\{\ddot{\theta}^t_i\}+f_a[C_{ax}]\{\dot{x}_i\}-e_a[C_{ay}]\{\dot{y}_i\}+\left[C^a_{\theta R}\right]\{\dot{\theta}_{ic}\}+f_a[K_{ax}]\{x_i\}-e_a[K_{ay}]\{y_i\}\\
&\qquad\qquad+\left[K^a_{\theta R}\right]\{\theta_{ic}\}+\left[F^p_{\theta ij}(t)\right]=\{0\}
\end{aligned}
\tag{1}
$$

where M_a, C_{ax}, K_{ax}, C_{ay} and K_{ay} are the $N \times N$ sub-matrices of mass, damping and lateral stiffness in the x and y directions of Building A, respectively. x_{ic}^t, y_{ic}^t and θ_i^t are the total displacements of centre of mass of the floors in the longitudinal and transverse directions, and the total twist of the floors about the vertical axis (z) in Building A, respectively. $F_{xij}^P(t)$ denotes the pounding forces in the x direction with the help of the non-linear viscoelastic model [11]. $F_{yij}^P(t)$ and $F_{\theta ij}^P(t)$ have been considered by the Coulomb friction model [12, 13]. x_i, y_i and θ_{ic} are the displacement vectors with respect to the base in the x and y directions of the centre of resistance (CR) and the twist of the floors with respect to the base. Moreover, two way asymmetric buildings are modelled as the CR being not coincident with the CM along the two horizontal plane axes. The static eccentricities of the centre of resistance from the centre of mass (e and f) in the x and y axes are the same for each floor deck, although the CR may vary from storey to storey. Hence, the CR associated with the adjacent buildings is assumed to lie at eccentricities e_a, f_a for Building A and e_b, f_b for Building B. The radii of gyration (r_a and r_b) of any rigid floor decks are about the centre of mass for each building. $K_{\theta R}^a$ and $K_{\theta M}^a$ in Eqns. (1) and (2) are the torsional stiffness matrix defined about the CR and the CM, respectively. Furthermore, C_{ax}, C_{ay} and $C_{\theta R}^a$ in Eqn. (1) are the damping matrices for Building A, assumed to be proportional to the stiffness matrices as defined in Eqn. (2).

$$\begin{gathered}\left[K_{\theta M}^a\right]=\left[K_{\theta R}^a\right]+e_a^2\left[K_{ay}\right]+f_a^2\left[K_{ax}\right] \\ \left[C_{ax}\right]=\alpha\left[K_{ax}\right],\left[C_{ay}\right]=\alpha\left[K_{ay}\right] \text{ and } \left[C_{\theta R}^a\right]=\alpha\left[K_{\theta R}^a\right]\end{gathered} \tag{2}$$

in which α is a constant value in terms of the ratio of the coefficient and stiffness of the buildings. The displacement vectors in the related directions of Building A without SSI effects can be defined by Eqn. (3).

$$\begin{gathered}\{x_{ic}\}=\{x_i\}-f_a\{\theta_{ic}\},\ \{\dot{x}_{ic}\}=\{\dot{x}_i\}-f_a\{\dot{\theta}_{ic}\},\ \{\ddot{x}_{ic}\}=\{\ddot{x}_i\}-f_a\{\ddot{\theta}_{ic}\} \\ \{y_{ic}\}=\{y_i\}+e_a\{\theta_{ic}\},\ \{\dot{y}_{ic}\}=\{\dot{y}_i\}+e_a\{\dot{\theta}_{ic}\},\ \{\ddot{y}_{ic}\}=\{\ddot{y}_i\}+e_a\{\ddot{\theta}_{ic}\}\end{gathered} \tag{3}$$

where x_{ic} and y_{ic} are displacement vectors of degrees of freedom of superstructure about the CM. x_{ic}^t, y_{ic}^t and θ_{ic}^t can be expressed in view of the following relationship of $x_{ic}^{'}$ and $y_{ic}^{'}$ vectors, which are the degrees of freedom of the superstructure defined as in Eqn. (4).

$$\begin{gathered}\{x_{ic}^t\}=x_o^a\{1\}+x_g\{1\}+\varphi_o^a\{h_i\}+\{x_{ic}\} \text{ and } \{x_{ic}^{'}\}=x_o^a\{1\}+\varphi_o^a\{h_i\}+\{x_{ic}\} \\ \{y_{ic}^t\}=y_o^a\{1\}+y_g\{1\}+\psi_o^a\{h_i\}+\{y_{ic}\} \text{ and } \{y_{ic}^{'}\}=y_o^a\{1\}+\psi_o^a\{h_i\}+\{y_{ic}\} \\ \{\theta_i^t\}=\theta_o^a\{1\}+\{\theta_{ic}\}\end{gathered} \tag{4}$$

where x_o^a, y_o^a, ψ_o^a and φ_o^a are the degrees of freedom at the base associated with translations and rocking about the x and y axes, respectively. θ_o^a is the twist about the z axis. After substituting in Eqns. (2), (3) and (4), and rearranging into to Eqn. (1), a more concise form for the $3N \times 3N$ sub-matrices of the superstructure resting on a rigid base on the left upper corner of M^a, C^a and K^a can be written herein. With reference to Figure 1, the equation of motion for the whole foundation system for Building A can be written for the translation in the x and y axes, twist about the z axis and rocking about the x and y axes, respectively as shown in Eqn. (5) [10].

$$\begin{aligned}
&m_o^a\left(\ddot{x}_g + \ddot{x}_o^a\right) + \{1\}^T\left[M_a\right]\left\{\ddot{x}_{ic}^t\right\} + P_{xa}(t) = 0\\
&m_o^a\left(\ddot{y}_g + \ddot{y}_o^a\right) + \{1\}^T\left[M_a\right]\left\{\ddot{y}_{ic}^t\right\} + P_{ya}(t) = 0\\
&r_a^2 m_o^a \ddot{\theta}_o^a + r_a^2\{1\}^T\left[M_a\right]\left\{\ddot{\theta}_i^t\right\} + T_a(t) = 0\\
&\sum_{i=0}^{N} I_{xi}\ddot{\psi}_o^a + \{h_i\}^T\left[M_a\right]\left\{\ddot{y}_{ic}^t\right\} + Q_{xa}(t) = 0\\
&\sum_{i=0}^{N} I_{yi}\ddot{\varphi}_o^a + \{h_i\}^T\left[M_a\right]\left\{\ddot{x}_{ic}^t\right\} + Q_{ya}(t) = 0
\end{aligned} \tag{5}$$

where I_{xi} and I_{yi} are moments of inertia of the i th floor about the axis through the CM and parallel to the longitudinal and transverse directions, respectively. m_o^a is the mass of the foundation of Building A. h_i and h_j are the column vector composed of the storey heights of Building A and Building B throughout the foundation to each floor, respectively. Earthquake ground accelerations in the x and y directions are shown as $\ddot{x}_g$ and $\ddot{y}_g$, respectively. $P_{xa}(t), P_{ya}(t), T_a(t), Q_{xa}(t)$ and $Q_{ya}(t)$ are the interaction forces of Building A based on frequency-independent soil springs and dashpots as shown in Eqn.(5) [4]. The definitions of spring and dashpot constants of the static impedance functions are clearly presented with various subscripts [10]. First assume that two buildings remain in the linear elastic range and hence they do not yield under earthquake excitation. In such a case, the equation of motion in Eqn. (6) for the couple buildings with the whole interactions such as the SSI, torsional coupling and the pounding involved responses of adjacent buildings modelled with elastic systems at each floor level as system is

$$\begin{bmatrix} M^a & 0 \\ 0 & M^b \end{bmatrix}\begin{Bmatrix} \ddot{U}^a(t) \\ \ddot{U}^b(t) \end{Bmatrix} + \begin{bmatrix} C^a & 0 \\ 0 & C^b \end{bmatrix}\begin{Bmatrix} \dot{U}^a(t) \\ \dot{U}^b(t) \end{Bmatrix} + \begin{bmatrix} K^a & 0 \\ 0 & K^b \end{bmatrix}\begin{Bmatrix} U^a(t) \\ U^b(t) \end{Bmatrix} + \begin{Bmatrix} F^P(t) \\ -F^P(t) \end{Bmatrix} = -\begin{Bmatrix} P^a(t) \\ P^b(t) \end{Bmatrix} \tag{6}$$

where M^a, C^a, K^a, M^b, C^b and K^b are the mass, damping and stiffness matrices of couple buildings, respectively. Moreover, $F^P(t)$, $P^a(t)$ and $P^b(t)$ are vectors containing the forces due to impact between floors with masses m_i, m_j and loading of the adjacent buildings in that order (see Eqns. (7), (8) and (9)). $\ddot{U}^a(t), \dot{U}^a(t), U^a(t), \ddot{U}^b(t), \dot{U}^b(t)$ and $U^b(t)$ are the vectors of acceleration, velocity and displacement of the system respectively.

$$M^a=\begin{bmatrix} [M_a] & \mathbf{0}_{N\times N} & \mathbf{0}_{N\times N} & \mathbf{0} & \mathbf{0} & \mathbf{0} & \mathbf{0} & \mathbf{0} \\ \mathbf{0}_{N\times N} & [M_a] & \mathbf{0}_{N\times N} & \mathbf{0} & \mathbf{0} & \mathbf{0} & \mathbf{0} & \mathbf{0} \\ \mathbf{0}_{N\times N} & \mathbf{0}_{N\times N} & r_a^2[M_a] & \mathbf{0} & \mathbf{0} & \mathbf{0} & \mathbf{0} & \mathbf{0} \\ \{1\}^T[M_a] & \{\mathbf{0}\}^T & \{\mathbf{0}\}^T & m_o^a & 0 & 0 & 0 & 0 \\ \{\mathbf{0}\}^T & \{1\}^T[M_a] & \{\mathbf{0}\}^T & 0 & m_o^a & 0 & 0 & 0 \\ \{\mathbf{0}\}^T & \{\mathbf{0}\}^T & r_a^2\{1\}^T[M_a] & 0 & 0 & r_a^2 m_o^a & 0 & 0 \\ \{\mathbf{0}\}^T & \{h_i\}^T[M_a] & \{\mathbf{0}\}^T & 0 & 0 & 0 & \sum_{i=0}^{N} I_{xi} & 0 \\ \{h_i\}^T[M_a] & \{\mathbf{0}\}^T & \{\mathbf{0}\}^T & 0 & 0 & 0 & 0 & \sum_{i=0}^{N} I_{yi} \end{bmatrix}_{(3N+5)\times(3N+5)} \tag{7}$$

where $\mathbf{0}$ and 1 are the $N\times 1$ column vectors whose elements are equal to zero and one, respectively.

$$K^a=\begin{bmatrix} [K_{ax}] & \mathbf{0}_{N\times N} & f_a[K_{ax}] & -[K_{ax}]\{1\} & \mathbf{0} & -[K_{ax}]\{\mathbf{f_a}\} & \mathbf{0} & -[K_{ax}]\{h_i\} \\ & [K_{ay}] & -e_a[K_{ay}] & \mathbf{0} & -[K_{ay}]\{1\} & +[K_{ay}]\{\mathbf{e_a}\} & -[K_{ay}]\{h_i\} & \mathbf{0} \\ \vdots & & [K_{\theta M}] & -[K_{ax}]\{\mathbf{f_a}\} & +[K_{ay}]\{\mathbf{e_a}\} & -[K_{\theta M}]\{1\} & +e_a[K_{ay}]\{h_i\} & -f_a[K_{ax}]\{h_i\} \\ & & \ddots & K_T+\{1\}^T[K_{ax}]\{1\} & 0 & \{\mathbf{f_a}\}^T[K_{ax}]\{1\} & 0 & \{1\}^T[K_{ax}]\{h_i\} \\ \vdots & & & & K_T+\{1\}^T[K_{ay}]\{1\} & \{\mathbf{e_a}\}^T[K_{ay}]\{1\} & \{1\}^T[K_{ay}]\{h_i\} & 0 \\ & & \text{symm} & & \ddots & K_\theta+\{1\}^T[K_{\theta M}]\{1\} & -\{\mathbf{e_a}\}^T[K_{ay}]\{h_i\} & \{\mathbf{f_a}\}^T[K_{ax}]\{h_i\} \\ \vdots & & & & & & K_\psi+\{h_i\}^T[K_{ay}]\{h_i\} & 0 \\ & \cdots & & \cdots & & \cdots & & K_\phi+\{h_i\}^T[K_{ax}]\{h_i\} \end{bmatrix} \tag{8}$$

$$C^a=\begin{bmatrix} [C_{ax}] & \mathbf{0}_{N\times N} & f_a[C_{ax}] & -[C_{ax}]\{1\} & \mathbf{0} & -[C_{ax}]\{\mathbf{f_a}\} & \mathbf{0} & -[C_{ax}]\{h_i\} \\ & [C_{ay}] & -e_a[C_{ay}] & \mathbf{0} & -[C_{ay}]\{1\} & +[C_{ay}]\{\mathbf{e_a}\} & -[C_{ay}]\{h_i\} & \mathbf{0} \\ \vdots & & [C^a_{\theta M}] & -[C_{ax}]\{\mathbf{f_a}\} & +[C_{ay}]\{\mathbf{e_a}\} & -[C_{\theta M}]\{1\} & +e_a[C_{ay}]\{h_i\} & -f_a[C_{ax}]\{h_i\} \\ & & & C_T+\{1\}^T[C_{ax}]\{1\} & 0 & \{\mathbf{f_a}\}^T[C_{ax}]\{1\} & 0 & \{1\}^T[C_{ax}]\{h_i\} \\ \vdots & & \ddots & & C_T+\{1\}^T[C_{ay}]\{1\} & \{\mathbf{e_a}\}^T[C_{ay}]\{1\} & \{1\}^T[C_{ay}]\{h_i\} & 0 \\ & & \text{symm} & & & C_\theta+\{1\}^T[C_{\theta M}]\{1\} & -\{\mathbf{e_a}\}^T[C_{ay}]\{h_i\} & \{\mathbf{f_a}\}^T[C_{ax}]\{h_i\} \\ \vdots & & & \ddots & \text{symm} & & C_\psi+\{h_i\}^T[C_{ay}]\{h_i\} & 0 \\ & \cdots & & \cdots & & \cdots & & C_\phi+\{h_i\}^T[C_{ax}]\{h_i\} \end{bmatrix}$$

$$P^a(t)=\begin{Bmatrix} [M_a]\{1\}\ddot{x}_g \\ [M_a]\{1\}\ddot{y}_g \\ \mathbf{0} \\ \left(m_o^a+\{1\}^T[M_a]\right)\ddot{x}_g \\ \left(m_o^a+\{1\}^T[M_a]\right)\ddot{y}_g \\ 0 \\ \{h_i\}^T[M_a]\ddot{y}_g \\ \{h_i\}^T[M_a]\ddot{x}_g \end{Bmatrix}_{(3N+5)\times 1}, U^a(t)=\begin{Bmatrix} [x'_{ic}] \\ [y'_{ic}] \\ [\theta_i^t] \\ x_o^a \\ y_o^a \\ \theta_o^a \\ \psi_o^a \\ \phi_o^a \end{Bmatrix}_{(3N+5)\times 1}, F^P(t)=\begin{Bmatrix} [F^P_{xij}(t)] \\ [F^P_{yij}(t)] \\ [F^P_{\theta ij}(t)] \\ 0 \\ 0 \\ 0 \\ 0 \\ 0 \end{Bmatrix}_{(3N+5)\times 1} \tag{9}$$

For simulating the pounding force during impact F^P_{xij}, $F^P_{\theta ij}$ $(i=1,2,..N;\ j=1,2,..,S)$, the nonlinear viscoelastic model is used between the storey levels of the two adjacent buildings, which is based on the following formula in Eqn. (10) as both approach period and restitution period of collisions [11, 14].

$$
\begin{aligned}
&F_{xij}^{p}(t)=0 \ \text{ for } \ \delta_{ij}(t)\le 0;\\
&F_{xij}^{p}(t)=\bar{\beta}\left(\delta_{ij}(t)\right)^{3/2}+\bar{c}_{ij}(t)\dot{\delta}_{ij}(t) \ \text{ for } \ \delta_{ij}(t)>0 \ \text{ and } \ \dot{\delta}_{ij}(t)>0;\\
&F_{xij}^{p}(t)=\bar{\beta}\left(\delta_{ij}(t)\right)^{3/2} \ \text{ for } \ \delta_{ij}(t)>0 \ \text{ and } \ \dot{\delta}_{ij}(t)\le 0;
\end{aligned}
\tag{10}
$$

$$
\begin{aligned}
&\bar{c}_{ij}(t)=2\bar{\xi}\sqrt{\bar{\beta}\sqrt{\delta_{ij}(t)}\frac{m_i m_j}{m_i+m_j}};\\
&\bar{\xi}=\frac{9\sqrt{5}}{2}\frac{1-e^2}{e\left(e(9\pi-16)+16\right)}\\
&\delta_{ij}(t)=x_{ic}^{'}(t)-x_{jc}^{'}(t)-D;\\
&\dot{\delta}_{ij}(t)=\dot{x}_{ic}^{'}(t)-x_{jc}^{'}(t);
\end{aligned}
\tag{11}
$$

where $\delta_{ij}(t)$ and $\dot{\delta}_{ij}(t)$ in Eqn. (11) is the total relative displacement and velocity between both buildings with respect to the foundation, respectively. On the other hand, the pounding forces in the transverse direction F_{yij}^{p} have been calculated by the Coulomb friction model [12, 15].

3 Properties of the structures

The dimensions of both Building A and Building B are rectangular in plan with $20\text{m}\times 15\text{m}$ and $25\text{m}\times 20\text{m}$, the larger plan dimensions being parallel to the longitudinal direction (x) for each building, respectively. The ratio of the base mass to the floor mass of the buildings is 3 for each building. The following basic values describing the structural characteristics in Table 1 have been used:

Table 1: Structural characteristics of buildings.

Storey no	Height of floor level, h_i, h_j (m)	Building A		Building B	
		$m_i\times 10^6$ (kg)	$k_i\times 10^8$ (N/m)	$m_j\times 10^6$ (m)	$k_j\times 10^8$ (N/m)
1F	2.85	0.30	3.46	0.4065	5.06
2F	5.7	0.30	3.46	0.4065	3.86
3F	8.55	0.30	3.46	0.4065	3.86
4F	11.4	0.30	3.46	0.4065	3.86
5F	14.25	0.30	3.46	-	-

Moreover, for the translation in the x and y axes, twist about the z axis and rocking about the x and y axes, the dimensions of rectangular base of adjacent buildings can be converted into an equivalent circular base having the same area as the plan of each building based on the formulas determined by Richart et al. [10]. Hence, the calculations of the radius of base mass determined by Richart et al. [10] are used with considering translations, rotation and rocking directions,

herein. The height of each storey is 2.85 m in both buildings. The moment of inertia of the rigid body for each building about the centroidal axes parallel to the x and y axes are evaluated by replacing each floor with a disc of radius (r_o). The translational stiffness in the transverse direction and the torsional stiffness about the center of mass for each storey for each building are proportional to the stiffness in the longitudinal direction of the same storey and given by the following formula in Eqn. (12).

$$\beta_y = \frac{k_{yi}}{k_{xi}} \quad \beta_y = \frac{k_{yj}}{k_{xj}} \quad \beta_t = \frac{k_{\theta i}}{r_a^2 k_{xi}} \quad \beta_t = \frac{k_{\theta j}}{r_b^2 k_{xj}} \tag{12}$$

The ratios, β_y and β_t are taken as 1.32 and 1.69 for both buildings. The constant of proportionality is evaluated on the basis of 2% of critical damping in the fundamental mode of superstructures in both buildings. The density of soil medium, ρ and Poisson's ratio, ν are taken to be 1922 kg/m^3 and 0.333, respectively. In order to examine the effectiveness of the rigorous method for the whole SSI systems with using the direct integration method to solve the equations of motion, two soil types are investigated in the range of the shear velocities, v_s of 65 m/sec (soft soil) and 300 m/sec (hard soil) have been specifically chosen for this study. Case I (v_s=65 m/sec) and Case II (v_s=300 m/sec) are created for the SSI systems resting on the soft and hard soils in order to investigate the seismic response of the adjacent buildings under large and small SSI effects, respectively. These cases are subjected to the NS and EW components of the 1940 Elcentro earthquake record along the x and y axes, respectively. Based on a dimensionless frequency, a_0 resulting from $0 \le a_o = \omega_f r_o / v_s \le 1.5$, the maximum wave frequencies of both $f_{max} = 2.1$ Hz, 9.7Hz of Building A, 1.8 Hz and 7.8 Hz of Building B for Case I and Case II, respectively. Most of the energy of the related ground motion is at frequencies less than 1.8 Hz. Hence, by using frequency independent spring and dashpot set for the coupled buildings, the SSI effects of the chosen cases can be conducted effectively. Furthermore, each coupled building has been modelled as reference buildings resting on a rigid base with a similar superstructure. The initial gap, D, between the buildings has been taken as 0.04 m. In order to consider the effect of pounding onto the coupled buildings, when the contact of the buildings in the longitudinal direction has been detected, the pounding forces in the transverse and vertical directions have been applied. For the response time histories of the whole SSI system of the coupled buildings, the rigorous method which uses the direct integration method to solve the equation of motion shown in Eqn. (1) is denoted as rigorous (Rig).

4 Results of fixed buildings for the SSI effects

The pounding of the adjacent buildings modelled as elostoplastic multi degree of freedom lumped mass systems with either elastic structural behaviour is studied under the created either Case I or Case II. Firstly, in order to investigate the SSI

systems on the behaviour of the coupled buildings with the large and small SSI effects, the total response histories of Case I and Case II based on the deformation vectors of both superstructures of the two buildings modelled as elastic systems in Figure 2 and Figure 3, respectively.

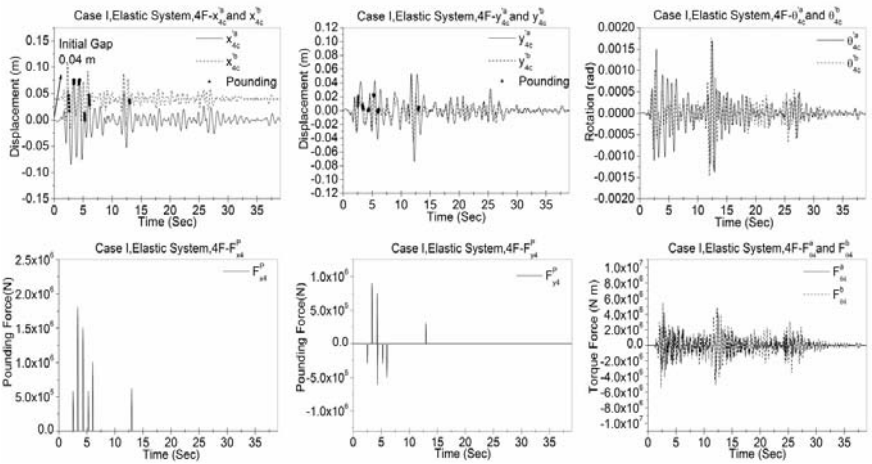

Figure 2: Total response time histories of Case I at the fourth floors of the adjacent buildings modelled as elastic systems under the 1940 Elcentro earthquake.

It can be seen from Figure 2 that both buildings came into contact six times based on the x directional displacements of the fourth floors during the earthquake. Due to collisions in x direction and the effect of torque force, the contacts between the buildings in the y axes are developed, although the pounding forces are not severe compared to the highest contact points in the x direction. While the lighter and more flexible Building A compared to Building B is subjected to more twist about its z axes at the top floor levels at the lowest period of the ground motion, the rotations of the top floor of Building B increase after the contact between the buildings. It can be clearly noted from Figure 3 that the number of contact points and the sensitivity of pounding forces in both directions are significantly increased between the buildings as modelled elastic systems. It shows the importance of the SSI effects on the seismic response histories of the adjacent buildings under the two directional 1940 Elcentro Earthquake. The roof twist of both buildings is considerably decreased for Case I compared to that of Case II. Figure 4 and Figure 5 show the deformation in the translations, rotations in the x and y axes and twist about the vertical z axes and of the foundations of the buildings modelled as elastic systems considering Case I and Case II, respectively.

By comparing Figure 4 and Figure 5, it can be seen that the values of the responses at the foundation for Case II (hard soil) are considerably reduced by reason of the small SSI effect. In order to investigate the effect of the buildings

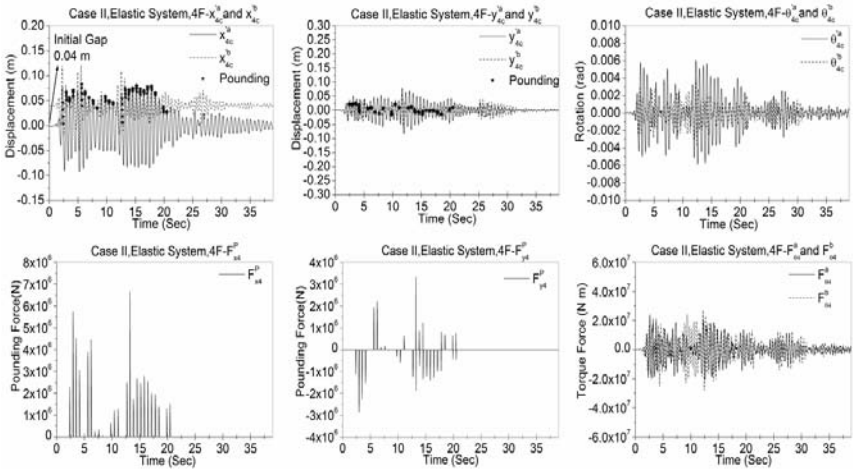

Figure 3: Total response time histories of Case II at the fourth floors of the adjacent buildings modelled as elastic systems under the 1940 Elcentro earthquake.

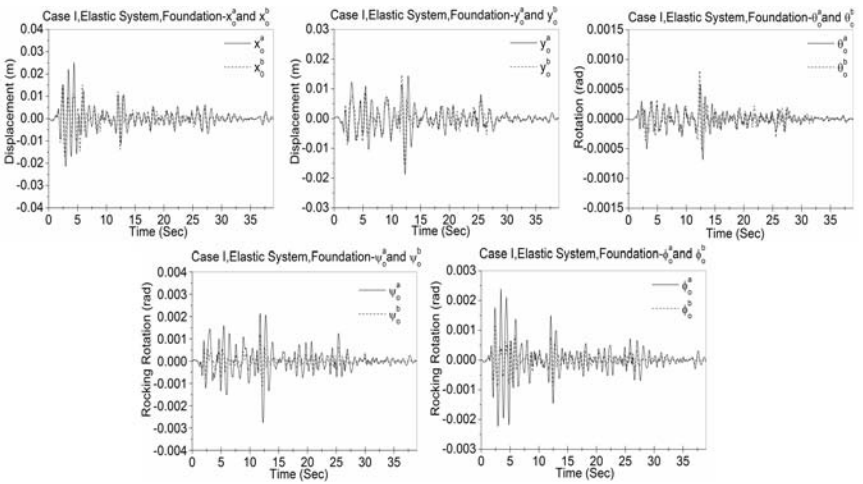

Figure 4: Total response time histories of Case I at the foundations of the adjacent buildings modelled as elastic systems under the 1940 Elcentro earthquake.

modelled as elastic system on the SSI effects, the deformation parameters with considering pounding between the buildings and the SSI forces are conducted here.

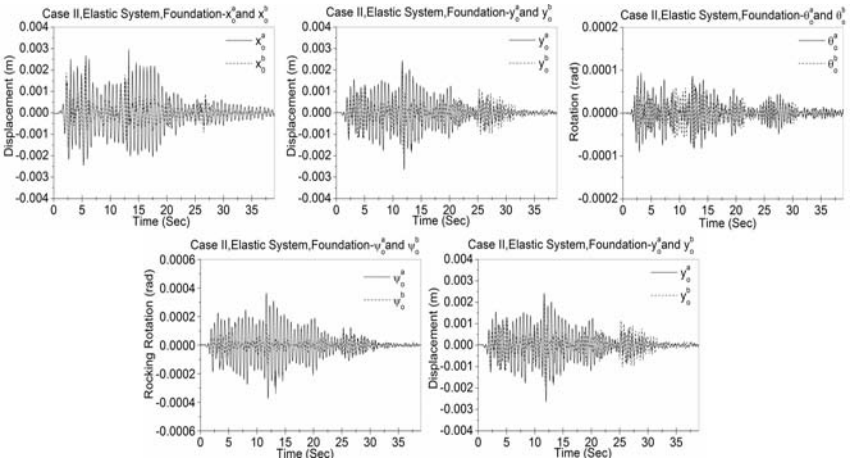

Figure 5: Total response time histories of Case II at the foundations of the adjacent buildings modelled as elastic systems under the 1940 Elcentro earthquake.

5 Conclusion

The values of the pounding force and the number of impacts are larger in the Case II compared to Case I. The results of further investigation show that the responses based on deformation vectors of superstructures for each building are significantly reduced by increasing shear wave velocity, while the SSI forces are increased at the foundation of the buildings. At high shear wave velocity, the top floor deformations of couple buildings are slightly on the conservative side. Finally, in increased shear wave velocity, the impact response of buildings is significantly severe.

References

[1] Hadi, M.N.S., Uz, M.E. Improving the dynamic behaviour of adjacent buildings by connecting them with fluid viscous dampers. in 2nd International Conference on Computational Methods in Structural Dynamics and Earthquake Engineering, COMPDYN 2009. Island of Rhodes, Greece: Institute of Structural Analysis & Seismic Research National Technical University of Athens, 280, 2009.

[2] Sivakumaran, K.S., Balendra, T. Seismic analysis of asymmetric multistorey buildings including foundation interaction and p-[delta] effects. Engineering Structures 1994; 16(8): 609-624.

[3] Thambirajah, B., Chan Weng, T. & Seng-Lip, L. Modal damping for torsionally coupled buildings on elastic foundation. Earthquake Engineering & Structural Dynamics 1982; 10(5): 735-756.

[4] Thambirajah, B., Chan Weng, T. & Seng-Lip, L. Vibration of asymmetrical building-foundation systems. Journal of Engineering Mechanics 1983; 109(2): 430-449.
[5] Uz, M.E., Hadi, M.N.S. Dynamic analyses of adjacent buildings connected by fluid viscous dampers. in Seventh World Conference on Earthquake Resistant Engineering Structures ERES VII. Limassol, Cyprus: Wessex Institute of Technology, 139-150, 2009.
[6] Novak, M., Hifnawy, L.E. Effect of soil-structure interaction on damping of structures. Earthquake Engineering & Structural Dynamics 1983; 11(5): 595-621.
[7] Jui-Liang, L., Keh-Chyuan, T. & Eduardo, M. Seismic history analysis of asymmetric buildings with soil–structure interaction. Journal of Structural Engineering 2009; 135(2): 101-112.
[8] Uz, M., Hadi, M.N. Investigating the effects of pounding for inelastic base isolated adjacent buildings under earthquake excitations. in Proceedings of the 21st Australian Conference on the Mechanics of Structures and Materials. Melbourne, Victoria, Australia: The Netherlands: CRC Press, pp. 329-334, 2010.
[9] Hadi, M.N.S., Uz, M.E. Inelastic base isolated adjacent buildings under earthquake excitation with the effect of pounding. in The 5th Civil Engineering Conference in the Asian Region and Australasian Structural Engineering Conference 2010 CECAR 5/ASEC 2010. Sydney, Australia, 155-201, 2010.
[10] Richart, F.E., Hall, J.R. & Woods, R.D. Vibrations of soils and foundations. Prentice-Hall, Englewood Cliffs; 1970.
[11] Jankowski, R. Earthquake-induced pounding between equal height buildings with substantially different dynamic properties. Engineering Structures 2008; 30(10): 2818-2829.
[12] Chopra, A.K. Dynamics of structures. Theory and applications to earthquake engineering. Englewood Cliffs: Prentice-Hall; 1995.
[13] Wriggers, P. Computational contact mechanics with 12 tables. Springer; 2006.
[14] Hadi, M.N., Uz, M. Base isolated adjacent buildings considering the effect of pounding and impact due to earthquakes. in International Congress on Advances in Civil Engineering. Trabzon, Turkey: Eser Ofset Matbaacilik, pp. 227-227, 2010.
[15] Jankowski, R. Experimental study on earthquake-induced pounding between structural elements made of different building materials. Earthquake Engineering & Structural Dynamics 2010; 39(3): 343-354.

Seismic strengthening of churches as a part of earthquake renewal in the Posočje region, Slovenia

M. Uranjek, B. Dolinšek & S. Gostič
Building and Civil Engineering Institute ZRMK, Slovenia

Abstract

Seismic activity of the Posočje region, located in the north-east of Slovenia is considerably high. Four major earthquakes have hit this area in the last three decades. Among buildings to be repaired and/or strengthened, churches represent a significant share of the building fund. Churches which are often classified as cultural heritage are usually an indispensable part of settlements and their identity. In order to preserve these prominent buildings for future generations, there is a need for attentive and consistent planning of preliminary research, strengthening procedures and their execution. If compared to ordinary buildings in the Posočje region, which are typically characterized by inadequate building quality, churches in this region are of better quality. Nevertheless, on account of their typical design, strengthening procedures are more complex and demanding, and therefore, adequate seismic resistance is harder to achieve compared to ordinary buildings. In the paper, some of the basic strengthening procedures applied on churches in the Posočje region are presented.
Keywords: church, strengthening, earthquake renewal, seismic resistance.

1 Introduction

Seismic activity of the Posočje region, located in the north-east of Slovenia is considerably high, namely four major earthquakes hit this area in last three decades. First earthquake in May 1976 reached the grade IX.-X. and the second one in September 1976 the grade of IX. according to EMS scale. Earthquakes in 1976 caused damage to around 12.000 buildings, of which 4.200 were completely destroyed. Consequently people in this area became aware of the danger and begun to construct buildings which were safer and more resistant to

WIT Transactions on The Built Environment, Vol 120, © 2011 WIT Press
www.witpress.com, ISSN 1743-3509 (on-line)
doi:10.2495/ERES110201

seismic actions. In 1998 the earthquake reaching the grade of VII.-VIII. damaged 4.000 buildings and destroyed 500 of them. The latest earthquake in 2004 with the grade of VI.-VII. caused damage to 1.800 buildings and destroyed 20 of them. Among buildings that have so far been repaired or some of the strengthening procedures were carried out, there is well over 150 buildings of cultural heritage, of which 54 churches. Because of their typical structural system which usually has to remain intact, selection of appropriate strengthening measures is a complex and demanding process. Therefore it is in most cases harder to achieve adequate seismic resistance for churches, than for ordinary buildings. Radical strengthening measures such as new reinforced concrete frames, or even additional load-bearing walls, which can be used to improve earthquake resistance of residential buildings, are not eligible for churches. In case of churches, adequate load bearing capacity of separate structural elements and the integrity of structure as a whole has to be achieved without visible (or distracting) modifications of the basic structural system.

2 Typical structural design and earthquake damage of churches

Although churches were mostly built by experience without detailed calculations, structural elements such as “sewn” corners of walls and iron wall ties (fig. 1) are proof that the builders of the past were familiar with the principles of improving the structural integrity of buildings subjected to seismic loads.

Figure 1: Sewn corners of a St. Michael church in Ljubinj and iron wall ties of the church of St. Andrew in Svino.

Churches are characterized by a complex structural system constructed out of several structural parts with different geometry and mechanical properties. Consequently, structural parts such as portal, nave, presbytery, bell tower (usually connected with nave, seldom self supporting) and sacristy, have rather

different response to seismic action. Nave as a central structural part of a church is characterised with high walls which are often not properly connected and anchored at floor and roof levels and in addition, most naves have no load-bearing walls in transverse direction, which makes them irregular in terms of earthquake resistant design. The irregularity of bell towers as a second most discernible part of a structural system is mainly due to its height/floor area ratio. Damage induced by an earthquake often occurs at connections and intersections of different structural parts of the church building. Usually the first elements to suffer the earthquake damage are heavy console elements e.g. campanulas and decorative elements such as jutting roof, especially if not properly anchored and connected to the base structure. Due to movements and oscillations of supporting walls, cracks are often formed in arches and vaults, but also in supporting walls themselves. On fig. 2 damage that occurred on bell tower of a church of St. Anton the Hermit and the console structure of a historical building in Bovec is presented.

Figure 2: Typical damage on bell tower of a church and console structure of a historical building.

3 Preliminary investigation

In order to maximize the accuracy of assessing the morphology, damage and mechanical properties of the structure, several methods of investigation should be used. A combination of non-destructive (NDT) and minor destructive (MDT) investigation techniques has proven to be very efficient. NDT techniques such as GPR measurement and pulse sonic tests can be performed on wider area of the wall, while MDT techniques (surface and depth sounding, coring, flat jack test), are preferred to be done locally in order to minimize the damage. In some rare cases (because of complexity and considerable costs) destructive (DT) investigation techniques may be performed.

3.1 NDT investigation techniques

GPR (Ground Penetrating Radar) measurements can be used to assess the morphology of the structure. The method is based on the emission and reflection of very short electromagnetic impulses by an antenna system. Reflection of the emitted impulses occurs at the interfaces between materials with different permittivities or conductivities, such as the interface between air (i.e. the voids) and the building material. Because the propagation velocity and the signal penetration depend on the electric and dielectric properties, the boundaries between different materials can be distinguished. GPR can be performed before and after grout injection to evaluate the quality of this strengthening technique (fig. 3).

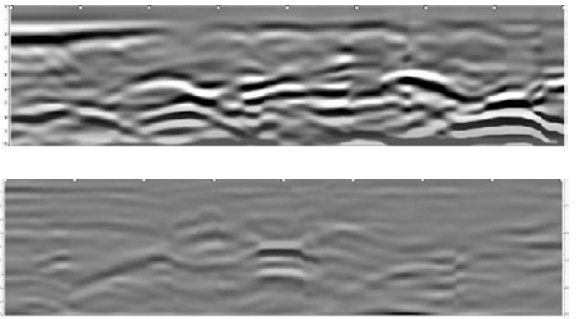

Figure 3: GPR profiles before (above) and after (below) grout injection.

Thermo-graphic measurements are usually used for detecting hidden mistakes in building envelopes, but the method can be successfully applied in the monitoring of the grout injection quality (fig. 4). Thermo-graphical measurements enable us to identify the wall areas with increased surface

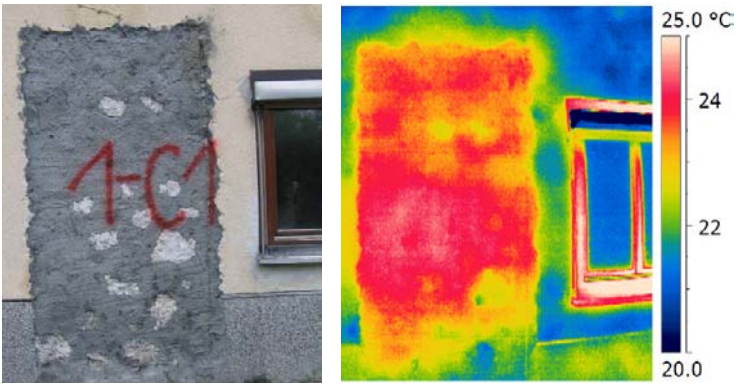

Figure 4: Digital and thermo-graphic photography of the wall 28 hours after grouting.

temperature during a given time interval after injection when, because of the hydration process, heat is released. It has to be emphasized that the measured temperature of the wall depends not only on the hydration but also on the external temperature. This is why the results need to be interpreted with knowledge of the external temperatures at the time of measurement, and a comparison of the measured temperatures between the injected and non-injected parts of the wall.

Sonic pulse test is based on the generation of sonic impulses at a selected point of the structure. Based on the time that the impulse takes to cover the distance between the transmitter and the receiver, the quality and homogeneity of the tested structure can be determined.

3.2 MDT investigation techniques

MDT investigation techniques such as surface and in-depth probing (fig. 5) and coring (fig. 6) on selected areas of the investigated building's structure (walls, foundations), reveal the morphology of the structure at tested positions.

Figure 5: Surface and in-depth probing of the walls.

Figure 6: Coring of the walls and in-depth probing of foundations.

Occasionally, more demanding MDT methods such as **double flat jack test** are used. Flat jack tests enable us to determine the deformability characteristics of the tested wall area. At first, two parallel cuts are made, after which a thin flat-jack is placed inside each of the cuts, and the oil pressure operating the jack is

gradually increased. LVDT`s placed between the two cuts enable the monitoring of vertical and lateral deformations during the test (fig. 7).

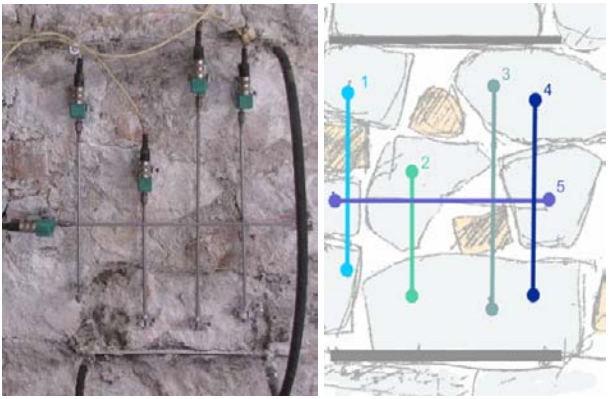

Figure 7: Set up of the measuring equipment for the double flat jack test.

3.3 DT investigation techniques

DT tests are usually carried out in-situ, although it is possible to cut out parts of a structure, carefully transport them, and proceed with the tests in the laboratory. Among DT investigation techniques in Slovenia, several in-situ shear tests were performed, usually on fixed-end wall specimens. Such specimens are loaded laterally by means of a hydraulic actuator by increasing the displacement up to the limit state. In-situ shear tests enable us to determine the shear resistance to lateral load and effective stiffness of the tested walls.

4 Evaluation of seismic resistance

Generally the seismic resistance of existing buildings is verified twice: in their existing state and state after strengthening. Seismic analysis of the building in its existing state reveals critical areas which have to be strengthened, while the basic aim of “after” analysis is to determine the level of seismic resistance reached for strengthened structure. For most churches under earthquake renewal in Posočje, seismic resistance was evaluated by means of non-linear static analysis using pushover method, based on the storey-mechanism approach. Based on the idealized bi-linear hysteresis envelopes of the individual walls the storey resistance envelope is calculated step-by-step by increasing the imposed displacements. In addition to other assumptions, the method assumes that the floors are rigid enough to allow distribution of seismic forces onto the walls and that the first vibration mode shape is the predominant one. The method can quite accurately describe the behaviour of simple masonry buildings with regular distribution of load bearing walls in both horizontal directions and adequate configuration of building in elevation. However, in case of more complex structural systems such as churches, with irregular structural layout and flexible

wooden floors, the drawbacks of the method become more obvious. Therefore, in order to determine the critical failure mechanism of the structure during an earthquake, the method can be used by performing seismic analysis at different levels, depending on geometric characteristics of the structure (fig. 8). The division of structure into macro elements correspond to the observed crack patterns after an earthquake.

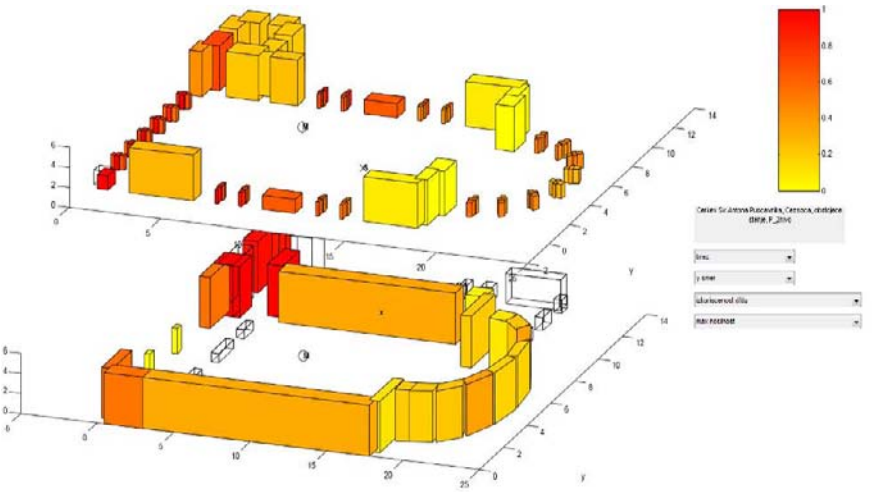

Figure 8: Actual/ultimate displacement ratio for limit state of a structure at two levels.

Recent research [6] has shown that for complex structures, such as churches, more realistic results can be obtained by using FME (Frame by Macro Elements) method, which takes into account the whole building response instead of just single storey response, and furthermore, allows modal analysis to be performed.

5 Strengthening procedures

In continuation, some of practically implemented strengthening procedures under post-earthquake renewal in the Posočje region are presented. There are also other strengthening procedures such as sewing of walls with grouted anchors, application of polymer grids or carbon fibre-reinforced polymer wraps, that won`t be described in this paper.

Tying walls with steel ties (fig. 9) can be applied at the level of individual inter-storey floor structures. In this way the integrity of a structure is improved, the horizontal load is distributed to the walls according to their stiffness, and the walls are better protected against excessive rocking and possible failure in the out-of-plane direction.

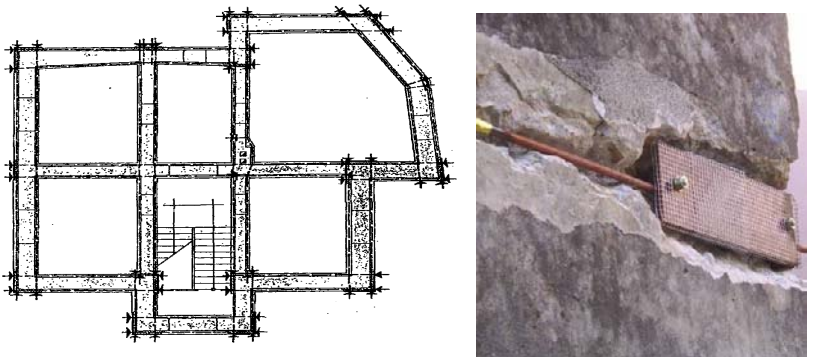

Figure 9: Tying of walls with steel ties.

Reinforced concrete tie-beams can be constructed at floor or roof level and anchored onto the load-bearing walls. Such method of strengthening improves structural integrity of a building and ensures more uniform behaviour of the structure. By anchoring the roof into the tie-beams possible uncontrolled movements of the roof elements and failure of head-walls is prevented.

Injected anchors applied at the middle of the wall`s cross section can, if properly designed and executed, successfully replace steel ties or reinforced tie-beams. This solution is similar to method used by the old builders. Namely connecting walls with ties, installed in the middle of the wall, has been prescribed even after the 1895 earthquake in Ljubljana [4]. Injected anchors can perform either as untensioned steel reinforcement or prestressed tendons. The execution of a borehole and examples of application are shown on fig. 10.

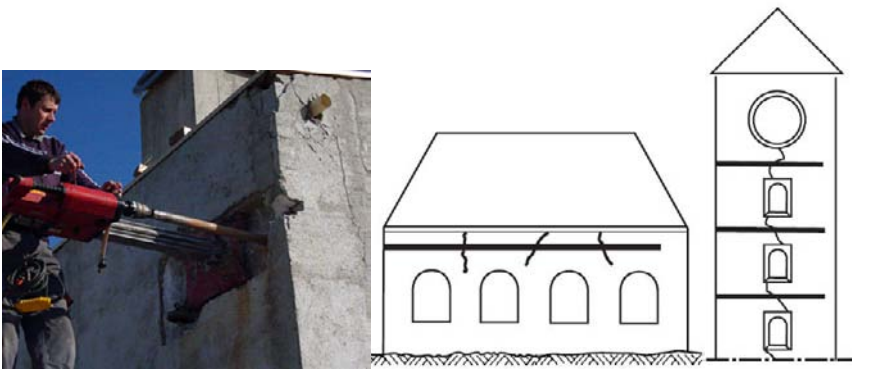

Figure 10: Application of injected anchors [3].

Repointing can be applied where bed-joints are relatively level, the mortar is poor and units are good. The resistance of a wall to vertical and lateral loading can be considerably improved by replacing a part of the existing mortar with mortar of better quality [5]. Although repointing is usually applied on brick

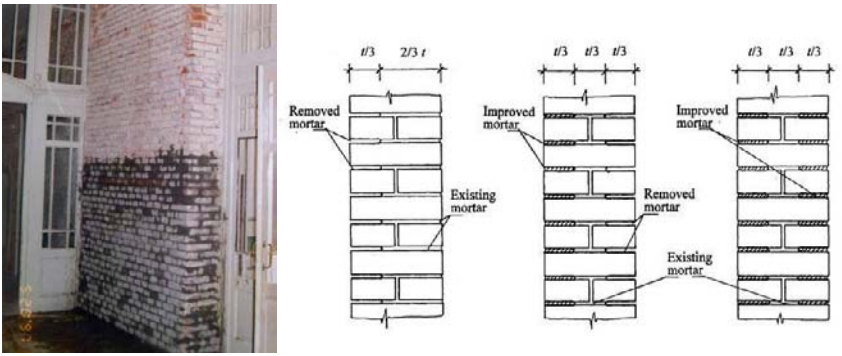

Figure 11: Repointing of a brick-masonry wall [5].

masonry, some authors [1] propose the application of the procedure also on stone masonry walls.

Injection grouting can be used to improve the mechanical properties of two or three-leaf stone masonry walls. Because of inadequate connections between separate stones, voids and poor quality of used mortar, the load bearing capacity of such walls, especially towards horizontal loading, is not sufficient. With grout injection technique, grout (liquid mixture made of water, binder and additives) is injected into a masonry wall (fig. 12) under moderate pressure (2-3 bars). The aim of the technique is to achieve better bonding between separate stones and leafs after the hardening of the injected material, and consequently to improve mechanical properties of the masonry. Work on site showed, that it is best to carry out injection grouting of all load-bearing walls, over their whole height of the structure. Damage that occurred in the buildings after strengthening and repeated earthquake has shown that grouting only parts of walls is not a good solution.

Strengthening of walls by applying **reinforced cement coating** (fig. 13) is usually used for strengthening of brick masonry. However, for more vulnerable structures such as bell towers, it can also be used for strengthening the stone

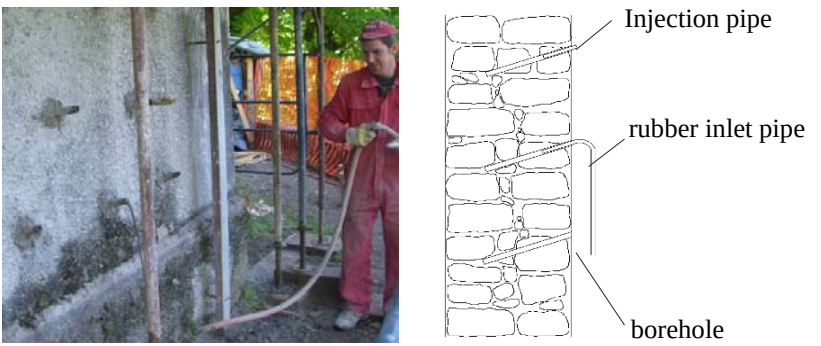

Figure 12: Injection grouting.

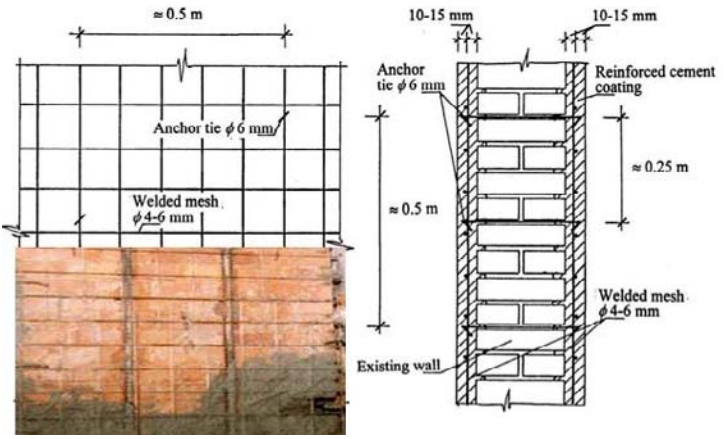

Figure 13: Application of reinforced cement coating on brick-masonry walls.

masonry in combination with application of steel ties and grout injection. By thicker layers amount of reinforcement can be increased and torcrete technology can be applied.

Strengthening the foundations. In the case of weak or shallow foundations it is necessary to widen or deepen them. That is achieved by constructing a reinforced concrete tie-beam along the outside edge of the foundations (fig. 14). New tie-beam should be anchored into the existing foundations by transverse anchors.

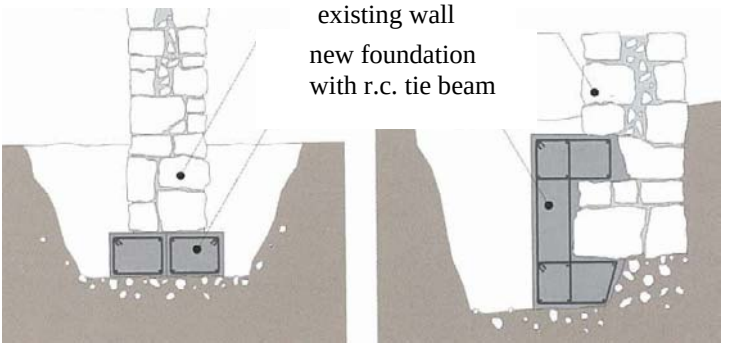

Figure 14: Strengthening of foundations [2].

Only carefully designed combination of strengthening procedures can provide adequate behaviour of the structure during the impact of an earthquake. An example of combining several strengthening procedures on the nave of St. Anton the Hermit is shown in fig. 15.

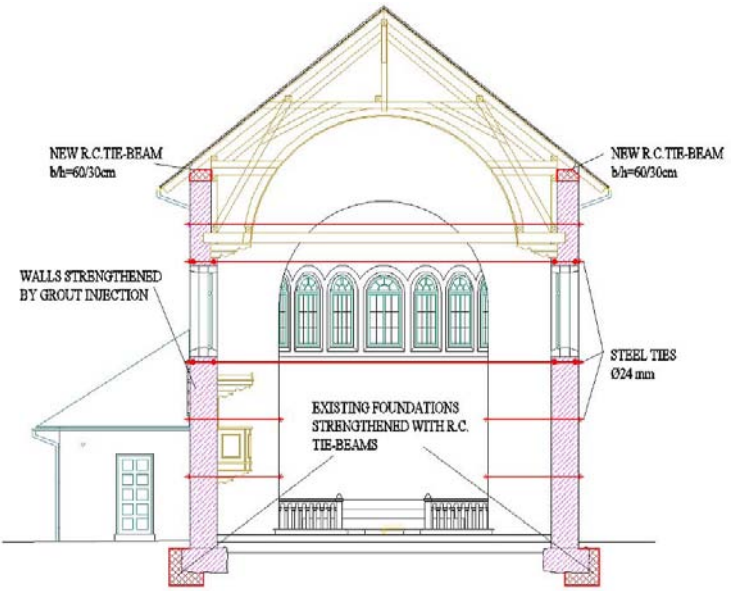

Figure 15: Strengthening procedures on the nave of St. Anton the Hermit`s church.

6 Conclusion

Some of the basic strengthening procedures applied on churches in the Posočje region are presented. Although churches are mostly of better quality than ordinary buildings, because of their typical design, strengthening procedures are more complex and demanding. Because churches are usually under cultural heritage protection, strengthening must be performed without substantial modifications of the basic structural system. Therefore, adequate seismic resistance is harder to achieve compared to ordinary buildings. In order to achieve optimal results, strengthening procedures should be carefully planned and implemented, based on the results of the preliminary investigations and static and seismic analysis.

References

[1] Corradi, M., Tedeschi, C., Binda, L., Borri, A., Experimental evaluation of shear and compression strength of masonry before and after reinforcement: Deep repointing. Construction and Building Materials, Vol. 22, Issue 4, pp. 463-472, 2008

[2] Deu, Ž., Renewal of residential buildings in the Slovenian countryside (in Slovenian). Kmečki glas, Ljubljana, 277 p., 2004

[3] Gigla, B., Bond strength of injection anchors as supplementary reinforcement inside historic masonry. 13th International Brick and Block Masonry Conference Amsterdam, July 4-7, 10 p., 2004
[4] Tomaževič, M. Expert evaluation of seismic strengthening of masonry buildings with injected anchors. ZAG, Ljubljana, 4 p., 1998
[5] Tomaževič, M., Earthquake-resistant design of masonry buildings. London: Imperial College Press, 268 p., 1999
[6] Naglič, A., Seismic analysis of religious buildings (in Slovenian). Graduation thesis, University of Ljubljana, Faculty of civil engineering and geodesy, Ljubljana, 146 p., 2011

Analysis of seismic stability of shells of revolution using probabilistic methods

M. Danieli, J. Bloch & I. Halperin
Department of Civil Engineering,
Ariel University Center of Samaria, Israel

Abstract

This work presents numerical methods of calculation of earthquake resistance of shells of revolution based on the application of the theory of random processes combined with the FEM. Probabilistic character of seismic effect is determined by using artificial accelerograms based on stochastic process. To illustrate the above methods of probabilistic analysis of seismic stability of structures, two real objects and one projected one are considered. Displacements, stresses, forces and moments resulting from the action of seismic load have been determined. Comparison of the results of calculation with those achieved using calculation of prescribed real accelerograms and building design codes have been made. Comparative analysis of the calculation results brings us to the conclusion that the difference between the results obtained using different methods can be quite significant. It means that when designing structures of the types of shells of revolution under consideration it is necessary to do calculations using all methods recommended by design codes as well as probabilistic methods.
Keywords: earthquake resistance, shell, revolution, FEM, probabilistic analysis.

1 Introduction

According to the existing building design codes (IS 413 [1], Eurocode 8 [2], UBC-1994 [3], etc.), the basic method for earthquake resistance analysis is the modal response spectrum analysis (Lindeburg [4], Chopra [5], etc). According to this method, the dynamic character of seismic effect is taken into account by means of various factors. Besides, in order to determine the response of building structures, it is recommended, for example, that calculations be done for recorded real, synthesized or simulated accelerograms (time history) geologic

WIT Transactions on The Built Environment, Vol 120, © 2011 WIT Press
www.witpress.com, ISSN 1743-3509 (on-line)
doi:10.2495/ERES110211

conditions as well as historic and archive data concerning the projected building site. Israeli standards (IS 413 [1]) consider such calculations as being additional; they do not replace principal calculations required by the standards. Since during an earthquake the vibrations of the base ground are non-stationary and chaotic which makes it impossible to form a judgment about the seismic stability of the whole structure by a response to some prescribed accelerograms, the approach based on application of the theory of random processes could be of certain interest (Housner [6], Bolotin [7], Newmark [8], Augusti et al. [9], etc.).

Accelerograms of an earthquake are considered to be non-stationary random processes represented by a product of a determined envelope and a stationary random process. The advantage of this approach consists in using generalized probabilistic characteristics of accelerograms (spectral densities and correlation functions) as initial data.

Equations of motion of the discrete model are given in Danielashvili et al. [10] within the framework of the FEM. They connect matrices of mass, damping and stiffness; vectors of structure joint displacement; and vector of space load distribution in joints. Seismic action in the form of non-stationary random vibrations of acceleration of the foundation is assumed to be the product of the determined envelope by stationary random process, the chart of its spectral density taking the form of a rectangle of calculation of the shell of revolution are given.

This paper uses artificial accelerograms of the ground. White noise ground acceleration time history has been modelled using simulation-based design methods (like Monte Carlo simulations) in accordance with the article by Ribakov and Agronovich [11].

To illustrate the above methods of probabilistic analysis of earthquake resistance of structures, two real objects and one projected one are considered. Displacements, stress, forces and moments resulting from the action of seismic load have been determined.

For comparative analysis of the calculation results, the calculation is also done for the prescribed real accelerograms El Centro Earthquake 1940 (Chopra [5]; etc.) and for the Israeli standards of earthquake resistance calculations (IS 413 [1]). These standards have been developed using Eurocode 8 [2] and uniform building code (UBC-1994[3]).

Analysis of seismic stability was carried out for all three buildings.

2 Buildings and seismic situation

2.1 Buildings

Ancient dome of a civil historical building (former mosque) in Ahaltsihe (Fig. 1) (Danieli et al. [12]).

The mosque built in the 18th century. The building is situated in a seismic area in South Caucasia, Georgia. Its dome was built of locally manufactured thin bricks (240x240x40 mm) using a lime clay mortar. The dome dimensions are as follows: its span is 16.2 m, rise – 8.0 m, shell thickness – 0.6-0.8 m. density 1.8 t/m^3; Module of Deformation $E=1.5\times 10^3$ MPa.

a b

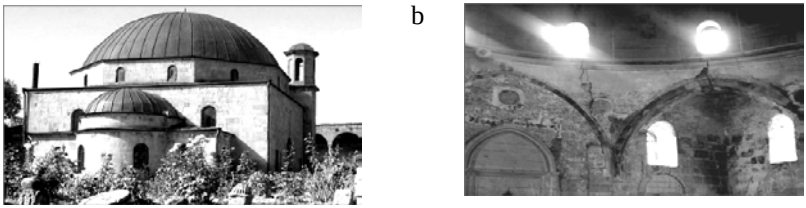

Figure 1: The civil historical building (former mosque) in Ahaltsihe. a - general view; b - cracks at the inner surface.

Building of the Museum of Defenders of Caucasian Passes near the city of Karachayevsk in the North Caucasia (Achvlediani [13]) (Fig. 2). The museum building is a reinforced concrete shell of revolution. Its walls are built in the form of a truncated cone with the height being 4.2 m, lower base diameter – 21.74 m and the upper base diameter – 19.65 m. The construction coating has the form of a sphere segment with the rise being 1.6 m. Thickness of the cone is 10 cm and of the sphere segment – 8 cm.

Compressive strength for concrete - 30 MPa.

a b

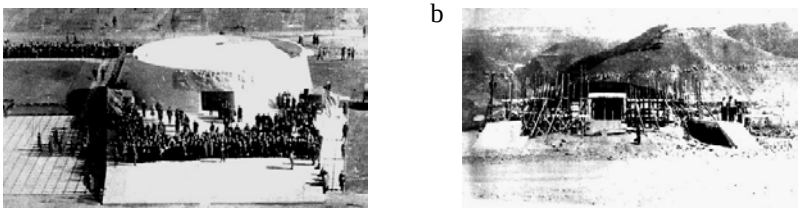

Figure 2: Building of the Museum of Defenders of Caucasian Passes. a - general view, b - view of the construction site.

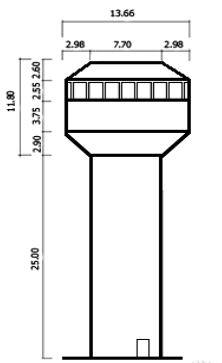

Figure 3: Water tower (project) (Halperin [14]).

The water tower (Fig. 3) construction is a coupled reinforced concrete shell of revolution consisting of a cylindrical shell (pillar) and a toroid shell (water tower). The height of the cylindrical shell is 25 m, its external diameter is 7.7 m

and its thickness is 20 cm; the external diameter of the toroid shell is 13.7 m, its internal diameter is 7.7 m and its thickness - 20 cm. Its height is 11.8 m. The bottom of the reservoir is at the mark of 25 m. Volume of the water reservoir is 500 m^3. Compressive strength for concrete - 30 MPa.

2.2 Seismic situation

The expected Richter magnitude for the Ahaltsihe area is M=7 (Gabrichidze [15]). The mosque in Ahaltsihe, built in the 18th century, was damaged by a series of major earthquakes: (a) in Akhalkalaki, Georgia, in 1899, at the distance of 45 km, M=5.4 (the magnitude has been estimated on the basis on the available descriptions of the earthquake consequences); (b) in Spitak, Armenia, in 1988, at 125 km, M=6.9; and (c) in Racha, Georgia, on April 29, 1991, at 125 km, M=6.9 (Gabrichidze [15]). This magnitude corresponds to the intensity I_0=9.5 on the MSK-64 twelve-step scale. Several thousands of aftershocks were registered later on, during four months. Their magnitudes varied between M = 6.2 and M = 5.9, being sometimes almost as powerful as the primary shock. The following map and chart illustrates this situation (Fig. 4).

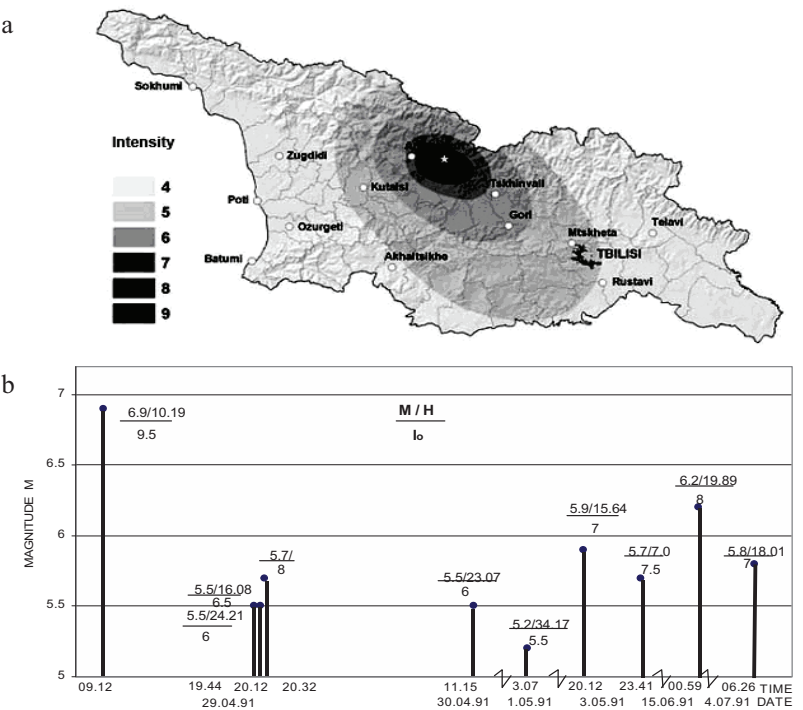

a - calculated earthquake intensity map; b - chart: primary shock and major secondary shocks (aftershocks) are shown. M - Richter magnitude; H - focus depth, km; I_0 - intensity on MSK-64 scale.

Figure 4: Seismic situation caused by the earthquake in Racha, Georgia, between April 29 and July 04, 1991.

Although the structure did not lose stability, the dome was damaged. Wide radial cracks appeared on the internal surface, mainly in relatively weak window areas (Fig. 1). At the bottom part they are as wide as 15 -20 mm. Tensile stresses in this area can be 0.045 MPa due to the dome weight. The conservation project of the ancient dome is presented in the paper (Danieli et al. [12]). Results of linear (under static vertical and seismic loads) and non-linear (under static vertical and seismic loads) structural numerical analysis structure for ancient stone dome only and stone dome in interconnected stone-reinforced concrete structure presented, respectively, in (Danieli et al. [16]) and (Bloch et al. [17]).

The distance between the epicentre of the Racha earthquake and Karachaevsk is approximately 175 km. Design ground acceleration for the Karachaevsk zone and the zone of the location of the water tower is 0.2g.

3 Analysis of earthquake resistance of shells of revolution

Analysis of seismic stability was carried out for all three buildings.

3.1 Seismic action

Seismic effect is prescribed as an artificial earthquake accelerogram borrowed from (Ribakov and Agronovich [11]). Modelling of artificial earthquake is done in the following way: a probability distribution function of a stochastic process or process realization should be assigned. The distribution is required for theoretical design and analysis. The simulation-based design methods (like Monte Carlo simulations) require generation of the excitation time histories.

At the first stage of this work an artificial white noise ground acceleration signal (earthquake) is generated using an originally developed algorithm implemented in MATLAB (*High performance Numeric Computational and visualization software. User's Guide.* The MathWorks Inc.) routines. The initial data for this algorithm is: the desired peak ground acceleration (PGA); the desired spectrum bandwidth (BW); and the duration of the earthquake (t_f). The following parameters have been selected in this study: PGA=0.3 g, BW=10 Hz and t_f=50 sec. These parameters were selected based on the available data on the ground acceleration for natural earthquakes including near field records. The proposed method and its program realization allow changing the parameters according to the required design conditions.

To use the data provided by Ribakov and Agranovich we have transformed them for the case of PGA=0.2 g. A white noise artificial ground acceleration time history for PGA-0.2 g, BW=10 Hz are shown in Fig. 5a. Corresponding pseudo-acceleration response spectrum for damping rations 0,02; 0,05; 0.1; 0.15 is shown in Fig. 6a.

3.2 Calculations of seismic stability

Calculations of seismic stability were done on the basis of the STRAP program - structural analysis and design software, version 8. Program STRAP uses Finite element calculation models. The basic method of the seismic analysis is the

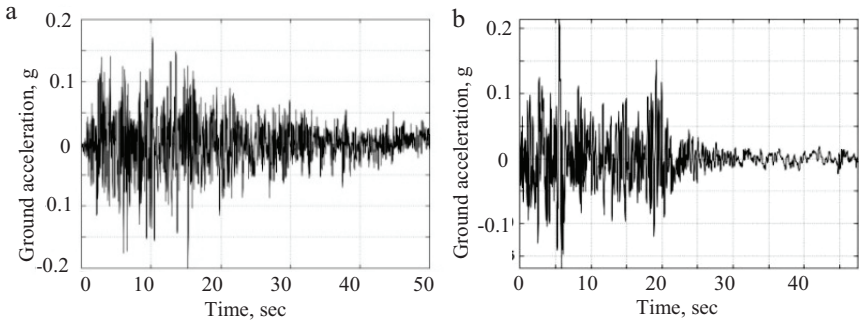

Figure 5: a - white noise artificial ground acceleration time history, PGA-0.2 g, BW=10 Hz; b - the ground acceleration of 1940 El Centro Earthquake. Magnitude M=7. Direction East-West.

modal response spectrum analysis. It consists of a dynamic analysis module and seismic analysis module. The dynamic analysis module analyses the modal shape of the model: solves for the natural frequencies and the corresponding mode shapes. The seismic analysis module calculates the earthquake response and the resulting moments and forces in the model based on the calculated mode shapes and code related factors. The mode shape analysis calculates "n" different mode shapes.

Calculations are made in accordance with the modal spectrum response method and by using STRAP dynamic analysis module. The maximum response (deflection, base shear, etc) for each shape is calculated from a "Response spectrum". It is a graph which gives the acceleration as a function of the natural period, T, of the model. In order to use STRAP dynamic analysis module a response spectrum was generated for two earthquake ground accelerations: artificial earthquake and 1940 El-Centro earthquake. In order to generate response spectrum, a time history analysis for a large number of single-degree-of-freedom structures with different natural periods and damping ratios was carried out by MATLAB routines. The response spectrums were generated by finding the maximum deflection for each structure (Fig. 6 a,b). The spectrum data was transferred to STRAP as a data file.

An estimate of the maximum total response is made from the maximum calculated modal values- SRRS (Sum of Root of the Sum of the Square) method.

Analysis of seismic stability of the above buildings is done using a discrete model. Finite element calculation models for all three buildings, respectively, are shown in Fig. 7. As a result of the calculations according to the STRAP program for all three buildings considered in this paper, forms and periods of natural vibrations (mode shape), displacements, stresses, forces and moments were determined. The first three forms of natural vibrations (mode shape) for all three buildings, respectively, are shown in Fig. 8.

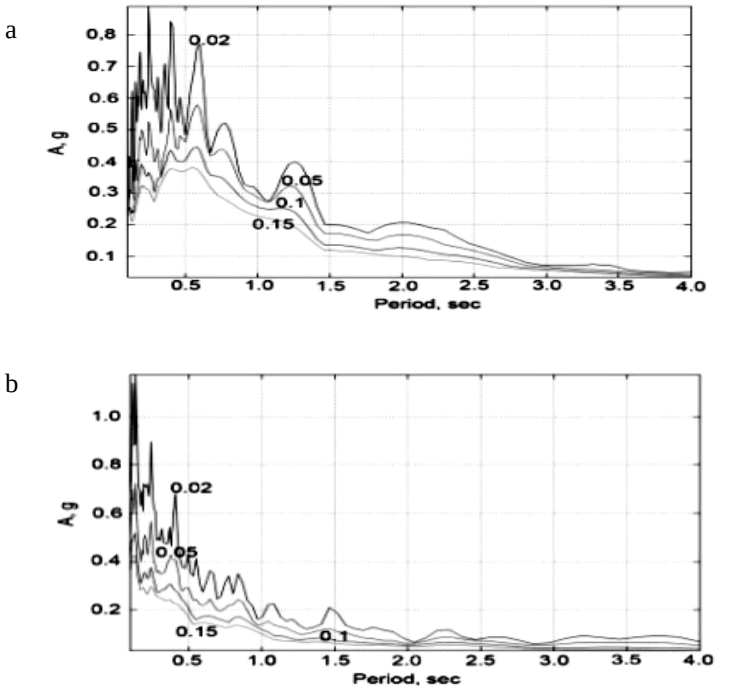

Figure 6: Pseudo-acceleration response spectrum. a - for artificial ground acceleration; b - for 1940 El Centro Earthquake ground acceleration. Numbers on the curves correspond to damping ratios.

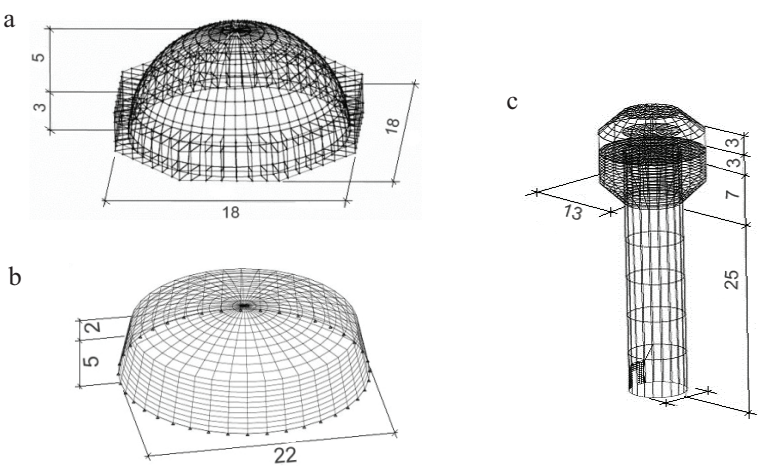

Figure 7: Finite element calculation models. a - ancient dome in Ahaltsihe; b - building of the Museum; c - water tower.

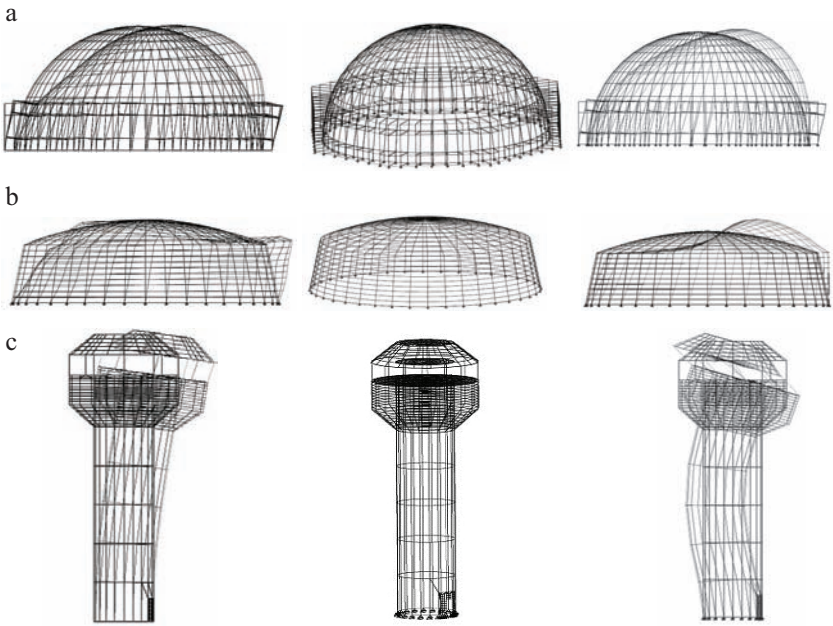

Figure 8: The first three forms of natural vibrations (mode shapes). a - ancient dome in Ahaltsihe; b - building of the Museum; c - water tower.

3.2.1 Probabilistic analysis

3.2.1.1 Calculation on the basis of the artificial earthquake accelerograms Seismic effect is prescribed as a white noise of the generated artificial ground acceleration (artificial earthquake accelerogram) (Fig. 5a). Corresponding pseudo-accelerations response spectrum for damping ratios 0.02; 0.05; 0.1; 0.15 is shown in Figure 6a. Some results of the calculations obtained are shown in Tables 1, 2 and 3.

3.2.2 Comparative analysis

3.2.2.1 Calculation on the basis of the earthquake EL Centro For comparative analysis, the seismic effect is prescribed as an accelerograms El Centro 1940; earthquake direction East-West (Fig.5b). Corresponding pseudo-accelerations response spectrum for damping ratios 0.02; 0.05; 0.1; 0.15 is shown in Figure 6b. Some results of the calculations obtained are shown in Tables 1, 2 and 3.

3.2.2.2 Calculation on the basis of the Israeli standard Calculations are also done of all three shells of revolution according to the Israeli standard calculations using the modal response spectrum analysis method combined with the SRSS (in Square Root of the Sum of the Squares e) method (IS 413 [1]). Some results of the calculations obtained are shown in Tables 1, 2 and 3.

Table 1: Dome in Ahaltsihe. Main results of structural analysis. Maximum values.

Parameters	Seismic loads			Static loads
	Artificial earthquake	EL Centro earthquake	IS- 413 1998	
Periods of natural vibrations, s: T_1; T_2; T_3	0.082; 0.050; 0.049			
Max. displacement, mm vertical, w horizontal, u	 0.27 0.88	 0.16 0.51	 0.13 0.42	 1.89 0.19
Maximum stress, MPa σ_{Ny} (+)/ σ_{Ny} (–) σ_{Nx} (+)/ σ_{Nx} (–)	 0.037/0.049 0.012/0.082	 0.214/0.028 0.007/0.047	 0.017/0.023 0.005/0.039	 – /0.17 0.02/0.15
Earthquake direction: horizontal Seismic zone factor – Z Site coefficient – S Seismic importance factor – I Reduction factor – K Damping ratio – ζ	 0.1	 0.1	 0.2 1.2 1.4 3.5 0.1	

Table 2: Building of the museum. Main results of structural analysis. Maximum values.

Parameters	Seismic loads			Static loads
	Artificial earthquake	EL Centro earthquake	IS- 413 1998	
Periods of natural vibrations, s: T_1; T_2; T_3	0.0283; 0.0273; 0.0239			
Max. displacement, mm vertical, w horizontal, u	 0.04 0.18	 0.02 0.07	 0.01 0.04	 3.630 0.087
Maximum stress, MPa σ_{Ny} (+)/ σ_{Ny} (–) σ_{Nx} (+)/ σ_{Nx} (–)	 0.139/0.096 0.121/0.346	 0.052/0.036 0.045/0.129	 0.027/0.018 0.026/0.067	 2.135/2.854 2.309/1.221
Earthquake direction: horizontal Seismic zone factor – Z Site coefficient – S Seismic importance factor – I Reduction factor – K Damping ratio – ζ	 0.05	 0.05	 0.2 1.5 1.2 2 0.05	

Table 3: Water tower. Main results of structural analysis. Maximum values.

Parameters	Seismic loads			Static loads
	Artificial earthquake	EL Centro earthquake	IS- 413 1998	
Periods of natural vibrations, s: T_1; T_2; T_3	0.5688; 0.1562; 0.1333			
Max. displacement, mm				
vertical, w	5.56	9.55	15.94	9.97
horizontal, u	1.72	42.73	71.22	44.57
Maximum stress, MPa				
σ_{Ny} (+)/ σ_{Ny} (–)	1.602/4.139	9.317/0.175	15.54/0.238	9.723/0.153
σ_{Nx} (+)/ σ_{Nx} (–)	1.584/0.628	1.398/1.174	2.331/1.596	1.459/1.029
Earthquake direction: horizontal				
Seismic zone factor – Z			0.2	
Site coefficient – S			1.5	
Seismic importance factor – I			1.2	
Reduction factor – K			5.5	
Damping ratio – ζ	0.05	0.05	0.05	

Remarks (Tables 1, 2, 3): "+"– tension; "–"– compression; "y"– meridian direction; "x"– ring direction.

4 Discussion of the calculation results

Comparative analysis of the calculation results (Tables 1, 2 and 3) brings us to the conclusion that the difference between the results obtained using different methods can be quite significant. Thus for the ancient dome and the shell of revolution of the museum artificial earthquake is more dangerous while for the water tower the earthquake EL Centro is more dangerous. It means that when designing structures of the types of shells of revolution under consideration it is necessary to do calculations using all methods recommended by design codes as well as probabilistic methods.

The above numerical data of the calculation (Tables 1 and 2) show a low level displacements as well as of stresses in respect of stresses of static loads for the two first shells of revolution of the cover of the ancient dome and reinforced shell revolution of the museum when they are affected by the most severe earthquakes. It shows that shells of revolution are highly effective and safe as far as their seismic stability is concerned.

At the same time, for the water tower (Table 3) displacements, especially horizontal displacements are significant and stresses of seismic action usually exceed the stresses of static loads. It demonstrates the high sensitivity of the water tower to seismic loads.

It should be stressed that Israeli standards (IS 413 [1]) do not consider shell-type constructions as an independent type of constructions which makes it difficult to select corresponding factors for them. Reduction factor "K" (factor of

reduction of seismic load, structural types factor) is of special importance since it varies from 2 to 7. That is why it is recommended to do research into determining this factor "K" and to single out shells of revolution into a separate group in standards for determining factor "K". This recommendation is especially important due to the fact that shells of revolution are as a rule long-span structures.

There are more convenient conditions for water towers, however, for they compose an independent group for determination of the Reduction factor "K". And this accounts for a relatively lesser discordance between the results of calculations obtained using various methods of analysis.

5 Conclusions

1. The above numerical data of the calculation show a low level of stresses and displacement of the shells of revolution of covers when affected by the most severe earthquakes which proves that the cover constructions in the form of shells of revolution are highly effective where their seismic stability is concerned.
2. When designing shells of revolution, it is recommended that calculations be done using all methods recommended by designers' standards including time history analysis and probabilistic methods.
3. We recommend that construction standards single out shell constructions as a separate group to make it easier to select true calculation factors, reduction factor K in particular. This conclusion is especially important due to the fact that shells of revolution are as a rule long-span structures.

Acknowledgements

Authors appreciate the assistance given by Dr. Y. Rybakov and Prof. G. Agranovich who provided the data for construction of accelerograms of artificial earthquakes. They also acknowledge Dr. G. Sirotin's contribution to preparing this paper for publication.

References

[1] Israeli Standard – 413. *Design provisions for earthquake resistance of structures*, Tel-Aviv, 1998 (in Hebrew).
[2] Eurocode 8 *Design Provisions for Earthquake Resistance of Structures*, 1993; 2000.
[3] Uniform Building Code. *Structural Engineering Design Provisions*, ch. 16, div. III - Earthquake Design, 1994.
[4] Lindeburg, M.R. *Seismic design of Building Structures.* Belmont, CA.
[5] Chopra, A.K. *Dynamics of Structures*, (2 ed.), Prentice Hall, N.J., 2001.
[6] Housner, G.W. *Characteristics of strong motion earthquakes*, Bull. Seismol. Soc. Am 37, pp.19-31, 1947.

[7] Bolotin, V.V. *Statistical Methods in Structural Mechanics*, Holden-Day, San Francisco, 1969.
[8] Newmark, N. M. and Rosenblueth, E. *Fundamentals of Earthquake Engineering*, Prentice-Hall, Englewood Cliffs, N.Y, 1971.
[9] Augusti, G., Baratta, A. and Casciati, F. *Probabilistic Methods in Structural Engineering*, Chapman and Hall: London-New York, 1984.
[10] Danielashvili, M., at al. Analysis of earthquake resistance of reinforced shells of revolution using probabilistic methods. *Spatial Structures of Buildings and Edifices*, Moscow, pp.8-12, 1996 (in Russian).
[11] Ribakov, Y. and Agronovich, G. Design of Hybrid Base Isolation Systems with Passive Friction Dampers, *Eur. Earthquake Eng. 3*, pp. 48-56, 2007.
[12] Danieli (Danielashvili), M, Gabrichidze, G., Goldman, A. and Sulaberidse, O. Experience in restoration and strengthening of stone made ancient domes in seismic regions. *Proc. of 7th US National Conf. on Earthquake Engineering*. Boston, MA, USA. Vol. II, pp. 1167-1175, 2002.
[13] Akhvlediani, N. V., Danielashvili , M. A., et al. Investigation, Design and Construction of Antiseismic Spatial Structures Based on the Theory of Limit Equilibrium. *Proc. of the Int. Cong. of IASS "Theor. and Exp. Studies of Spatial Structures"*. Moscow, Vol. 4, pp. 190-201, 1985.
[14] Halperin, Y. *Water Tower, student's graduation work*, Dep. of Civil Engineering, Ariel University Center of Samaria, Israel, 2009.
[15] Gabrichidze, G. (ed.) *Engineering Analysis of the Racha Earthquake Consequences in Georgia, 1991*, Metsnereba, Tbilisi, Georgia, 1996 (in Russian).
[16] Danieli (Danielsvilli), M., Aronchik, A., Bloch, J. Seismic safety of an ancient stone dome strengthened by an original method. *Proc. of 13th World Conf. on Earthquake Eng.* Vancouver, B.C., Canada, paper No 2789 (SD-R), 2004.
[17] Bloch, J., Aronchik, A., Danieli (Danielashvili), M. Ancient Stone Dome Strengthening in Seismic Regions by an Original Method and Non-Linear Stress-Strain Analysis Problems. *Proc. of the 8th US Nat. Conf. on Earthquake Eng. (8NCEE)* San Francisco ,California, USA, paper No 31 (SD-R), 2006.

Evaluating a rigid-plastic method to estimate the earthquake ductility demand on structures

M. C. Porcu & G. Carta
Dipartimento di Ingegneria Strutturale, University of Cagliari, Italy

Abstract

In order to evaluate the reliability of a rigid-plastic method in estimating the earthquake displacement ductility demand, the present paper applies the method to hundreds of different elastic-plastic oscillators under more than thirty recorded earthquakes. The mean ratio of the predicted value over the exact value of the displacement ductility demand is computed and plotted as a function of the vibration period of the oscillator for different values of the yield acceleration. The results show that, whatever the oscillator and the earthquake, the rigid-plastic method leads to a generally conservative estimate of the inelastic displacement demand. Mean errors less than 15% are found both for comparatively short-period oscillators and for comparatively long-period oscillators. For medium-period oscillators, the relative mean error is generally less than 30%, even for very high levels of ductility demand. Some advantages of the rigid-plastic method with respect to other approximate methods are also discussed in the paper.
Keywords: earthquake ductility demand, seismic inelastic displacement prediction, rigid-plastic method.

1 Introduction

The assessment of the earthquake ductility demand on structures is often carried out by means of approximate methods, most of which are based on the theory of linear elastic oscillators, cf. e.g. Rosemblueth and Herrera [1]; Gulkan and Sozen [2]; Iwan [3]; Kowalsky et al. [4]; Newmark and Hall [5]; Miranda [6].

An alternative method was proposed by Paglietti and Porcu [7] and subsequently improved by Porcu and Carta [8, 9], which predicts the maximum plastic displacement of an elastic-plastic oscillator from that of a rigid-plastic

WIT Transactions on The Built Environment, Vol 120, © 2011 WIT Press
www.witpress.com, ISSN 1743-3509 (on-line)
doi:10.2495/ERES110221

oscillator possessing the same ratio between yield strength and mass (yield acceleration). The peak displacement of the latter can be obtained from the earthquake rigid-plastic pseudo-spectrum, which is a single-curve response diagram (Paglietti and Porcu [7]; Domingues Costa et al [10]; Porcu and Mascia [11]). Section 2 recalls how the rigid-plastic method can be applied in practice.

To evaluate the reliability of such a method, the present paper analyses the results from hundreds of different elastic-plastic oscillators subjected to a significant variety of recorded ground motions. The mean ratio between estimated and calculated values of the displacement ductility demand is evaluated as a function of the period *T* of the oscillator for different values of the yield acceleration. The results provided in Section 3 show that the rigid-plastic method is generally conservative. Moreover, it leads to small relative errors both in the short and in the long period range. Whereas in the medium period range the error may reach 30%. In order to keep the errors of the rigid-plastic method below small percentage also in this range, an improvement of the empirical formula to be applied for medium period oscillator would be advisable. It should be noted, however, that these errors usually refer to high levels of ductility demand.

Some favourable features of the rigid-plastic method are finally discussed in Section 4. The method may be, in fact, faster to apply than other approximate methods available in current literature, which usually require iteration procedures to estimate the ductility demand on a structure. In addition, it singles out the range of periods in which the considered elastic-plastic oscillators may plastically yield under a given earthquake. This is a general result, which can be exploited by any method that aims to predict the earthquake inelastic displacement demand. Also when compared to other approximate methods, the rigid-plastic method is shown to provide good enough estimates, even when the plastic displacements are very large.

Other authors adopted a rigid-plastic approximation to model the response of ductile structures (e.g. Makris and Black [12]; Hibino et al. [13]). A rigid-plastic approach was also recently proposed by Domingues Costa et al. [14], which predicts the maximum plastic displacements of MDOF buildings by means of equivalent generalized SDOF systems. Thanks to this, the rigid-plastic method applied in the present paper could also be exploited to assess the seismic ductility demand of MDOF systems.

2 The rigid-plastic method prediction

The earthquake ductility demand of an elastic-perfectly-plastic oscillator can be defined by means of the following ratio:

$$\mu = \frac{u_{\max}}{u_y}, \tag{1}$$

also referred to as the ductility factor or displacement ductility ratio (Chopra [15]). Here $u_{\max}$ is the absolute value of the maximum displacement of the

oscillator, while u_y is the absolute displacement at yield. When the elastic-plastic oscillator deforms into the plastic range, $u_{\max}$ is greater than u_y and, consequently, the ductility factor becomes greater than unity. In this case, $u_{\max}$ can be decomposed as follows:

$$u_{\max} = u_y + u_{\max}^P , \tag{2}$$

where $u_{\max}^P$ denotes the absolute value of the maximum plastic displacement. The ductility ratio then becomes:

$$\mu = 1 + \frac{u_{\max}^P}{u_y} , \tag{3}$$

On the other hand, the absolute displacement at yield u_y is given by:

$$u_y = \frac{F_y}{k} = \frac{T^2}{4\pi^2}\ a_y , \tag{4}$$

k, T, F_y and a_y being the stiffness, the natural period of vibration, the yield strength and the yield acceleration of the oscillator, respectively. The yield acceleration is given by the ratio between the yield strength F_y and the mass M of the oscillator, and represents the maximum acceleration that the oscillator may reach during the motion (Chopra [15]; Paglietti and Porcu [7]). All displacements are here intended to be relative to the ground.

In view of eq. (4), the ductility factor can be also expressed as:

$$\mu = 1 + \frac{4\pi^2}{T^2 a_y}\ u_{\max}^P \tag{5}$$

This equation shows that assessing the ductility demand for an elastic-plastic oscillator requires that $u_{\max}^P$ be known. For a given earthquake, $u_{\max}^P$ depends on the oscillator vibration period T, damping ratio ξ and yield acceleration a_y. It should be calculated by numerical integration of the non-linear equations of motion of the elastic-plastic oscillator.

The rigid-plastic method proposed by Porcu and Carta [9] provides a simpler, though approximate, way to predict $u_{\max}^P$. It leads to the following formulae:

$$u_{\max}^P = u_{\max}^{RP} \quad \text{for } T \le 0.13T^* , \tag{6a}$$

$$u_{\max}^P = u_{\max}^{RP} + \overline{\Delta u}^{\,p} \quad \text{for } 0.13T^* \le T \le T^* , \tag{6b}$$

$$u_{\max}^{P} = u_{\max}^{RP} \frac{T - \bar{T}}{T^* - \bar{T}} \quad \text{for } T^* \le T \le \bar{T}\,, \tag{6c}$$

$$u_{\max}^{P} = 0 \quad \text{for } T > \bar{T}\,, \tag{6d}$$

where

$$\overline{\Delta u}^{\,p} = -0.039\, a_y \left[\frac{2.5\left(\bar{T} + T^*\right)\left(1 - \sqrt{\frac{a_y}{g}}\right)}{\sqrt[4]{\xi}} - \frac{\left(T^*\right)^2}{\bar{T}} - 1 \right] \left[\left(\frac{T}{T^*}\right)^2 - 1.13\left(\frac{T}{T^*}\right) + 0.13 \right]. \tag{7}$$

In the above formula time should be expressed in seconds.

In equations (6a)-(6c) $u_{\max}^{RP}$ represents the maximum displacement that would be reached under the given earthquake by a rigid-plastic oscillator possessing the same yield acceleration as that of the elastic-plastic oscillator under consideration. For a given earthquake $u_{\max}^{RP}$ only depends on a_y, and can be calculated by integrating the non-linear equations of motion of the rigid-plastic oscillator, which are simpler than those of the elastic-plastic one (Paglietti and Porcu [7]). Alternatively, and more quickly, it can be obtained from the rigid-plastic pseudo-spectrum of the earthquake, (cf. Paglietti and Porcu [7]; Porcu and Mascia [11]; Domingues Costa et al. [10]). An instance of how obtaining $u_{\max}^{RP}$ from a rigid-plastic pseudo-spectrum, for a given value of a_y, is provided in Figure 1.

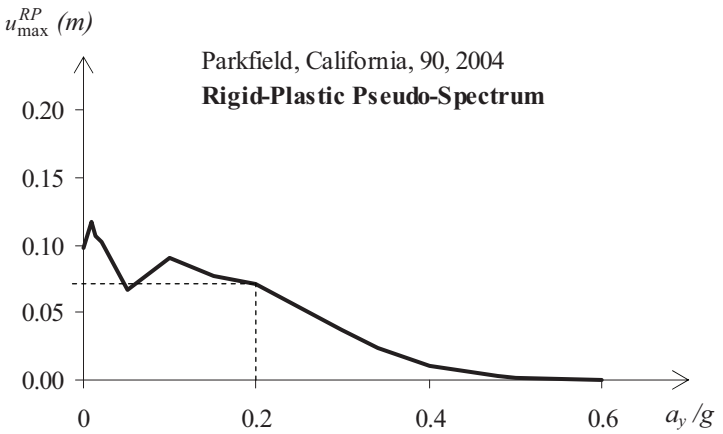

Figure 1: Obtaining $u_{\max}^{RP}$ from the earthquake rigid-plastic pseudo-spectrum.

Quantities T^* and $\bar{T}$ appearing in eqns (6) and (7) are two characteristic values of period that depend on the earthquake and are function of a_y and ξ. They can easily be obtained by intercepting the displacement elastic response spectrum with the following curves (Porcu and Carta [8]):

$$u^*(T, a_y) = \frac{a_y T^2}{4\pi^2}\sqrt{\frac{8\pi^2 u_{\max}^{RP}}{a_y T^2} + 1}\,, \tag{8}$$

$$u_y\left(T, a_y\right) = \frac{a_y T^2}{4\pi^2} \tag{9}$$

Figure 2 shows how obtaining T^* and $\bar{T}$ from an elastic response spectrum.

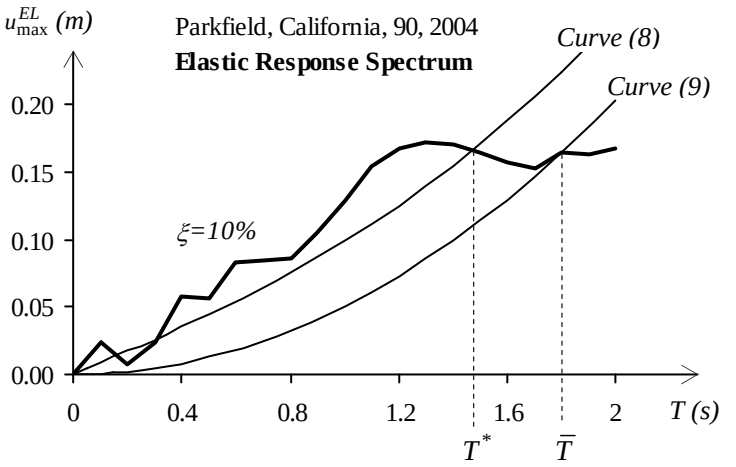

Figure 2: Determining T^* and $\bar{T}$ from the elastic displacement response spectrum (for $a_y = 0.2g$).

Once that $u_{\max}^{RP}$ is taken from the rigid-plastic pseudo-spectrum and the pair of characteristic periods T^* and $\bar{T}$ are found from the elastic response spectrum, $u_{\max}^{p}$ can be predicted directly from eqns (6) and (7). An example on how to get such a prediction is given in Figure 3.

By introducing the estimated value of $u_{\max}^{p}$ into eqn (5), the ductility factor μ is finally obtained. For the same instance considered in Figures 1-3, Figure 4 plots both the predicted and the "exact" values of the ductility factor μ. Figure 4 shows that μ tends to unity as T tends to $\bar{T}$. Indeed, for $T = \bar{T}$ it is $u_{\max}^{p} = 0$ and, therefore, $\mu = 1$, as follows from eqn (5). According to eqn (5),

moreover, for any given value of a_y the ductility factor tends to infinity as T tends to zero. This makes a direct comparison between predicted and "exact" values of μ inaccurate in the short-period range. For this reason, the ratio between predicted and exact values of μ will instead be considered in the next section, which allows for a comparison in the whole range of periods.

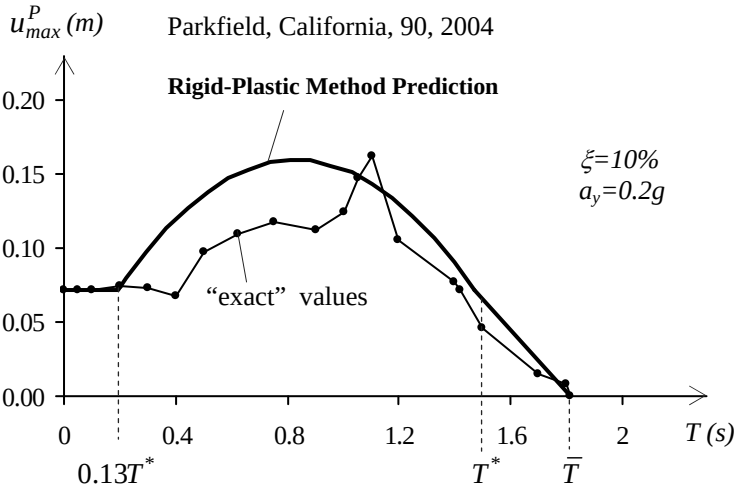

Figure 3: Predicting the peak plastic displacements through the rigid-plastic method.

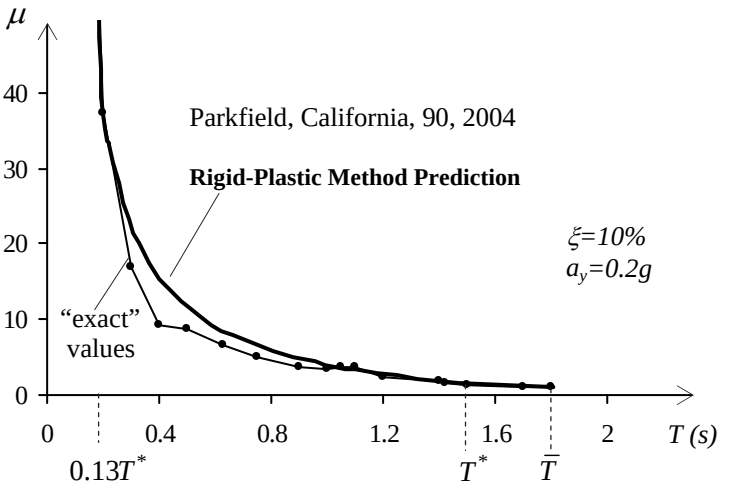

Figure 4: Predicting the ductility factor μ by means of the rigid-plastic method.

3 Mean relative errors in the rigid-plastic prediction

In order to evaluate the relative errors that can be made when estimating the earthquake ductility demand by means of the rigid-plastic method, the ratio between the earthquake displacement ductility factor as estimated by means of the rigid-plastic method, say $\tilde{\mu}$, and the "exact" value μ of the same factor computed by a non-linear time-history analysis will be considered below. In view of eq. (3), this ratio can be expressed as:

$$r = \frac{\tilde{\mu}}{\mu} = \frac{u_y + \tilde{u}^P_{\max}}{u_y + u^P_{\max}}, \tag{10}$$

where $\tilde{u}^P_{\max}$ indicates the plastic displacement estimated through eqns (6) and (7) and $u^P_{\max}$ the calculated "exact" value. The ratio r gives the relative error we introduce when estimating the ductility factor μ with the rigid-plastic method. A comparison between eqn (10) and eqn (3) shows that r also gives the ratio between the estimated and the calculated total displacements.

As the estimated and the calculated values of the plastic displacement tend to coincide, the ratio r tends to unity, which means that no error is committed in estimating the ductility demand, or, similarly, the total displacement. This obviously happens if T equals zero (rigid-plastic behaviour), and also when T is equal to T^*, since in both these cases $u^p_{\max} = \tilde{u}^P_{\max}$. On the other hand, r is equal to unity also when $T \geq \overline{T}$, since it is $u^p_{\max} = \tilde{u}^P_{\max} \equiv 0$. In all these cases, the rigid-plastic method predicts the earthquake displacement demand exactly. Otherwise, some errors can be produced.

Table 1: Earthquakes considered in the present investigation.

1	Ardal (Iran), LONG, 1977	17	Landers (California), LCN000, 1992
2	Cape Mendocino (Cal), PET090, 1992	18	Loma Prieta (Cal), CLS000, 1989
3	Cartago (Costa Rica), LONG, 1991	19	Mammoth Lakes(Cal), LLUL000, 1999
4	Chamoli (India), N20E, 1999	20	Montenegro, N-S, 1979
5	Chi Chi (Taiwan), CHY041N, 1999	21	Morgan Hill (Cal), CYC195, 1984
6	Coalinga (California), D-TSM360, 1983	22	N. Palm Springs (Cal), NPS300, 1986
7	Duzce (Turkey), DZC270, 1999	23	Parkfield (California), C02065, 1966
8	Edgecumbe (New Zealand), N07W, 1987	24	Parkfield (California), 90, 2004
9	El Salvador, LONG, 2001	25	San Fernando (California), S16E, 1971
10	Erzincan (Turkey), N279, 1992	26	South Iceland, LONG, 2000
11	Friuli (Italy), E-W, 1976	27	Spitak (Armenia), GUK000, 1988
12	Gazli (Uzbekistan), E-W, 1976	28	Superstitn Hills (Cal), B-SUP135, 1987
13	Imperial Valley (Cal), H-BCR230, 1979	29	Tabas (Iran), N74E, 1978
14	Irpinia (Italy), A-STU270, 1980	30	Tabas (Iran), TAB-LN, 1978
15	Kobe (Japan), N35W, 1995	31	Trinidad, B-RDE000, 1980
16	Kocaeli (Turkey), ATS000, 1999	32	Victoria (Mexico), CPE045, 1980

To evaluate the extent of these errors, a numerical investigation was carried out. By referring to the earthquakes listed in Table 1, the value of the ratio r as defined by eqn (10) was computed for elastic-plastic oscillators possessing different realistic values of a_y and a damping ratio ξ=10%. The latter is a typical value for damping ratio when stress is at the yield point, cf. Chopra [15]. For each earthquake and for each value of a_y, different values of natural period, ranging from zero to $\overline{T}$, were considered.

For each value of T, the mean value of the ratio r, say M_r, was finally obtained. The resulting diagram is presented in Figure 5. It shows that, whatever the yield acceleration and whatever the natural period T of the elastic-plastic oscillator, the rigid-plastic method does on average provide a conservative estimate of the displacement ductility factor (values of M_r larger than one). In particular, the mean relative errors are generally lower than 30%. They are very low for $T < 0.2s$ and always lower than 15% for $T > 0.75s$.

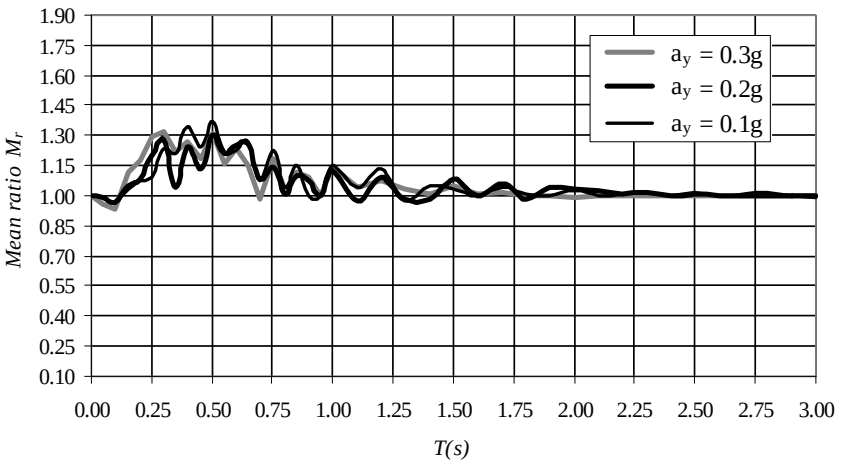

Figure 5: Mean ratio of predicted to calculated maximum displacements for different values of a_y (ξ=10%).

4 Evaluating the rigid-plastic method

Most of the approximate methods proposed in current literature estimate the earthquake ductility demand μ by means of parameters that are function of μ itself. As a consequence, they usually require iteration procedures which may also imply convergence problems, cf. e.g. Chopra and Goel [16]; Miranda and Akkar [17]. An in-depth evaluation of the accuracy of some of these methods was done by Miranda and Ruiz Garcia [18] and by Akkar and Miranda [19].

On the contrary, the rigid-plastic method does not involve any iteration procedure. Should the rigid-plastic pseudo-spectrum and the elastic response spectrum of the considered earthquake be available, the method predicts the inelastic displacement demand on any elastic-plastic oscillator by means of a direct procedure, see Section 2.

What is more, the rigid-plastic method spots the range of periods in which the inelastic demand prediction actually needs to be obtained under a given earthquake. This range is always given by $0 \le T \le \overline{T}$. The actual value of $\overline{T}$, which is different for different earthquakes and for different values of a_y and ξ, may be easily obtained from the elastic response spectrum of the considered earthquake, see Figure 2. General as it is, this result could be adopted by any approximate method that aims at estimating the earthquake ductility demand on elastic-plastic oscillators.

Within the above range, the rigid-plastic method gives a good estimate of the peak plastic displacement of comparatively short-period oscillators (say $T \le 0.25s$) and comparatively long-period oscillators ($T > 0.75s$), see Figure 5. On the contrary, high errors are generally encountered in the short period range when other approximate methods are adopted, as can be inferred from the diagrams presented by Miranda and Ruiz Garcia [18] and by Akkar and Miranda [19]. For $T > 0.75s$ the rigid-plastic method prediction is on average comparable with that of other approximate methods (cf. e.g. the results presented by Miranda and Ruiz Garcia [18] and by Akkar and Miranda [19]).

In the medium period range the rigid-plastic prediction may be, however, less satisfactory. Here the empirical formula (7) plays a fundamental part for the rigid-plastic prediction. Most of the mean errors found in the range $0.25\text{s} \le T \le 0.75s$ (see Figure 5) can be actually put down to the appliance of such a formula. It should be noted that in the same range of periods some other approximate methods might give a better prediction on average (cf. Miranda and Ruiz Garcia [18]; Akkar and Miranda [19]). This could denote the need for an improvement of formula (7).

The following points should be noted, though. The mean ratio M_r plotted in Figure 5 is relevant to assigned values of a_y, which may entail very high values of μ in the short-medium period range ($\mu > 10$), as Figure 4 shows. This means that the rigid-plastic method is able to estimate very high values of μ with reasonably narrow mean errors. On the contrary, rather low values of μ are usually assigned when evaluating the mean errors relevant to other approximate methods (for example μ ranging from 2 to 6 is considered by Miranda and Ruiz Garcia [18]). In addition, the errors relevant to these methods generally increase as μ increases, this being especially so in the medium period range (cf. Miranda and Ruiz Garcia [18]; Akkar and Miranda [19]). This means that also in the medium period range the rigid-plastic prediction can in fact be good enough, even when compared to that obtained by means of other approximate methods.

5 Conclusions

With the aim of evaluating the extent of the relative errors that can be made when the maximum seismic displacement of an elastic-plastic oscillator is estimated by means of the rigid-plastic method, a numerical investigation was carried out in the present paper. The results show that this method leads -on average- to conservative and fairly good predictions, whatever the oscillator and the earthquake, and even when the plastic displacements are very large. Mean relative errors lower than 15% are found both for short-period and long-period oscillators. For medium period oscillator the error is generally less than 30%. A profitable feature of the method is that of obtaining the ductility demand prediction directly in the range of periods where inelastic displacements may actually occur under a given earthquake. Moreover, the rigid-plastic prediction does not involve any iterative procedure, as many other approximate methods do. For short-period oscillators the mean error is generally much lower than that relevant to most of the other approximate methods. For medium-period and long-period oscillators, a comparable mean error may be found with respect to other methods. Especially as the ductility demand increases.

Acknowledgements

The recorded accelerograms considered in this paper were obtained from:
ESD – The European Strong-Motion Database, http://www.isesd.cv.ic.ac.uk
PEER Strong Motion Database, http://peer.berkeley.edu/smcat
COSMOS Virtual Data Center, http://db.cosmos-eq.org

References

[1] Rosemblueth, E. & Herrera, I., On a kind of hysteretic damping. *Journal of Engineering Mechanics Division ASCE*, **90**, pp. 37–48, 1964.
[2] Gulkan, P. & Sozen, M., Inelastic response of reinforced concrete structures to earthquakes motion. *ACI Journal*, **71**, pp. 604–610, 1974.
[3] Iwan, W.D., Estimating inelastic response spectra from elastic spectra. *Earthquake Engineering and Structural Dynamics*, **8**, pp. 375–388, 1980.
[4] Kowalsky, M., Priestley, M.J.N. & McRae, G.A., Displacement-based design of RC bridge columns in seismic regions. *Earthquake Engineering and Structural Dynamics*, **24**, pp. 1623–1643, 1995.
[5] Newmark, N.M., & Hall, W.J., *Earthquake Spectra and Design*, Earthquake Engineering Research Institute: Berkeley, CA, 1982.
[6] Miranda, E., Inelastic displacements ratios for structures on firm sites. Journal of Structural Engineering, **126**, pp. 1150–1159, 2000.
[7] Paglietti, A. & Porcu, M.C., Rigid-plastic approximation to predict motion under strong earthquakes. *Earthquake Engineering and Structural Dynamics*, **30**, pp. 115–126, 2001.

[8] Porcu, M.C. & Carta, G., Rigid-plastic bound to the seismic inelastic response of flexible elastic-plastic oscillators. *European Earthquake Engineering*, **3**, pp. 3–9, 2007.
[9] Porcu, M.C. & Carta, G., Rigid-plastic seismic analysis to predict the structural ductility demand. *International Journal of Applied Engineering Research*, **4(3)**, pp. 309–325, 2009.
[10] Domingues Costa, J.L., Bento, R., Levtchitch, V. & Nielsen, M.P., Simplified non-linear time-history analysis based on the Theory of Plasticity. *Proc. of the ERES 2005 Conference*, WIT Press: Southampton, UK, pp. 375-386, 2005.
[11] Porcu, M.C. & Mascia, M., Rigid-plastic pseudo-spectra: peak response charts for seismic design. *European Earthquake Engineering*, **3**, pp. 37–47, 2006.
[12] Makris, N. & Black, C.J., Dimensional analysis of rigid-plastic structures under pulse-type excitations. *Journal of Engineering Mechanics*, **130(9)**, pp. 1006–1018, 2004.
[13] Hibino, Y., Toshikatsu, I., Domingues Costa, J.L. & Nielsen, M.P., Procedure to predict the storey where plastic drift dominates in two-storey building under strong ground motion. *Earthquake Engineering and Structural Dynamics*, **38(7)**, pp. 929–939, 2008.
[14] Domingues Costa, J.L., Bento, R., Levtchitch, V. & Nielsen, M.P., Rigid-plastic seismic design of reinforced concrete structures. *Earthquake Engineering and Structural Dynamics*, **36**, pp. 55–76, 2007.
[15] Chopra, A.K., Dynamics of Structures. Theory and Application to Earthquake Engineering, Prentice Hall: New Jersey, 2001.
[16] Chopra, A.K. & Goel, R.K., Evaluation of NSP to estimate seismic deformation: SDF systems. *Journal of Structural Engineering*, **126(4)**, pp. 482-490, 2000.
[17] Miranda, E. & Akkar, S.D., Evaluation of iterative schemes in equivalent linear methods. *Earthquake Engineering Research Institute*, 2003.
[18] Miranda, E. & Ruiz Garcia, J., Evaluation of approximate methods to estimate maximum inelastic displacement demands. *Earthquake Engineering and Structural Dynamics*, **31**, pp. 539–560, 2002.
[19] Akkar, S.D. & Miranda, E., Statistical evaluation of approximate methods for estimating maximum deformation demands on existing structures. *Journal of Structural Engineering*, **131**, pp. 160-172, 2005.

This page intentionally left blank

Comparison of buckling load for H-shaped compression members with different eccentric bracing methods

Y. Kimura[1] & Y. Yoshino[2]
[1]*Tohoku University, Japan*
[2]*Nagasaki University, Japan*

Abstract

In Japanese design code, the bracing for the compression members is supported to be set up on the centroid of its section. On the other hand, the braces may be not jointed at the centroid for the compression members in the real structures, and be eccentrically jointed on the section of members. If non-structural members are used as bracings, it is more effective to design the space frame. These members are supported to be effective to restrain the buckling deformation for the compression members, and then most of non-structural members are plurally or continuously jointed. Our previous papers have evaluated the effect of the eccentric braces to restrain the buckling deformation for H-shaped compression members with an eccentric brace at the center of the member, and with continuously eccentric braces, respectively. But the effect for the continuously eccentric braces may be different from that for an eccentric brace at the center of the compression member. If it makes the effect of each eccentric bracing equivalent, it is more practical to design the compression members with eccentric braces in the space structures.

This paper compares the elasto-plastic buckling behavior for H-shaped compression members with eccentric braces at the center of members to that with continuously eccentric braces, and suggests the unified estimation method for the effect of the bucking restraint for each eccentric bracing.

WIT Transactions on The Built Environment, Vol 120, © 2011 WIT Press
www.witpress.com, ISSN 1743-3509 (on-line)
doi:10.2495/ERES110231

1 Elastic buckling load for H-shaped compression members with different eccentric braces

1.1 Development of elastic buckling load for H-shaped compression members with eccentric different braces

In this section, the elastic buckling load for H-shaped compression members with eccentric braces is developed by the energy method and the eigen-value analyses.

When an H-shaped compression member with eccentric brace is laterally and torsionally buckled, the potential energy U is expressed as the following in reference to Kimura.

Then the flexural and torsional buckling deformation with web distortion occurs as shown in Fig. 1 (Bleich [3]).

$$U = \frac{1}{2}\int_0^l \Big[EI_1 u_1''^2 + EI_2 u_2''^2 + GK_w \beta'^2 + GK_1(\beta' - \alpha_1')^2 + GK_2(\beta' - \alpha_2')^2 + \frac{4D_w}{d}(\alpha_1^2 + \alpha_1\alpha_2 + \alpha_2^2) - P_1 u_1'^2 - P_2 u_2'^2 \Big] dx + \frac{1}{2}\left\{ {}_A K_\beta (\beta - \alpha_1)^2 \Big|_{x=\frac{l}{2}} + {}_A K_u u_0^2 \Big|_{x=\frac{l}{2}} \right\} \tag{1}$$

where EI_i is the flexural rigidity of each flange for H-shaped member, GK_i is the torsional rigidity of each flange and GK_w is the torsional rigidity of web. D_w is the flexural rigidity of web plate for H-shaped members. ${}_AK_u$ is the lateral rigidity of the brace and ${}_AK_\beta$ is the rotational rigidity of the brace. d is the distance between both flanges and l is the length of H-shaped members. P_i and u_i are the compression load and the lateral displacement at the center of the flanges, u_0 is the lateral displacement at the brace point. β is the torsional angle, and α_i is the rotational angles of each flange due to web distortion. The suffix, i, represents 1 and 2, and it means each flange.

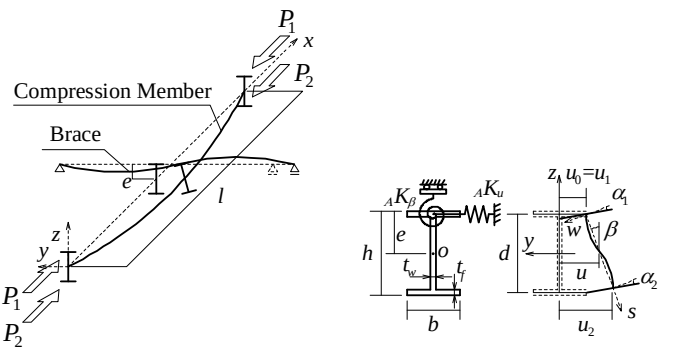

(a) Buckling Deformation for Compression Members

(b) Bracing Models and Buckling Deformation of Section

Figure 1: Buckling deformation for H-shaped compression members with eccentric braces (Type A).

In this paper, it is constantly assumed that the cross section of H-shaped member is symmetric, then $EI_1=EI_2=EI_f$, $GK_1=GK_2=GK_f$ and $P_1=P_2=P_f$. Then it is also assumed that braces are set up at upper flange, so u_0 is equal to u_1.The ratio of eccentric distance to web depth, e/h, is equal to 0.5. Web deformation is expressed in the deflection curve with α_1 and α_2.

$$w = \frac{s(s-d)^2}{d^2}\alpha_1 + \frac{s^2(s-d)}{d^2}\alpha_2 \tag{2}$$

The boundary condition is simple support to strong and weak axis. Lateral deformation of member and web deformation are expressed in the function of sine curves in the following

$$\begin{aligned} u_1 &= a_1 \sin\frac{\pi}{l}x + a_2 \sin\frac{2\pi}{l}x, \quad u_2 = b_1 \sin\frac{\pi}{l}x + b_2 \sin\frac{2\pi}{l}x \\ \alpha_1 &= c_1 \sin\frac{\pi}{l}x + c_2 \sin\frac{2\pi}{l}x, \quad \alpha_2 = d_1 \sin\frac{\pi}{l}x + d_2 \sin\frac{2\pi}{l}x \end{aligned} \tag{3}$$

Torsional angle, β, is expressed with the lateral deformation of flanges, $u_1$and u_2 as the following

$$\beta = \frac{u_2 - u_1}{d} \tag{4}$$

The lateral deformation, u_1 and u_2 at the center of the member are expressed with the eccentric distance, e and the torsional angle, β_0.

$$u_1 = (e - \frac{d}{2})\beta_0 \ , \ u_2 = (e + \frac{d}{2})\beta_0 \ u_1 = (e - \frac{d}{2})\beta_0 \ , \ u_2 = (e + \frac{d}{2})\beta_0 \tag{5}$$

The relationship between the lateral deformation, u_1 and u_2 is obtained from Eqs. (4) and (5) as the following.

$$u_1 = \frac{2e-d}{2e+d}u_2 \ u_1 = \frac{2e-d}{2e+d}u_2 \tag{6}$$

In this paper, the eccentric distance e in the range of $e \geq d/2$ is adopted.

Substituting Eq. (6) for Eq. (1), the buckling load P_{cr} is obtained as the following

$$\begin{aligned} P_{cr} = {} & EI_y(\frac{\pi}{l})^2 + \frac{2}{d^2}\{GK_w + (\tau_1+\tau_2)GK_f + \tau_1\frac{2_A K_\beta}{l}(\frac{l}{\pi})^2\} + \frac{2_A K_u}{l}(\frac{l}{\pi})^2 \\ & - \sqrt{(\frac{2}{d^2})^2\{GK_w + (\tau_1+\tau_2)GK_f + \tau_1\frac{2_A K_\beta}{l}(\frac{l}{\pi})^2\}^2 + \{\frac{2_A K_u}{l}(\frac{l}{\pi})^2\}^2} \end{aligned} \tag{7}$$

$$P_{cr} = 4EI_y(\frac{\pi}{l})^2 \tag{8}$$

where $P_{cr}=2P_f$ and $EI_y=2EI_f$, τ_1 is the reduction of the rotational rigidity and the upper flange torsional rigidity, and τ_2 is the reduction of the lower flange torsional rigidity. Where l_b is the buckling length. Eq. (7) is the equation for the flexural-torsional buckling load with web deformation. Eq. (8) is the equation for

Euler's buckling load for $l_b=l/2$. Where, the relationship between the torsional angle β_0 and the rotational angle of each flange α_1 and α_2 is expressed with τ_1 and τ_2.

$$\beta_0-\alpha_1=\tau_1\beta_0\ ,\ \beta_0-\alpha_2=\tau_2\beta_0 \tag{9}$$

τ_1 and τ_2 are obtained from Eq. (9) as the following

$$\tau_1=\frac{\frac{6D_w}{d}\{GK_f(\frac{\pi}{l})^2+\frac{2D_w}{d}\}}{\{GK_f(\frac{\pi}{l})^2+\frac{4D_w}{d}+\frac{2\ {}_AK_\beta}{l}\}\{GK_f(\frac{\pi}{l})^2+\frac{4D_w}{d}\}-(\frac{2D_w}{d})^2} \tag{10}$$

$$\tau_2=\frac{\frac{6D_w}{d}\{GK_f(\frac{\pi}{l})^2+\frac{2D_w}{d}+\frac{2K_\beta}{l}\}}{\{GK_f(\frac{\pi}{l})^2+\frac{4D_w}{d}+\frac{2\ {}_AK_\beta}{l}\}\{GK_f(\frac{\pi}{l})^2+\frac{4D_w}{d}\}-(\frac{2D_w}{d})^2} \tag{11}$$

The smaller value of P_{cr} obtained from Eqs. (7) and (8) can be used as the buckling load for H-shaped compression members with eccentric braces. Similarly, elastic buckling load for H-shaped compression members with continuously eccentric braces is obtained by the energy method and the eigen-value analyses. When H-shaped compression member with continuously eccentric brace is laterally and torsionally buckled, the potential energy U is expressed as the following in reference to Kimura and Amamoto [2].

Then the flexural and torsional buckling deformation with the web distortion occurs as shown in Fig. 2 (Bleich [3]).

$$U=\frac{1}{2}\int_0^l\Big[EI_1u_1''^2+EI_2u_2''^2+GK_w\beta'^2+GK_1(\beta'-\alpha_1')^2+GK_2(\beta'-\alpha_2')^2 \\ +\frac{4D_w}{d}(\alpha_1^{\ 2}+\alpha_1\alpha_2+\alpha_2^{\ 2})-P_1u_1'^2-P_2u_2'^2\Big]dx+\frac{1}{2}\Big\{{}_BK_\beta(\beta-\alpha_1)^2+{}_BK_uu_0^{\ 2}\Big\} \tag{12}$$

$${}_AK_u={}_BK_ul\ ,\ {}_AK_\beta={}_BK_\beta l \tag{13}$$

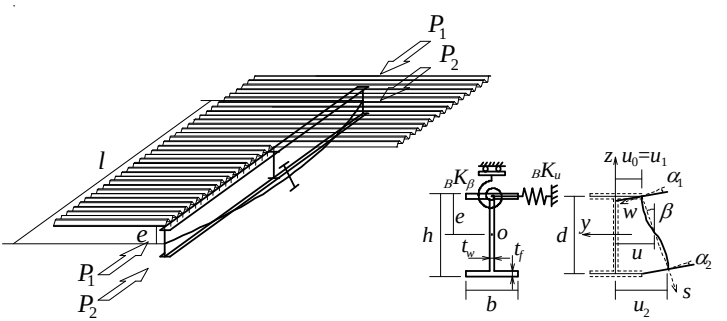

(a) Buckling Deformation for Compression Members

(b) Bracing Models and Buckling Deformation of Section

Figure 2: Buckling deformation for H-shaped compression members with continuously eccentric braces (Type B).

Then it is defined that the case of the rigidity multiplied by length of members in eq. (13) is equivalent to the bracing rigidity for the case of eccentric braces at the center of members as Eqs. Lateral deformation of member and web deformation are expressed in the function of sine curves in the following

$$u_0 = u_1 = a_1 \sin\frac{n\pi}{l}x\,, \quad u_2 = a_2 \sin\frac{n\pi}{l}x$$
$$\alpha_1 = b_1 \sin\frac{n\pi}{l}x\,, \quad \alpha_2 = b_2 \sin\frac{n\pi}{l}x \tag{14}$$

Substituting Eq. (6), (14) for Eq. (12), the buckling load P_{cr} is obtained as the following

$$P_{cr} = EI_y(\frac{n\pi}{l})^2 + \frac{2}{d^2}\{GK_w + (\tau_1+\tau_2)GK_f + \tau_1 {}_BK_\beta(\frac{l}{n\pi})^2\} + {}_BK_u(\frac{l}{n\pi})^2$$
$$-\sqrt{(\frac{2}{d^2})^2\{GK_w + (\tau_1+\tau_2)GK_f + \tau_1 {}_BK_\beta(\frac{l}{n\pi})^2\}^2 + \{{}_BK_u(\frac{l}{n\pi})^2\}^2} \tag{15}$$

The buckling load for H-shaped compression members with continuously eccentric braces is obtained from Eq. (15), with the order of buckling mode, *n*, for the lowest buckling load in this equation. Eq. (15) is the equation for the flexural-torsional buckling load with web deformation. τ_1 and τ_2 is obtained from Eq. (9) as the following

$$\tau_1 = \frac{\frac{6D_w}{d}\{GK_f(\frac{n\pi}{l})^2 + \frac{2D_w}{d}\}}{\{GK_f(\frac{n\pi}{l})^2 + \frac{4D_w}{d} + {}_BK_\beta\}\{GK_f(\frac{n\pi}{l})^2 + \frac{4D_w}{d}\} - (\frac{2D_w}{d})^2} \tag{16}$$

$$\tau_2 = \frac{\frac{6D_w}{d}\{GK_f(\frac{n\pi}{l})^2 + \frac{2D_w}{d} + {}_BK_\beta\}}{\{GK_f(\frac{n\pi}{l})^2 + \frac{4D_w}{d} + {}_BK_\beta\}\{GK_f(\frac{n\pi}{l})^2 + \frac{4D_w}{d}\} - (\frac{2D_w}{d})^2} \tag{17}$$

Fig. 3 shows the numerical analysis model for the H-shaped compression members with eccentric brace. Marc 2008 is used for the numerical analyses. Type A represents the eccentrically braced members at the center of structural members, and Type B represents structural members with continuously eccentric braces. The compression member consists of 4 node shell elements, and the eccentric brace is replaced on the lateral and rotational springs. In Type B, The spacing between bracings, *l'*, is equal to 250 mm. Then the value of lateral and rotational rigidity of springs are calculated as ${}_BK_u l'$ and ${}_BK_\beta l'$, respectively. The boundary condition is simple supports to strong and weak axis, and three kinds of the cross-sectional shapes are adopted as shown in Table 1.

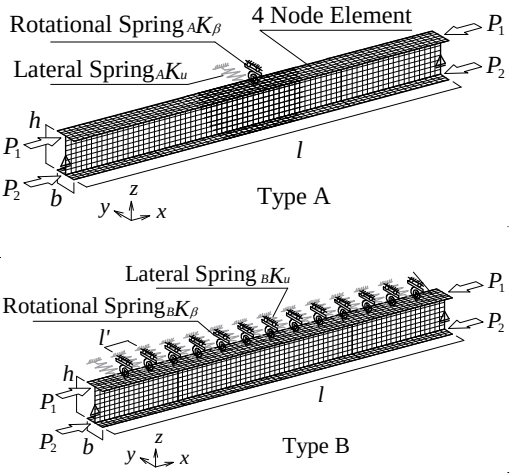

Figure 3: Numerical analysis models.

Table 1: Cross-sectional shape of H-shaped members.

b/h	h	b	t_w	t_f	
0.5	300	150	6.5	9	
0.68	294	200	8	12	
1	300	300	10	15	(mm)

1.2 Comparison of equivalent bracing rigidity for H-shaped compression members with different eccentric braces

Fig. 4 shows the relationship between the elastic buckling stress, σ_{cr}, for H-shaped compression members with eccentric braces and slenderness ratio, λ.

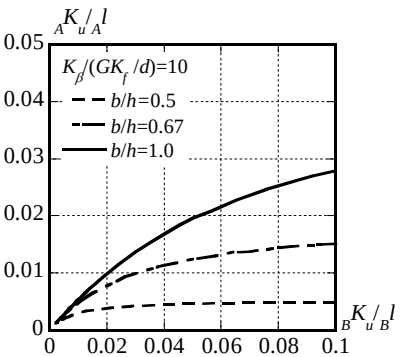

Figure 4: Elastic buckling stress for H-shaped compression members with eccentric braces.

The buckling load for H-shaped compression members with eccentric braces (in Type A) is obtained from Eqs. (8) and (9), and the smaller value of P_{cr} obtained from both expressions, is used. The buckling load for the case of continuously eccentric braces (in Type B) is obtained from Eq. (16). For the small slenderness ratio, if bracing rigidity in Type A is equal to that in Type B, ${}_AK_u={}_BK_u l$, ${}_AK_\beta={}_BK_\beta l$, the elastic buckling stress in Type A is constantly higher than that in Type B. In this case, the buckling stress for Type A is equal that for Type B, when the lateral and rotational rigidity of Type A (K_u,K_β) is in half of that for Type B (${}_BK_u=0.5\ {}_AK_u$, ${}_BK_\beta=0.5\ {}_AK_\beta$), respectively. In addition, the buckling stress for Type B with n=2 is constantly higher than that for perfect support for Type A. Then the plots ▼, ▽ in Fig. 4 are the points to change from the lateral-torsional buckling to Euler's Buckling for $l_b=l/2$ in Type A, and ▼ in Fig.4 is the point to change from the buckling load for n=1 to buckling load for n=2 in Type B.

Fig. 5 shows the relationship between the lateral rigidity ratio, ${}_AK_u/{}_Al$ for Type A and that, ${}_BK_u/{}_Bl$ for Type B, when the bucking mode changes such as the plots, ▼, ▽ and ▼ in Fig. 4.

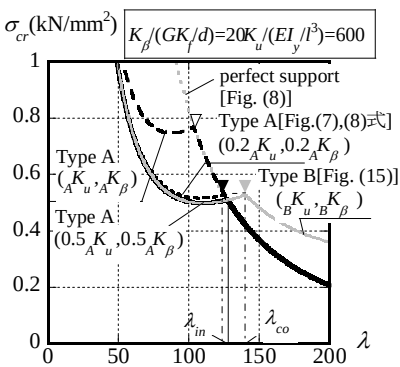

Figure 5: Comparison of lateral rigidities between Type A and Type B.

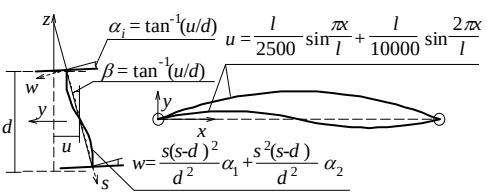

Figure 6: Initial impressions.

${}_AK_u/{}_Al$, and ${}_BK_u/{}_Bl$ are expressed as the ratio of the lateral rigidity to length for Type A and for Type B. The parameter is the cross-sectional shape. The lateral rigidity ratio for Type B, ${}_BK_u/{}_Bl$, is constantly higher than that for Type A, ${}_AK_u/{}_Al$. It is shown that wide flange, b/h=1.0, requires the higher rigidity, ${}_AK_u/{}_Al$ than the other at the some ${}_BK_u/{}_Bl$.

2 Evaluation of elasto-plastic buckling stress for H-shaped compression members with different eccentric bracings

2.1 Elasto-plastic buckling behavior for H-shaped compression members with different eccentric bracings

In this section, elasto-plastic buckling behavior for H-shaped compression members with eccentric braces at the center of the members and with continuously eccentric braces is confirmed by the elasto-plastic large deformation analyses. Marc version 2008 is used [MSC, 2008]. The analyses models and boundary condition are same as the eigen-value analyses models in the previous section. Material properties for H-shaped members are shown in Table 2. Initial impressions of the lateral displacement, u, the torsional angle, β, and the rotational angle of each flange due to the web distortions, α_i, are described as the function of sine curves in the followings.

$$u = \frac{l}{2500}\sin\frac{\pi x}{l} + \frac{l}{10000}\sin\frac{2\pi x}{l} \tag{18}$$

$$\beta = \tan^{-1}(u/d) \tag{19}$$

$$\alpha_i = \tan^{-1}(u/d) \tag{20}$$

where the suffix i represents 1 and 2, and it means each flange. The web distortion is expressed in the deflection curve with α_1 and α_2 as the following.

Table 2: Material properties of H-shaped members.

E (kN/mm^2)	E_{st} (kN/mm^2)	σ_y (N/mm^2)	σ_u (N/mm^2)
206	2.74	294	436

In this section, the lateral and rotational rigidities of braces are expressed as the ratio of rigidities of braces to minimum required rigidities, K_u/K_{u0} and $K_\beta/K_{\beta 0}$. For continuously eccentric bracing, the value of the bracing rigidity from n=1 to n=2 is defined as the required rigidity. The coordinates K_u/K_{u0} and $K_\beta/K_{\beta 0}$ at the required rigidity are expressed as k_0. For numerical analyses, four points on the curve of k_0 in Fig. 7 are selected, and these coordinates are expressed as K_M, $2.5K_B$, $5K_U$ and $10K_U$. When a distance from (K_u/K_{u0}, $K_\beta/K_{\beta 0}$)=(1,1) to the curve of k_0 is shortest, the coordinates K_u/K_{u0} and $K_\beta/K_{\beta 0}$ on the curve of k_0 are defined as K_M. For $2.5K_B$ the value of $K_\beta/K_{\beta 0}$ on the curve of k_0 is fixed at 2.5, and then the value of K_u/K_{u0} depends on cross-sectional shapes and slenderness ratio. For $5K_U$ and $10K_U$, the value of K_u/K_{u0} on the curve of k_0 is fixed at 5.0 and 10, and then the value of $K_\beta/K_{\beta 0}$ depends on cross-sectional shapes and slenderness ratio. Non-structural members in the real truss structures have less than the required rigidity, so that $0.25k_0$ to $0.5k_0$ of bracing rigidities are selected as the analytical parameters in Appendix. For example, the coordinates on the curve of $0.5k_0$ are half of the coordinate on the curve of k_0, thus the values of K_u/K_{u0} and $K_\beta/K_{\beta 0}$ for $0.5k_0$ are half of these for k_0, respectively.

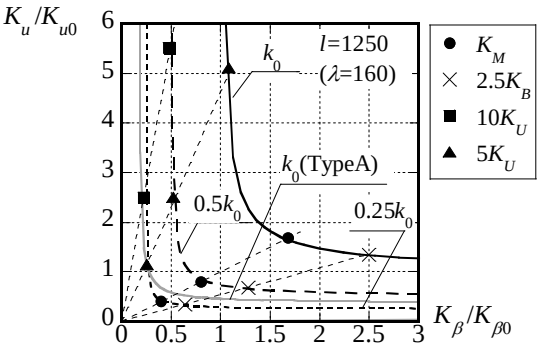

Figure 7: Lateral and rotational rigidity of continuously eccentric braces.

Fig. 8 shows the elasto-plastic buckling behavior for H-shaped compression members with different type of braces. Figs. 8 (a)~(d) represent the relationship between the compression load, P/P_y, the lateral displacement, u/l, the torsional angle, β, the rotational angle of each flange due to the web distortions, α_1, α_2, and the axial displacement, δ/δ_y, respectively. Then the plots ▼, ▼ in Fig. 8 (a) are the points at the maximum load, P_m, and ▽, ▽ in Fig. 8 (a) are the yielding points. Where the maximum load, P_m, is defined as the elasto-plastic buckling load. u, β, α_1 and α_2 in Figs. 8 (b)~(d) are the displacement at the center of members. The elasto-plastic buckling load, P_m, for Type A with $2.5K_B$ is almost equal to that for Type B. On the other hand, the elasto-plastic buckling load, P_m, for Type B with $10K_U$ is much larger than that for Type A with $10K_U$. The torsional angle, β , at P_m for Type B with $10K_U$ is larger than that for Type A.

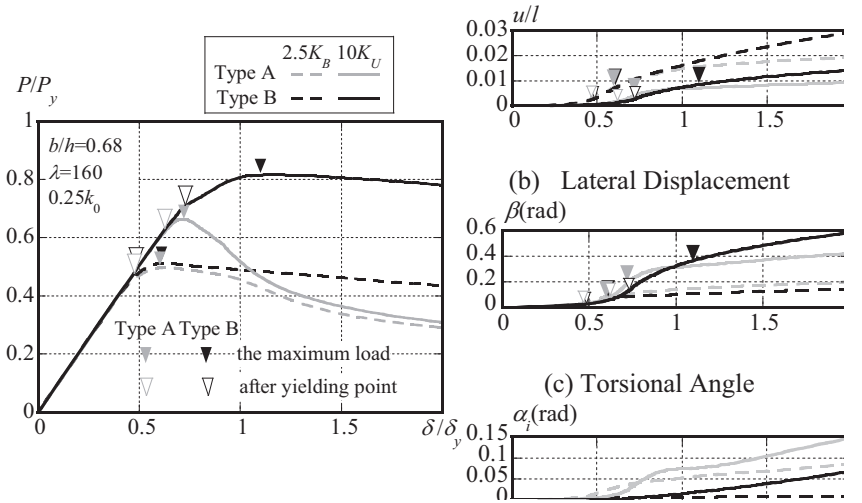

Figure 8: Elasto-plastic buckling behavior for H-shaped compression members with eccentric braces.

After yielding, the torsional angle, β, for Type B increase rapidly. After yielding for H-shaped compression members, the reduction in the torsional rigidity for members is small, even though the torsional angle is larger. Then the members keep their strength after the members are inelastically buckled.

Fig. 9 shows the relationship between the lateral displacement, u_1, and the torsional displacement, u_2-u_1, at P_m for different type of bracing rigidity.

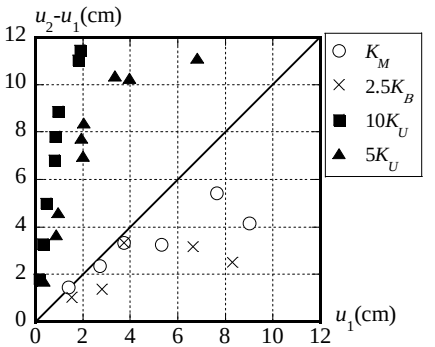

Figure 9: Relationship between lateral displacement and torsional displacement.

u_1 is the lateral displacement of upper flange, and u_2-u_1 is the difference of lateral deformation between upper and lower flanges at P_m . Then for fig. 9, u_1 and u_2-u_1 is defined as lateral displacement and torsional displacement. For K_M and 2.5K_B, the lateral displacement, u_1, is much larger than the torsional displacement,u_2-u_1, and for 10K_U and 5K_U, u_2-u_1 is much larger than u_1. When the lateral displacement is larger than the torsional displacement, the buckling mode of H-shaped members is called as the predominantly lateral buckling mode. Similarly, when the torsional displacement is larger than the lateral displacement, the buckling mode of H-shaped members is called as the predominantly lateral buckling mode. Therefore, the buckling mode for K_M, 2.5K_B is predominantly lateral buckling mode and The buckling mode for 10K_U, 5K_U is predominantly torsional buckling mode. The relationship between the predominantly bucking deformation and the buckling stress must be investigated.

2.2 Elasto-plastic buckling behavior for H-shaped compression members with different eccentric bracings

Fig. 10 show the relationship P_m for Type A and that for Type B. Fig. 10(a) compares the buckling load for the for Type A with or without the vertical stiffener, and Fig. 10(b) show the buckling load for the different type of braces. For Type A, the elasto-plastic buckling load, P_m, with the vertical stiffener is larger than that without the vertical stiffener, because the web distortion is restrained by the vertical stiffener. For predominantly lateral buckling mode, the elasto-plastic buckling load, P_m for Type A is almost equal to that for Type B.

On the other hand, for predominantly lateral buckling mode, the elasto-plastic buckling load, P_m for Type B with $10K_U$ and $5K_U$ is higher than that for Type A, because the torsional rigidity for Type A is higher than that of Type B due to continuously eccentric bracing.

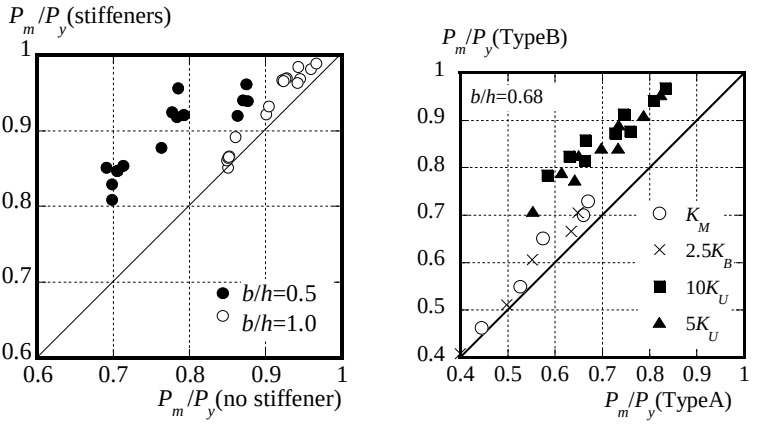

(a) with or without the vertical stiffener (b) different type of braces

Figure 10: Relationship elasto-plastic buckling load.

Fig. 11 shows the relationship between lateral rigidity ratio ${}_BK_u/{}_BK_{u0}$, and the modified ratio, ${}_B\bar{K}_u/{}_BK_{u0}$ for Type B. The plots represent the numerical analyses results for three kinds of the cross section. H-shaped members for Type B possess the only elasto-plastic buckling load for Type A with ${}_B\bar{K}_u/{}_BK_{u0}=1({}_AK_u/{}_AK_{u0}=1)$, even though ${}_BK_u/{}_BK_{u0}$ for Type B increases. The curve closed from solution of Eq. (21) is represented as the following in reference to the numerical analyses results.

$$ {}_B\bar{K}_u/{}_BK_{u0} = 1-0.3\sqrt{{}_BK_{u0}/{}_BK_u} \tag{21} $$

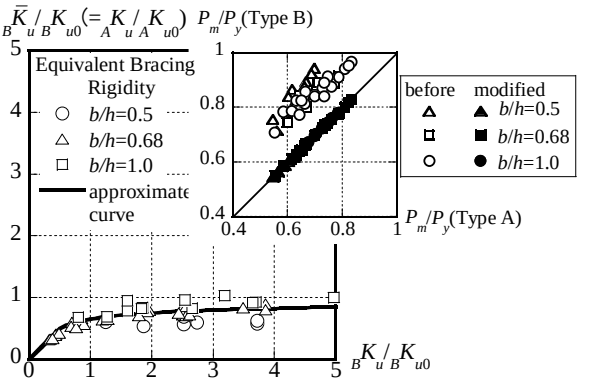

Figure 11: Evaluation of equivalent bracing rigidity.

Then the elasto-plastic buckling load for Type A and Type B can be evaluated using the equivalent rigidity of eq. (21).

3 Conclusion

1) When the buckling mode of H-shaped members is the predominantly torsional buckling mode, the elasto-plastic buckling load for Type B is higher than that for Type A.
2) When the buckling mode is the predominantly torsional buckling mode, the equivalent bracing rigidity for the elasto-plastic buckling load of type A equal to that for Type B is obtained from Eq. (21).
3) When the buckling mode is the predominantly torsional buckling mode, the equivalent bracing rigidity for the elasto-plastic buckling load of type A equal to that for Type B is obtained from Eq. (21).

Appendix

Fig. A1 shows the coordinates of bracing rigidity of non-structural members for the real truss structure. Symbols show the case of non-structural members with channel section and angle section. The black solid curve represents the case of required bracing rigidity. According to Fig. A1, part of the non-structural member does not possess the required bracing rigidity.

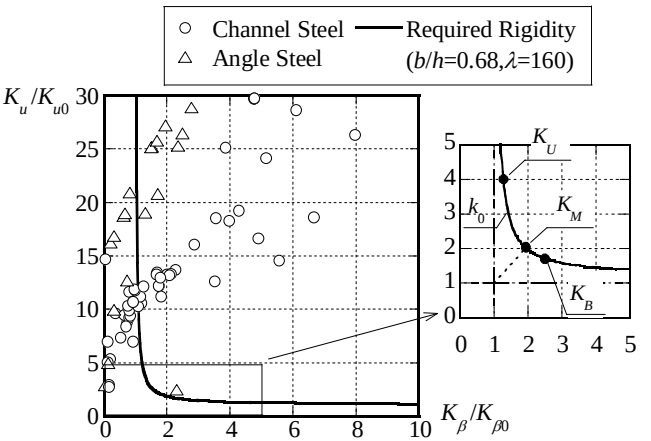

Figure A1: Bracing rigidity of non-structural members for real truss structures.

References

[1] Y Kimura, A Amamoto (2006). Effect of Web Deformation on Buckling Load for H-Shaped Compression Member with Eccentric Braces, Journal of Structural Construction Engineering, AIJ. 600, 187-194 (in Japanese)

[2] Y Kimura, A Amamoto (2009). Effect of Lateral and Rotational Restraint for Eccentric Braces on Flexural-Torsional Buckling Load with Web Deformation for H-Shaped Compression Members AIJ. 637, 583-591 (in Japanese)
[3] Hans H Bleich (1952). Buckling Strength of Metal Structures, McGraw-Hill Book Co., 142-147.

This page intentionally left blank

The effects of multiple vertical baffles on sloshing phenomenon in rectangular tanks

M. Hosseini[1] & P. Farshadmanesh[2]
[1]*Graduate School of Civil Eng. Dept., South Tehran Branch of the Islamic Azad University (IAU), Tehran, Iran*
[2]*Hydraulic Structures Group, Civil Eng. Dept., South Tehran Branch of the Islamic Azad University (IAU),Tehran, Iran*

Abstract

One of the phenomena in storage tanks subjected to earthquake excitations is the sloshing of impounded liquid. The use of baffles for reducing the sloshing effects has been taken into consideration by some researchers in recent years, however, the use of multiple baffles has not been taken into consideration so much. In this study the effect of using multiple vertical baffles in rectangular tanks has been investigated numerically by Finite Element Analyses. After verification of the numerical modeling, tanks with various scales were analyzed subjected to both harmonic and seismic excitations with various intensities to find out the effect of scaling factor. Then, various number of vertical baffles form 1 to 4, were considered at the upper level of the tank and analyses were repeated to realize the effect of baffles on the sloshing. The maximum water level fluctuation was calculated for comparison. Different values were also considered for the submerged depth of baffles to find the more effective depth in decreasing the sloshing effect. Numerical results show that for each series of earthquakes with similar frequency content it is possible to find an optimal number of baffles to minimize the sloshing effect. Also for each number of baffles it is possible to find an optimal submerged depth of baffles for minimizing the sloshing effect.
Keywords: water level fluctuation, scaling factor, hydro-dynamic pressure, THA.

1 Introduction

In tanks subjected to earthquake excitations sloshing of liquid is one of the most important phenomena, and past earthquakes have shown that this phenomenon

WIT Transactions on The Built Environment, Vol 120, © 2011 WIT Press
www.witpress.com, ISSN 1743-3509 (on-line)
doi:10.2495/ERES110241

can result in sever damages to water storage tanks. To prevent tanks against sloshing induced damages, the use of baffles have been suggested and studied by some researchers since mid 60s [1], however, just few studies have been conducted on using baffles for reducing the earthquake induced sloshing effects.

Shaaban and Nash [2], as one of the first works in this regard, in 1977 studied on response of partially filled liquid-storage circular cylindrical tank with or without an interior cylindrical baffle under seismic actions using Finite Element (FE) technique. They worked on an elastic cylindrical liquid storage tank attached to a rigid base slab. Their studied tank was either empty or filled to an arbitrary depth with an in-viscid, incompressible liquid. They presented a FE analysis for both tank and liquid, to investigate the free vibration of the coupled system permitting determination of natural frequencies and associated mode shapes. They employed Sanders shell theory to express the strain-displacements relationship in the derivation of the shell FE. They determined the response of the tank to artificial earthquake excitation, and performed similar investigations with the addition of an elastic cylindrical perforated baffle to control the system natural frequencies.

In 1999 Gedikli and Ergüven [3] worked on the seismic analysis of a liquid storage cylindrical tank with a rigid baffle. In that study the fluid was assumed to be incompressible and in-viscid, and its motion was assumed to be ir-rotational. They implemented method of superposition of modes to compute the seismic response, and used the boundary element method to evaluate the natural modes of liquid in the tank. In that study the linearized free surface conditions was taken into consideration.

In 2000 Yasuki and his colleagues [4] conducted a study on suppression of seismic sloshing in cylindrical tanks with baffle plates. The purpose of that study was proposing the evaluation model of damping characteristics of cylindrical tank with ring baffle plates. They carried out shaking table tests, in which the location and geometry of the baffle plates were varied, with sinusoidal excitation. Their experimental results showed that the damping characteristic is dependent on the location and geometry of baffle plates. Their model for solid baffle plates was extended to be applicable to both solid and perforated baffle plates, and the validity of their evaluation model was confirmed with the experimental results.

In 2007 Maleki and Ziyaeifar [5] conducted a study on damping enhancement of seismic isolated cylindrical liquid storage tanks using baffles. At first, they analyzed the velocity contours in a cylindrical tank to determine the most effective shape of baffle. Then, they determined the damping coefficients analytically for horizontal ring shape and vertical blade shape baffles. To estimate the sloshing height level and the damping ratio, they developed a methodology, based on Tank Body Spectra, in which the higher sloshing amplitude and the relative fluid velocity with respect to baffles in base isolated tanks are taken into consideration. The results of that study show that the average damping ratio of sloshing mode due to ring baffle increases with a decrease in liquid height and highest damping may be achieved for height to radius ratios of 1.0 to 1.5.

Finally in 2010 Wu [6] conducted a thorough study the nonlinear liquid sloshing in a 3D tank with baffles, in which the mechanism of liquid sloshing and the interaction between the fluid and internal structures were investigated. He applied a developed 3D time-independent finite difference method to solve liquid sloshing in tanks with or without the influence of baffles under the ground motion of six-degrees of freedom. He solved the 3D Navier-Stokes equations and transformed to a tank-fixed coordinate system, and considered the fully nonlinear kinematic and dynamic free surface boundary conditions for fluid sloshing in a rectangular tank with a square base. In that study the fluid was assumed incompressible. The complicated interaction in the vicinity of the fluid-structure interface was solved by implementing one dimensional ghost cell approach and the stretching grid technique near the fluid-structure boundaries were used to catch the detailed evolution of local flow field. A PC-cluster was established by linking several single computers to reduce the computational times due to the implementation of the 3D numerical model.

It is seen in the review of the literature that the analysis of baffled tanks in general is very complicated and time consuming, even with just one or two baffle(s). That is possibly why the use of multiple baffles has not been studied so much. In this study the effect of using multiple vertical baffles on sloshing phenomenon in rectangular tanks has been investigated based on conducting several dynamic analysis cases, by using a powerful Finite Element Analysis (FEA) program. The tanks considered for the study, and the details of analyses cases are discussed in the following sections of the paper.

2 Features of the tanks considered for the study

In this study the typical double-compartment aboveground water tanks, used in water supply system in Iran, were used. The general geometric features of the tanks, considered for the study, are shown in Figure 1.

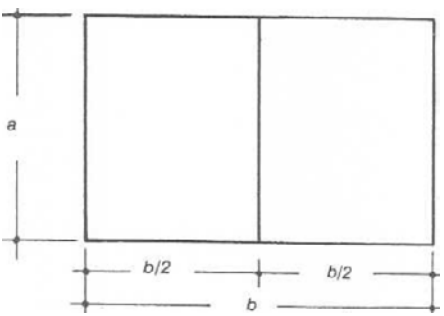

Figure 1: General geometric plan features of the double-containment tanks considered for the study.

To have the minimum length of the tank's wall (to minimize the amount of required construction materials) for a given tank's area, in the case of double-compartment tanks shown in Figure 6, it can be shown easily that *b* should be

around 1.5a. Also usually the water depth in the tank, *h*, is considered not to be less than 0.1 of the width, a, and not more than 6 meters. The common specifications of tanks with different water volumes or capacities, based on the above conditions, are as shown in Table 1.

Table 1: Common specifications of tanks with different water volumes, and their fundamental sloshing period.

The tank water capacity (m^3)	Tank water height, *h*, in the tank (m)	a (m)	*b*=1.5a	*h*/a	*h*/*b*	*T* (sec)
125	3.0	5.270	7.905	0.758	0.569	2.619
250	3.0	7.453	11.180	0.536	0.402	3.197
500	3.0	10.540	15.811	0.379	0.284	4.029
1000	3.0	14.907	22.360	0.268	0.201	5.270
5000	4.0	28.867	43.301	0.184	0.138	8.408
10000	5.0	36.514	54.772	0.182	0.136	9.502
15000	5.5	42.640	63.960	0.171	0.128	10.523
20000	5.5	49.236	73.854	0.148	0.111	12.019
30000	6.0	57.735	86.602	0.138	0.103	13.434

The values of the first or fundamental sloshing modes of tanks in Table 1 have been calculated based on the following formula which gives the natural angular frequencies of sloshing modes in tanks [8]:

$$\omega_n^2 = \pi(2n-1)\left(\frac{g}{a}\right) tanh\,[(\pi(2n-1)\left(\frac{h}{a}\right)] \quad (1)$$

where *n* is the sloshing mode number and *g* in the acceleration of gravity. Based on the above explanations, and considering the exponentially growth of the required computational time with number of elements in the FEA, on the one hand, and the time step size in the time history analysis, on the other, explained in the next section of the paper, in this study the following values were considered as the basic case of the tank for analyses:

a = 1.00 m
b = 1.50 m
h = 0.15 m

By using some appropriate scaling factors these dimensions can be used for tanks of real size, such as those given in Table 1. The scaling requirements are explained in the following section, after the explanation about the finite element modeling and its verification. along with the presentation of numerical results.

3 Finite element modeling and its verification - scaling effects

A powerful FEA program was selected for modeling the tanks in this study. In order to verify the numerical modeling of the tanks in FEA at first the numerical finite element model of a tank, previously tested at the Hydraulic Institute of Stuttgart University on shake table by Goudarzi and his colleagues (results were published in 2010 [7]), was developed by the employed computer program, and the results were compared. Verification results can be found in a previous work of the authors [8], and include the cases of sinusoidal base excitations at the first sloshing mode (resonance), and also a frequency lower the resonance frequency. Another important factor, which affects the required time for the response analysis, is the size of the tank [8]. In fact, the required analysis time for a scaled-down model of a tank is several times less than that of the real tank. The main reason behind this fact is in the size of the time step for analysis of a scaled-down tank. Actually, considering that based on Equation (1) the sloshing frequencies vary inversely with variation of the square root of the tank's length, shown in the equation by 'a', it can be easily seen that the sloshing period in a scaled model, T_m, is related to the sloshing period in the prototype tank, T_p, by:

$$\frac{T_m}{T_p} = \sqrt{\frac{L_m}{L_p}} \tag{2}$$

where L_m and L_p are respectively the length of the scaled model tank and that of the prototype tank. On this basis, it is clear that the sloshing period in a scaled-down model with the length of 1/36 (for example) of the real size tank will be 6 times shorter than the sloshing period in the prototype tank. This means that the size of the time step of the earthquake digitized record, considered for analyzing the scaled-down model, should be also scaled down by the same factor of 6 to keep the proportions of the excitation periods with respect to the sloshing period in the prototype tank. Accordingly, the duration of the record, used for the scaled-down model, will be 6 time shorter than the real record, although the number of time steps is the same as the original record. It is clear that using a much shorter time step in time history analysis leads to much higher convergence rate, which in turn, reduces the required analysis time to a great extent. On this basis, it was decided in this study to use a scaled-down model tank with the length of 1.0 meter, which is almost 1/36 of a tank with 10000 m^3 capacity, as shown in Table 1. This capacity relates to a very common set of tank features, as shown in table 1, with 5.0 m water height, and plan dimensions of 36.5 m by 54.8 m. In the 1/36 scaled-down model with 1.00 meter length and of 0.15 meter water height, the periods of the first three modes can be calculated based on the corresponding natural frequencies given by Equation (1) in previous section. Their values are respectively 1.708, 0.693, and 0.511 seconds.

The last points which should be taken into consideration for increasing the speed of FEA are the width of the tank model. Regarding that in this study the effects of using multiple vertical baffles is the main concern; the base excitation and accordingly the induced sloshing have been assumed to occur in just one main direction of the tank length. On this basis, it was important to know if the

tank's width, which is the dimension in direction perpendicular to the excitation direction, does have any effect on the analyses results. For this purpose various values were considered for the parameter *b* and by using a specific excitation the analysis was repeated, of which the results are shown in Figure 2.

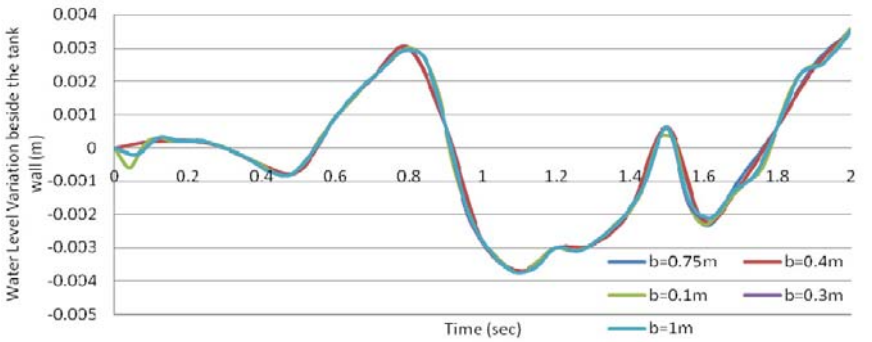

Figure 2: Effect of the width of the tank model on the water level variation when excitation is along the tank's length.

Figure 2 indicates that, as long as the excitation is just in one main direction of the tank plan, the tank dimension perpendicular to the excitation direction does not have any major effect on the response values. On this basis, in all of the next analyses cases, a constant value of 0.1 m was used for the width of the tank model, as shown in Figure 3, to reduce the time required for the analyses.

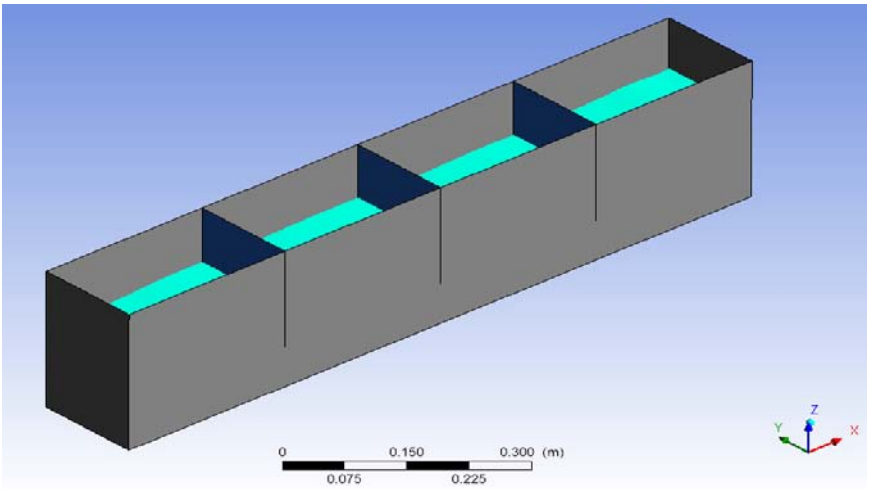

Figure 3: A 3-baffle tank model with reduced width to decrease the time required for FEA.

4 Sloshing response to harmonic base excitations

The first set of dynamic response analyses of the modeled tanks is related to the sloshing response to base harmonic excitation with constant amplitude having the form of $u_b(t) = u_0 sin\omega t, u_0 = 5\ mm$ with the frequency of each of the first 3 sloshing modes. Figure 8 shows a sample of the water surface profile in the case of excitation with the 1st sloshing mode frequency, when various number of baffles are used. In case of using just one baffle it has been considered to be at the middle of the tank's length, and in cases of using 2, 3, or 4 baffles they have been considered equally spaced, so that the tank's length have been divided accordingly into 3, 4, or 5 parts of equal lengths. Figures 4 to 6 show the maximum water level variation beside the tank wall in cases of harmonic excitation with the frequency of respectively the 1st, the 2nd, and the 3rd sloshing mode in the tank, when using no, 1, 2, 3, or 4 baffle(s).

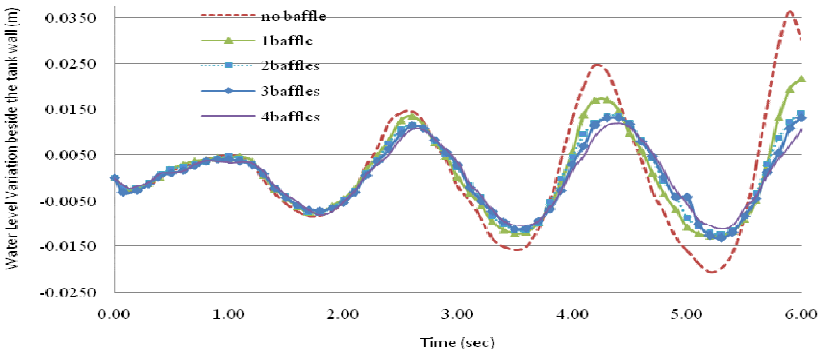

Figure 4: Water level variation beside the tank wall in the first sloshing mode with various numbers of baffles.

It can be seen in Figure 4 that using more vertical baffles results in more reduction in the maximum water level variation, when the excitation frequency is equal to the frequency of the first sloshing mode. Figure 5 shows that when the excitation frequency is equal to that of the second sloshing mode, using two baffles leads to increase, rather than decrease, of the maximum water level variation comparing with the case of using no baffle, however, the maximum water level variation is less than its values in the case of excitation with the first sloshing mode frequency. Also, Figure 5 shows that when the excitation frequency is equal to that of the third sloshing mode, using more baffles again results in more increase in the maximum water level variation comparing with the case of using no baffle, however, the maximum water level variation is less than its value in the case of excitations with the first and second sloshing mode frequencies. Furthermore, comparing Figures 4 to 6 it can be observed that the rate of increase in the maximum amplitude of water level variations, and reaching its steady state response increases with increasing the excitation frequency. This implies that the water body shows larger values of damping when it is subjected to higher frequency excitations. After realizing the effects

of using multiple vertical baffles in sloshing response to harmonic excitations, by considering some appropriate earthquake records the sloshing response to seismic excitations, and the effect of using multiple vertical baffles in that case was studied, as explained in the next section of the paper.

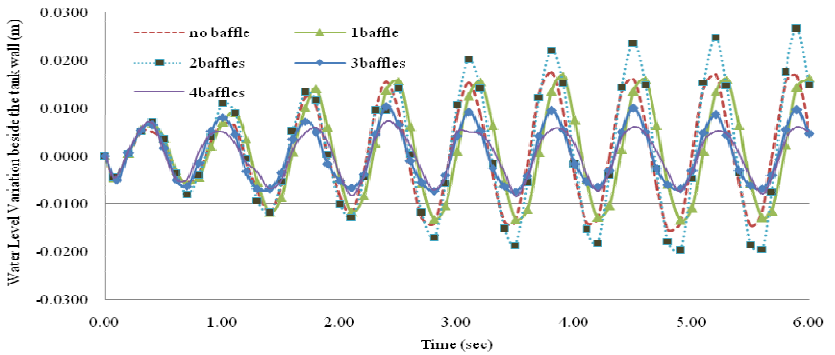

Figure 5: Water level variation beside the tank wall in the second sloshing mode with various numbers of baffles.

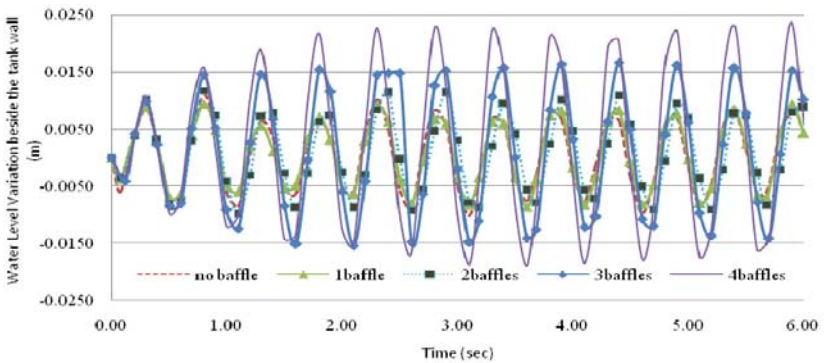

Figure 6: Water level variation beside the tank wall in the third sloshing mode with various numbers of baffles.

5 Sloshing response to seismic base excitations

To investigate the effect of using multiple vertical baffles in the sloshing response in tanks, when subjected to seismic excitations, some earthquake records were considered based on their frequency content, and were applied with various scales. The earthquake records were selected by considering the sloshing frequencies of tanks with real size, which are generally low, for tanks with common sizes, which as shown in Table 1, have sloshing periods in range of 2.5 to 13.5 seconds. Among the available earthquakes, San Fernando earthquake of 1971, Tabas, Iran earthquake of 1978, Northridge earthquake of 1994, Chi-Chi, Taiwan earthquake of 1999, and Kocaeli earthquake of 1999 were considered.

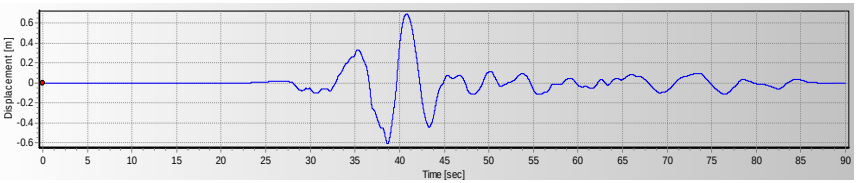

(a) Chi-Chi earthquake (Chy101N record)

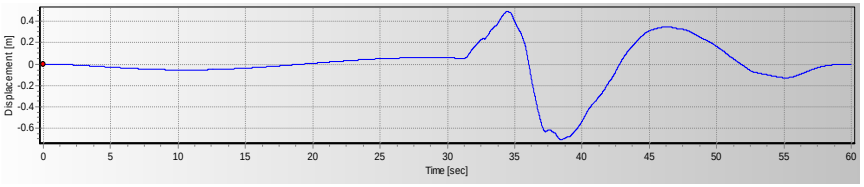

(b) Kocaeli earthquake (Sakarya record)

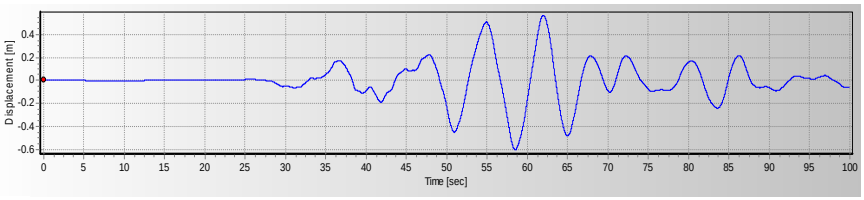

(c) Chi-Chi earthquake (Chy59 record)

Figure 7: The displacement histories of some of the selected earthquakes.

All of the selected records have long period oscillations in their displacement history in the period range of 2.5 to 10 seconds, as it can be seen in Figure 7.

The displacement histories of these earthquakes, when scaled-down in time by a factor of 1/6, as explained in the previous section, have displacement oscillations in the period range of around 0.5 to 1.5 seconds. To reduce the required analysis time, only the 3 to 6 seconds of the strong ground motion parts of the scaled records, containing about 4 to 12 major oscillations, were used in time history analyses. As mentioned before, the variation of water level beside either the tank wall or the baffle(s) is a good response value for studying the sloshing phenomenon and the effect of using baffles on it. These variations, corresponding to scaled versions of some of the aforementioned records, shown in Figure 7, obtained by using the scaled-down tank models, in case of using no baffle comparing to the cases of using 1, 2 or 3 baffles are presented in Figures 8 to 10. More results cannot be given here because of lack of space, and can be found in the main report of the study [9].

It is seen in Figures 6 to 8 that using baffles generally leads to decrease in the water level variations (the maximum water rising), and using more baffles results in more decrease in water level rising. However, similar analyses by using other earthquake records, such as San Fernando, Tabas, and Northridge showed that using more than 3, and in some cases 2, baffles does not change the results so

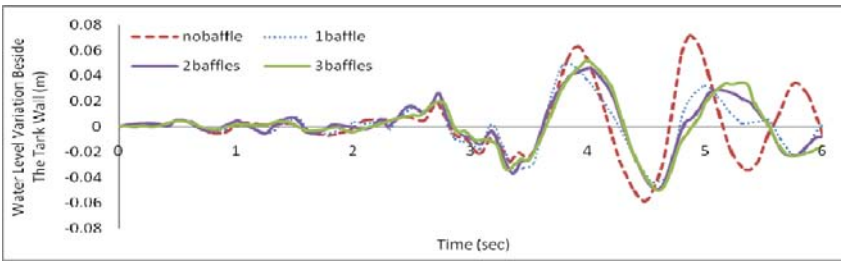

Figure 8: The water level variations beside the wall of 1/15 scaled-down 250 m^3 tank with no, 1, 2, and 3 baffle(s) subjected to the scaled record of Chi-Chi earthquake (Chy101N record).

much. Therefore, it can be recommended that 2 baffles are used in tanks of the sizes around the size of the studied tanks.

The other studied issue was the effect of the submerged depth of the baffle in the sloshing response. For this purpose a tank of 70 cm length and 20 cm width with 50 cm water depth, with just one baffle, subjected to a sinusoidal base motion of $u_b(t) = u_0 sin\omega t, u_0 = 20\ mm\ and\ \omega = 6.55$ (the resonance case) was considered (Figure 9).

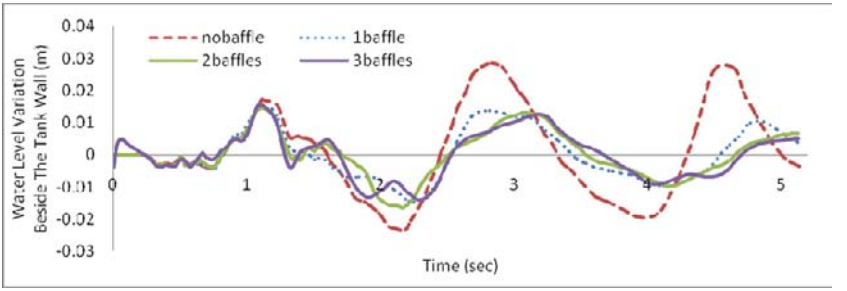

Figure 9: The water level variations beside the wall of 1/36 scaled-down 10000 m^3 tank with no, 1, 2, and 3 baffle(s) subjected to the scaled record of Kocaeli earthquake (Sakarya record).

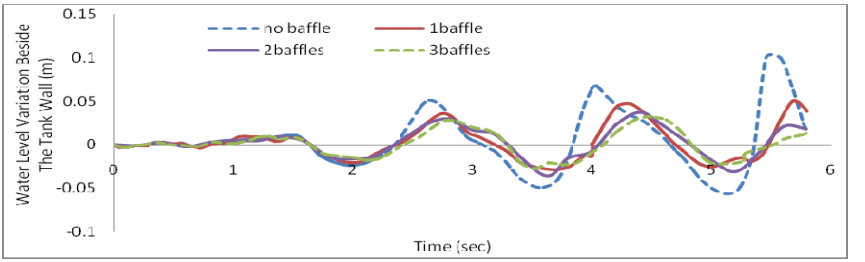

Figure 10: The water level variations beside the wall of 1/20 scaled-down 1000 m^3 tank with no, 1, 2, and 3 baffle(s) subjected to the scaled record of Chi-Chi earthquake (Chy59 record).

Four values were used for the submerged depth of the baffle. The results can be seen in Figure 10.

It is seen in Figure 10 that using a baffle submerged depth of more than 20 cm does not change the maximum water level variations. Therefore, it is recommend to use an optimal submerged baffle depth in each tank based on its geometric features and water depth.

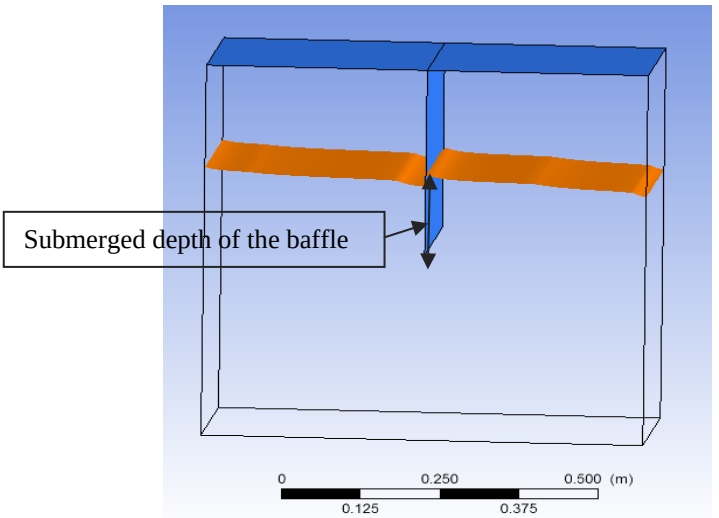

Figure 11: Considered tank for studying the effect of the baffle submerged depth.

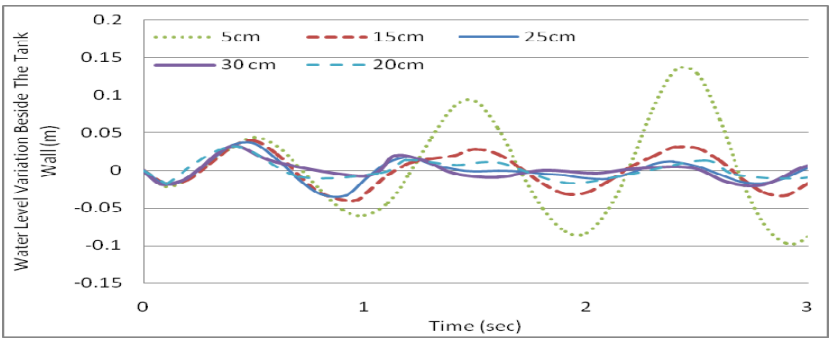

Figure 12: The effect of the baffle submerged depth on the sloshing response.

6 Conclusions

Based on the numerical results of this study it can be concluded that:

- Using scaled down numerical models of tanks, which results in shorter time steps, and accordingly shorter durations, for time history analyses lead to significant reduction of the required analysis time.

- When the excitation is in one of the main directions of the tank, the width of tank model can be chosen as small as 10 cm. This also will lead to reduction of the required analysis time.
- Using 2 or 3 vertical baffles, equally spaced along the tank's length, can reduce the sloshing effect to a great extent, and using more baffles does not change the results so much.
- Using an optimal submerged depth for the baffles is possible, and it depends on the geometric features the tank and the water depth.

References

[1] Abramson, H.N., The dynamic behavior of liquids in moving containers, NASA SP-106, National Aeronautics and Space Administration, Washington DC, 1966.
[2] Shaaban, Samia H. and Nash, William A, Effect of a baffle on response of a liquid storage tank to seismic excitation, *Proc. of Canadian Congress of Applied Mechanics*, Quebec, Canada: Universite Laval, pp 695-696, 1977.
[3] Gedikli, A. and Ergüven, M. E., Seismic analysis of a liquid storage tank with a baffle, *Journal of Sound and Vibration*, Volume 223, Issue 1, Pages 141-155, Elsevier, 27 May 1999.
[4] Yasuki, Otori, Yoshio, Masuko, and Chizuko, Kurihara, Suppression of Seismic Sloshing in Cylindrical Tanks with Baffle Plates (in Japanese), *Denryoku Chuo Kenkyujo Abiko Kenkyujo Hokoku* (Journal Name), No. U98076; 24p, 2000.
[5] Maleki, Abbas and Ziyaeifar, Mansour, Damping enhancement of seismic isolated cylindrical liquid storage tanks using baffles, *Engineering Structures*, Vol. 29, Issue 12, pp 3227-3240, Elsevier, December 2007.
[6] Wu, Chih-Hua, Nonlinear liquid sloshing in a 3D tank with baffles, Ph.D. thesis submitted to Department of Marine Environment and Engineering, National Sun Yat-sen University (NSYSU), Taiwan, 2010.
[7] Goudarzi, M.A., Sabbagh-Yazdi, S.R. and Marx, W., Investigation of sloshing damping in baffled rectangular tanks subjected to the dynamic excitation, *Bulletin of Earthquake Engineering*, 8:1055–1072, 2010.
[8] Hosseini, M. and Farshadmanesh, P., Simplified Dynamic Analysis of Sloshing Phenomenon in Tanks with Multiple Baffles Subjected to Earthquake, *Proc. of COMPDYN 2011, III ECCOMAS Thematic Conf. on Comp. Methods in Struc. Dyn.s and Earthq. Eng.*, Greece, 26–28 May 2011.
[9] Farshadmanesh, P., Optimizing the Use of Baffles in Rectangular Liquid Storage Tanks Subjected to Earthquakes, M.Sc. thesis under supervision of professor Mahmood Hosseini, submitted to Civil Eng. Dept. of the South Tehran Branch of the Islamic University, Tehran, Iran, 2011.

Masonry block construction in Haiti

L. Holliday[1], C. Ramseyer[2] & F. H. Grant[3]
[1]*Division of Construction Science, University of Oklahoma, Norman Oklahoma, USA*
[2]*Department of Civil Engineering, University of Oklahoma, Norman, Oklahoma, USA*
[3]*Department of Industrial Engineering, University of Oklahoma, Norman, Oklahoma, USA*

Abstract

Most of the building failures in Haiti during the January 12th, 2010 earthquake were CMU block buildings. It is the locally preferred building material. Since it is difficult to import materials into Haiti, CMU block is made with local sand (sometimes beach sand which includes a significant amount of salt) and aggregate and only requires Portland cement to be imported. The blocks are made in a press-type machine without steam and at comparatively little pressure. The blocks contain as little as 1/30th Portland cement by volume and are left in a yard to dry cure, rather than moist curing. The blocks are sometimes so weak that they must be handled by workers with two hands or they break under their own weight. Tests at the University of Oklahoma reveal the blocks have an extremely low compressive strength (as low as 300 psi). Given the typical construction techniques used in Haiti, which include heavy concrete slab roof, focusing on hurricane resistance rather than earthquakes, the current CMU block fabrication method was a recipe for disaster that was realized.

OU researchers worked with local Haitian organizations, primarily at Christianville Mission, to improve the quality of CMU blocks in Haiti. They provided guidelines for the CMU block mix, and curing instructions. Tests show the compressive strength of the CMU block has increased by more than three times with relatively little additional cost. This paper discusses the problems with current fabrication techniques for CMU block in Haiti, changes which can be made with relatively little cost or effort, and the resulting improvements in block strength realized.

Keywords: masonry, Haiti, earthquake.

WIT Transactions on The Built Environment, Vol 120, © 2011 WIT Press
www.witpress.com, ISSN 1743-3509 (on-line)
doi:10.2495/ERES110251

1 Introduction and history of Christianville

Christianville has a long and rich history in its mission work for children. It began in the 1960s as an orphanage. Legend has it that "Papa Doc", the infamous dictator of Haiti, originally donated the land for the orphanage and hired a woman from Jamaica to run it. It operated in this mode for several years. One of the sons of that woman, Wayne Herget, is still involved with Christianville. He currently lives in Atlanta, but has spent as much as 15 years living in Haiti and knows the country and local community well.

This mission was expanded to agriculture education, which eventually replaced the orphanage function. It began as an education source for raising pigs, and expanded to raising freshwater fish, primarily Tilapia. This still exists today except that the pig production was replaced by goat production as it is a more efficient conversion of feed to protein. Egg farming was also added about 10 years ago and the mission now produces 800 eggs per day, used primarily for food for the students attending the mission education program. There is also a building owned by the Haitian Fisheries Ministry on the grounds of Christianville. This is an education resource for visiting students and scholars concerned with fish production. It is a recently constructed building but was heavily damage during the earthquake.

A church in Indiana, First Christian, eventually adopted the education component of Christianville and, over many years, built several buildings to support education. These buildings included a preschool, elementary school, high school, and college. Most of these original buildings were destroyed or heavily damaged in the earthquake of 2010. The mission is now working on rebuilding some of those buildings and redefining the scope of its education mission.

Christianville also houses other missions in the form of a medical clinic, and eye clinic, and a dental clinic. These are sponsored by various or individuals agencies in the US. They have little connection to the Christianville education mission other than proximity.

Christianville also hosts mission teams and has a facility to house and feed these teams. Most of them are now focused on repairing or rebuilding damaged buildings. They have two dormitory facilities also with private rooms for some of the longer term volunteers.

2 Building practices and materials

In recent times there has been a shortage of wood in Haiti and this has led to a trend in which building construction there relies heavily on Portland cement. Buildings are sometimes constructed of reinforced concrete but this requires wooden formwork, in a land where 1"x4" wooden formwork pieces are so valuable, they are recycled till they will no longer function. Building with CMU block requires less formwork and therefore it has become the more popular choice for construction. Most buildings seen from the street in Port of Prince are constructed of CMU block walls (or sometimes reinforced concrete walls) with

Figure 1: Typical buildings in Port-au-Prince, Haiti shown following the earthquake.

reinforced concrete slab roofs and floors (Figure 1). After the earthquake it is obvious upon inspection that these buildings were constructed with little steel reinforcement and poor connection details.

3 Lack of building materials and building standards

There are many factors that contribute to the poor quality of construction in Haiti. There are no building or material standards in place to control the quality of construction. In addition to this, years of poverty have slowly reduced the quality of materials made in-country. For example, during building inspections at Christianville, it was noted that older buildings were built with better quality concrete and masonry block. Over the years, in an attempt to save money, the amount of Portland cement used was reduced. In the most recently built buildings, the CMU block was of such poor quality that workers had to handle the blocks with two hands. Otherwise the blocks would break apart under their own weight. In addition to the poor materials used in construction, the methods of construction also reduce building quality. Residents build their own homes and are therefore left to determine the important structural details themselves. In addition to this homes are built slowly as resources are available. If a homeowner is able to save a few funds they put this into building materials as a way to slowly save for a home. This pace makes it difficult to hire craftsmen who would be trained to construct with recommended standards.

4 Performance of CMU block buildings

There were several buildings at Christianville built of CMU block. Of the CMU block buildings there were two different structural systems at Christianville: 1)

buildings built entirely of CMU block and 2) building built of a hybrid of reinforced concrete beams and columns with CMU block walls.

Most of the buildings constructed using CMU were a hybrid of reinforced concrete frames and CMU walls. The reinforced concrete frames are built with little attention to detailing at beam-column connections which results in low moment capacity of the frames [1]. Because of these low moment capacity frame connections, the building relies heavily on the CMU walls to resist lateral loads [2]. Additionally, as seen in Figure 2, it is very common for the second story to cantilever over the first story. This creates a structural irregularity in the perimeter wall system where a great deal of the lateral load resisting system is located.

Figure 2: Newly constructed building which is a hybrid of reinforced concrete and CMU block.

There were seven hybrid buildings at Christainville and of these seven buildings, four were two-story buildings which all collapsed or were damaged beyond repair. The three one- story hybrid system buildings performed better. Only one collapsed, one was severely damaged, and one remained undamaged. It is worth noting that the undamaged building had a lightweight steel roof. Several of these hybrid buildings that failed were newly constructed buildings where the CMU block performed poorly as a shear wall (figures 4-6).

There were four buildings constructed of CMU blocks (without reinforced concrete beams and columns) with light-weight steel roofs that consisted of steel trusses or bar joists with metal panels. All four of these building performed well and showed almost no signs of damage.

Figure 3: Wall shear failure in newly constructed hybrid reinforced concrete and CMU block (left outside view, right inside view).

Figure 4: Newly constructed building with a hybrid system of reinforced concrete with CMU block.

5 Block making in Haiti

CMU blocks used in building construction in Haiti are made locally. They are often made with hand operated mechanical presses as shown in Figure 5. They

Figure 5: Machine used to make CMU block in Haiti.

Figure 6: Sample of Haitian concrete (left) and a typical US concrete sample (right). Note the Haitian concrete is loose and chalky and able to leave a chalk line with very little pressure.

are made with local sand and gravel. These ingredients are often of poor quality. The sand may contain salt and the gravel is typically smooth shaped rather than jagged in shape so the bond to the cement paste is not as strong as it could be. The Portland cement, which is the only imported ingredient, is often of poor quality and visual inspection indicated (by a gritty texture of the powder) that it

was partially hydrated. Workers interviewed said the mix for the block consisted of mostly sand and gravel with as little as 1/30th Portland cement. Rather than having a characteristic gray color found in a properly produced CMU, these blocks have so little Portland cement they are white or yellow in color. The newly constructed blocks are placed (uncovered) in the sun to dry and with no attention to typical curing processes such as controlled humidity. Blocks are not steamed during curing and often formed under little or no pressure. Figure 6 shows a sample of Haitian concrete next to a typical US sample of concrete. Blocks are sometimes so weak that workers must lift blocks with two hands or else blocks fall apart. Visual inspections indicate the block is of poor quality and testing verified this.

6 Testing of CMU block

Samples from several CMU block buildings were tested at the Donald G. Fears Structural Engineering Laboratory at the University of Oklahoma [3–7]. The first set of samples was taken from the buildings damaged during the earthquake. The results from the compression tests of these samples are shown in Table 1. In the case of the building shown in Figures 2 and 3, the mortar coating the blocks had a higher compressive strength than the blocks themselves.

Table 1: Compressive test results for Haitian CMU samples.

Sample description	Compressive strength (psi)
Block samples from the building shown in Figure 4	
Sample 1	745
Sample 2	545
Sample 3	1135
Block samples from the building shown in Figures 2 and 3	
Sample 1	890
Sample 2	555
Samples from an older building (hybrid structural system)	
Sample 1	655
Sample 2 (interior mortar coating)	1908
Samples of Haitian locally purchased CMU block	
Sample 1 (made of local Marl aggregate)	470
Sample 2 (made of river rock aggregate)	493
Sample 3	1538
Sample 4	1282

After confirming the poor strength of the blocks purchased in Haiti, Christianville officials decided to begin making their own block to have greater control over the quality of block used to rebuild. Christianville purchased a block maker (figure 5) and researchers at OU advised the officials on CMU block making. The amount of Portland cement was increased to 1/6th by volume. The sand and/or small aggregate used in the mix was not smooth river

sand and the blocks were moistened during curing. Christianville officials found it difficult to keep the block moist during the entire 28 days of curing, but did moisten the blocks several times a day. Samples of the improved blocks were tested and the results are shown in Table 2. Visual inspection of the samples indicated there is still a portion of the Portland cement that is not activated and therefore there is still room for improvement in the curing process, but overall the compressive strength was improved.

Table 2: CMU block sample compressive strength after improved mix and curing.

Sample description	Compressive strength (psi)
Sample 1	1198
Sample 2	1937

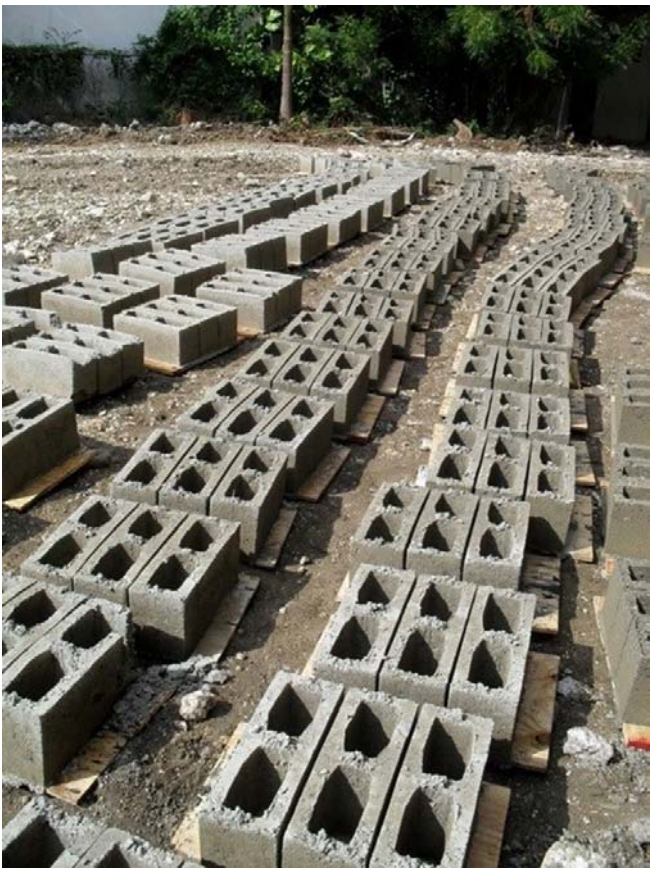

Figure 7: Newly constructed CMU blocks made in Haiti with an improved mix and curing techniques. Note: The improved CMU blocks are now grey in color.

7 Conclusions

Over years of harsh economic conditions in Haiti the quality of building materials steadily declined until the Earthquake of 2010 clearly illustrated these deficiencies. Changing a few key practices in the block making process increased the compressive strength by roughly 200%. The number of samples for testing is small and testing should continue as the production of block continues. In the future, a hand testing machine for easily checking the compressive strength of a block in the field would help control the quality of CMU blocks made in developing areas where commercial testing is not available. The authors are working on the design of a block testing system that can be built in the field. It is based on a lever system with known force (weight) application, without hydraulic measurement. It will be a low cost application that will measure threshold strength of the block for a pass/no pass evaluation.

References

[1] ACI Committee 318,Building Code Requirements for Structural Concrete (ACI 318-08) and Commentary (ACI 318R-08), American Concrete Institute, Farmington Hills, MI, 2008
[2] Masonry Standards Joint Committee (MSJC), *Specification and Commentary for Masonry Structures(ACI 530.1-05/ASCE 6-05/TMS 602-05)*, Farmington Hills, MI, 2006
[3] ASTM Standard C90, *Standard Specification for Loadbearing Concrete Masonry Units (C90-11)* ASTM International, West Conshohocken, PA, 2011
[4] ASTM Standard C1714, *Standard Specification for Preblended Dry Mortar Mix for Unit Masonry (C1714/C1714M-10)*, ASTM International, West Conshohocken, PA, 2010
[5] ASTM Standard C140, *Standard Test Methods for Sampling and Testing Concrete Masonry Units and Related Units (C140-11)* ASTM International, West Conshohocken, PA, 2011
[6] ASTM Standard C270, *Standard Specification for Mortar for Unit Masonry (C270-10*), ASTM International, West Conshohocken, PA, 2010
[7] ASTM Standard C144, *Standard Specification for Aggregate for Masonry Mortar (C144-04)* ASTM International, West Conshohocken, PA, 2004

This page intentionally left blank

Interpretation of microseismic effects from response to large coal mine blasts

C. H. Dowding[1] & J. E. Meissner[2]
[1]*Northwestern University, Evanston, USA*
[2]*University of Illinois, Urbana, USA*

Abstract

Response of a residential structure to ground motions generated by large, surface coal mine blasts can provide information regarding the cracking severity of microseismic events. Microseismic events produced by small earthquakes, mine-collapse and reservoir induced seismicity, etc. can lead to concern on the part of those who feel the ground motion. These concerns can be addressed by reference to low frequency blast generated ground motions that have not caused cracking. This paper presents measured response of a structure to motions producing peak particle velocities of 10 to 19 mm/s and ground displacements of 0.3 mm at 5 to 15 Hz, which can be employed to interpret microseismic phenomena of any sort. Measured responses include velocity responses of the superstructure and midwall as well as vibratory response of existing cracks in walls. Response spectra of these blast generated motions are compared to those generated by moment magnitude five midcontinent earthquakes to determine the relative impact. The structure was inspected for crack extension after each blast and none were found
Keywords: response spectrum, cracking, earthquakes, blasting, mining, micrometer, crack, response, humidity, temperature, climate, microseismic.

1 Response to large surface coal mine blast induced ground motions

This article presents structural and crack response of a test house to unusually high amplitude, low frequency ground motions from surface coal mining. These measurements provide a comparison between excitation and structure response velocities and dynamic and long term micrometer crack response. Comparison of these mine-blast induced excitation ground motions with those produced by a

WIT Transactions on The Built Environment, Vol 120, © 2011 WIT Press
www.witpress.com, ISSN 1743-3509 (on-line)
doi:10.2495/ERES110261

small, moment magnitude five, mid-continent earthquake at the same structure allows an assessment of the potential for cosmetic cracking by small earthquakes and other microseismic activity such as that induced by mine collapse or construction of large reservoirs.

Walls of the house were thoroughly inspected for cracking before and after each blast. The walls were divided into inspection grids, which were visually inspected by the same person in the same fashion in each instance over a period of some 6 months. No new cracks or extensions, not even cosmetic, were observed through the 02 April blast when observation of crack response ceased. (Dowding and Lucole [1]).

The test house was located near a surface coal mine in central Indiana, which involved large-scale cast blasting. The walls, interior and exterior, were constructed with a standard wood stud frame and were covered with gypsum drywall board on the interior and aluminum siding and a half-height brick wall on the exterior. Locations of instruments to measure velocity and crack response in the test house are shown in Figures 1 and 2.

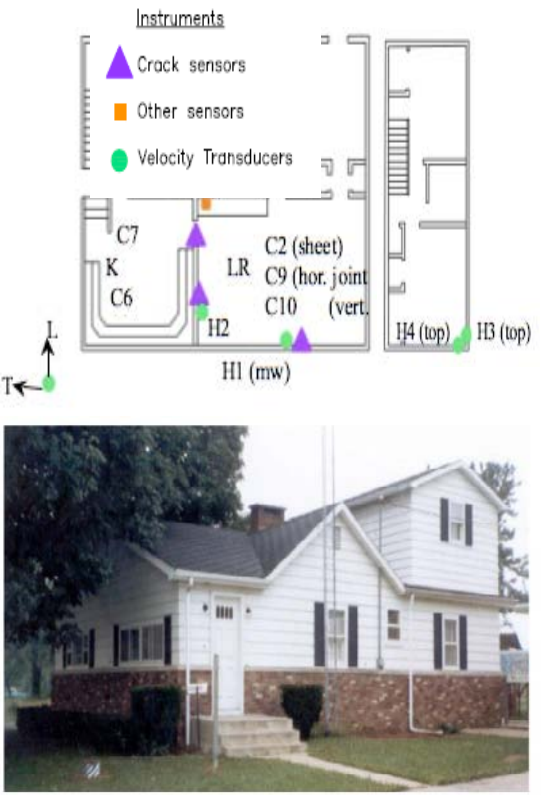

Figure 1: Photograph of test house and plan view showing instrument locations.

Figure 2: Context and details of instrumentation: top - illustration of crack gauges spanning joints and cracks: mid - photograph of the instrumented room: bottom - details of velocity transducers and crack gauges.

A typical coal mine blast, 600 to 360 meters (2000 to 1200 ft) away from the house involved 54, 30 m (100 ft) deep holes arranged in six rows (in a direction radial to the house). Each hole was loaded with ~306 kg (675 lbs) of explosive with four decks and thus ~76 kg of explosive per delay. Such a shot would produce ground motions with peak particle velocities of 0.14 ips to 0.75 ips (3.5 mm/s to 19 mm/s) and dominant frequencies of 5 to 25 Hz (Dowding and Lucole [1]).

Table 1 summarizes three of the most intense of a number of the low frequency, high amplitude ground motions at the test house. As seen in the table, these large and distant surface coal mine blasts produced ground motions both in the 5 to 7 and the 10 to 25 Hz frequency range. These motions bound the natural frequencies of the super structures (5–7) as well as walls and floors (10–25) of residential structures.

Table 1: Summary of excitation and response of test house.

Date	Time	Frequency (Hz)			Peak Velocity (mm/s)							Amplification		Crack Response (μm)		
		L	T	V	L	T	V	H1	H2	H3	H4	Wall	Struct	C7	C9	C10
1-Jan	9:03	21	21	25	19.3	10.4	10.9	72.3	18.2	16	17.9			3		
23-Feb	14:47	28	9	36	10.4	6.6	8.1	25.3	15.4	10.3	8.3	4.23	2.78	1.8	0.7	1.8
2-Apr	14:40	6	9	5	10.2	5.1	7.0	23.6	11.6	24.2	24.9	3.56	2.84	6.4	0.4	3.4

2 Test house and instrumentation

More than a dozen dynamic crack deformation, velocity, and air-blast transducers were continuously monitored by computer to record ground motion and environmentally induced wall and crack deformation. As shown in Figure 1, crack and wall deformation gauges were concentrated in the first floor living room C6, C7, C9 and C10. Ground motions (L, T, and V) particle velocities and air blast overpressure were measured outside at the northwest (upper left in Figure 1) corner nearest the mining. Out of plane, or horizontal, wall motions (H1 and H2) were recorded at mid height and mid span of exterior (H1) and at interior (H2) first-story walls and at an upper corner of the second story (H3 and H4).· Thus H1 and H2 measure wall response, while H3 and H4 measure superstructure response.

Context (top) and details (bottom) of the instrument installation are shown in Figure 2. Instrumented dry wall joints are located in the living room as shown in the upper drawing by dashed lines and center photograph by the white plaster coating over the paper taped joints. Horizontal and vertical un-cracked dry wall joints are C9 and C10. Un-cracked locations near the centers of the drywall sheets are C2 and C6. Drywall joint crack, C7, shown in the bottom right most photograph, is at the doorway (adjacent to C6) between the living room and the kitchen. This crack is not fully extended, and did not extend during the observation period. Out-of-plane, mid-wall motions were measured with Geospace HS1 LT velocity transducers with a flat response between 3 and 250 Hz shown in the bottom left photograph. Ground motions were measured with same velocity transducers.

Micrometer deformation gauges, which measure distance between the sensor and target, allow recording of both static and dynamic opening and closing of cracks because of their long-term stability. Thus long-term phenomena such as change in crack width in response to daily, weekly, or seasonal changes in weather related temperature and humidity, as well as foundation response to changes in the water table can be measured by the same gauge that records the dynamic response to vibrations. A close-up view of one of these gauges, C7, is shown in the bottom right of Figure 2. This inductance deformation gauge measures the proximity of the aluminum target to the magnetic field induced by the sensor. These industrial-grade sensors, manufactured by Kaman, have a resolution of 0.0001 mm (0.004 mil or 0.000004 in.). In the configuration shown they can sense strains as small as 7 micro in/in (μmm/mm.) between bases spaced 15 mm (0.6 in) apart (Kaman [2]). LVDTs can be employed as well (Dowding [3]).

3 Time histories of coal mine blasting ground motions

Figure 3 presents time histories of ground motion (L, V, T) in upper third, wall (H1 and H2) and superstructure (H3 and H4) velocity response in the middle third, and crack C7 and the most active wallboard joint (C10) in the lower third.

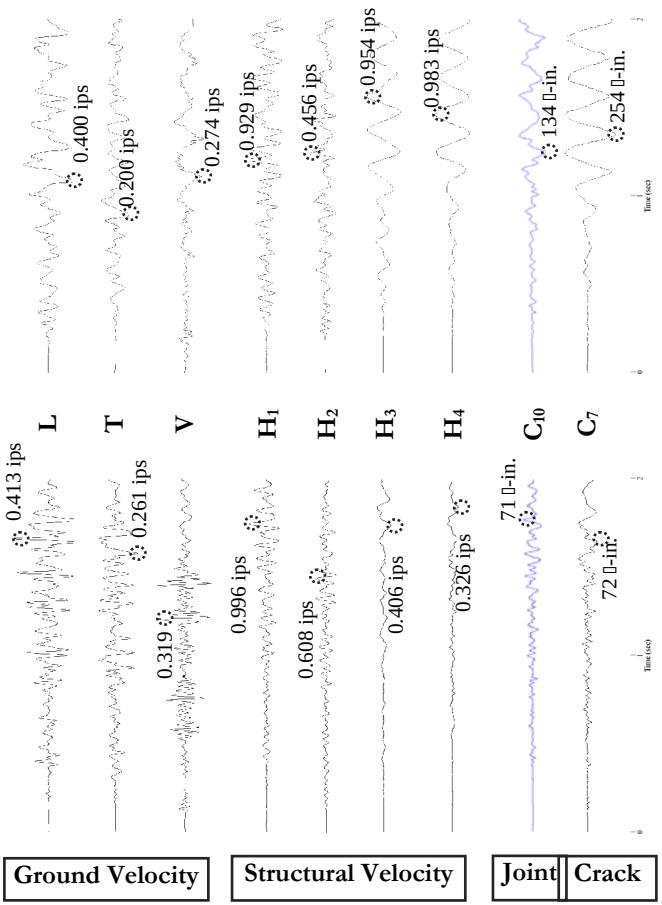

Figure 3: Time histories of blast induced ground motion, structural response, and cracked (C7) and un-cracked drywall joint response (C10). Low frequency excitation shows joint response follows the motion of the upper story. 2/23/87 on the left and 4/2/87 on the right. (1 ips = 25.4 mm/s, 1 μ-in = 0.025 μm).

These excitation and response motions are those associated with blasts on 23 Feb and 2 April that had low dominant frequencies of horizontal ground motion and greatest super structure response (H3 and H4). Peak particle velocities were 10 mm/s in the longitudinal direction. Times of the peak values are encircled in the figures.

These time histories show that the higher frequency components are most effective in exciting the higher natural frequency walls (H1 and H2) and the lower frequency ground motions are most influential in exciting the super structure (H3, H4). As shown in Table 1, the dynamic crack responses are roughly proportional to the peak particle velocity of the ground motions. The vertical drywall joint (C10) responds the most and is more responsive than the horizontal joint (C9). However, its response is still smaller than that for the cracked joint (C7).

4 Moment magnitude five earthquakes at the test house

Three Wabash Valley Seismic Zone (WVSZ) earthquakes are described in Table 2 below. The Wabash River forms the southern boundaries between Illinois and Indiana near the test house. “Seismicity within the WVSZ is thought to occur in a complex horst and graben system of Precambrian igneous and metamorphic units at depths between 12 and 20 km” (Herrmann et al. [4]). The 1987 and 2008 events are associated with similar enough release energies to be directly comparable. While release energy for the 2002 event is smaller, comparisons without conversions can be made because variability of ground motion due to topography and stratigraphy over large distances is larger in magnitude (Street et al. [5]) than differences caused by differences in magnitude.

Table 2: Mid continent earthquakes (After Herrmann et al. [4]).

DATE	TIME	LAT(N)	LON(W)	Mw	Energy
		deg	deg		Ergs x 10^18
19870610	23:48:55	38.71	87.95	4.96	11
20020618	17:37:17	37.99	87.87	4.5	4
20080418	9:37:00	38.45	87.89	5.23	13

These earthquake induced ground motions were also measured by seismographs that monitor mine blast induced ground motions. Blast vibration seismographs are required by law, and thus one or more these instruments are required by law to be located near all coal mines. Since the region surrounding the Wabash Valley contains many surface coal mines, there exists a rich database of earthquake information that is not normally part of typical earthquake networks. The 2005 article by Street et al describes motions from the 2002 earthquake that were recorded at some 46 such stations at epicentral distances of 40 to 180 km.

Digital blast seismographs have capabilities that are similar to modern strong motion seismographs. They record motions in all three orthogonal directions, typically record motions from 5 to 10 seconds, and have a flat response from 3 to 100 Hz (down 10 to 15% at 2 Hz). A set of time histories of horizontal ground motions from the 1987 (100 and 160 km) and 2002 (50 km) events are shown in Figure 4.

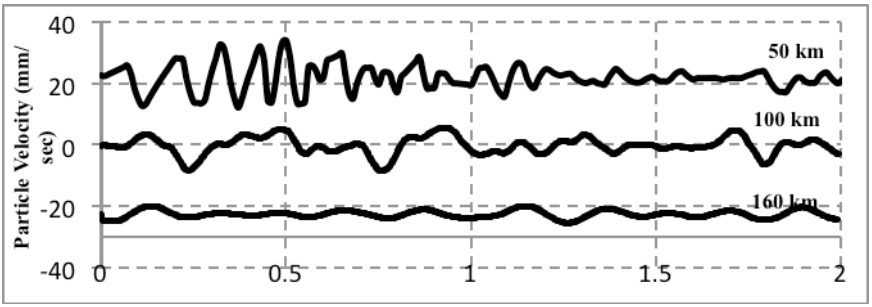

Figure 4: Comparison of moment magnitude 5 motions at distances of 50 to 160 km shows declining amplitude and frequency.

This article introduces structural responses to ground motions from the 1987, Mw 4.96 earthquake that were measured by blast seismographs at Blanford, Indiana and Greenville, Kentucky some 100 and 160 km from the epicenter. These motions were recorded in 2 second segments interspersed with periods of non-recording while the machine stored data. Peak horizontal ground velocities (PHV) measured at these two locations are compared with those measured with strong motion instruments from the equally energetic 2008 event in Figure 5. Peaks recorded with blast seismographs are at the high end of the frequency range of motions measured with strong motion seismographs. Horizontal particle velocities larger than 0.25 and 0.20 cm/s lasted some 10 seconds at the closer and further distances respectively for the 1987 event.

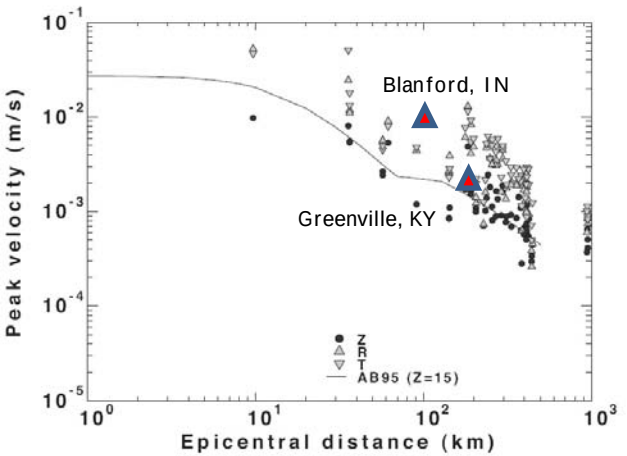

Figure 5: Comparison of peak particle (ground) velocity for 1987, Mw =4.96 event (large Δs) with that for 2008 (Mw = 5.23). From Herrmann et al. [4].

5 Comparison of mid-continent earthquake and large coal mine blast induced ground motions

Five percent damped pseudo-velocity response spectra of the maximum horizontal component of the blast ground motions from Table 1 are shown in Figure 6. None of these ground motions and thus spectra caused cracking in the test structure (Dowding and Lucole [1]). No cracks were caused despite ground motions with a peak particle velocity of 19 mm/s. Therefore any earthquake ground motions whose spectra fall below the dotted lines in Figure 6 in the high frequency region (f > 5 Hz, and T < 0.14 sec for earthquakes) will not cause even cosmetic, hair sized cracking (Dowding [6]).

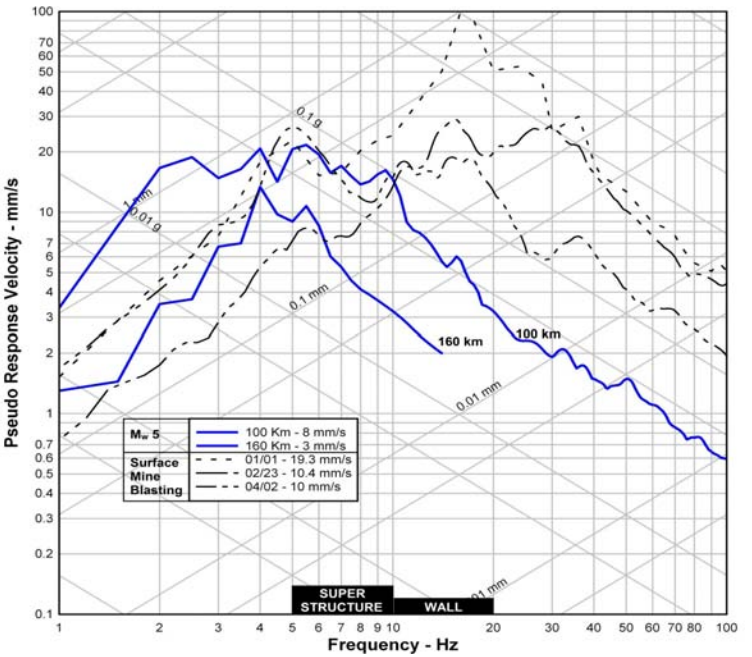

Figure 6: Comparison of response spectra from large surface mining blasts (dotted) that did not cause even cosmetic cracking with those from a moment magnitude five earthquake at distances of 100-160 km (solid lines).

Also shown are maximum horizontal component, pseudo velocity response spectra from the moment magnitude five1987 earthquake in Table 2 measured at 100-160 km. The response spectrum at 100 km was derived from measurements at the test house with the same transducers.

Low frequency mine-blast induced ground motions produce similar pseudo velocities and relative displacements in the frequency range of 5 to 10 Hz as do the earthquake induced ground motions. Mid-continent earthquakes of this

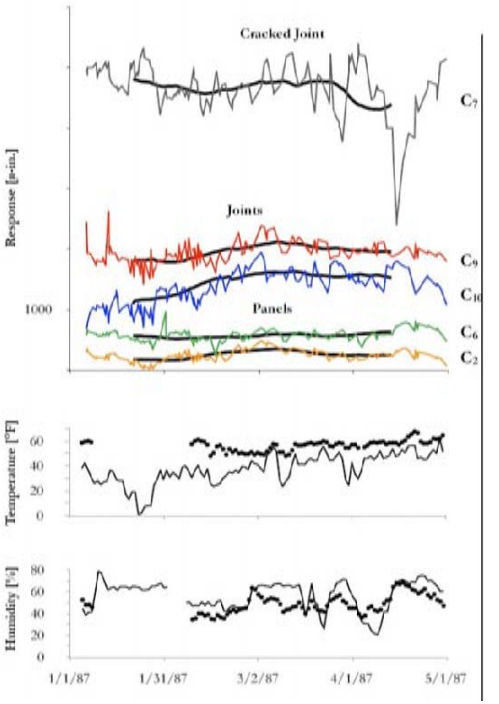

Figure 7: Crack and drywall joint responses compared with time variation of temperature and humidity. In-door temp and humidity (dots) are less variable than out-of-doors (solid line). Crack (C7) is highly responsive to the large, sustained drop in humidity at the end of April.

moment magnitude have return periods of some 6 years. The 5 to 10 Hz range is important because it encompasses the range of natural frequencies for the super structures of typical, 1 to 2 story homes.

Response spectra from the low frequency blast induced ground motions are more easily distinguished from those of the mid-continent earthquake with the frequency abscissa than with a period abscissa. Both sets of ground motions (earthquake and coal mine blasting) result from similar ground displacements, and produce similar relative displacements in the 5 to 10 Hz range. As described below, climatological effects produced an order of magnitude greater change in crack width than did the non-damaging (non-cracking) coal mining ground motions (Dowding [3, 6]).

6 Comparison of climatological and vibratory responses

Figure 7 compares four months of responses of the two un-cracked (C9, C10) and one cracked (C7) drywall joints, and two un-cracked drywall sheets (C2, C6)

to temperature and humidity-induced, climatological effects. Variation in temperature and humidity inside and out is presented on the bottom. Joint, crack and sheet responses are plotted to the same scale at the top for comparison. Responses to other longer-term environmental effects such as changes in the ground water table and frost heave at this structure are described in Dowding [6]. Crack responses in Figure 7 are also compared to those of some 30 others in 20 some other structures in Dowding [3].

Responses at the center of drywall sheets (C2, C6) are small. Positions such as these are regularly used to measure the null response. The null response describes the response of the crack gauge metal and un-cracked mounting material to changes in temperature and humidity. Comparison to the crack response (C7) shows that dry wall sheet response is so small as to be inconsequential compared to the crack response. It is also small compared to the response of the un-cracked paper tape joints.

Responses to long-term climatological effects of the un-cracked, literally paper-thin, plaster covered (and thus weak) drywall joints (C9, C10) are less than 1/10th that of the cracked drywall joint (C7). Significant changes in exterior humidity, marked with circles, seem to drive the largest long-term crack response. The large response of cracks to changes in temperature and humidity has been observed in residential structures constructed with wood frames as in the United Sttes and with and cement block as in Europe (Dowding [3]).

Even for high peak particle velocities (10 to 19 mm/s) and a mix of low (4 to 8 Hz) and higher frequency (9 to 28) excitation motions, climatological response is greater than vibratory response for both un-cracked wall weaknesses (drywall joints) and cracks as shown by the bar chart comparisons in Figure 8. The ratio of dynamic crack response to climatological response is small even for low frequency excitation events. This ratio is 1/10 for typical weather events and even smaller for extreme humidity events such as in April as described in Dowding [3,6].

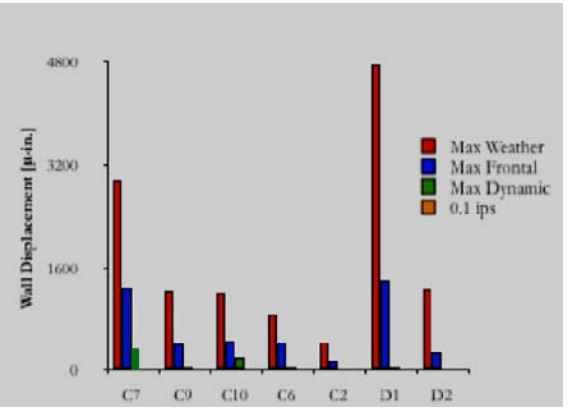

Figure 8: Bar chart comparison of crack/joint/ sheet response induced by weather and dynamic motion.

7 Discussion

Evaluation of ground motions from microseismic events should be based upon considerations of amplitude, dominant frequency, and number of significant pulses at the structures of concern. Such considerations are included in time histories of the ground motion that allows the calculation of response spectra as compared in this paper.

As shown in this paper, residential structures are naturally resistant to low level ground motions. Not even cosmetic cracks are produced or extended by ground motions described in this paper. Other studies by the US Bureau of Mines addressed response of weak wall coverings of residential structures to low frequency blast induced ground motions (Siskind et al. [7]). They should not be overlooked when assessing the importance of human activity induced microseismic events.

Typical changes in humidity and temperature produce far more crack and drywall joint response than typical ground motions. This observation sheds light on the absence of observations of cracking at particle velocities below 12 mm/s (Dowding [3, 6]). At some time in the past climatologically induced distortion has already opened cracks further than at present and typical vibrations do not induce sufficient distortion to exceed this historical state.

8 Conclusions

Ground motions from high intensity, low excitation frequency surface coal mine blasting and distant Mw 5 earthquakes were found to be similar. This similarity allows mining experience to be employed in the assessment of effects from similar microseismic events and small earthquakes when the peak ground motions are similar. Comparison of these events is best made with pseudo velocity response spectra, the details of which are best observed by description with frequency rather than period. Structural and crack response to these surface coal mine blast and microseismic events (when response spectra are similar), can be summarized as follows:

1) Dynamic crack responses are an order of magnitude smaller than those induced by changes in temperature and humidity from a passing weather front
2) Cracks respond more than weak un-cracked joints to both ground motions and climatological effects
3) Ground motions that exceed 12 mm/s and reached 19 mm/s did not extend a highly responsive crack nor did they produce new cracks in the weak paper-plaster joints between wallboards.

Acknowledgements

The authors are indebted to all those who have contributed to this project. The Indiana test house was owned by Peabody Coal Co., without whose cooperation decades ago this project would not have been possible. Instruments were

installed by Digital Vibration Incorporated. We are also grateful for the financial support of the Infrastructure Technology Institute at Northwestern University through its block grant from the U.S. Department of Transportation to develop and deploy new instrumentation to construct and maintain the transportation infrastructure.

References

[1] Dowding, C.H. and Lucole, S.W. Comparison of Environmental and Blast Response. Digital Vibration Report for Peabody Coal Company. 1988. www.iti.northwestern.edu/acm/publications.htm
[2] Kaman Precision Products. Kaman High Performance Non-Contact Position Sensors. 2011. www.kamansensors.com.
[3] Dowding, C.H. Micrometer Crack Response to Vibration and Weather. *International Society of Explosive Engineers*. Cleveland, OH, USA. 2008.
[4] Herrmann, R.B, Wither, M, Benz, H. The April 18, 2008 Illinois Earthquake, An ANSS Monitoring Success. *Seismological Research Letters*. V 79. No. 6. Nov/Dec. 2008.
[5] Street, R., Weigand, J., Woolery, E.W., Hart, P. Ground-motion Parameters of the Southwestern Indiana Earthquake of 18 June 2002 and the Disparity between the Observed and Predicted Values. Seismological Research Letters. V 76. No. 4. July/Aug. 2005.
[6] Dowding, C.H. *Construction Vibrations.* 3rd Ed. Prentice Hall, Saddle River, NJ, USA. 1996.
[7] Siskind, D.E., Stagg, M.S., Kopp, J.W., and Dowding, C.H. Structure Response and Damage Produced by Ground Vibrations from Surface Blasting. *Report of Investigations 8507*. US Bureau of Mines. Washington, D.C. 1980.

Author Index

This page intentionally left blank

Structural Studies, Repairs and Maintenance of Heritage Architecture XII

Edited by: ***C.A. BREBBIA****, Wessex Institute of Technology, UK and* ***L. BINDA****, Politecnico di Milano, Italy*

This book looks deeper into the importance of the historial identity of a region, town or nation. It is clear that we have the necessity to look beyond borders and share experiences and knowledge regarding heritage preservation.
This book contains papers covering the latest advances in this field, presented at the twelfth and latest in a series of now-biennial conferences that began in 1989. The series is recognised as the most important conference on the topic. It covers such topics as: Heritage Architecture and Historical Aspects; Regional Architecture; Preservation of Archaeological Sites; Maritime Heritage; Heritage Masonry Buildings; Adobe Restorations; Wooden Structures; Structural Issues and Restoration; Seismic Vulnerability and Vibrations; Assessment; Retrofitting and Reuse of Heritage Buildings; Surveying and Monitoring; Material Characterisation and Problems; Simulation and Modelling; New Techniques and Materials; Non-destructive Techniques; Experimental Validation and Verification; Performance and Maintenance; Environmental Damage, Social and Economic Aspects; and Guidelines; Codes and Regulations.

WIT Transactions on the Built Environment, Vol 118
ISBN: 978-1-84564-526-7 eISBN: 978-1-84564-527-4
Published 2011 / 784pp / apx £247.00

Learning from Failure

Long-term Behaviour of Heavy Masonry Structures

Edited by: ***L. BINDA****, Politecnico di Milano, Italy*

On March 17 1989, the Civic Tower of Pavia collapsed without any apparent warning sign, killing four people. After an experimental and analytical investigation lasting nine months, the collapse cause was found in progressive damage dating back many years and due mainly to the heavy dead load put on top of the existing medieval tower when realising a massive bell-tower in granite. Other case histories have been collected: the collapse of the St. Marco bell-tower in Venice in 1902; the damages to the bell-tower of the Monza Cathedral; and to the Torrazzo in Cremona. Later on, in 1996 the collapse of the Noto Cathedral showed that similar progressive damage can take place in pillars of churches and cathedrals. Experimental research to demonstrate the reliability of this interpretation has been ongoing since 1989 and is described in the book. After a careful interpretation of the experimental results, also based on experiences from rock mechanics and concrete, the modelling of the phenomenon for massive structures as creep behaviour of masonry was implemented.

The book will help architects and engineers deal with the continuous damage of heavy structures and understand the signs of the phenomenon. It includes models and guidelines for on-site investigation, monitoring and repair of the damaged structures.

Series: Advances in Architecture,Vol 23
ISBN: 978-1-84564-057-6 eISBN: 978-1-84564-298-3
Published 2008 / 256pp / £84.00

Seismic Prevention of Damage

A Case Study in a Mediterranean City

Edited by: ***M. MAUGERI****, Università di Catania, Italy*

The destructive earthquakes of Kocaeli and Düzce in Turkey exemplify the high seismic risk of the Mediterranean area, close to the contact between various tectonic plates and therefore frequently shaken by earthquakes of medium or high intensity.

The scientific, social and political awareness of the seismic risk prompted the Italian Department of Civil Protection to fund a Research Project on earthquake damage scenarios for a high-risk area in the Mediterranean. A subsequent Research Project, focussed on detailed scenarios and actions for seismic prevention of damage, was financed by the 'Istituto Nazionale di Geofisica e Vulcanologia' (INGV).

A multidisciplinary team researched the analysis and mitigation of seismic risk in Catania, a mid-sized Mediterranean city subjected to medium-high earthquake risk. This book summarises the results of the two-year project, which involved geology, geophysics, geotechnical, structural and transportation engineering and urban planning.

The book includes material that will be valuable to many specialists including environmental, civil, earthquake and civil defence engineers, geologists, geophysicists and town planners, and will be a useful guideline for seismic hazard assessment and seismic risk evaluation, prevention and mitigation.

Series: Advances in Earthquake Engineering, Vol 14
ISBN: 1-84564-004-7
Published 2005 / 424pp / £149.00